



HAL
open science

All-optical neurophysiology with scanless two-photon excitation

Imane Bendifallah

► **To cite this version:**

Imane Bendifallah. All-optical neurophysiology with scanless two-photon excitation. Neuroscience. Sorbonne Université, 2023. English. NNT : 2023SORUS241 . tel-04229359

HAL Id: tel-04229359

<https://theses.hal.science/tel-04229359>

Submitted on 5 Oct 2023

HAL is a multi-disciplinary open access archive for the deposit and dissemination of scientific research documents, whether they are published or not. The documents may come from teaching and research institutions in France or abroad, or from public or private research centers.

L'archive ouverte pluridisciplinaire **HAL**, est destinée au dépôt et à la diffusion de documents scientifiques de niveau recherche, publiés ou non, émanant des établissements d'enseignement et de recherche français ou étrangers, des laboratoires publics ou privés.



THÈSE DE DOCTORAT DE SORBONNE UNIVERSITÉ

Spécialité :

NEUROSCIENCES

École doctorale ED158 – Cerveau Cognition Comportement

Préparée au laboratoire de Microscopie d'ingénierie du front d'onde - Département de Photonique

Institut de la Vision – Paris, France

Présentée par

Imane BENDIFALLAH

Pour obtenir le grade de

DOCTEUR DE SORBONNE UNIVERSITÉ

Sujet de la thèse :

All-optical neurophysiology with scanless two-photon excitation

Co-dirigée par

Dr. Serge CHARPAK et Dr. Valentina EMILIANI

Supervisée par

Dr. Ruth SIMS

Présentée et soutenue publiquement le 30 Juin 2023

Devant le jury composé de

Dr. Serge CHARPAK – Directeur de thèse

Dr. Valentina EMILIANI – Co-directrice de thèse

Pr. Sylvain GIGAN – Président du jury

Dr. Amanda FOUST – Rapportrice

Pr. Andrew PLESTED – Rapporteur

Dr. Jérémie BARRAL - Examineur

Dr. Sophie BRUSTLEIN - Examinatrice

Dr. Cathie VENTALON – Examinatrice

*To my father,
For everything*

SUMMARY

Understanding the mechanisms underlying sensory perceptions requires, on one hand, to identify the neurons composing the networks involved, and on the other hand to decipher the spatial and temporal patterns of activation of the different cells in response to a stimulus. Electrophysiological methods have allowed neuroscientists to record and manipulate neuronal activity with high fidelity, but they suffer from poor spatial resolution or have a very low yield. The development of two-photon optogenetics in the last twenty years, along with new complex optical methods, has revolutionized the field of neuroscience by allowing to control as well as record the activity of neuronal populations with single cell resolution, in so-called all-optical experiments.

During my thesis, I worked on the two-photon characterization of tools for both aspects of all-optical manipulation of neuronal circuits. First, in collaboration with the laboratories of Peter Hegemann and J. Simon Wiegert, I characterized a construct composed of an excitatory and an inhibitory rhodopsin (called BiPOLES) under two-photon excitation. Using Computer Generated Holography (CGH) illumination, organotypic hippocampal slices expressing the construct and electrophysiology, I determined the two-photon activation spectrum of the construct and identified the optimal wavelengths for photo-activation and -inhibition. I was able to show that action potentials could be photo-evoked in a reliable manner under 1100 nm illumination, and that 920 nm light inhibited both current- or photo-induced action potentials, via shunting inhibition.

The second part of my thesis consisted of demonstrating the usability of scanless approaches for two-photon voltage imaging in densely labelled samples. Using organotypic hippocampal slices expressing the voltage indicator JEDI-2P and Generalized Phase Contrast (GPC) coupled to temporal focusing (TF) illumination, we were able to optically record single and trains of action potentials up to 125 Hz, with acquisition rates varying from 500 Hz to 1 kHz. We also showed that sub-threshold events (as small as 1 mV) were detectable by averaging. This was illustrated by recordings of spontaneous activity in single and multiple cells. Finally, by co-expression with the soma-localized rhodopsin ChroME-ST, we photo-evoked action potentials and recorded them, enabling to infer the precise timing of the firing of evoked action potentials.

RÉSUMÉ EN FRANÇAIS

Afin de comprendre les mécanismes qui sous-tendent les perceptions sensorielles, il est nécessaire, d'une part, d'identifier les neurones qui composent les réseaux concernés et, d'autre part, de déchiffrer les schémas spatiaux et temporels d'activation des différentes cellules en réponse à un stimulus. Les méthodes électrophysiologiques ont permis aux scientifiques d'enregistrer et de

manipuler l'activité neuronale avec une grande fidélité, mais elles pâtissent d'une mauvaise résolution spatiale ou d'un rendement très faible. Le développement de l'optogénétique biphotonique au cours des vingt dernières années, ainsi que de nouvelles méthodes optiques complexes, a révolutionné le domaine des neurosciences en permettant de contrôler et d'enregistrer l'activité des populations neuronales avec une résolution cellulaire, dans des expériences dites "tout-optique".

Au cours de ma thèse, j'ai travaillé sur la caractérisation biphotonique d'outils pour les deux aspects de la manipulation tout-optique des circuits neuronaux. Tout d'abord, en collaboration avec les laboratoires de Peter Hegemann et de J. Simon Wiegert, j'ai caractérisé une construction composée d'une rhodopsine excitatrice et d'une rhodopsine inhibitrice (appelée BiPOLES), sous excitation biphotonique. En utilisant l'illumination par holographie digitale (CGH), des tranches organotypiques d'hippocampe exprimant la construction et la technique du patch-clamp, j'ai exploré le spectre d'activation biphotonique de la construction et déterminé les longueurs d'onde optimales pour la photo-activation et l'inhibition. J'ai pu montrer que des potentiels d'action pouvaient être photo-évoqués de manière fiable à 1100 nm, et que la lumière de 920 nm permettait d'inhiber les potentiels d'action induits par le courant ou la lumière, via l'inhibition par shunting.

La deuxième partie de ma thèse consistait à démontrer que les approches sans balayage pouvaient être utilisées pour l'imagerie de voltage biphotonique dans des échantillons densément marqués. En utilisant des tranches organotypiques d'hippocampe exprimant l'indicateur JEDI-2P et la technique de contraste de phase généralisé (GPC) couplé à l'approche de focalisation temporelle (TF), nous avons pu enregistrer optiquement des potentiels d'action uniques et des trains de potentiels d'action jusqu'à 125 Hz, à des vitesses d'acquisition variant de 500 Hz à 1 kHz. Nous avons également montré que les événements de faible amplitude (jusqu'à 1 mV) pouvaient être détectés en moyennant plusieurs répétitions. Des enregistrements d'activité spontanée de multiples cellules ont pu être réalisés. Enfin, en co-exprimant la rhodopsine ChromE-ST et JEDI-2P, nous avons photo-évoqué des potentiels d'action et les avons enregistrés, ce qui nous a permis de déduire le moment précis du déclenchement des potentiels d'action.

Contents

SUMMARY	3
RÉSUMÉ EN FRANÇAIS	3
ACKNOWLEDGMENTS	8
LIST OF ABBREVIATIONS	10
I. INTRODUCTION	12
1. Context	12
2. How do neurons communicate?	13
a. Neurons are excitable cells	13
b. Action potentials	15
c. Synapse	16
d. Excitatory and inhibitory post-synaptic potentials: integration of inputs	18
3. Electrophysiology for recording and manipulating the neuronal activity	19
4. Molecular tools for optogenetics and functional imaging	21
a. Delivery strategies	21
b. Actuators to manipulate the neuronal activity	22
c. Fluorescent indicators to read-out neuronal activity	28
5. Optical methods applied to optogenetics and fluorescence functional imaging	35
a. Single- and multi-photon excitation	35
b. Two-photon writing and reading of large neuronal circuits	38
II. CHAPTER 1: Results – Bidirectional manipulation of neuronal activity: BiPOLES	46
1. Motivation and requirements	46
2. State of the art	47
3. Paper	49
Abstract	49
Introduction	49
Results	51
Discussion	68
Methods	71
References	87
4. Discussion	90
a. Other possible combinations	90
b. Perspectives	93
III. CHAPTER 2: Results – Scanless two-photon voltage imaging	96
1. State of the art	96

a. Single-photon voltage imaging	96
b. Two-photon voltage imaging	98
2. Paper: submitted version.....	101
Abstract.....	101
Introduction	102
Results.....	103
Discussion.....	122
Methods.....	125
References	135
Acknowledgements.....	138
3. Discussion.....	139
a. Voltage imaging at 1030 nm	140
b. Outlook	143
IV. CONCLUSION AND FUTURE OUTLOOK.....	144
REFERENCES.....	146
ANNEX: Scanless two-photon voltage imaging: Supplementary Information.....	159

ACKNOWLEDGMENTS

This manuscript compiles the work I have achieved during the past three and a half years. It has been a true adventure with many people involved and I would like to thank them for helping me along the way.

First, I would like to express my deepest and warmest gratitude to the members of the lab:

My supervisor Valentina Emiliani, for giving me the opportunity to pursue a PhD in her lab, believing in me for this project and for patiently listening and guiding me in the more difficult moments. I also want to thank Serge Charpak for accepting to co-supervise my work and for his insights regarding my work.

Ruth Sims, for her friendship, her kind supervision during these years, her infinite patience with which she replied to every question about optics I had and still have, and for making these recordings in the dark and these week-ends working at the lab more fun. I could not have dreamt of a better lab partner.

Eirini Papagiakoumou for her supervision of the project and her investment, but also for her empathy, her patience and her help whenever I needed it.

Valeria Zampini, for her empathy, her advice and the kindness she always shows.

Soledad Domínguez for being the most supportive and fun friend. I am thrilled that you are back in the lab after these years abroad.

Aysha Mohamed-Lafirdeen for her friendship and never-ending support. I wish you the best in the new adventure you are about to start.

Dimitrii Tanese for his participation in the voltage imaging project, as well as for every project we worked together and for always being available to help me and answer my many questions with enthusiasm.

Joe Chan and Christianne Grimm for their participation to the voltage imaging project, and François Blot for helping me make the leap from *in vitro* to *in vivo* preparations.

All the PhD students from the team, past and present, for welcoming me into the office and particularly Ornella Riehm for being the best deskmate one could have.

Christophe Tourain, Vincent de Sars, and Laurence Tricot, for their help, support and for always being so friendly and the other members of the team for their constant support and the kind environment they participated to create.

I wish to thank the members of my Thesis Advisory Committee, Marco Diana and Cathie Ventalon (who also kindly accepted to be part of my thesis jury).

I thank Amanda Foust and Andrew Plested for accepting to review and evaluate this manuscript, and Sylvain Gigan, Jérémi Barral and Sophie Brustlein for accepting to be part of my thesis jury.

All of this would not have been achieved without the support of my family and friends. Therefore, I would like to thank first my father and my mother, for their sacrifice and continual support, as well as my sister and my brother, for the strength they provided me. I want to thank all my friends for their encouragements and particularly Marie for being the best listener possible and Karine for the coffee/lunch/ice cream breaks that made the working days even better.

Finally, I want to thank my three little stars, for shining light on our lives by their presence.

LIST OF ABBREVIATIONS

1P	Single-photon
2P	Two-photon
AAV	Adeno Associated Virus
ACR	Anion Conducting channelRhodopsin
AOD	Acousto-Optic Deflector
CGH	Computer Generated Holography
CHO	Chinese Hamster Ovary
ChR	Channelrhodopsin
ChR1	Channelrhodopsin-1
ChR2	Channelrhodopsin-2
EPSC	Excitatory Post Synaptic Current
EPSP	Excitatory Post Synaptic Potential
FOV	Field Of View
FRET	Förster Resonance Energy Transfer
GECI	Genetically Encoded Calcium Indicator
GEVI	Genetically Encoded Voltage Indicator
GFP	Green Fluorescent Protein
GPC	Generalized Phase Contrast
GPCR	G Protein Coupled Receptor
IPSC	Inhibitory Post Synaptic Current
IPSP	Inhibitory Post Synaptic Potential
KCR	Kalium Channelrhodopsin
LED	Light Emitting Diode
NA	Numerical Aperture
PCF	Phase Contrast Filter
PMT	PhotoMultiplier Tube
sCMOS	Scientific Complementary Metal–Oxide–Semiconductor
SFO	Step Function Opsin
SLM	Spatial Light Modulator
SNR	Signal-to-Noise Ratio
TF	Temporal Focusing
VSD	Voltage Sensing Domain

I. INTRODUCTION

1. Context

Understanding the mechanisms underlying sensory perceptions is one of the main goals of neuroscience. This requires, on one hand, to identify the neurons composing the networks involved and how they are connected to one another, and on the other hand to decipher the spatial and temporal patterns of activation of the different cells in response to a stimulus. Thus, methods capable of recording and manipulating the activity of individual neurons are necessary.

Over the past century, tremendous efforts from neuroscientists have permitted the investigation of neuronal circuits. Electrophysiological methods have allowed neuroscientists to record and manipulate neuronal activity with high fidelity. However, they suffer either from poor spatial resolution in the case of extracellular methods or have a very low yield (intracellular recordings).

The development of optogenetics in the last twenty years, along with the development of *ad hoc* illumination methods, has revolutionized the field of neuroscience by enabling noninvasive mapping of brain function with cell type specificity. Most of these experiments have used visible light to illuminate large regions of the brain and genetic targeting strategies to isolate a specific cell type. However, this experimental strategy can only synchronously activate entire populations of neurons, thereby controlling them as an ensemble, in a non-physiological manner, as neurons fire very complex patterns and sequences when they compute. Therefore, understanding the mechanisms underlying neuronal computation requires more sophisticated illumination approaches that enable to manipulate single cells or subgroups of cells with single cell resolution and millisecond temporal precision. This led scientists to develop new methods of illumination to control the activity of neurons with single-cell resolution, as well as new optogenetic tools allowing fast and efficient responses, and new laser systems to reach an increasingly large number of neurons with minimal photodamage effects. These approaches termed “circuit optogenetics” (Chen, Papagiakoumou, and Emiliani 2018) combined with calcium or voltage indicators open the way for precise all-optical circuit investigation of neuronal circuits.

During my PhD, I worked on the characterization of tools for two-photon bidirectional manipulation of neuronal circuits and reading out of the neuronal activity. The results are described and divided into two main chapters that follow a brief introduction aiming to review the biological and physical principles underlying optogenetics and fluorescence functional imaging.

Chapter I is centered on the two-photon characterization of a new optogenetic construct for the bidirectional manipulation of neurons (called BiPOLES). The corresponding publication is provided.

The second part of my work consisted in the characterization of two-photon scanless imaging approaches for simultaneous voltage imaging and optogenetics in vitro. The results are summarized in Chapter II and the preprint (under review) is attached.

2. How do neurons communicate?

Neurons, or nerve cells, are the signaling units of the nervous system. They are composed of a cell body (or soma), dendrites, an axon and axon terminals. The soma is the metabolic center of the cell, which contains the nucleus, and the endoplasmic reticulum, where proteins are synthesized. Two different kinds of processes arise from the soma: the dendrites and the axon. Dendrites are organized in branches, the so-called dendritic tree, and are the main receiver of inputs from other neurons. The axon is a long tubular process that extends from the soma and carries out the signal to other cells over variable distances, ranging from 100 μm to 1 m (*Debanne et al. 2011*). Inputs received on the dendritic tree propagate to the soma where they are integrated and can lead to the generation of highly stereotypical electrical events, called action potentials, in a specialized region of the axon near its origin, called the axon initial segment. Near its end, the axon branches out to constitute the axon terminals that will contact other neurons at specialized regions of communication called synapses.

The next sections will introduce the molecular and cellular basis of neuronal excitability, and how electrical signals are generated and propagated through the nervous system.

a. Neurons are excitable cells

The excitability of a neuron results from the differences in electrical charges and specific ion concentrations on both sides of the plasma membrane, between the extra- and intra-cellular compartments. Although both the extracellular fluid and the cytoplasmic environment are electrically neutral at rest, the external side of the plasma membrane and the inner surface accumulate negative charges differently, with an excess of net negative charges on the intracellular side of the cell membrane. This leads to a difference in electrical potential (or voltage) across the plasma membrane, the so-called membrane potential (V_m) that can be summarized as:

$$\Delta V_m = V_{in} - V_{out}$$

where ΔV_m corresponds to the membrane potential of a neuron, V_{in} to the potential inside the cell and V_{out} to the potential outside it. In practice, ΔV_m is usually taken as being equal to V_{in} since V_{out} , measured by the grounded reference is equal to 0 mV. The membrane potential varies from its resting value when receiving inputs from other neurons. A depolarization corresponds to an increase of the membrane potential value, whereas a decrease of ΔV_m is called a hyperpolarization.

This resting membrane potential, essential for neuronal excitability, relies on the uneven distributions of distinct ions across the plasma membrane, whose lipid bilayer nature prevents their free diffusion

and acts as a selectively permeable membrane. Ions can only passively cross the membrane through open ion channels or be actively transported through by ion pumps. The cytoplasmic compartment of a neuron is comprised of a high concentration of potassium ions (K^+) and very low amounts of sodium (Na^+) and chloride (Cl^-) ions, whereas the extracellular environment is composed of a high concentration of Na^+ and Cl^- , with a low concentration of K^+ .

At rest, the plasma membrane of neurons is permeable to K^+ and, to a lesser extent, Na^+ via resting or leak channels, which remain open at these membrane potential values and let ions move freely across the membrane. The diffusion of these ions is driven by two forces: 1) the chemical gradient of each ion and 2) the electrical gradient which depends on the electrical membrane potential. For each ion able to diffuse through the plasma membrane, there is a corresponding membrane potential where both forces are exactly balancing each other. This potential, called equilibrium potential, or E_X , can be calculated from the Nernst equation as:

$$E_X = \frac{RT}{zF} \ln \frac{[X]_{out}}{[X]_{in}}$$

where R is the gas constant, T the temperature in Kelvin, z the valence of ion X , F the Faraday constant, and $[X]_{out}$ and $[X]_{in}$ the concentrations of ion X outside and inside the cell, respectively.

Since K^+ ions are highly concentrated in the intracellular environment they tend to diffuse from the cytoplasm of a neuron to the extracellular fluid, which leads to the excess of positive charges on the outer surface of the plasma membrane and the polarization of the cell towards the potassium equilibrium potential ($E_K \approx -90$ mV). In parallel, Na^+ ions diffuse from the extracellular compartment to the cytoplasm, following the Na^+ chemical gradient. As a result, and because the plasma membrane at rest is more permeable to K^+ than to Na^+ , the resting membrane potential obtains a value far from the sodium equilibrium potential ($E_{Na} \approx +55$ mV) and slightly more positive than E_K , where the fluxes of Na^+ and K^+ will be balanced, usually in the range between -60 and -70 mV.

To balance the constant efflux of K^+ and influx of Na^+ that would eventually remove the chemical gradients of both ions (thus reducing the polarization of the plasma membrane), the action of the Na^+ - K^+ pump, an ATPase, is necessary. It uses the energy resulting from the hydrolysis of one ATP molecule to actively transport three Na^+ ions and two K^+ ions against their respective chemical gradients, allowing the K^+ and Na^+ ionic gradients to be maintained. Moreover, since the pump is not electroneutral (it does not transport an equal amount of charge into and out of the cell), its action results in an excess of positive charges outside of the cell, thus participating in maintaining a negative membrane potential at rest. The importance of this function, present in all neurons and most excitable

cells (such as cardiac cells) is such that it is estimated to account for approximately 50 % of the total brain energy consumed (*Erecińska and Silver 1994*).

b. Action potentials

Neurons receive thousands of chemical or electrical inputs on their dendritic tree from other neurons and these inputs can change the balance between ion fluxes, leading to a depolarization or a hyperpolarization of the membrane potential. If the membrane potential is depolarized above a certain threshold (typically around -55 mV), an action potential could be generated as a result of the opening of Na_v channels (those sensitive to voltage, or voltage-gated) in the axon initial segment. These are fast, transient and highly stereotypical electrical events that constitute the signals by which information is propagated and encoded in the nervous system.

The opening of the Na_v channels clustered in the initial segment of the axon renders the membrane more permeable to Na^+ . The following influx of Na^+ exceeds the efflux of K^+ leading to a further depolarization, which causes more Na_v channels to open along the axon, creating a positive feedback loop and thus increasing the speed and the amplitude of the depolarization towards E_{Na} .

Within milliseconds, these voltage-gated Na^+ channels enter a state of inactivation that blocks the conduction of Na^+ ions, as an auto-regulatory process (*Bähring and Covarrubias 2011*). Voltage-gated K^+ channels (K_v channels) exhibit a higher voltage threshold than Na_v channels. As a result, they open later than the Na_v channels, while the latter are already inactivating (*Johnston, Forsythe, and Kopp-Scheinflug 2010*). This results in the repolarization phase of the action potential toward E_{K} (≈ -90 mV). Since K_v channels display slower kinetics than Na_v channels, it takes several milliseconds for all of them to return to their closed state, which can lead to a brief period of hyperpolarization following an action potential [Figure I.2.1].

In the immediate aftermath of an action potential, the still inactivated Na_v channels prevent the generation of another action potential in a period known as the absolute refractory period, which lasts approximately one millisecond. The transition of the Na_v channels from the inactivated state to the resting state, combined with the hyperpolarization due to K_v channels closing kinetics, are the basis of the relative refractory period that can be observed after the absolute one, where another action potential can be evoked, but only following a stronger stimulus than was needed for the first action potential.

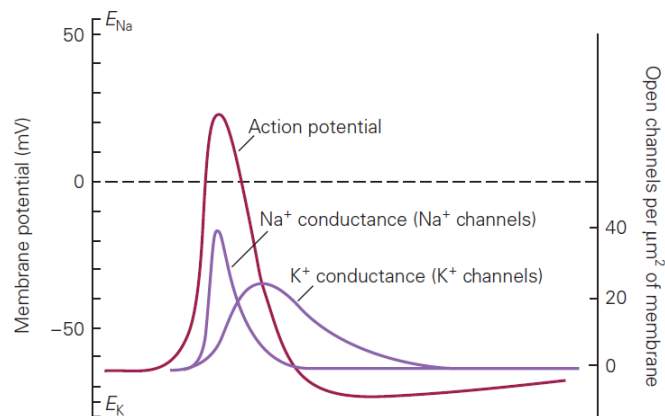


Figure 1.2.1. Schematic diagram of the role of Na⁺ and K⁺ conductances for the generation of an action potential. The rapid opening of the voltage-gated Na⁺ channels induce the fast depolarization step of the action potential (from Kandel et al eds. *Principles of Neural Science*, 6e. McGraw Hill; 2021).

After being initiated in the axon initial segment, action potentials travel along the axon to the axon terminals and the synapses.

c. Synapse

The synapse, first described by Ramón y Cajal at the end of the 19th century, corresponds to the site of communication between two neurons. There are two main types of synapses: electrical and chemical.

Electrical synapses rely on gap junction channels, which are specialized protein structures that provide a structural and cytoplasmic continuity between neurons and allow ion currents to flow between the pre- and post-synaptic neurons. Thus, they are used primarily to send simple and fast depolarizing signals. They are often involved in escape responses in a variety of organisms and also allow the synchronous firing of interconnected cells (Purves and Williams 2004).

Chemical synapses, on the other hand, are composed of a pre-synaptic terminal, a synaptic cleft (the space between the pre- and the post-synaptic neuron, 20 – 40 nm) and the post-synaptic neuron. They are more numerous and complex than their electrical counterparts, but the key difference between the two types of synapses is the ability of chemical synapses to modulate the strength of the connections through a process called synaptic plasticity, essential in memory and learning (Kandel et al. 2021).

Chemical synaptic transmission is accomplished by releasing chemicals known as neurotransmitters, from the pre-synaptic terminal into the synaptic cleft and their binding to receptors in the post-synaptic cell membrane. There can be different types of receptors in a synapse, each receptor being specific to one neurotransmitter and determining the effect of the synaptic potential (excitatory or inhibitory) by the type of ion channels that are gated.

The presynaptic terminal contains synaptic vesicles, each containing several thousand molecules of neurotransmitters. When the action potential arrives at the axon terminal, the membrane depolarization leads to the opening of voltage-gated Ca^{2+} channels. This Ca^{2+} signal induces a signaling cascade that results in the fusion of the vesicles to the plasma membrane and the release of neurotransmitters in the synaptic cleft through a process called exocytosis (Südhof 2012). Contrary to Dale's principle, which states that a neuron releases a single neurotransmitter in each of its synapses, studies have shown that neurons can actually release more than one neurotransmitter (Tritsch, Granger, and Sabatini 2016) which can even be co-packaged in a single vesicle and co-released (Kim et al. 2022).

The neurotransmitters then diffuse through the synaptic cleft to the post-synaptic cell membrane, where they bind to specific receptors. Neurotransmitters can directly or indirectly open specific ion channels that let ions flow through them according to their electrochemical gradient, leading to a transient depolarization or a hyperpolarization of the plasma membrane of the post-synaptic cell in the vicinity of the synapse that is then propagated to the soma [Figure 1.2.2]. The constant activation of the post-synaptic receptors is avoided by eliminating the neurotransmitter molecules from the synaptic cleft, either by reabsorption in the axon terminal or by degradation.

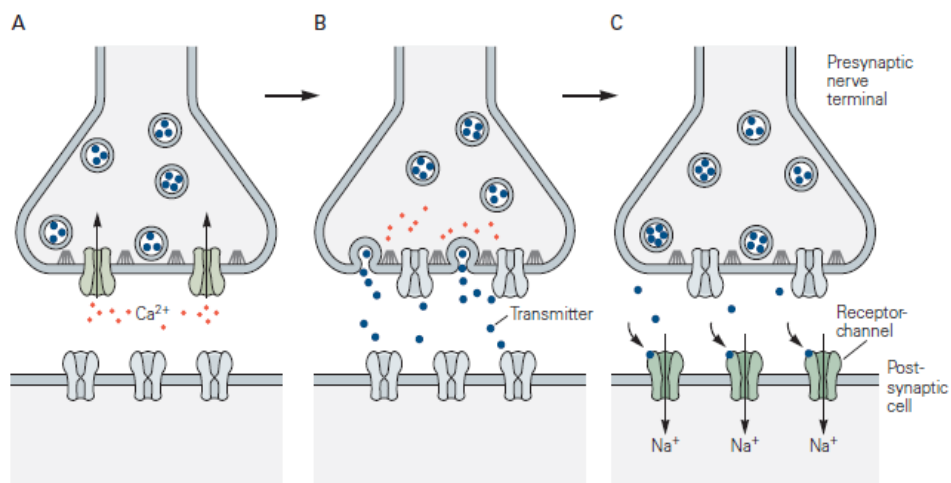


Figure 1.2.2. Schematics of the different steps of the synaptic transmission. (A) The action potential depolarization arrives at the synaptic terminal and induces the opening of voltage-gated Ca^{2+} channels. **(B)** The increase of intracellular Ca^{2+} concentration leads to the fusion of synaptic vesicles to the plasma membrane, releasing the neurotransmitters into the synaptic cleft. **(C)** The neurotransmitters bind to their receptors (here a Na^{+} ionotropic receptor) in the membrane of the post-synaptic cell, opening the pore and letting Na^{+} ions flow through into the cell. (from Kandel et al eds. *Principles of Neural Science*, 6e. McGraw Hill; 2021).

The vast majority of excitatory synapses are glutamate-gated. Glutamate is released by the presynaptic neuron in the synaptic cleft where it can bind to glutamatergic receptors such as AMPA/kainate or NMDA receptors. Once activated, these channels conduct Na^{+} and K^{+} ions with equal permeability, and to some extent Ca^{2+} . On the other hand, inhibition is mainly gated by GABA_A and

GABA_B receptors. GABA_A receptors are ligand-gated chloride channels, which are permeable to Cl⁻ ions. The electrochemical gradient of Cl⁻ leads to the influx of Cl⁻, hyperpolarizing the cell. GABA_B receptors are metabotropic receptors: they mediate inhibition via second messengers that lead to the activation of K⁺ channels and inactivation of voltage-gated Ca²⁺ channels.

d. Excitatory and inhibitory post-synaptic potentials: integration of inputs

Synaptic transmission induces a transient (10 – 20 ms) depolarization or hyperpolarization in the post-synaptic cell, depending on the released neurotransmitter, referred to as Excitatory or Inhibitory Post-Synaptic Potentials (EPSPs or IPSPs) respectively. Typical neurons receive hundreds to thousands of excitatory and inhibitory inputs per millisecond that are spatially and temporally integrated in the dendritic tree and the soma of the postsynaptic neuron through a process called neuronal integration that shapes the response of the neuron to the inputs received. Although the dendritic tree is considered the main receiver of synaptic inputs in a neuron (with axo-dendritic synapses), axo-somatic and axo-axonic synapses are also common. Excitatory synapses are typically axo-dendritic whereas inhibitory synapses occur mostly on the soma, the axon initial segment or the shaft of the dendritic tree.

EPSPs, which can be as small as 1 mV or less, are too small to reach the threshold for the generation of an action potential. PSPs are typically attenuated between the dendrites and the soma of a neuron and the axon initial segment, the region where action potentials are generated. Therefore, many EPSPs must be integrated together to depolarize a cell sufficiently to trigger an action potential. At the same time, however, neurons also receive IPSPs that could prevent the firing of an action potential. Thus, the net effect of these inputs on a neuron depends on several factors. The strength of each connection, functionally defined as the amplitude of membrane potential variation produced in the post-synaptic cell as a response to an action potential in the pre-synaptic cell, is of key importance to determine the output generated as a result of the inputs integration. Moreover, since inputs attenuate while propagating through the neural processes, synapses located close to the axon initial segment are more effective. Indeed, a given postsynaptic current generated on the soma will produce a greater change in membrane potential at the trigger zone of the axon initial segment, and therefore have a greater influence on action potential output than an equal current generated at a distal dendritic spine. Finally, the timing of the signals received also influences the output generated by the post-synaptic neuron. Since EPSPs and IPSPs are transient events that typically last between 10 to 20 ms, they must occur on a short timescale to be summed and have a significant impact on the membrane potential of a neuron.

3. Electrophysiology for recording and manipulating the neuronal activity

Electrophysiology is a field in neuroscience that explores the electrical activity of neurons or brain regions and the cellular and molecular mechanisms that control these signals. A variety of techniques have been developed and refined over the last two centuries, and they offer exquisite temporal resolution. Each of them allows the study of neuronal activity on a different scope.

Electrophysiological methods can be divided into two main categories: extracellular recordings and intracellular ones. In the case of extracellular recordings, a metal electrode is placed in the extracellular environment of a neuron (or neurons) of interest. Action potentials can be detected by measuring the difference of potential between the recording and ground electrodes since they transiently but significantly modify the membrane potential on the outside of active cells. Although it is not possible to record single EPSPs or IPSPs with these methods, extracellular approaches have proved useful to investigate the synchronicity of multiple neurons, to understand how a pharmacological component affects the firing properties of a neuron, or the role of a group of neurons in the processing of a sensory stimulus. Since most of the work of this thesis has been performed using intracellular recordings, and patch-clamp specifically, this section will focus on these types of recordings.

The very first voltage recording of an action potential was performed by Hodgkin and Huxley on the giant squid axon more than 80 years ago, by piercing its plasma membrane with an electrode (*Hodgkin and Huxley 1939*). The development of microelectrodes and micropipettes that followed led to the emergence of the voltage clamp technique, which permitted the recordings of both the membrane potential and the current of individual cells. However, the impalement of the cell membrane generated large leakage currents. Since then, Neher and Sakmann developed the patch-clamp technique that allowed recordings of unprecedented quality (*Neher and Sakmann 1976*). The technique even enabled recording electrical currents from single ion channels, a discovery for which they were awarded the Nobel Prize in Physiology and Medicine in 1991.

Here, a glass micropipette filled with an electrolyte solution and linked to an electrode is approached and pressed against the surface of the cell to be recorded. By applying a gentle suction through the micropipette, it is then possible to establish a high resistance seal (called a $G\Omega$ seal, or gigaseal) between the pipette and the plasma membrane, which creates an electrical isolation and allows ionic currents to flow into the pipette and not through the seal, thus increasing the quality of the recordings.

Different patch-clamp configurations exist and should be used depending on the questions of interest [Figure 1.3.1]. The first one, called cell-attached, corresponds to the creation of the gigaseal described above and is the first step to achieving other configurations. This configuration is mostly used to record

spontaneous cell firing activity or synaptic potentials (Perkins 2006) and displays several advantages, the main one being that the plasma membrane of the cell of interest is not ruptured. Thus, the intracellular environment of the cell is not disturbed, which allows accurate recordings of the membrane potential, and more stable recordings in time.

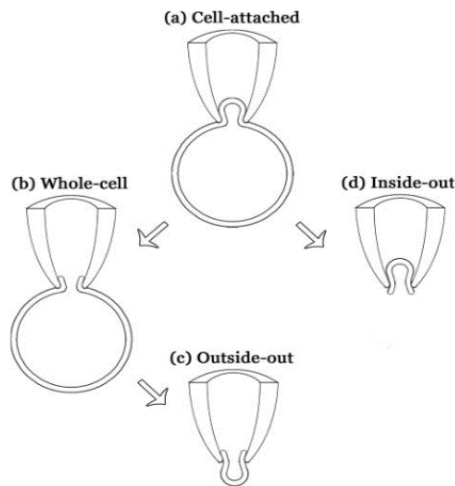


Figure 1.3.1. Schematic diagram of the different patch-clamp configurations. (a) The cell-attached configuration is obtained by creating the gigaseal. (b) The whole cell configuration is achieved by rupturing the cell membrane with suction of electrical zap. From the whole-cell or the cell attached configurations, gently withdrawing the pipette leads to the outside-out (c) or the inside-out (d) configurations respectively. (from Zhao Y. et al, *Proceedings of the Institution of Mechanical Engineers, Part N: Journal of Nanoengineering and Nanosystems*, 2008).

From the cell-attached configuration, it is possible to rupture the patch of plasma membrane attached to the pipette by applying a gentle suction or a voltage pulse. This “whole-cell” configuration, one of the most popular to study electrical activity at the cellular level, is characterized by an electrical and physical continuity between the intracellular compartment of the cell and the pipette. This access to the internal environment of the cell allows the voltage of the whole cell to be controlled or “clamped” at a desired value and to observe the currents generated from all the ion channels at the plasma membrane, for example in response to a pharmacological compound. In current-clamp mode, on the other hand, the current flowing into or out of the cell is controlled while the membrane potential of the cell is free to vary and can be monitored. Thus, action potentials, EPSPs and IPSPs can be recorded at the cellular level.

Although the other configurations were not used in this work, it is still interesting to mention their existence and their uses. They form the group of cell-excised configurations and are particularly useful for studying single ion channels and their unitary ionic currents. Inside-out and outside-out configurations can be obtained by gently withdrawing the pipette from the cell-attached or whole-cell configurations respectively. In both cases, a small patch of the plasma membrane is excised and remains attached to the tip of the micropipette. The difference between the two lies in the side of the plasma membrane in contact with the bath solution, the cytoplasmic one for the inside-out configuration and the outside one for the outside-out configuration. Perfusing pharmacological

compounds in the bath solution allows the study of intracellularly or extracellularly ligand-gated ion channels.

Electrophysiological methods permitted the expansion of our understanding of neuronal activity. They allow the detection of action potentials, and EPSPs and IPSPs in the case of intracellular recordings, with excellent temporal resolution. The techniques, although challenging to perform, have become widely popular to study neuronal activity and brain function.

However, they also display disadvantages that have led scientists to explore other ways of recording and manipulating the neuronal activity. Extracellular recordings allow the recordings of a large population of neurons, but they suffer from poor spatial resolution and it is not possible to excite or inhibit specific neurons using these approaches. On the contrary, intracellular recordings offer excellent spatial as well as temporal resolution, but recording simultaneously from more than a couple of neurons is extremely challenging (*Peng et al. 2019*), especially *in vivo*. Moreover, electrophysiological recordings from small cellular compartments such as dendrites (*Davie et al. 2006*) can be extremely difficult to achieve.

Over the last twenty years, new optical methods have revolutionized the field of neuroscience, with the potential to tackle the issues that electrophysiological approaches cannot solve. They rely on the use of light to manipulate and read out neuronal activity. Tremendous efforts from scientists led to the engineering of multiple probes to optically manipulate and read out the neuronal activity (called actuators and indicators respectively). In parallel, the development of sophisticated optical techniques allowed to achieve the degree of temporal and spatial precision needed to explore neuronal networks, *in vivo*. This will be discussed in depth in the following sections.

4. Molecular tools for optogenetics and functional imaging

a. Delivery strategies

Optogenetics and fluorescent functional imaging require the delivery of actuators and indicators to the neurons of interest. Actuators, and many indicators, are proteins, which means that they can be genetically encoded; the DNA sequence of the protein, under the control of a promoter specific to the neuronal population of interest, can be delivered to these cells to be expressed using the endogenous machinery. This requires a vector that acts as a vehicle to deliver the gene of interest directly into the cell. Several approaches have been developed to deliver genes to cells and they can be classified in non-viral and viral strategies.

Non-viral strategies include electroporation or chemical transfection. In both these approaches, a plasmid containing the transgene is used. Plasmids are circular, double-stranded DNA molecules

capable of independent replication. Electroporation uses short, high-voltage pulses applied to the sample to transiently and reversibly break the plasma membrane, allowing the plasmid to enter the cells. Chemical transfection, on the other side, is based on endocytosis. It uses positively charged lipids that can interact with the negatively charged DNA molecules. This complex cationic lipid – nucleic acid can then interact with the plasma membrane through endocytosis which transfers the DNA into the cell (*Fus-Kujawa et al. 2021*). From then, it can be transported into the nucleus and the proteins of interest can be synthesized. Since plasmids do not integrate into the host genome, expression is transient in mitotic cell populations. Moreover, the transfection efficiency depends on several factors such as the DNA quantity, the ratio of transfection reagent to DNA quantity and the incubation time for the complex lipid – DNA to form. Therefore, a procedure of optimization is often necessary to establish the optimal parameters for efficient transfection.

On the other hand, viral-mediated gene delivery takes advantage of the natural capacity of viruses to enter into host cells and exploit the native transcription machinery to drive the expression of the transgene. Different viral vectors exist among which lentiviruses, adeno-associated viruses (AAVs) or rabies viruses can be distinguished. They all display advantages and disadvantages that need to be considered when planning an experiment. Since I have mainly used AAVs in this work, I will focus on these here. AAVs are composed of a single-stranded DNA molecule trapped in the capsid that forms the envelope of the virus (≈ 20 nm). They display several serotypes with distinct capsid proteins that confer specific properties such as infectivity for a specific cell type or tissue diffusion (*Thompson and Towne 2018*). Serotypes known to efficiently express in the nervous system in mice include AAV 8 and 9 (*Zincarelli et al. 2008*). The main disadvantage of using AAVs is the relatively small packaging capacity which limits the transgene to < 4.7 kb, preventing the use of very large promoters. However, several shorter fragments of promoters can still confer a high level of neural specificity, such as the CaM kinase II α (CaMKII α) that targets excitatory neurons. Moreover, since they do not integrate into the host genome, they display low immunogenicity. Thus, they represent an efficient way to drive long-term expression in non-dividing cells such as neurons.

b. Actuators to manipulate the neuronal activity

The idea of rendering cells sensitive to light to study brain function has driven neuroscientists since Francis Crick suggested in 1979 that the major challenge facing neuroscience was the need to control one type of cell in the brain while leaving others unaltered (*Crick 1979*), and the first proof of principle was performed more than thirty years ago in 1988. Khorana et al showed that the expression of a rhodopsin, a photoreceptor protein, induced a light sensitivity in *Xenopus* oocytes, which then displayed light-dependent ionic currents (*Khorana et al. 1988*). Since then, the discovery of cation-conducting channelrhodopsins in 2002 – 2003 (*Nagel et al. 2002; 2003*), and their use in neurons in

2005 (Boyden et al. 2005), combined with new optical technologies led to the emergence of an interdisciplinary field, named optogenetics. The expression of these rhodopsins under the control of genomic promoters specific to certain types of neurons enabled to precisely target specific neuronal populations of interest. By shining light on these neurons, it became possible to control the activity of precise neurons.

To explore the cellular mechanisms and the networks underlying brain function, precisely timed gain-of-function or loss-of-function of specified events from specific cells may be necessary. In the first case, this would require controlling the action potential firing patterns of multiple neurons with high temporal resolution and fidelity, to replay the neuronal activity that can be observed during a behavioral task, for example. In the second case, being able to inhibit specific responses in neurons could prove useful to understand their roles. Another useful paradigm would be to silence one or multiple neurons over an extended period of time, in reversible “loss-of-function”-like experiments. To do this, efficient tools that generate enough photocurrent, and with kinetics matching the requirements of the experiment to perform are necessary.

i. Rhodopsins

The rhodopsin superfamily is naturally present in a plethora of diverse organisms such as bacteria, plants and animals. Rhodopsins can be divided into two types: microbial (type I) or animal (type II) rhodopsins. Although they do not share any sequence homology, both groups are composed of a seven-transmembrane-domains apoprotein, named opsin that forms an internal pocket for the covalently linked retinal, which acts as the chromophore.

Microbial rhodopsins consist of light-gated ion pumps or channels, that transduce light energy to produce ion currents. Upon photon absorption, the conformational change from all-*trans*-retinal to 13-*cis*-retinal induces a change in the structure of the protein, transiently opening the pore to let ions pass through. They have been the most widely used for optogenetics experiments over the last fifteen years because of their direct action on the membrane potential of a given neuron, similar to endogenous channels involved in neuronal excitability.

Type II rhodopsins are part of the G Protein-coupled receptors (GPCR) family which, when activated, initiate G protein-mediated signaling cascades. The conformational change from the 11-*cis*-retinal to all-*trans*-retinal by the absorption of light energy activates the rhodopsin and the signaling cascade that ensues. They play a role in a variety of stimulus perceptions such as vision and are implicated in circadian rhythms and pupillary constriction (Ernst et al. 2014). The rest of this section will focus mainly on type I rhodopsins, as they are the most widely used in optogenetics.

Microbial rhodopsins exhibit different absorption spectra, activation/deactivation kinetics and ion selectivities, forming an ever-expanding optogenetic toolbox from which scientists can choose the appropriate rhodopsin, depending on the type of experiment to perform.

Rhodopsins are sensitive to visible light, but they do not respond to all wavelengths equally. Indeed, they display an excitation spectrum that can be drastically different between the different rhodopsins. Some like PsChR (*Govorunova et al. 2013*) are more sensitive to blue light while others like Chrimson have more red-shifted spectra (*Klapoetke et al. 2014*). However, it is important to note that all rhodopsins, even the most red-shifted Chrimson, exhibit a non-negligible absorbance in the blue range of their excitation spectra. This property is crucial and must be considered when selecting a rhodopsin, especially if it is to be combined with a fluorescent reporter of activity in an all-optical experiment, to avoid inadvertent activation of the rhodopsin when recording neuronal activity.

Rhodopsins can also be characterized by their activation/deactivation kinetics. Under continuous illumination, the sum of all unitary ionic currents typically displays three phases with kinetics in the millisecond range for most channelrhodopsins. The first phase represents the rise of the photocurrent to reach the peak and is characterized by the time constant τ_{on} . Then the photocurrent decreases to a steady-state (second-phase) before returning to zero after the light is turned off (final phase, characterized by τ_{off}) [Figure I.4.2]. This photocycle can be modeled by a four-state model with two closed states and two open states with different conductances (*Ernst et al. 2008*).

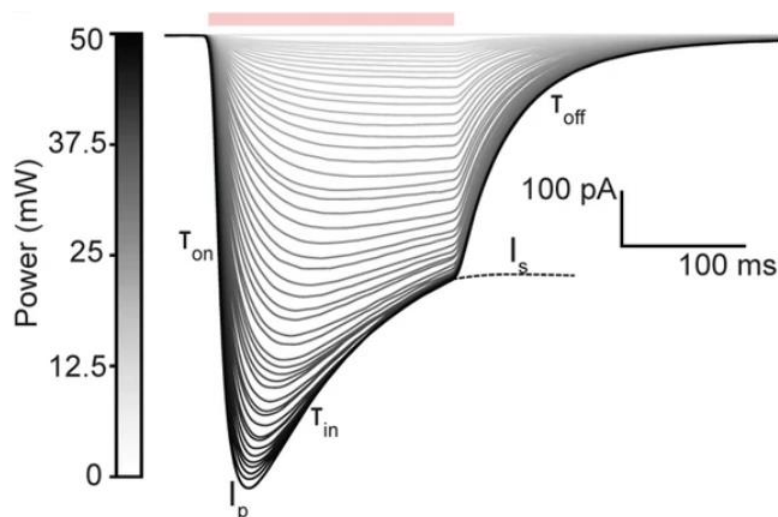


Figure I.4.2. Photocurrent traces recorded in CHO cells expressing the rhodopsin ChRmine. Recordings were acquired in whole cell voltage clamp under two-photon illumination at 920 nm at different powers ranging from 0 to 50 mW. Here, the different characteristics of the photocurrent are labelled. Photocurrent increases with power until saturation is reached. (*from Sims R.R., Bendifallah I., et al. (2023). Optical Manipulation and Recording of Neural Activity with Wavefront Engineering. In: Papagiakoumou, E. (eds) All-Optical Methods to Study Neuronal Function. Neuromethods, vol 191. Humana, New York, NY.*)

The kinetics of channelrhodopsins affect the ability to modulate neuronal activity with high temporal precision. For example, reliably evoking fast trains of action potential requires the use of a rhodopsin with fast off kinetics (short τ_{off}), similar to what is observed endogenously (in the order of the millisecond). However, using this type of fast rhodopsins usually necessitates higher light intensities to trigger action potentials, which may damage the cells and thus, may not be the best option if triggering fast action potential firing is not necessary. On the other hand, slow rhodopsins may prove useful for certain experiments if the necessity for prolonged illumination arises, for example for extended inhibition. Indeed, using an excitatory rhodopsin with slow off kinetics has been demonstrated to induce an extended depolarization called a plateau potential, caused by the persistent inward current generated by the rhodopsin, and may even lead to no more action potentials (Gunaydin et al. 2010).

Finally, the ion selectivity of a rhodopsin and its mode of action (ion pump or channel) is crucial because it will determine if its activation will lead to a depolarization or a hyperpolarization of the cell. This will be discussed more thoroughly in the next two subsections.

ii. Photo-activation

Photo-activation, or photostimulation of a neuron using a rhodopsin relies on a sufficient depolarization of the cell membrane potential, such that it reaches the threshold for the generation of an action potential. Since the single channel conductance of most rhodopsins is three to four orders of magnitude smaller than that of endogenous ion channels (Barrett, Magleby, and Pallotta 1982; Nagel et al. 2003), a first challenge is to achieve a high level of functional expression of the rhodopsin. Several approaches have been applied to improve the level of functional expression. For instance, the addition of soma-targeting sequences, such as the C-terminal targeting sequence from the soma-localized potassium channel Kv2.1, is used to improve membrane trafficking (Gradinaru, Thompson, and Deisseroth 2008). Codon optimization has also been shown to significantly improve expression and has even been used to engineer new rhodopsins (Gradinaru et al. 2010; Wietek and Prigge 2016).

In addition, excitatory channelrhodopsins benefit from being strongly selective to cations that generate depolarizing currents. Since the depolarizing phase of an action potential is mainly driven by Na^+ ions, the ideal excitatory rhodopsin would be one that is highly conductive to these ions.

The first channelrhodopsins to be identified, ChR1 and ChR2 are cation-selective, but their conductances to H^+ ions are 10^6 times higher than their Na^+ and Ca^{2+} ones (Nagel et al. 2002; 2003). Upon activation, cations flow into the cell, inducing a depolarization of the cell that can trigger action potentials. However, the increased concentration of H^+ ions inside the cell shifts the cytoplasmic pH

to more acidic values, thus modifying and potentially damaging the cell physiology under prolonged illumination (Hayward et al. 2023).

To counter this issue, many new excitatory rhodopsins have been engineered, such as ChRmine, a cation-conductive channelrhodopsin that displays a robust Na^+/K^+ permeability under similar ion concentrations found *in vivo* in the mammalian brain, in physiological conditions (Marshall et al. 2019). Nevertheless, proton-permeable channelrhodopsins are still widely used, like ChroME (Mardinly et al. 2018a) or Chrimson (Klapoetke et al. 2014), because the advantages that they display (fast kinetics and red-shifted spectrum respectively) outweigh the issue of acidification that can arise upon extended illumination.

As an alternative to using channelrhodopsins, and although the technique is not strictly part of optogenetics, neurotransmitter uncaging has also proved to be successful and relies on light to photoactivate neurons. In this case, a neurotransmitter (usually glutamate for excitation) is synthetically linked to a chemical “cage”, rendering the caged compound inert. Upon illumination at a specific wavelength, the neurotransmitter is released from the cage and is able to bind to its specific receptors. However, some disadvantages of the technique must be noted. For example, the approach necessitates continuous perfusion of the caged compound in the bath *in vitro*, and complex surgeries and perfusion *in vivo*. Moreover, targeting genetically identified cells can only be achieved by precisely directing light to them, which may represent a challenge if their morphology does not enable them to be distinguished from their neighbors.

iii. Photo-inhibition

Photo-inhibition is the process of using light to silence targeted cells, an essential approach to understand the role of precise neurons in behavior or sensory perceptions. Depending on the question of interest, the requirements for the inhibitory rhodopsins can vary in their kinetics or efficiency. Indeed, some experiments may require extended periods of inhibition, or fast and precise inhibition of specific events. It is then important to choose the rhodopsin with the corresponding characteristics according to the experiment.

The first tools used to silence neurons were light-driven ion pumps. Unlike channelrhodopsins, ion pumps actively translocate ions in one direction only. In optogenetics, chloride (such as NpHR and its more recent variant eNpHR3.0) and proton pumps (such as Arch) are used most widely (Chow, Han, and Boyden 2012). Upon activation by light absorption, they translocate single ions from the extracellular environment to the cytoplasm. Consequently, they necessitate relatively high light irradiance, and extended illumination to generate a photocurrent of a high enough amplitude to efficiently induce inhibition. Despite extensive optimization to improve the membrane trafficking

(*Gradinaru et al. 2010*) and consequently the amplitude of evoked photocurrents, these pumps still suffer from many disadvantages, the main being strong inactivation upon extended illumination (*Wiegert et al. 2017*). This is partly due to the increased or reduced concentration of Cl^- or H^+ ions respectively in the cytoplasmic compartment that inexorably happens since Cl^- and H^+ ions only move in one direction when using pumps, contrary to when using ion channels.

Anion-conducting channelrhodopsins (ACRs), discovered in 2015 (*Govorunova et al. 2015*), are selective to Cl^- ions, which pass through the pore of the channel, according to their electrochemical gradient. ACRs also display a significantly higher conductance (2 folds higher for GtACR2 compared to eNpHR3.0), allowing the generation of large outward photocurrent when the membrane potential is depolarized and shifts away from the equilibrium potential of chloride, which is close to the resting membrane potential of a neuron. This leads to an efficient “shunting” of the membrane depolarization to E_{Cl} , because the depolarization of the membrane potential of the neuron increases the chloride driving force, thus increasing the chloride influx that will balance the current responsible for the activation. However, since the efficiency of ACRs depends on the chloride concentration gradient, Cl^- ions can actually flow outward in cells with a high intracellular chloride concentration, such as neurons in the developmental stages (*Watanabe and Fukuda 2015*), or some compartments, such as the axon, and induce a depolarization instead of a hyperpolarization, and in some cases can even lead to the generation of antidromic action potentials. This issue is also observable when using pumps, like in the case of eNpHR3.0, which has been demonstrated to temporarily change the equilibrium potential of chloride and lead to GABA_A -mediated excitation (*Raimondo et al. 2012*).

Light-gated potassium channels are a good alternative to tackle these issues because K^+ ions are the main ions involved in the repolarization/hyperpolarization phase of the action potential in neurons. Furthermore, since the equilibrium potential of potassium (≈ -90 mV) is more negative than that of chloride (≈ -70 mV), the photocurrent induced is more likely to efficiently hyperpolarize the cell. Constructs have been engineered using neuronal K^+ channels that were modified by addition of photoactive sensing domains and displayed slow kinetics (*Alberio et al. 2018*). These tools, which belong to the class of rhodopsins named step function opsins, can be activated with a short and low-intensity pulse of light and remain open for tens of minutes. Some can even be closed by another pulse of light at a different wavelength (*Rodriguez-Rozada et al. 2022*). On the other side, potassium channelrhodopsins, discovered in 2022, such as Kalium Channelrhodopsins (KCRs) (*Govorunova et al. 2022*) or WiChR (*Vierock et al. 2022*) are extremely promising for fast and precise neuronal silencing. These channelrhodopsins display faster kinetics (in the millisecond timescale) and are highly potent and strongly selective to K^+ ions (despite a small Na^+ conductance). Consequently, one can predict that they will become widely used in optogenetics, for precise inhibition of specific events.

Other methods using light for silencing neuronal activity include GABA uncaging (*Rial Verde et al. 2008*) or synaptic transmission blocking. As an example, eOPN3, a G_i/o -coupled rhodopsin from mosquito, was shown to be able to suppress synaptic transmission through suppression of Ca^{2+} channel activity and inhibition of the induced vesicle release machinery (*Mahn et al. 2021*). However, this approach does not suppress the spiking activity of the targeted cell, only the synaptic transmission. Moreover, it is not activated by two-photon excitation and thus, may not be suitable for all applications.

c. Fluorescent indicators to read-out neuronal activity

As highlighted previously, optical methods are capable of both manipulating and recording neuronal activity. Unlike electrophysiological approaches which directly record the electrical activity, optical approaches usually rely on the change in fluorescence properties (intensity, excitation or emission wavelength) of a fluorescent sensor to translate the neuronal activity. This variation of fluorescence is conventionally measured as the change in fluorescence intensity relative to the resting fluorescence intensity ($\Delta F/F_0$) such as:

$$\Delta F/F_0 = (F_t - F_0)/F_0$$

Where F_t is the fluorescent value at a given time t and F_0 is the resting fluorescence value.

Another important parameter in fluorescent functional imaging is the signal to noise ratio (SNR). It corresponds to the ratio of the signal change to the shot noise of baseline fluorescence (or standard deviation of baseline fluorescence) and can be expressed as follows:

$$SNR = (\Delta F/F_0) \times \sqrt{N}$$

Where $\Delta F/F_0$ is the change in fluorescence intensity relative to the resting fluorescence intensity and N is the number of photons detected (*Hires, Tian, and Looger 2008*).

The SNR describes the quality of the measurement; a SNR value above 1 must be achieved to be able to distinguish a relevant signal from the background noise. Noise can come from two main sources. The shot noise, or photon noise, results from the statistical uncertainty that occur when recording a discrete number of photons over a discrete interval of time and space. The second source of noise is the read-out noise from the camera, that comes from the amplification of the photons detected and the digitization of the signal.

There are different types of functional imaging relying on fluorescence, such as synaptic release imaging (*Marvin et al. 2013; Beyene et al. 2019*), voltage imaging (*Peterka, Takahashi, and Yuste 2011*) or calcium imaging (*Grienberger and Konnerth 2012*). Although all these techniques are now used to read-out neuronal activity, calcium imaging has benefited from tremendous efforts in the

development and optimization of both sensors and optical techniques in the last decades and is consequently the most used technique for reading out neuronal activity in all-optical experiments.

i. Calcium imaging

a. Principle and history

The development of the first calcium indicators in 1980 and their ability to track calcium concentration changes revolutionized the field of life sciences (*Tsien 1980*). Indeed, it became possible to optically record neuronal activity in a less invasive manner than with electrophysiological methods. Since then, numerous efforts have permitted the engineering and optimization of new fluorescent calcium indicators that rely on a variation in fluorescence properties of the indicator binding to the cytosolic Ca^{2+} , to indicate a change in intracellular Ca^{2+} concentration (*Zhou, Belavek, and Miller 2021*).

In neuroscience, calcium imaging is mostly used to detect neuronal activity via action potentials, since the depolarization of the plasma membrane during an action potential induces the opening of voltage-gated Ca^{2+} channels, and an increase in intracellular Ca^{2+} concentration.

b. Different types of indicators

Today, many indicators are available to visualize calcium transients in cells. They can be classified based on their mode of action: ratiometric or intensity-based. Ratiometric indicators (*Grynkiewicz, Poenie, and Tsien 1985; Miyawaki et al. 1997*) allow estimation of the actual Ca^{2+} concentration in the cell based on a difference in absorbance or emission wavelength according to the free or Ca^{2+} -bound state of the fluorescent molecule. Although they allow access to more information on the calcium dynamics, it is the intensity-based indicators that have been preferred to optically read-out the neuronal activity, mostly because they can provide enough information on the firing pattern of the neurons imaged and necessitate the use of only one wavelength [Figure I.4.3]. For this reason, this section will mostly focus on them.

Among intensity-based indicators, dyes and genetically encoded calcium indicators (GECIs) can be distinguished. Dyes are synthetic, fluorescent, Ca^{2+} -binding molecules that need to be loaded into the preparation. Engineering efforts have focused on rendering them more performant (*Paredes et al. 2008*), but despite these efforts, they remain a challenge to use in living animals because of their poor water solubility and their non-specific targeting.

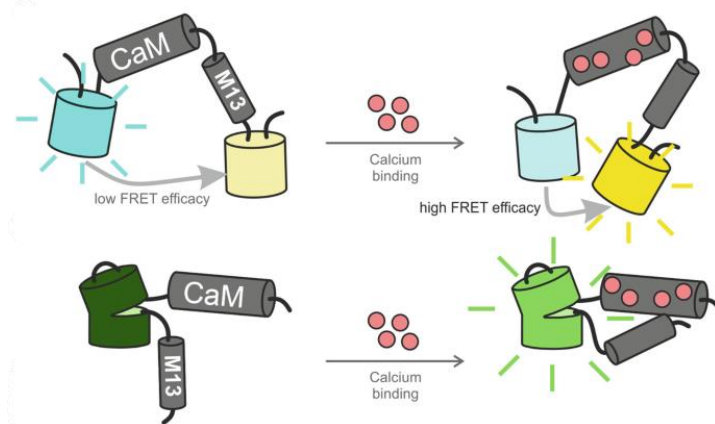


Figure 1.4.3. Schematic diagram of two different types of genetically encoded calcium indicators (GECIs). (Upper) FRET-based GECIs show a low FRET efficacy when free from calcium and a higher FRET efficacy upon calcium binding, following an increase in the intracellular compartment. (Lower) Single-FP-based GECIs, such as GCaMP, undergo a conformational change in the circularly permuted FP, which results in increased fluorescence, upon binding Ca^{2+} ions. (from Mollinedo-Gajate I., Song C., Knöpfel T. *Genetically Encoded Fluorescent Calcium and Voltage Indicators*. In: Barrett, J., Page, C., Michel, M. (eds) *Concepts and Principles of Pharmacology. Handbook of Experimental Pharmacology*, vol 260. Springer, Cham., 2019).

GECIs allow the precise targeting of genetically defined subpopulations of neurons. Their expression is stable over time, which enables recordings to be conducted over long periods, which is useful when studying memory or neuronal development for instance (Jercog, Rogerson, and Schnitzer 2016; Robinson et al. 2020). The last forty years of engineering and optimization have also led to bright and photostable indicators, that display a large $\Delta F/F_0$ in response to calcium transients, in the range of tens of percent for a single action potential for the newest variants (Grødem et al. 2023). These indicators, along with advanced optical methods, are able to report the neuronal activity of hundreds of neurons simultaneously in living animals (Prevedel et al. 2016a; Demas et al. 2021).

Among GECIs, GCaMP and its variants are the most popular for reading out the neuronal activity. They are composed of a circularly permuted GFP coupled to the Ca^{2+} sensing complex Calmodulin – M13. The binding of Ca^{2+} to the calmodulin induces a conformational change in the circularly permuted fluorescent protein, which results in increased fluorescence (Nakai, Ohkura, and Imoto 2001). Due to extensive optimization, they display many advantages such as high $\Delta F/F_0$ in response to single action potentials and good SNR. However, GFP-based GECIs necessitate blue excitation light that can cause phototoxicity. Indeed, organic molecules naturally present in cells can absorb blue light and become degraded, which causes the production of reactive oxygen species. These can oxidize DNA or proteins and induce mutations or render them non-functional respectively (Icha et al. 2017). Furthermore, blue light is highly scattered in tissue because of its shorter wavelength. Finally, as highlighted previously, rhodopsins all exhibit a non-negligible absorbance in the blue range of their excitation spectra. As a result, in an all-optical configuration, the blue light used to image the neuronal activity could induce the inadvertent activation of rhodopsin-expressing neurons, a phenomenon also known as crosstalk.

For these reasons, engineering efforts have also focused on the development of red-shifted GECIs by replacing the GFP with a red fluorescent protein such as mRuby or mApple, but their performances still do not match the GCaMPs ones. Specifically, they are less bright, which results in a decreased SNR and their maximum responses are still three- to four-fold less than that of the GCaMP variants (*Zhao et al. 2011; Akerboom et al. 2013*). Furthermore, some of the red-shifted GECIs exhibit photoswitching, where a transient increase in the red fluorescence can be detected upon blue light illumination. This renders a crosstalk-free combination with a rhodopsin impossible (*Dana et al. 2016*).

Recently, a new type of indicator has been developed. Chemigenetic indicators are hybrids composed of a Ca^{2+} sensing protein (for example the calmodulin – M13 complex) coupled to a circularly permuted protein that can bind synthetic fluorescent dyes (HaloTag protein) (*Deo et al. 2020*). As for intensity-based GECIs, the conformational change induced by the binding of Ca^{2+} to the calmodulin – M13 complex leads to an increase in the fluorescence intensity of the dye. This approach, combined with the use of dyes in the far-red spectrum, has allowed the successful engineering of bright red indicators, which is one of the limitations of the current GECIs.

Even though they are the most widely used fluorescent indicators in optogenetics and all-optical experiments, calcium indicators also suffer from being indirect reporters of electrical activity. Indeed, the kinetics of calcium transients following action potentials are significantly slower than the electrical events. This is due to the delayed inactivation of the voltage-gated Ca^{2+} channels and the kinetics of calcium extrusion that are 10- to 100-fold longer than an action potential (*Dana et al. 2019*). Moreover, the kinetics of the indicators themselves may distort even more the temporal profile of the calcium transients. Therefore, it can be difficult to infer the precise timing of the events, or to follow fast action potential trains. In addition, they are not well suited for detecting hyperpolarizing events or subthreshold activity (EPSPs or IPSPs) in the soma (*Lin and Schnitzer 2016*).

ii. Voltage imaging

a. Technique and inherent challenges

Voltage indicators directly translate changes in the membrane potential of neurons into a variation of fluorescence intensity, overcoming the limitations of the indirect reporters such as calcium indicators. The field emerged more than 50 years ago with the first optical recordings of action potentials (*Tasaki et al. 1968*). But although this approach to read-out neuronal activity is revolutionary, it faces some inherent challenges.

The first challenge originates from the fact that the plasma membrane is very thin (a few nanometers) and the electric field that generates the membrane potential of the cell decreases exponentially with distance from the membrane and is only significant in the Debye length (≈ 10 angstroms). For this

reason, the voltage indicator needs to be in close proximity to the membrane to report the changes in membrane potential, unlike calcium indicators that can bind Ca^{2+} throughout the entire cytoplasm. But because the plasma membrane's overall volume is significantly smaller than the intercellular compartment of a neuron (2 – 7 % of the cell volume for the somatic plasma membrane vs 60 % for the soma), the maximum number of voltage indicator molecules that can be inserted in it, without altering its properties and function, is limited. Their number per cell is thus estimated to be 20-fold less than that of a calcium indicator (*Evans et al. 2023*). This means that the optical signal relies on a low photon budget that can be only partially overcome by illuminating the cells with higher intensities. Unfortunately, this leads to an increasing risk of photobleaching, that can lead to lower and lower signal. Thus, voltage indicators must display a high SNR to be able to report the membrane potential changes with certainty. Since the SNR is proportional to the square root of the number of photons detected, one way to achieve this is to develop very bright indicators whose fluorescence would decrease following a depolarization of the membrane potential. Another way would be to engineer indicators that would display very low baseline fluorescence and brighten with positive voltage changes. This approach proved to reduce the rate of photobleaching by half in some cases (*Abdelfattah et al. 2020*) and possible photodamage that would arise with high illumination intensities.

Another challenge comes from the small amplitude of the signals of interest. Indeed, one of the major goals of voltage imaging is to detect not only action potentials, but also EPSPs and IPSPs. These signals, that can be as small as 1 mV or less, can be extremely challenging to observe optically; the induced change in fluorescence intensity may be difficult to distinguish from the noise without averaging. To tackle this problem, indicators would need to display a high sensitivity in the physiological range of membrane potential (ideally between -90 and + 40 mV approximately). Voltage indicators can effectively be characterized by their sensitivity curves, which represents the $\Delta F/F_0$ as a function of membrane potential change. The ideal voltage indicator to measure EPSPs and IPSPs would show a sensitivity curve with a steep slope around the resting membrane potential, which would mean that the indicator generates large responses to voltage changes in this range (*Bando, Wenzel, and Yuste 2021*). On the other hand, the sensitivity curve could also be shifted towards high amplitude voltage changes to engineer a voltage indicator that would act as an action potential detector.

The last challenge that needs to be met concerns the timescale of the electrical events of interest. For example, an action potential has a typical duration on the order of the millisecond. Thus, the kinetics of the voltage indicators is a crucial parameter. Indeed, an indicator with slow kinetics may not be able to follow precisely the fast depolarization of the membrane potential, which would result in a small variation of the fluorescence intensity and the impossibility to infer the precise timing of the action potential, whereas a fast indicator would be more likely to follow the action potential depolarization

and display a higher optical response. However, if the precise timing of the electrical event to image is not an essential parameter to obtain, a slower indicator would improve the detectability of the event by extending the optical signal in time, enabling to record the activity with lower frame rates and longer dwell time (*Bando, Sakamoto, et al. 2019*).

In summary, the ideal voltage indicator depends on the precise experimental paradigm and the type of events to be detected. The voltage imaging toolbox has been expanded over the last twenty years and it is now possible to find a suitable sensor based on the experiment to be performed.

b. Different types of indicators

As a result of extensive efforts from scientists to develop new probes that would allow the optical recordings of electrical events, many indicators are now available. They can be classified into voltage-sensitive dyes or genetically encoded voltage indicators (GEVIs).

Voltage-sensitive dyes are small fluorescent organic molecules that can insert in the plasma membrane and respond to voltage changes. They were the first type of voltage sensors to be identified and their modes of action include a variety of mechanisms such as repartitioning (where the chromophore moves in or out of the plasma membrane depending on the voltage change), reorientation (where the variation of membrane potential is accompanied by a change in the relative alignment of the chromophore with respect to the membrane) or electrochromism (where the excitation or emission wavelength of the chromophore can be altered by the changes in membrane potential). The kinetics of these dyes, a crucial parameter to record fast neuronal activity, depends on their mechanism of action, from several milliseconds for the slower ones to several microseconds for the fastest ones (*Loew et al. 1985*). They display two main advantages: their molecular brightness and their photostability, which are the reasons why they are still used for reading out neuronal activity despite their inherent drawbacks. Firstly, phototoxic effects (also called photodynamic effects) can be observed as a (sometimes irreversible) reduction of the electrical activity of the illuminated neuron (*Cohen, Salzberg, and Grinvald 1978*), which limits the illumination intensity and recording time. Secondly, it is only possible to target a specific sub-population of cells by loading the dye intracellularly, a technique that is highly invasive and very challenging, even for a handful of neurons (*Canepari, Djuricic, and Zecevic 2007*).

Genetically encoded voltage indicators (GEVIs) have been developed to tackle the latter issue. GEVIs can be categorized into three groups based on their voltage sensing mechanism. The first GEVI (developed in 1997) falls into the first category of voltage sensitive domain (VSD) based GEVIs. Named FlaSh, it was engineered from a VSD of a voltage-gated potassium channel fused to a modified GFP, so that voltage-dependent rearrangements in the VSD induced variations in the fluorescence of the

GFP (Siegel and Isacoff 1997). Since then, numerous efforts have been made to generate more efficient VSD-based GEVIs, by using the VSD of a phosphatase (Murata et al. 2005) and circularly permuted fluorescent proteins (St-Pierre et al. 2014; Chamberland et al. 2017; Villette et al. 2019), with faster kinetics (on the millisecond timescale) and higher $\Delta F/F_0$ that can reach now 50 % for a 100-mV change in membrane potential (Zhuohe Liu et al. 2022a). Most VSD-based GEVIs are negative-going indicators, and despite efforts to make them brighter, they still suffer from a relatively low SNR when imaged at high sampling rates compared to other GEVIs. However, they have still been successfully used to record neuronal activity *in vivo*, up to 400 μm deep in the mouse brain (Zhuohe Liu et al. 2022a). Some other attempts have been made to engineer positive-going indicators, that display more than 100 % $\Delta F/F_0$ for a 100-mV voltage change (Evans et al. 2023). Other VSD-based GEVIs exploited FRET between two fluorescent proteins with overlapping absorption and emission spectra respectively (Akemann et al. 2012). Here, the voltage-induced change of conformation of the VSD induces an energy transfer between the donor protein and the acceptor one, increasing the fluorescence intensity of the acceptor. The ratio of signals between the donor and the acceptor pair allows to distinguish signals due to voltage changes from artifacts due to sample motion, heartbeat or blood flow *in vivo* for instance. Nevertheless, engineering large responses with FRET VSD-based GEVIs has proven to be difficult (Lin and Schnitzer 2016).

A second type of GEVIs utilizes microbial rhodopsins as voltage sensors. They rely on the fluorescence generated by the rhodopsin itself upon protonation of the retinal Schiff base, which links the retinal to the apoprotein. With these indicators, a change in membrane potential alters the electrochemical potential of protons on the Schiff base, and therefore alters the fluorescence of the protein. The first rhodopsin-based GEVI (proteorhodopsin optical proton sensor, or PROPS) was not usable in eukaryotic cells because it could not localize in the plasma membrane (Kralj et al. 2011) but other constructs have been able to successfully record action potentials, such as Archon (Piatkevich et al. 2018). However, despite their sub-millisecond kinetics and large responses of 30 to 90 % $\Delta F/F_0$ for a 100-mV voltage change, their low brightness, due to a quantum yield significantly lower than that of the GFP (< 0.01 versus 0.79 for GFP), renders them difficult to use without large illumination intensities (Gong 2015). To overcome this, rhodopsins have been combined with fluorescent proteins to achieve significantly brighter indicators. In this configuration, the absorption spectrum of the rhodopsin is overlapping with the emission spectrum of the fluorescent protein. Therefore, the fluorescent protein serves as a FRET donor while the rhodopsin acts as a FRET acceptor. When the membrane potential gets depolarized, a change in the absorption spectrum occurs in the rhodopsin, which can be measured by the quenching of the combined fluorescent protein, consequently decreasing the fluorescence of the sensor through a mechanism called electrochromic FRET, or eFRET (Bando, Grimm, et al. 2019). This

allowed the development of indicators capable of achieving higher SNR, while keeping the advantages of rhodopsin-based GEVIs, namely fast kinetics and large responses properties (*Gong et al. 2015; Kannan et al. 2018; 2022*).

This eFRET approach has also been used recently in hybrid (or chemigenetic) indicators (Abdelfattah et al. 2019b). They combine a dye-capture protein domain, the HaloTag, to a microbial rhodopsin. Since it uses synthetic dyes that were developed to be bright and photostable, this technique has allowed the engineering of promising indicators that exhibit the same advantages as the rhodopsin-based GEVIs.

Over the last fifty years, extraordinary efforts have been made to develop the most efficient probes for fluorescent functional imaging as well as optogenetics. Scientists have focused on engineering indicators of neuronal activity and actuators with various properties, including kinetics, brightness or absorption/emission spectrum. Combined with the development of new and sophisticated optical methods, this has allowed to investigate neuronal function in a less invasive manner.

In the next section, I will review the most used optical approaches for optogenetic and imaging as well as the physical principles of single- and two-photon excitation.

5. Optical methods applied to optogenetics and fluorescence functional imaging

The most popular approaches for optogenetic stimulation and functional imaging use widefield visible light illumination, also referred as widefield single-photon excitation. Indeed, the absorption spectra of both rhodopsins and probes for functional imaging fall in the visible range. This technique enables efficient excitation of large brain regions but does not achieve single cell resolution. Confocal microscopy does achieve it, but only offers a short penetration depth and therefore is not adapted for single cell photostimulation or imaging in depth. These limitations can be solved by replacing single-photon excitation with two-photon excitation, an approach which has transformed the last decades of neuroscience research, as recognized by the Brain Prize in 2015 given to its pioneers Winfried Denk, Arthur Konnerth, Karel Svoboda and David W. Tank.

In the following section, I will present the principles of single- (1P) and two-photon (2P) excitation and discuss the challenges to use 2P excitation for optogenetics and functional imaging.

a. Single- and multi-photon excitation

In single-photon (1P) excitation, one photon of an appropriate wavelength is absorbed by an atom, ion or a molecule, which induces the promotion of an electron to a high energy state (S1). Once excited, the molecule relaxes to the lowest vibrational state of S1 before returning spontaneously

from its "high" energy state to its original ground state (S_0). This return to the fundamental state is accompanied by the emission of a photon which energy corresponds to the difference between the ground and excited levels [Figure I.5.1, left]. In the case of rhodopsins, this absorption phenomenon leads to the photoisomerization of the retinal from the all-*trans* to the 13-*cis* configuration, which leads to the opening of the channel that will let ions pass through or to the translocation of one ion in the case of pumps.

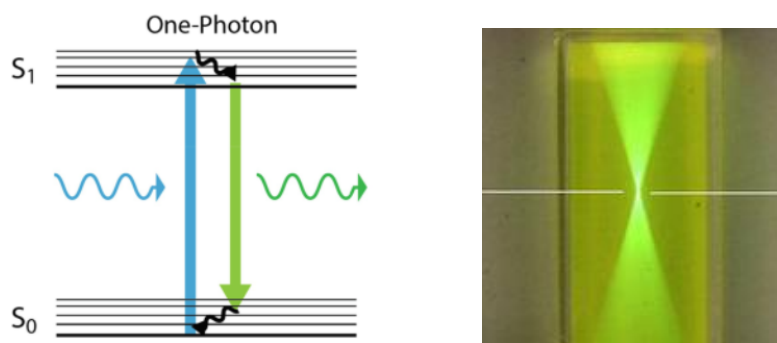


Figure I.5.1. Single-photon excitation. (Left) Simplified Jablonski diagram showing the absorption of a single photon of suitable wavelength is sufficient to reach the excited state S_1 . The return of the excited molecule to the ground state S_0 is accompanied by the emission of another photon of lower energy. (adapted from Sancataldo, G., Barrera, O., Vetri, V. *Two-Photon Imaging*. In: Nechyporuk-Zloy, V. (eds) *Principles of Light Microscopy: From Basic to Advanced*. Springer, Cham., 2022). **(Right)** Excitation volume generated by single photon excitation. White line represents the focal plane. (adapted from images from Xu research group, [url](#)).

1P excitation is a linear process, since the probability of absorption of the exciting photon by the molecule is proportional to the light intensity, which means that all elements reached by the illumination light will be excited [Figure I.5.1, right]. In optogenetics, this implies that the targeting of the neurons relies exclusively on the genetic targeting which leads to the possible inadvertent activation of cells out of the focal plane. In the case of 1P functional imaging, out-of-focus fluorescence can be generated, possibly inducing a deterioration of the SNR. Avoiding this requires confocal approaches, where a focused laser beam (a diffraction limited spot) is raster scanned across the field of view using galvanometric mirrors. A pinhole aperture, placed in the image plane in front of the detector, allows the fluorescence emitted from the focal plane to pass through it to the detector, and block photons emitted from planes below and above [Figure I.5.2]. The detection axis consists of photomultiplier tubes (PMTs) that use the photoelectric effect to convert the detected photons at a given location of the sample into an electrical signal that is then amplified. The final image is reconstructed by integrating the fluorescence measured at each point. However, these approaches are highly sensitive to scattering, a phenomenon where photons are deviated from their original trajectory by the medium they travel through, and thus offer very limited penetration depth.

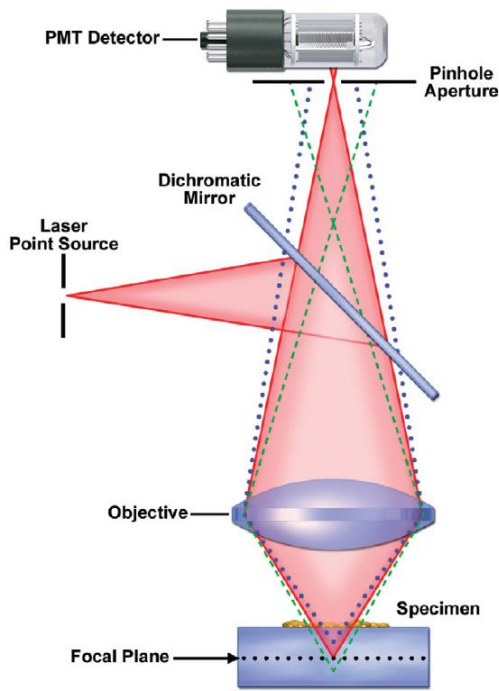


Figure I.5.2. Principle of a confocal laser scanning microscope. The light emitted from the focal plane (red) passes through the pinhole aperture and is detected by the PMT detector. Light emitted from planes below and above (dashed green and blue lines respectively) is blocked, eliminating out-of-focus fluorescence. (Murphy D.B., Davidson M.W. *Confocal laser scanning microscopy*. In *Fundamentals of Light Microscopy and Electronic Imaging*, 2nd ed.; Murphy, D.B., Ed.; John Wiley and Sons: New York, NY, USA, 2012).

Multi-photon excitation can overcome these issues. In 1931, Maria Göppert-Mayer first described the theory of two-photon absorption, which was verified experimentally only 30 years later. In this process, two photons, usually of the same wavelength and half the energy required to excite a molecule, are absorbed quasi-simultaneously and induce the same effect as a single-photon absorption [Figure I.5.3, left]. Because 2P excitation relies on the simultaneous absorption of two photons, its probability is proportional to the square of the light intensity. As a result, the light intensity is too weak outside of the focal plane to efficiently excite the molecules and axial confinement is reached without the need of a pinhole aperture [Figure I.5.3, right]. Moreover, 2P excitation uses near infrared (IR) wavelengths and, since longer wavelengths are less sensitive to scattering, 2P excitation allows to reach deeper structures in the brain, up to 500 - 700 μm in thick tissue or live animals (Svoboda and Yasuda 2006).

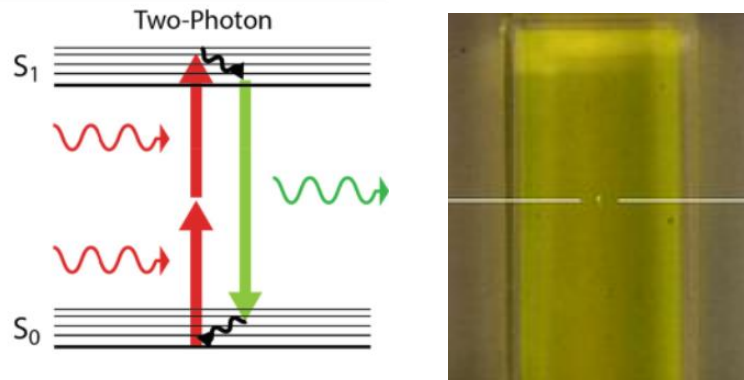


Figure I.5.3. Two-photon excitation. (Left) Simplified Jablonski diagram showing that the simultaneous absorption of two photons of lower energy allows to reach the excited state S₁. The return of the excited molecule to the ground state S₀ is accompanied by the emission of another photon of lower energy. (adapted from Sancataldo, G., Barrera, O., Vetri, V. *Two-Photon Imaging*. In: Nechyporuk-Zloy, V. (eds) *Principles of Light Microscopy: From Basic to Advanced*. Springer, Cham., 2022). **(Right)** Excitation volume generated by two-photon excitation. White line represents the focal plane. Contrary to single-photon excitation, only molecules in the focal plane are excited by two-photon excitation. (adapted from images from Xu research group, [url](#)).

However, the probability of 2P excitation (or 2P cross section) is significantly lower than that of 1P excitation. For example, in the situation where 1P excitation ($\lambda = 450 \text{ nm}$) of GFP molecules expressed in a cell would require 3 mW to reach saturation (the condition where each molecule in the illumination volume absorbs one photon), saturation with 2P excitation using a continuous wave (CW) laser ($\lambda = 900 \text{ nm}$) would require 25 W. Therefore, 2P excitation requires higher power to reach the same signal, which can lead to heating and irreducible damage of the cells if a certain limit is reached (Podgorski and Ranganathan 2016). To avoid this, the use of ultrashort (ten to hundreds of femtoseconds) pulsed with low repetition rate laser sources is crucial because it allows to temporally confine photons, resulting in high peak power pulses but lower average power, effectively reducing the risk of heating the sample. In our example, the use of a pulsed laser (pulse duration = 100 fs, repetition rate = 80 MHz) would decrease the required power to 80 mW (Papagiakoumou, Ronzitti, and Emiliani 2020).

b. Two-photon writing and reading of large neuronal circuits

Since its first demonstration in 1990 (Denk, Strickler, and Webb 1990), 2P laser scanning microscopy has become the most widely used technique for fluorescence imaging in thick tissue or live animals. However, the use of a diffraction limited spot has also its limitations when used to excite reporters or actuators with a low-density distribution or low 2P cross section with consequent generation of weak signals. This can be overcome by increasing the dwell time but has a cost in temporal resolution especially for multi target excitation. In this section, I will discuss these limitations and review the different approaches that have been proposed to solve these challenges.

i. Scanning techniques

The most conventional configuration for 2P scanning imaging uses a similar approach used for 1P confocal microscopy. A 2P diffraction limited spot is raster scanned across the field of view using galvanometric mirrors and, since 2P excitation inherently generates axially confined fluorescence, the emitted fluorescence can be detected using PMTs, without using a pinhole aperture [Figure I.5.4].

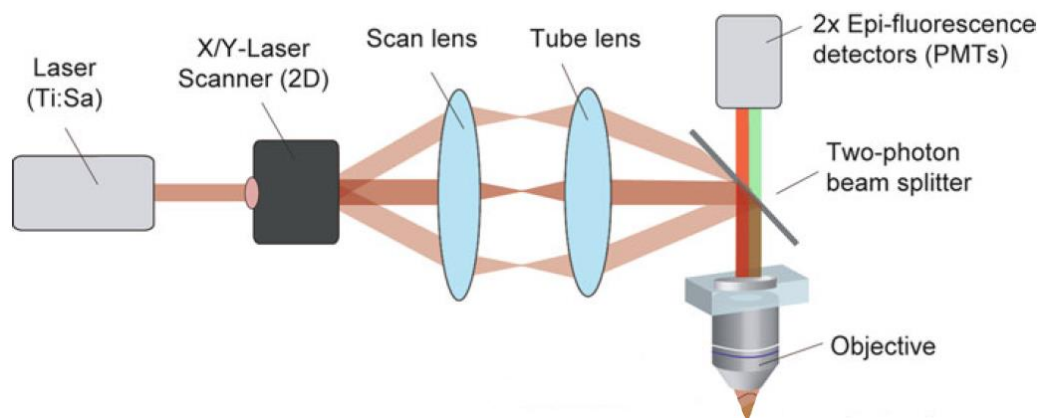


Figure I.5.4. Schematics of a two-photon laser scanning microscope. The light emitted by the laser is scanned using galvanometric mirrors (X/Y- laser scanner) and is reflected to the sample by a dichroic mirror (two-photon beam splitter). The fluorescence photons pass through the dichroic mirror and are detected by the PMT detector. (adapted from Bonnan, A., Grewe, B., Frick, A. *Calcium Imaging Techniques In Vitro to Explore the Role of Dendrites in Signaling Physiological Action Potential Patterns*. In: Badoer, E. (eds) *Visualization Techniques. Neuromethods*, vol 70. Humana Press, Totowa, NJ., 2012).

This approach, although largely used for morphological fluorescence imaging and functional imaging (combined with calcium indicators), is limited by the speed of the galvanometric mirrors, that leads to a maximum frame rate of 5 to 15 Hz for a typical field of view ($200 \times 200 - 500 \times 500 \mu\text{m}^2$), depending on the number of pixels and the dwell time (the time the laser beam stays at a defined location). These limitations can be overcome by using resonant scanners, that can oscillate at higher frequencies, to reach 30 Hz. Faster acquisition rates (up to tens of kHz) with raster scanning can be achieved by drastically reducing the field of view, sometimes to a single line (Fisher *et al.* 2008). Nonetheless, these modalities may not be the most time effective if the targeted cells, thus the regions of interest (ROIs) are sparsely distributed across a large field of view (FOV). In this case, it may be more interesting to only image these ROIs, rather than imaging the whole plane.

To address this, random access microscopy techniques have been developed. They allow the laser beam to be quickly moved across multiple positions, in order to image only the targets of interest, usually by using acousto-optic deflectors (AODs). Acoustic waves, when propagating in a crystal in the AOD, create a diffraction grating that deflects the incoming laser beam by an angle that corresponds to specific parameters of the acoustic waves. Because these acoustic waves can be modulated within

a few microseconds to any given position in the FOV, this technique offers better temporal resolution than conventional raster scan and enables recordings up to kilohertz rates (*Villette et al. 2019*).

Fast scanning enables to follow more accurately the dynamics of neuronal activity as it gives a better temporal resolution. But it requires reducing the dwell time, which for the imaging of weak signals (because, e.g., of low 2P-cross section, low fluorophore density within the focal volume, low available power), will drastically decrease the signal to noise ratio.

Laser scanning methods have also been the first approach used for 2P photostimulation of neurons (*Rickgauer and Tank 2009*). In this case, to illuminate a sufficiently large number of rhodopsins, the laser beam is scanned in a spiral-like trajectory on the surface of the cell soma, activating sequentially the rhodopsins on the cell's surface. In this configuration, the temporal resolution T for the photostimulation of N cells can be described as:

$$T = ((n \times R_t + (n - 1) \times S_{t1}) \times N + S_{t2} \times (N - 1)) \approx (n \times R_t + S_{t2}) \times N$$

Where n is the number of locations visited within each cell, R_t the dwell time, S_{t1} the scanning time to move from one position to the next one within one cell and S_{t2} the scanning time to move from one cell to the next one. These parameters need to be carefully chosen according to the rhodopsin kinetic properties (open time, rise time τ_{on} and closing time τ_{off}) and expression efficiency. Precisely, the rhodopsin rise time and the expression levels will define the necessary dwell time R_t which, depending on the channel opening time will also determine the scanning time S_{t1} . In general, to maximize the temporal photocurrent integration, spiral scanning has been preferentially combined with rhodopsins that display slow τ_{off} (5 – 30 ms) (*Rickgauer and Tank 2009; Packer et al. 2015*). However, this has limited the achievable temporal resolution and fidelity of photo-evoked action potentials to the generation of spikes up to 20 Hz and of millisecond timescale jitter (*Emiliani et al. 2015*).

For multicell excitation, each cell is sequentially visited and spiral scanned, this inherently limits the maximum number of cells that can be photoactivated or inhibited within a few milliseconds to just a few (*Xue et al. 2022*).

As described in the following section, one way to overcome the limitations of scanning excitation for photostimulation and imaging is to increase the spot size to cover the entire cell and/or to multiplex the excitation light at multiple positions. In this way the temporal resolution T for the excitation of N cells will be independent of N and be only limited by the single cell dwell time.

ii. Parallel methods

The need to achieve multicell excitation with high temporal precision and fidelity has driven the development of so-called parallel methods, where the excitation spot is enlarged to cover the whole

cell surface, and/or the excitation beam is multiplexed at multiple locations. Three main methods can be distinguished to increase the illumination spot size and will be reviewed here.

In the first, and simplest configuration, the spot size is simply expanded to cover the whole cell surface. This is achieved by underfilling the back aperture of the objective to obtain a so-called “low-numerical aperture (low-NA) gaussian beam” [Figure I.5.6].

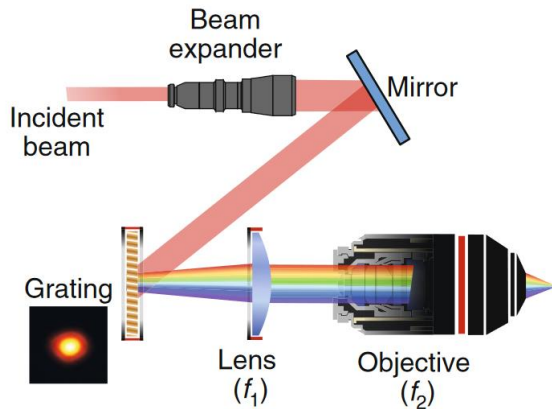


Figure I.5.6. Implementation of low-numerical aperture gaussian beam. The laser beam is expanded using a beam expander to obtain the correct size. Here, a diffraction grating is added in the optical path to achieve the temporal focusing effect (see below). (adapted from Papagiakoumou E. et al, *Scanless two-photon excitation with temporal focusing, Nature Methods, 2020*).

Computer-generated holography (CGH) involves the use of a spatial light modulator (SLM), a device based on a matrix of liquid crystals that can be individually tuned to control their refractive index and modulate the phase of the beam wavefront. Here, an image of the desired shape is used to calculate an interference pattern (or hologram) that can be displayed on the SLM, using a Fourier-transform based algorithm (the Gerchberg & Saxton algorithm, GSA). Once illuminated by the laser beam, this would reproduce the desired shape at the focal plane [Figure I.5.7].

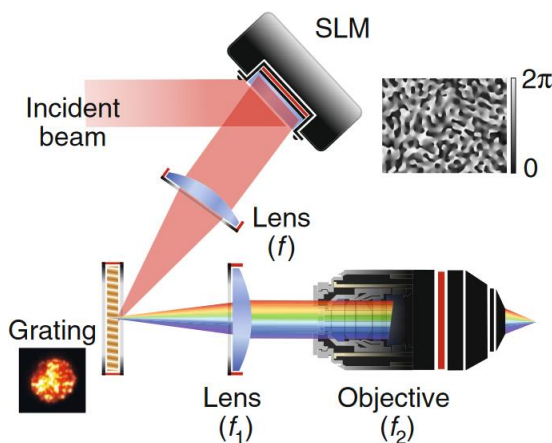


Figure I.5.7. Implementation of Computer Generated Holography. The laser beam is illuminating the SLM which displays a hologram to reproduce the desired shape at the focal plane. As above, a diffraction grating is added in the optical path to achieve the temporal focusing effect (see below). (adapted from Papagiakoumou E. et al, *Scanless two-photon excitation with temporal focusing, Nature Methods, 2020*).

Generalized phase contrast (GPC), is an interferometric technique where the desired image is obtained by the interference between a signal and a reference wave traveling along the same axis. With this method, the phase of the laser beam is shaped via the SLM, by using a binary $[0, \pi]$ phase map to obtain the desired intensity distribution. The beam modulated by the SLM passes then through a phase contrast filter (PCF) that applies a selective phase shift to the non-diffracted light. The

interference between the signal wave, modulated by the SLM and the phase shifted wave, generates the desired target intensity pattern at the focal plane, with a homogenous intensity (Sims et al. 2023) [Figure I.5.8].

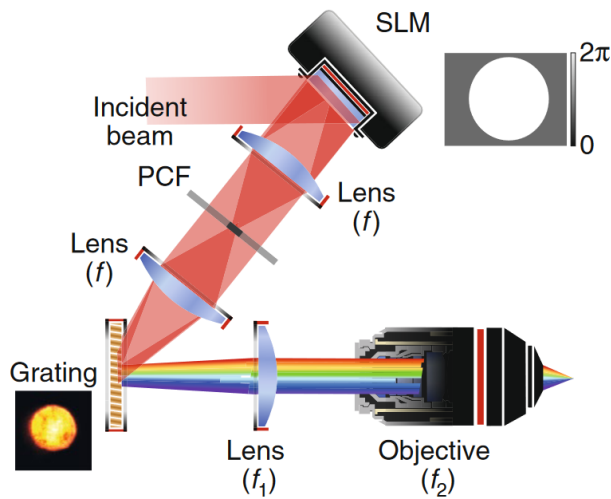


Figure I.5.8. Implementation of Generalized Phase Contrast. The laser beam is illuminating the SLM which displays a binary phase mask. The modulated beam travels then through the Phase Contrast Filter (PCF) that applies a selective phase shift to the non-modulated light. As above, a diffraction grating is added in the optical path to achieve the temporal focusing effect (see below). (adapted from Papagiakoumou E. et al, *Scanless two-photon excitation with temporal focusing*, *Nature Methods*, 2020).

Among these three approaches, the generation of low-NA gaussian beam is the simplest one to be implemented but can only generate a single fixed gaussian shape with an inhomogeneous intensity profile, with more intensity in the center than in the periphery. CGH is a more complex implementation but enables the generation of arbitrary excitation shapes, to cover a single or multiple target(s) in 2D and 3D. However, the light distribution within each spot typically displays intensity variations of high spatial frequency, called speckles. This is due to the algorithm used to calculate the hologram that modulates only the phase of the beam, allowing the phase at the focal plane to vary freely. Some methods to smooth the phase profile exist, although they cost in light efficiency and/or temporal resolution (Golan and Shoham 2009; Aharoni and Shoham 2018). Similar to CGH, GPC enables precise generation of arbitrary excitation shapes and with a smooth intensity profile but requires the use of a phase contrast filter and is limited to the generation of 2D patterns. Moreover, this method has a lower efficiency in terms of power. The comparison of the three approaches for the specific case of 2P voltage imaging will be more extensively discussed in Chapter II.

Extending the size of the illumination spot is an efficient method for fast and precise excitation of single or multiple targets (Accanto et al. 2018; 2019). However, parallel illumination also comes with a main disadvantage: the deterioration of the axial resolution that scales linearly with the size of the spot in the case of CGH and quadratically for low-NA gaussian beams and GPC (Papagiakoumou et al. 2008; Papagiakoumou, Ronzitti, and Emiliani 2020). This issue has been overcome by combining parallel approaches with a technique called temporal focusing (TF) (Oron and Silberberg 2015). Briefly, TF uses a diffraction grating to separate and diffract the different frequency components of the laser beam, which are only recombined at the focal plane, effectively decoupling the size of the spot and

its axial resolution (Papagiakoumou, Ronzitti, and Emiliani 2020) [Figure I.5.9]. Combined with CGH, GPC or low-NA gaussian beams, it enables the generation of axially confined shapes with micrometer axial resolution independently of the lateral extension of shapes.

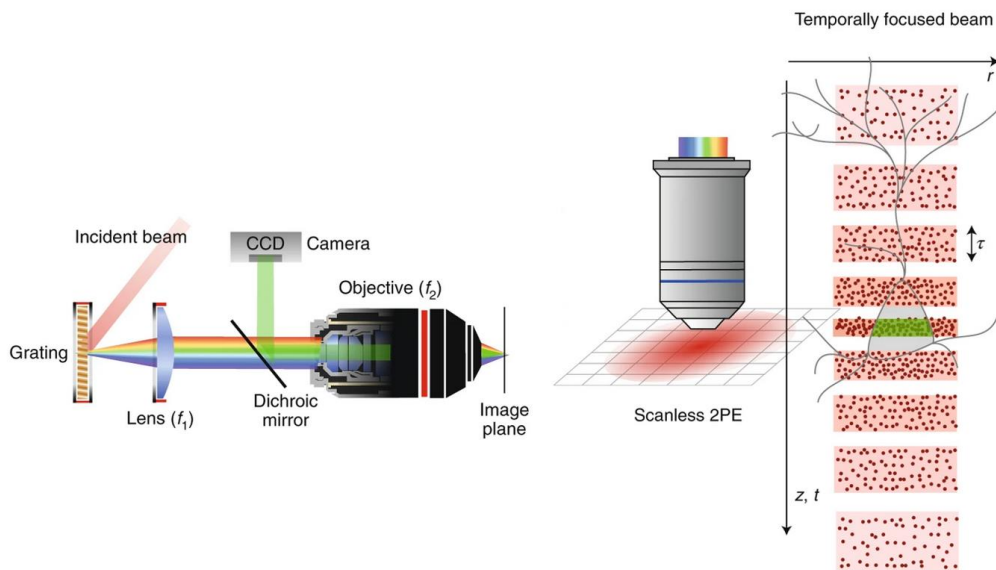


Figure I.5.9. Implementation of temporal focusing. (Left) The different wavelengths composing the incident beam are diffracted by a diffractive grating. The different frequency components will only be recombined at the focal plane. **(Right)** Representation of the axial propagation of a temporally focused beam. Here, the photons (represented as red dots) are temporally confined at the focal plane, resulting in efficient two-photon absorption. (adapted from Papagiakoumou E. et al, Scanless two-photon excitation with temporal focusing, Nature Methods, 2020).

The possibility of shaping light in 3D is a major advantage of CGH and it has been successfully applied for 3D multitarget optogenetic stimulation (Hernandez et al. 2016; dal Maschio et al. 2017). As for 2D, for 3D dense distribution of targets, the quick loss of axial resolution requires using TF. In this case, because axially shifted excitation planes cannot be simultaneously imaged on the TF diffraction grating, generation of 3D temporally focused shapes requires the use of a second SLM, which generates 2D or 3D distribution of diffraction limited spots centered at the locations of the chosen targets. When combined with a first light shaping path (CGH-TF, GPC-TF, or low-NA-Gaussian-beam-TF), this will enable to multiplex, at the location of the diffraction limited spots, the temporally focused shape generated at the TF diffraction grating.

Overall, shaped illumination enables to reach efficient single cell excitation by covering the whole cell soma and simultaneous multitarget excitation by multiplexing the shaped excitation at multiple locations. Multitarget excitation is then reached with a temporal resolution T that only depends on the cell dwell time:

$$T = R_t$$

Holographic light multiplexing can also be combined with spiral scanning. In this case, a single SLM is used to generate multiple diffraction limited spots and combined with a galvanometric mirror to generate multiple spirals at the locations of the targets. Here, the temporal resolution will be:

$$T = (n \times R_t)$$

2P parallel approaches also enable increased temporal resolution when used for fast functional imaging in combination with camera detection. Combined with 2P excitation, scanless patterned illumination enabled fast scanless imaging of GCaMP6 signals in the intact mouse brain at the same time as 1P optogenetic inhibition with Archaelhodopsin (*Bovetti et al. 2017*). Through a fiber bundle, patterned illumination also enabled fast Ca²⁺ imaging and multitarget excitation in freely moving mice (*Accanto et al. 2023*).

In this thesis, I will demonstrate how 2P scanless excitation also enables high contrast multitarget voltage imaging in densely labelled cell populations (see chapter II).

II. CHAPTER 1: Results – Bidirectional manipulation of neuronal activity: BiPOLES

In this chapter, I will present the first part of my PhD work on the characterization of a new optogenetic tool for the bidirectional manipulation of neuronal activity, named BiPOLES. This work has been achieved in collaboration with the laboratories of Peter Hegemann, who developed the construct, and J. Simon Wiegert, who performed the single-photon characterization in neurons. My work consisted of demonstrating the usability of two-photon excitation for the bidirectional manipulation of neuronal activity with BiPOLES. It was achieved under the supervision of Valentina Emiliani and Eirini Papagiakoumou. The optical setup was designed and built by Ruth Sims, a post-doc from the lab. Together, we designed the experiments and performed them, and I was in charge of the analysis of the electrophysiological data. The results are summarized in Figure 5 and Supplementary Figure 10 of the publication.

This chapter starts with a description of the advantages of bidirectional tools for controlling neuronal activity, followed by a brief state of the art of the different tools already available. The publication is then presented, followed by an appendix with some unpublished data on new constructs developed by the laboratories of Peter Hegemann and J. Simon Wiegert, that I characterized under 2P excitation.

1. Motivation and requirements

The field of neuroscience has benefited tremendously from “gain-of-function” or “loss-of-function” experiments. They allowed a better understanding of the roles of the cells, networks or regions targeted. As highlighted in the introduction, electrophysiological recordings have been the gold standard technique to perform these experiments, as well as pharmacology and ablation/lesions of specific cells or regions, in the case of “loss-of-function” experiments. The advent of optogenetics added the possibility to both activate and inhibit specific neurons, in a precise, fast and reversible manner. Since then, bidirectional interrogation of neuronal circuits has been mostly performed in separate experiments, with photo-activation on one side and photo-inhibition on the other (*Felix-Ortiz et al. 2016; Lacagnina et al. 2019; Jackman et al. 2020*). However, being able to combine these experiments into a single one, with the possibility to bidirectionally control the neuronal activity, would be extremely useful in many applications, such as investigating the role of ensembles of cells involved in a specific behavior or in response to a stimulus. Specific subsets of neurons could also be controlled bidirectionally, to test their necessity and sufficiency for perception of cortical activity (*Dagleish et al. 2020*) or recalling of cortical ensembles (*Carrillo-Reid et al. 2019*).

This would require the co-expression in the same cells of both an excitatory and an inhibitory rhodopsin, ideally with spectrally orthogonal properties, so that photo-activation of one rhodopsin would not inadvertently activate the other. However, as pointed out in the introduction, rhodopsins are sensitive to a relatively broad band of the spectrum. As a result, crosstalk is inevitable when using multicolour excitation. Therefore, the ratio of expression between both rhodopsins must also be tightly controlled to precisely control neuronal activation and inhibition in a reproducible manner in all co-expressing cells.

2. State of the art

The most common approach used to co-express both an excitatory and an inhibitory rhodopsin in neurons is to rely on two separate vectors to deliver the DNA sequence of both rhodopsins to the same neurons, usually under the control of the same promoter to maximize co-expression (*Han and Boyden 2007; Xie, Power, and Prasad 2022*). Although they successfully demonstrated bidirectional modulation of the neuronal activity *in vitro* and in some cases *in vivo* (X. Li et al. 2005; F. Zhang et al. 2007; Xie, Power, and Prasad 2022), the expression levels of both proteins can vary significantly between cells, with some of them expressing only one or the other construct, rendering the establishment of a reproducible protocol for precise photostimulation or inhibition extremely challenging.

To counter this issue, different strategies have been developed to deliver both rhodopsins with a single vector. One of them relies on the introduction of a self-cleaving viral peptide bridge (2A peptide sequence) in between both rhodopsin genes, under the control of a single promoter. 2A peptide sequences are small sequences that, during translation, can make the ribosome skip the synthesis of its C-terminal end, effectively causing a separation between the first protein translated and the downstream one. This approach has been used in several studies to achieve co-expression of the excitatory channelrhodopsin ChR2 (or its enhanced version ChR2(H134R)) and a chloride rhodopsin pump, typically Halo (*Han et al. 2009*) or NpHR (*Tang et al. 2009*). For example, eNPAC, as well as its shorter version eNPAC2.0 (*Gradinaru et al. 2010*) is comprised of the chloride rhodopsin pump eNpHR3.0, a 2A peptide sequence, and the channelrhodopsin ChR2. Although this approach achieved more control on the relative levels of expression of both rhodopsins, several drawbacks need to be mentioned. First, the protein downstream of the 2A peptide sequence is typically less expressed than the upstream one (*Ziqing Liu et al. 2017*), and the expression ratio may vary in between cells. Secondly and most importantly, the membrane trafficking of each protein is independent from the other, thus the actual number of each rhodopsin localized at the plasma membrane and functional may not be stoichiometric.

Another way to deliver two proteins with a single vector is the gene fusion strategy (Ståhl, Nygren, and Uhlén 1997), which has also been used to co-express two antagonistic rhodopsins (Kleinlogel et al. 2011). Here, a single promoter controls the expression of both ChR2 and NpHR, whose DNA sequences are fused, with a small sequence in between to maintain the topology of both proteins. Indeed, since the C-terminal of ChR2 is intracellular and the N-terminal of NpHR is extracellular, their direct fusion would result in a non-functional protein. Thus, the authors added a fragment of the transmembrane β -subunit of a rat H^+/K^+ -ATPase to link ChR2 and NpHR. This strategy enabled a strict stoichiometry of the levels of expressions of both rhodopsins. However, the membrane trafficking of this construct was not as efficient as individually expressed rhodopsins, thus reducing the efficiency of the construct for precise and reliable control of neuronal activity.

All of the above strategies have used ChR2 as the excitatory rhodopsin, and a chloride or proton pump as the inhibitory one. However, as outlined in the introduction, pumps are not as efficient as ion channels and, therefore require higher light intensities as well as extended illumination to efficiently induce inhibition, even with single-photon excitation. Replacing the rhodopsin pump with an ACR would increase the efficiency of the photo-inhibition. Moreover, it could enable the use of the construct with two-photon excitation.

To summarize, an efficient construct for bidirectional manipulation of the neuronal activity would display separate spectra for photo-activation and -inhibition, a 1:1 stoichiometric expression between the excitatory and the inhibitory rhodopsins and high amplitude photocurrents. Ideally, it would also perform well under two-photon excitation, to enable its use in depth *in vivo*. The BiPOLES construct presented in this paper exhibits all these properties.

3. Paper

BiPOLES is an optogenetic tool developed for bidirectional dual-color control of neurons

Johannes Vierock^{1,8}, Silvia Rodriguez-Rozada^{2,8}, Alexander Dieter², Florian Pieper³, Ruth Sims⁴, Federico Tenedini⁵, Amelie C.F. Bergs⁶, Imane Bendifallah⁴, Fangmin Zhou⁵, Nadja Zeitzschel⁶, Joachim Ahlbeck³, Sandra Augustin¹, Kathrin Sauter^{2,5}, Eirini Papagiakoumou⁴, Alexander Gottschalk⁶, Peter Soba^{5,7}, Valentina Emiliani⁴, Andreas K. Engel³, Peter Hegemann¹, J. Simon Wiegert^{2*}

¹Institute for Biology, Experimental Biophysics, Humboldt University Berlin, D-10115 Berlin, Germany

²Research Group Synaptic Wiring and Information Processing, Center for Molecular Neurobiology Hamburg, University Medical Center Hamburg-Eppendorf, 20251 Hamburg, Germany

³Department of Neurophysiology and Pathophysiology, University Medical Center Hamburg-Eppendorf, 20246 Hamburg, Germany

⁴Wavefront-Engineering Microscopy Group, Photonics Department, Institut de la Vision, Sorbonne Université, INSERM, CNRS, Institut de la Vision, F-75012 Paris, France

⁵Research Group Neuronal Patterning and Connectivity, Center for Molecular Neurobiology Hamburg, University Medical Center Hamburg-Eppendorf, 20251 Hamburg, Germany

⁶Buchmann Institute for Molecular Life Sciences and Institute of Biophysical Chemistry, GoetheUniversity, Max-von-Laue-Strasse 15, 60438 Frankfurt, Germany

⁷LIMES Institute, University of Bonn, Bonn, Germany

⁸These authors contributed equally: Johannes Vierock, Silvia Rodriguez-Rozada

*correspondence to: simon.wiegert@zmnh.uni-hamburg.de

Abstract

Optogenetic manipulation of neuronal activity through excitatory and inhibitory opsins has become an indispensable experimental strategy in neuroscience research. For many applications bidirectional control of neuronal activity allowing both excitation and inhibition of the same neurons in a single experiment is desired. This requires low spectral overlap between the excitatory and inhibitory opsin, matched photocurrent amplitudes and a fixed expression ratio. Moreover, independent activation of two distinct neuronal populations with different optogenetic actuators is still challenging due to blue-light sensitivity of all opsins. Here we report BiPOLES, an optogenetic tool for potent neuronal excitation and inhibition with light of two different wavelengths. BiPOLES enables sensitive, reliable dual-color neuronal spiking and silencing with single- or two-photon excitation, optical tuning of the membrane voltage, and independent optogenetic control of two neuronal populations using a second, blue-light sensitive opsin. The utility of BiPOLES is demonstrated in worms, flies, mice and ferrets.

Introduction

To prove necessity and sufficiency of a particular neuronal population for a specific behavior, a cognitive task, or a pathological condition, faithful activation and inhibition of this population of neurons is required. In principle, optogenetic manipulations allow such interventions. However, excitation and

inhibition of the neuronal population of interest is commonly done in separate experiments, where either an excitatory or inhibitory microbial opsin is expressed. Alternatively, if both opsins are co-expressed in the same cells, it is essential to achieve efficient membrane trafficking of both opsins, equal subcellular distributions, and a tightly controlled ratio between excitatory and inhibitory action at the specific wavelengths and membrane potentials, so that neuronal activation and silencing can be controlled precisely and predictably in all transduced cells. Precise co-localization of the two opsins is important when local, subcellular stimulation is required, or when control of individual neurons is intended, for example with 2-photon holographic illumination¹. Meeting these criteria is particularly challenging in vivo, where the optogenetic actuators are either expressed in transgenic lines or from viral vectors that are exogenously transduced. Ideally, both opsins are expressed from the same gene locus or delivered to the target neurons by a single viral vector. Moreover, for expression with fixed stoichiometry, the opsins should be encoded in a single open reading frame (ORF).

Previously, two strategies for stoichiometric expression of an inhibitory and an excitatory opsin from a single ORF were reported using either a gene fusion approach² or a 2A ribosomal skip sequence^{3,4}. In both cases, a blue-light sensitive cation-conducting channel for excitation was combined with a red-shifted rhodopsin pump for inhibition. The gene fusion approach was used to systematically combine the inhibitory ion pumps halorhodopsin (NpHR), bacteriorhodopsin (BR) or archaerhodopsin (Arch) with a number of channelrhodopsin-2 (ChR2) mutants to generate single tandem-proteins². While this strategy ensured co-localized expression of the inhibitory and excitatory opsins at a one-to-one ratio and provided important mechanistic insights in their relative ion-transport rates, membrane trafficking was not as efficient as with individually expressed opsins, thus limiting the potency of these fusion constructs for reliable control of neuronal activity.

The second strategy employed a 2A ribosomal skip sequence³ to express the enhanced opsins ChR2(H134R)⁵ and eNpHR3.0 as independent proteins⁵ at a fixed ratio from the same RNA⁴. These bicistronic constructs, termed eNPAC, and eNPAC2.0⁶, were used for bidirectional control of neuronal activity in various brain regions in mice⁶⁻⁹. While membrane trafficking of the individual opsins is more efficient compared to the gene fusion strategy, the expression ratio might still vary from cell to cell. Moreover, subcellularly targeted co-localization (e.g. at the soma) is not easily achieved. Finally, functionality is limited in some model organisms such as *D. melanogaster*, since rhodopsin pumps are not efficient in these animals^{10,11}.

In addition to activation and inhibition of the same neurons, also independent optogenetic activation of two distinct neuronal populations is still challenging. Although two spectrally distinct opsins have been combined previously to spike two distinct sets of neurons¹²⁻¹⁵, careful calibration and dosing of blue light was required to avoid activation of the red-shifted opsin. This typically leaves only a narrow spectral and energetic window to activate the blue- but not the red-light-sensitive rhodopsin. Thus, dual-color control of neurons is particularly challenging in the mammalian brain where irradiance decreases by orders of magnitude over a few millimeters in a wavelength-dependent manner^{16,17}.

In order to overcome current limitations for bidirectional neuronal manipulations and to facilitate spiking of neuronal populations with orange-red light exclusively, in this work we systematically explore the generation of two-channel fusion proteins that combine red-light activated cation- channels and blue-light activated anion-channels enabling neuronal spiking and inhibition with red and blue light, respectively. With respect to previous bidirectional tools, inversion of the excitatory and inhibitory action spectra restricts depolarization to a narrow, orange-red spectral window since the inhibitory opsin compensates the blue-light-activated currents of the excitatory red-shifted channel. We show that among all tested variants, a combination of *GtACR2*¹⁸ and Chrimson¹² termed BiPOLES (for Bidirectional Pair of Opsins for Light-induced Excitation and Silencing) proves most promising and allows 1) potent and reliable blue-light-mediated silencing and red-light-mediated spiking of pyramidal neurons in hippocampal slices; 2) bidirectional control of single neurons with single-photon illumination and 2-photon holographic stimulation; 3) dual-color control of two distinct neuronal populations in combination with a second blue- light-sensitive ChR without cross-talk at light intensities spanning multiple orders of magnitude; 4) precise optical tuning of the membrane voltage between the chloride and cation reversal potentials; 5) bidirectional manipulations of neuronal activity in a wide range of invertebrate and vertebrate model organisms including worms, fruit flies, mice and ferrets.

Results

Engineering of BiPOLES and biophysical characterization in HEK cells

To identify suitable combinations of opsins for potent membrane voltage shunting or depolarization with blue and red light, respectively, we combined the blue- or green-light sensitive anion-conducting channelrhodopsins (ACRs) Aurora¹¹, iC++¹⁹, *GtACR1* and *GtACR2*¹⁸ with the red-light sensitive cation-conducting channelrhodopsin (CCR) Chrimson¹²; or conversely, the blue-light sensitive *GtACR2* with the red-light sensitive CCRs bReaChES²⁰, f-Chrimson, vf-Chrimson²¹ and ChRmine²² (Fig. 1a). We fused these opsin-pairs with different linkers, expanding previous rhodopsin fusion strategies^{2,23} to obtain optimal expression and membrane targeting. The linkers were composed of the Kir2.1 membrane trafficking signal (TS)⁴, different arrangements of a cyan or yellow fluorescent protein, and the transmembrane β helix of the rat gastric H⁺/K⁺ ATPase (β HK) to maintain correct membrane topology of both opsins² (Fig. 1a).

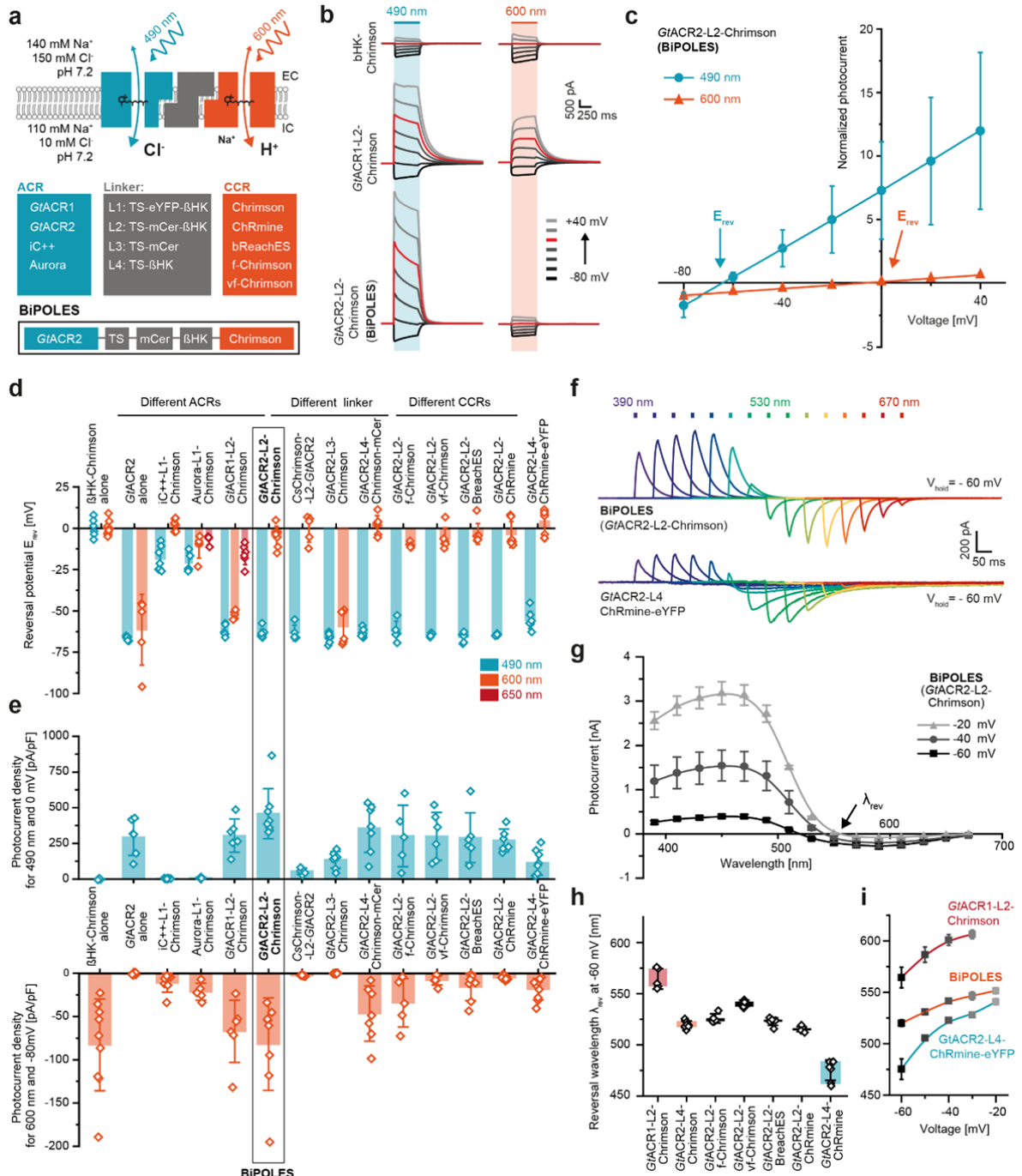


Figure 1. Development of BiPOLES and biophysical characterization. **(a)** Molecular scheme of BiPOLES with the extracellular (EC) and intracellular (IC) ionic conditions used for HEK293-cell recordings. The blue-green-light-activated natural anion channels GtACR1 and GtACR2 or the engineered ChR-chimeras iC++ and Aurora were fused to the red-light-activated cation channels Chrimson, ChRmine, bReaChES, f-Chrimson or vf-Chrimson by different transmembrane spanning linker regions consisting of a trafficking signal (ts), a yellow or cyan fluorescent protein (eYFP, mCerulean3) and the β HK transmembrane fragment. The fusion construct termed BiPOLES is indicated by a black frame. **(b)** Representative photocurrents of β HK-Chrimson-mCerulean (top), GtACR1-ts-mCerulean- β HK-Chrimson (middle) GtACR2-ts-mCerulean- β HK-Chrimson (BiPOLES, bottom) in whole-cell patch clamp recordings from HEK293 cells at 490 nm and 600 nm illumination. **(c)** Normalized peak photocurrents of BiPOLES at different membrane voltages evoked at either 490 or 600 nm (see panel b, mean \pm SD; n = 8 independent cells; normalized to the peak photocurrent at -80 mV and 600 nm illumination). **(d)** Reversal potential of peak photocurrents during 500-ms illumination with 490, 600, or 650 nm light as shown in (b) (mean \pm SD). **(e)** Peak photocurrent densities for 490 nm and 600 nm excitation at 0 mV (close to the reversal potential of protons and cations) and -80 mV (close to the reversal potential for chloride) measured as shown in (b) (mean \pm SD; for both (d) and (e) n = 5 biological independent cells for Aurora-L1-Chrimson, CsChrimson-L2-GtACR2 and GtACR2-L2-f-Chrimson; n = 6 for GtACR2, tACR1-L2-Chrimson and GtACR2-L2-vf-Chrimson; n = 7 for iC++-L1-Chrimson, GtACR2-L3-Chrimson, GtACR2-L4-Chrimson-mCer, GtACR2-L2-BreachES and GtACR2-L2-ChRmine; n = 8 for GtACR2-L2-Chrimson and n = 9 for β HK-Chrimson and GtACR2-L4-ChRmine-ts-eYFP-er). **(f)** Representative photocurrents of BiPOLES (top) and GtACR2-L4-ChRmine-ts-eYFP-er (bottom) with 10 ms light pulses at indicated wavelengths and equal photon flux at -60 mV. **(g)** Action spectra of BiPOLES at different membrane voltages (λ_{rev} = photocurrent reversal wavelength, mean \pm SEM, n = 9 independent cells for -60 mV, n = 4 for -40 mV and n = 2 for -20 mV). **(h)** Photocurrent reversal wavelength λ_{rev} at -60 mV (mean \pm SD, n = 5 independent cells for GtACR1-L2-Chrimson and GtACR2-L2-f-Chrimson, n = 6 for GtACR2-L2-vf-Chrimson and GtACR2-L2-ChRmine, n = 7 for GtACR2-L4-ChRmine-ts-eYFP-er, n = 8 for GtACR2-L2-BreachES and n = 9 for GtACR2-L2-Chrimson). **(i)** λ_{rev} of GtACR1-L2-Chrimson, BiPOLES and GtACR2-L4-ChRmine-TS-eYFP-ER at different membrane voltages (mean \pm SD; n = 5 biological independent cells for GtACR1-L2-Chrimson, n = 7 for GtACR2-L4-ChRmine-ts-eYFP-er and n = 9 for GtACR2-L2-Chrimson). The data presented in this figure are provided in the Source Data file.

For a detailed biophysical evaluation, we expressed all ACR-CCR tandems in human embryonic kidney (HEK) cells and recorded blue- and red-light evoked photocurrents in the presence of a chloride gradient. In all constructs, except the one lacking the β HK-subunit (L3, Fig. 1a), blue-light-activated currents were shifted towards the chloride Nernst potential whereas red-light-activated currents were shifted towards the Nernst potential for protons and sodium (Fig. 1b-d, Supplementary Fig. 1), indicating functional membrane insertion of both channels constituting the tandem constructs. Reversal potentials (Fig. 1d) and photocurrent densities (Fig. 1e) varied strongly for the different tandem variants indicating considerable differences in their wavelength-specific anion/cation conductance ratio and their membrane expression. Photocurrent densities were not only dependent on the identity of the fused channels, but also on the sequence of both opsins in the fusion construct as well as the employed fusion linker. In contrast to a previous study², the optimized linker used in this study did not require a fluorescent protein to preserve functionality of both channels (L4, Fig. 1a, d, e). Direct comparison of red- and blue-light evoked photocurrent densities with those of β HK-Chrimson and GtACR2 expressed alone indicated that most tandem constructs harboring a GtACR reached similar membrane expression efficacy as the individually expressed channels (Fig. 1e).

At membrane potentials between the Nernst potentials for chloride and protons, blue and red light induced outward and inward currents, respectively in all GtACR-fusion constructs. (Fig. 1e-g, Supplementary Fig. 1). The specific wavelength of photocurrent inversion (I_{rev}) was dependent on the absorption spectra and relative conductance of the employed channels as well as on the relative ionic driving forces defined by the membrane voltage and the respective ion gradients (Fig. 1g-i). The red-

shift of I_{rev} for the vf-Chrimson tandem compared to BiPOLES reflects the reduced conductance of this Chrimson mutant (Fig. 1h, Supplementary Fig. 1c), as already previously shown^{21,24}, whereas the blue-shift of I_{rev} for the ChRmine tandem with L4 (Fig. 1f, h) is explained by the blue-shifted activation spectrum of ChRmine compared to Chrimson²⁵ and its presumably large single channel conductance. Switching the L4 linker to L2 shifted I_{rev} to longer wavelengths for the ChRmine fusion constructs at the expense of ChRmine photocurrents (Fig. 1e, h), pointing to a stronger impact of the protein linker on the ChRmine photocurrent compared to other red-shifted CCRs (Fig. 1e).

Among all tested combinations, *Gt*ACR2-L2-Chrimson – from here on termed BiPOLES – was the most promising variant. First, it showed the largest photocurrent densities of all tested fusion constructs (Fig. 1e,f), second, reversal potentials for blue or red light excitation were close to those of individually expressed channels (-64 ± 3 mV and -5 ± 6 mV for BiPOLES compared to -66 ± 2 mV and 0 ± 5 mV of *Gt*ACR2 and bHK-Chrimson expressed alone, Fig. 1c, d, Supplementary Fig. 1b) and third, peak activity of the inhibitory anion and excitatory cation current had the largest spectral separation among all tested variants (150 ± 5 nm, Fig. 1f, g). Thus, BiPOLES enables selective activation of large anion and cation currents with spectrally well-separated wavelengths (Fig. 1e). BiPOLES was remarkably better expressed in HEK-cells than the previously reported ChR2-L1-NpHR fusion construct² and featured larger photocurrents at -60 mV than the bistrionic construct eNPAC2.0⁶ (Supplementary Fig. 2 a-c). Moreover, employing an anion channel with high conductance instead of a chloride pump, which transports one charge per absorbed photon and is weak at negative voltage, yielded chloride currents in BiPOLES expressing cells at irradiances 2 orders of magnitude lower than with eNPAC2.0 (Supplementary Fig. 2 d-f). Anion conductance in BiPOLES was sufficiently large to compensate inward currents of Chrimson even at high irradiance, driving the cell back to the chloride Nernst potential, which is close to the resting membrane voltage (Supplementary Fig. 2 d-f). We further verified the implementation of an anion-conducting channel by testing whether sufficient blue-light hyperpolarization could be achieved with a rhodopsin pump²⁶ instead of a channel. Replacing *Gt*ACR2 with a putatively potent blue-light sensitive pump led to barely detectable outward currents at the same irradiance due to low ion turnover of the proton pump under the given voltage and ion conditions (Supplementary Fig. 2 d, g).

Evaluation of BiPOLES in CA1 pyramidal neurons

Next, we validated BiPOLES as an optogenetic tool for bidirectional control of neuronal activity. In CA1 pyramidal neurons of rat hippocampal slice cultures, illumination triggered photocurrents with biophysical properties similar to those observed in HEK cells (Fig. 2a, b, Supplementary Fig. 3a-c). We observed membrane-localized BiPOLES expression most strongly in the somatodendritic compartment (Fig. 2c, Supplementary Fig. 3d). However, some fraction of the protein accumulated inside the cell in the periphery of the cell nucleus, indicating sub-optimal membrane trafficking of BiPOLES. To enhance membrane trafficking, we generated a soma-targeted variant (somBiPOLES) by attaching a C-terminal Kv2.1-trafficking sequence²⁷. Soma targeting has the additional benefit of avoiding expression of the construct in axon terminals, where functionality of BiPOLES might be limited due to an excitatory chloride reversal potential and subsequent depolarizing action of *Gt*ACR2^{28,29}. somBiPOLES showed

strongly improved membrane localization restricted to the cell soma and in proximal dendrites with no detectable intracellular accumulations (Fig. 2c, Supplementary Fig. 3d). Compared to BiPOLES, blue- and red-light mediated photocurrents were enhanced and now similar in magnitude to those in neurons expressing either Chrimson or soma-targeted *GtACR2* (*somGtACR2*), alone (Fig. 2d, Supplementary Fig. 4a, 5a, b). Passive and active membrane parameters of BiPOLES- and somBiPOLES-expressing neurons were similar to non-transduced, wild-type neurons (Supplementary Fig. 6), indicative of good tolerability in neurons.

To verify the confinement of somBiPOLES to the somatodendritic compartment despite the improved expression, we virally transduced area CA3 in hippocampal slice cultures with somBiPOLES and recorded optically evoked EPSCs in postsynaptic CA1 cells. Local illumination with red light in CA3 triggered large excitatory postsynaptic currents (EPSCs), while local red illumination of axon terminals in CA1 (635 nm, 2 pulses of 5 ms, 40 ms ISI, 50 mW mm⁻²), did not trigger synaptic release, indicating absence of somBiPOLES from axonal terminals (Supplementary Fig. 3e, f). Thus, despite enhanced membrane trafficking, somBiPOLES remained confined to the somatodendritic compartment.

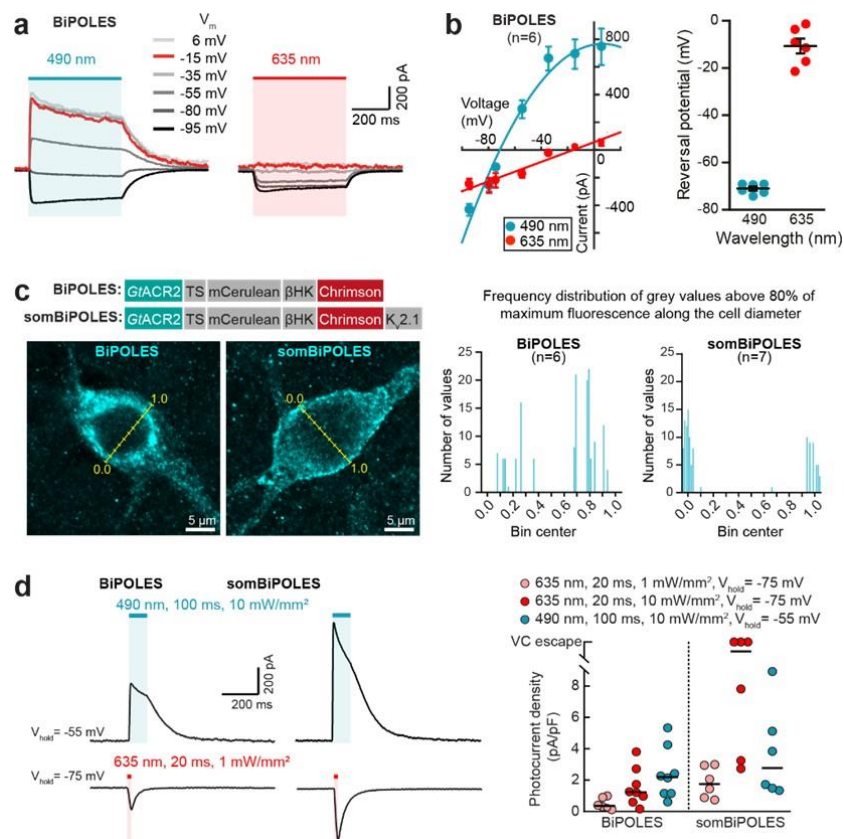


Figure 2. Expression and functional characterization of BiPOLES and somBiPOLES in hippocampal neurons. (a) Representative photocurrent traces of BiPOLES in CA1 pyramidal neurons at indicated membrane voltages (V_m : from -95 to +6 mV) upon illumination with 490 or 635 nm (500 ms, 10 mW mm⁻²). (b) Left: quantification of photocurrent-voltage relationship (symbols: mean \pm SEM, n = 6 cells, lines: polynomial regression fitting, $R^2 = 0.98$ and 0.94 , for 490 and 635 nm, respectively). Right: reversal potential under 490 or 635 nm illumination (black lines: mean \pm SEM, n = 6 cells). (c) Left: Molecular scheme of BiPOLES and somBiPOLES as used in neurons. Representative maximum-intensity projection images of immunostainings showing expression of BiPOLES or soma-targeted BiPOLES (somBiPOLES) in CA3 pyramidal neurons of organotypic hippocampal slices. Yellow lines indicate the bins used to measure fluorescence intensity along the cell equator. Right: Frequency distribution of grey values above 80% of the maximum fluorescence intensity measured along the cell diameter in BiPOLES- (n = 6 cells) and somBiPOLES-expressing CA3 cells (n = 7 cells). Note improved trafficking of somBiPOLES to the cell membrane, shown by the preferential distribution of brighter pixels around bins 0.0 and 1.0. (d) Left: Representative photocurrent traces measured in BiPOLES- or somBiPOLES-expressing CA1 pyramidal neurons. Inward cationic photocurrents evoked by a 635 nm light pulse (20 ms, 1 mW mm⁻²) were recorded at a membrane voltage of -75 mV, and outward anionic photocurrents evoked by a 490 nm light pulse (100 ms, 10 mW mm⁻²) were recorded at a membrane voltage of -55 mV. Right: Quantification of photocurrent densities evoked under the indicated conditions. Note that photocurrent densities were strongly enhanced for somBiPOLES compared to BiPOLES (black horizontal lines: medians, $n_{\text{BiPOLES}} = 8$ cells, $n_{\text{somBiPOLES}} = 6$ cells). The data presented in this figure are provided in the Source Data file.

Having shown that somBiPOLES is efficiently expressed in CA1 pyramidal cells, we next systematically benchmarked light-evoked spiking and inhibition parameters for somBiPOLES by direct comparison to Chrimson or somGtACR2 expressed in hippocampal CA1 pyramidal neurons, respectively (Fig. 3, Supplementary Figs. 4, 5). To compare spiking performance in somBiPOLES or Chrimson expressing CA1 pyramidal cells, we delivered trains of 5-ms blue (470 nm), orange (595 nm) or red (635 nm) light pulses at irradiances ranging from 0.1 to 100 mW mm⁻². Action potential (AP) probability in somBiPOLES neurons reached 100% at 0.5 mW mm⁻² with 595 nm and 10 mW mm⁻² with 635 nm light, similar to neurons expressing Chrimson alone (Fig. 3b, c). In pyramidal cells, APs could be reliably driven up to 10-20 Hz with somBiPOLES (Supplementary Fig. 7c) similar to Chrimson alone, as shown previously¹². Delivering the same number of photons in a time range of 1 - 25 ms did not alter the AP probability, but longer pulses increased sub-threshold depolarization (Supplementary Fig. 7d).

In contrast to orange or red light, APs were not evoked at any blue light irradiance in somBiPOLES neurons due to the activity of the blue-light sensitive anion channel. On the contrary, neurons expressing Chrimson alone reached 100% AP firing probability at 10 mW mm⁻² with 470 nm (Fig. 3b, c). Using light ramps with gradually increasing irradiance enabled us to precisely determine the AP threshold and to quantitatively compare spiking efficacy of different excitatory opsins. The irradiance threshold for the first AP was similar for somBiPOLES and Chrimson at 595 nm (0.74 ± 0.06 mW mm⁻² for somBiPOLES and 0.68 ± 0.05 mW mm⁻² for Chrimson) reflecting that the functional expression levels were similar. In contrast, blue light triggered APs at 0.95 ± 0.09 mW mm⁻² in Chrimson expressing cells, but never in somBiPOLES or BiPOLES neurons (Fig. 3d, e, Supplementary Fig. 7a, b). Thus, somBiPOLES enables neuronal excitation exclusively within a narrow spectral window restricted to orange-red light, avoiding inadvertent blue-light mediated spiking.

Next, we quantified the silencing capacity of somBiPOLES and compared it to somGtACR2 alone – the most potent opsin for blue-light mediated somatic silencing^{28,29} – by measuring the capacity to shift the threshold for electrically evoked APs (i.e. rheobase, see Methods). Both variants similarly shifted the

rheobase towards larger currents starting at an irradiance of 0.1 mW mm⁻² with 490 nm light, leading to a complete block of APs in most cases (Fig. 3g, h). Neuronal silencing was efficient under 490 nm-illumination, even at high irradiances (up to 100 mW mm⁻² Fig. 3g), showing that blue light cross-activation of Chrimson in somBiPOLES did not compromise neuronal shunting.

We compared somBiPOLES with eNPAC2.0, the most advanced optogenetic tool currently available for dual-color excitation and inhibition^{4,6,7}. In eNPAC2.0 expressing CA1 pyramidal neurons, depolarizing and hyperpolarizing photocurrents were present under blue and yellow/orange light, respectively (Supplementary Fig. 8a), consistent with its inverted action spectrum compared to BiPOLES (Supplementary Fig. 2). Compared to BiPOLES (Supplementary Fig. 3c) peak photocurrent ratios were more variable between cells (Supplementary Fig. 8a), indicative of different stoichiometries between ChR2(HR) and eNpHR3.0 in different neurons, probably because membrane trafficking and degradation of both opsins occur independently. Moreover, blue-light-evoked spiking with eNPAC2.0 required approx. 10-fold higher irradiance compared to somBiPOLES and did not reach 100% reliability (Supplementary Fig. 8c), which might be explained by cross-activation of eNpHR3.0 under high blue irradiance (see also Supplementary Fig. 2d). Blue-light-triggered APs could not be reliably blocked with concomitant yellow illumination at 10 mW mm⁻² (Supplementary Fig. 8b). Further on, activation of eNPAC2.0 (i.e., eNpHR3.0) with yellow light (580 nm) caused strong membrane hyperpolarization followed by rebound spikes in some cases (Supplementary Fig. 8d). Finally, and consistent with photocurrent measurements in HEK cells (Supplementary Fig. 2e, f), silencing of electrically evoked APs required 100-fold higher irradiance with eNPAC2.0, compared to somBiPOLES, until a significant rheobase-shift was observed (Supplementary Fig. 8e).

In summary, somBiPOLES is suitable for potent, reliable neuronal activation exclusively with orange-red light and silencing with blue light. somBiPOLES displays similar potency for neuronal excitation and inhibition as Chrimson and som*Gt*ACR2 alone.

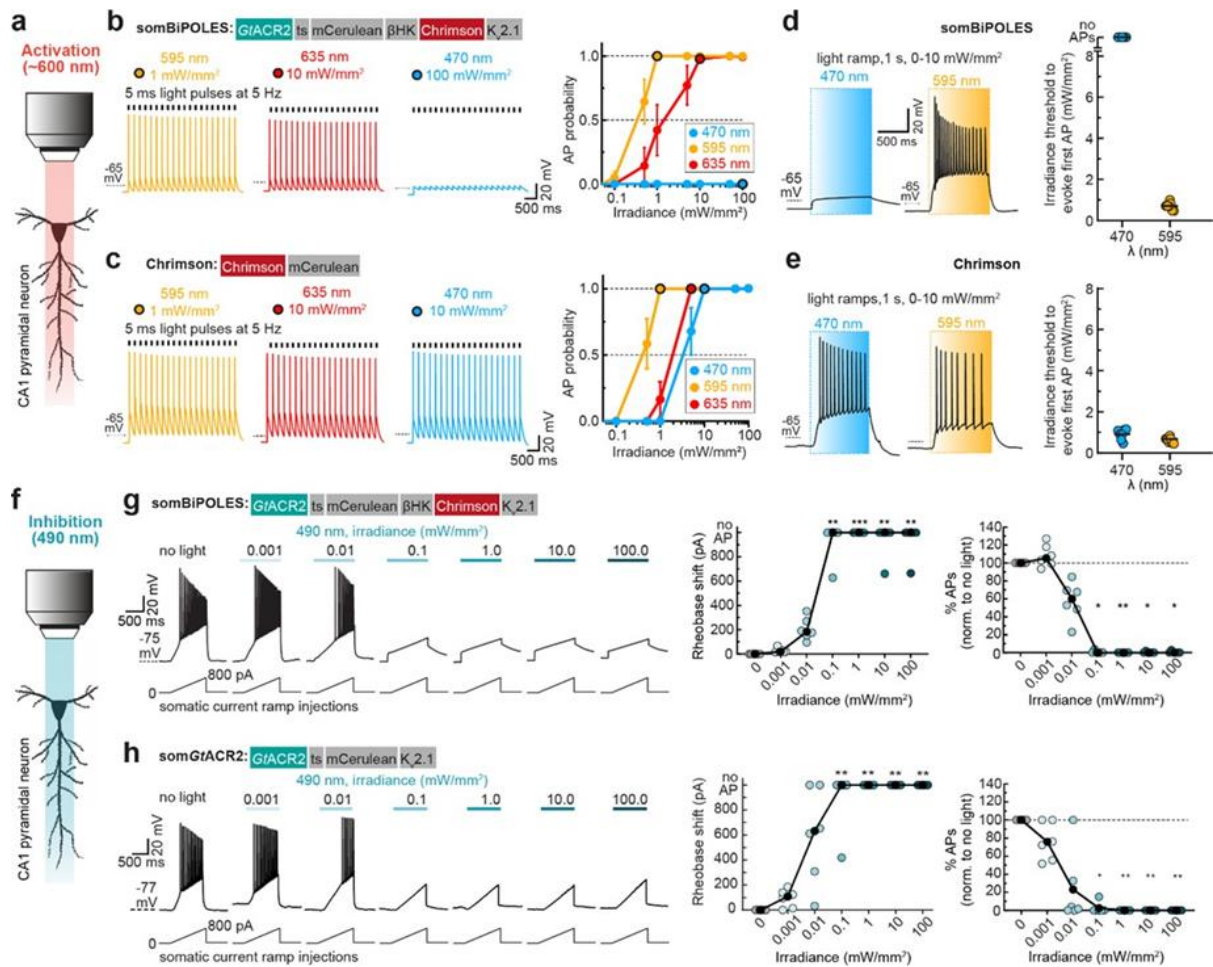


Figure 3. somBiPOLES allows potent dual-color spiking and silencing of the same neurons using red and blue light, respectively. (a) Quantification of neuronal excitation with somBiPOLES or Chrimson only. (b) Optical excitation is restricted exclusively to the orange/red spectrum in somBiPOLES-expressing neurons. Left: Example traces of current-clamp (IC) recordings in somBiPOLES-expressing CA1 pyramidal cells to determine light-evoked action potential (AP)-probability at different wavelengths. Right: quantification of light-mediated AP probability at indicated wavelengths and irradiances (symbols correspond to mean \pm SEM, n = 8 cells). Black outlined circles correspond to irradiance values shown in example traces on the left. (c) Same experiment as shown in (b), except that CA1 neurons express Chrimson only (symbols correspond to mean \pm SEM, n = 7 cells) Note blue-light excitation of Chrimson, but not somBiPOLES cells. (d) Light-ramp stimulation to determine the AP threshold irradiance. Left: Representative membrane voltage traces measured in somBiPOLES-expressing CA1 pyramidal neurons. Light was ramped linearly from 0 to 10 mW mm⁻² over 1 s. Right: Quantification of the irradiance threshold at which the first AP was evoked (black horizontal lines: medians, n = 7 cells). (e) Same experiment as shown in (b), except that CA1 neurons express Chrimson only (black horizontal lines: medians, n = 7 cells). The threshold for action potential firing with 595 nm was similar between somBiPOLES- and Chrimson-expressing neurons, while somBiPOLES cells were not sensitive to blue light. (f) Quantification of neuronal silencing with somBiPOLES or somGtACR2 only. (g) somBiPOLES mediates neuronal silencing upon illumination with blue light. Left: Current ramps (from 0 - 100 to 0 - 900 pA) were injected into somBiPOLES-expressing CA1 pyramidal cells to induce APs during illumination with blue light at indicated intensities (from 0.001 to 100 mW mm⁻²). The injected current at the time of the first action potential was defined as the rheobase. Right: Quantification of the rheobase shift and the relative change in the number of ramp-evoked action potentials. Illumination with 490 nm light of increasing intensities activated somBiPOLES-mediated Cl⁻ currents shifting the rheobase to higher values and shunting action potentials. (h) Same experiment as shown in (g), except that CA1 neurons express somGtACR2 only. Note similar silencing performance of somBiPOLES and GtACR2. In (h, g) black circles correspond to medians, n_{somBiPOLES} = 6 cells, n_{somGtACR2} = 6 cells, one-way Friedman test, *p < 0.05, **p < 0.01, ***p < 0.001. The data presented in this figure and details on the statistical analysis are provided in the Source Data file.

BiPOLES allows various neuronal manipulations with visible light

We evaluated BiPOLES and somBiPOLES in the context of three distinct neuronal applications: bidirectional control of neuronal activity, optical tuning of membrane voltage, and independent spiking of two distinct neuronal populations.

We first tested the suitability of BiPOLES and somBiPOLES for all-optical excitation and inhibition of the same neurons (Fig. 4a). Red light pulses (635 nm, 20 ms, 10 mW mm⁻²) reliably triggered action potentials (APs) in somBiPOLES expressing neurons (Fig. 4b), while APs were triggered only in approx. 50% of BiPOLES expressing neurons under these stimulation conditions (Supplementary Fig. 7e), due to a higher irradiance threshold to evoke APs in those cells (Supplementary Fig. 7a, b). Concomitant blue illumination (490 nm, 10 mW mm⁻²) for 100 ms reliably blocked red-light evoked APs in all cases. As expected from an anion conducting channel, blue light alone had only a minor impact on the resting membrane voltage, due to the close proximity of the chloride reversal potential to the resting potential of the cell (Fig. 4b, Supplementary Fig. 7e) In contrast, neurons expressing Chrimson alone showed APs under red and blue illumination (Supplementary Fig. 4b).

Aside from dual-color spiking and inhibition, a major advantage of the fixed 1:1 stoichiometry between an anion and cation channel with different activation spectra in BiPOLES is the ability to precisely tune the ratio between anion- and cation-conductance with light (Fig. 1f, g, Supplementary Fig. 3c). In neurons this allows to optically tune the membrane voltage between the chloride reversal potential and the action potential threshold (Fig. 4c). Optical membrane voltage tuning was achieved either by a variable ratio of blue and orange light at the absorption peak wavelengths of GtACR2 and Chrimson

(Fig. 4d) or by using a single color with fixed irradiance over a wide spectral range (Fig. 4e). Both approaches yielded reliable and reproducible membrane voltage shifts. Starting from the chloride Nernst potential when only *GtACR2* was activated with blue light at 470 nm, the membrane depolarized steadily with an increasing 595/470 nm ratio, eventually passing the action potential threshold (Fig. 4d). Similarly, tuning a single wavelength between 385 nm and 490 nm clamped the cell near the Nernst potential for chloride, while shifting the wavelength peak further towards red led to gradual depolarization, eventually triggering action potentials at 580 nm (Fig. 4e). Depending on the available light source both methods allow precise control of anion and cation fluxes at a fixed ratio and might be applied for locally defined subthreshold membrane depolarization in single neurons or to control excitability of networks of defined neuronal populations.

Since BiPOLES permits neuronal spiking exclusively within the orange-red light window, it facilitates two-color excitation of genetically distinct but spatially intermingled neuronal populations using a second, blue-light-activated ChR (Fig. 4f). To demonstrate this, we expressed somBiPOLES in CA1 VIP interneurons and CheRiff, a blue-light-sensitive ChR (I_{\max} 378 = 460 nm)³⁰ in CA1 pyramidal neurons (Fig. 4g, see Methods for details). Both CA1 and VIP neurons innervate Oriens-Lacunosum-Moleculare (OLM) interneurons. Therefore, exclusive excitation of CA1 cells or VIP interneurons is expected to trigger excitatory (EPSCs) and inhibitory (IPSCs) postsynaptic currents, respectively. CheRiff-expressing pyramidal cells were readily spiking upon blue, but not orange-red illumination up to 10 mW mm⁻² (Fig. 4h, Supplementary Fig. 9). Conversely, as expected, red light evoked APs in somBiPOLES-expressing VIP neurons, while blue light up to 100 mW mm⁻² did not evoke APs (Fig. 4h). Next, we recorded synaptic inputs from these two populations onto VIP-negative GABAergic neurons in stratum-oriens (Fig. 4i). As expected, blue light triggered EPSCs (CheRiff) and red light triggered IPSCs (somBiPOLES), evident by their respective reversal potentials at 8.8 ± 10.4 mV and -71.4 ± 13.1 mV (Fig. 4i). Thus, somBiPOLES, in combination with the blue-light sensitive CheRiff enabled independent activation of two distinct populations of neurons in the same field of view.

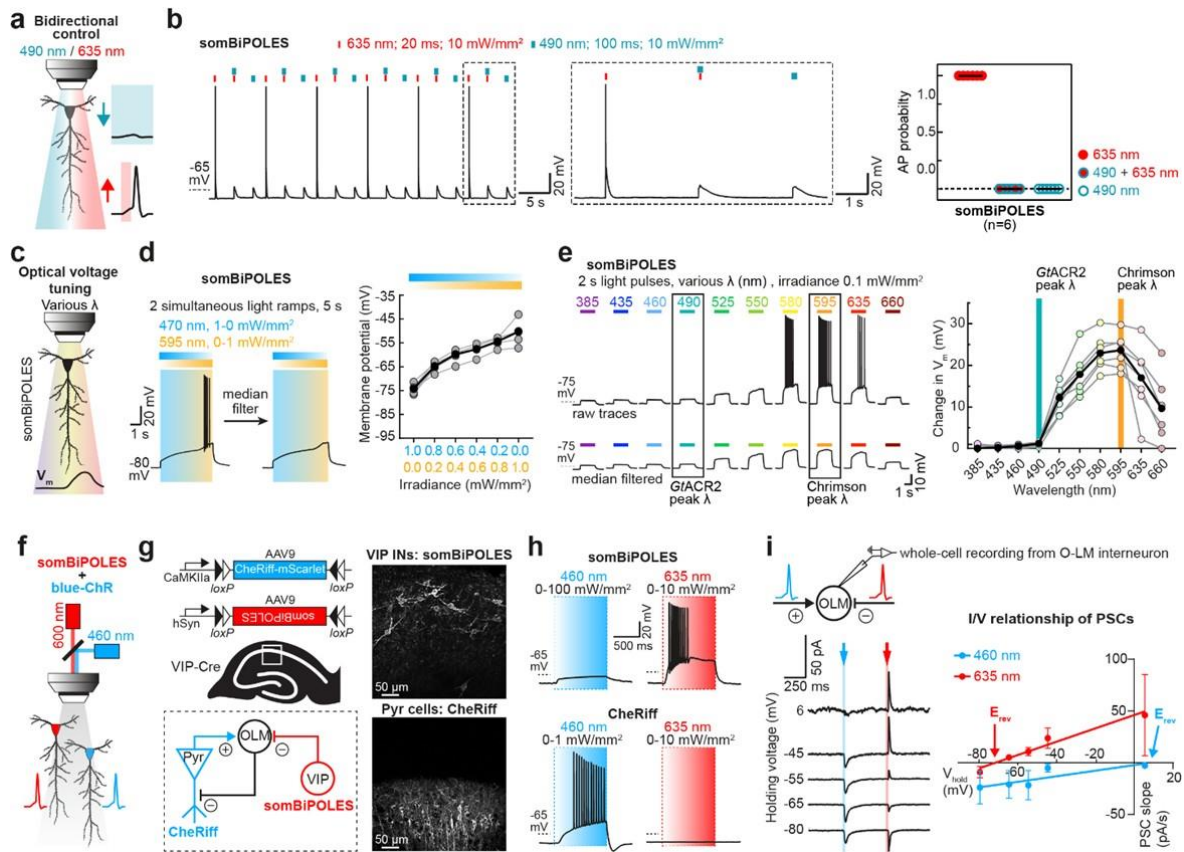


Figure 4. Applications of BiPOLES: bidirectional control of neuronal activity, optical voltage tuning and independent dual-color excitation of two distinct neuronal populations. (a) Schematic drawing illustrating bidirectional control of neurons with blue and red light. (b) Current-clamp characterization of bidirectional optical spiking-control with somBiPOLES. Left: Voltage traces showing red-light-evoked APs, which were blocked by a concomitant blue light pulse. Right: quantification of AP probability under indicated conditions (black horizontal lines: medians, $n = 6$ cells). (c) Schematic drawing illustrating control of membrane voltage with somBiPOLES. (d) Left: Representative membrane voltage traces from a somBiPOLES-expressing CA1 pyramidal cell during simultaneous illumination with 470- and 595-nm light ramps of opposite gradient. Voltage traces were median-filtered to reveal the slow change in membrane voltage during the ramp protocol. Right: Quantification of membrane voltage at different 595/470 nm light ratios (black circles: medians, $n = 5$ cells). (e) Left: representative membrane voltage traces of somBiPOLES in CA1 pyramidal neurons upon illumination with different wavelengths and equal photon flux. As in (d) voltage traces were median-filtered to eliminate action potentials and reveal the slow changes in membrane voltage during the light protocol. Right: Quantification of membrane potential along the spectrum showing optical voltage tuning at the indicated wavelengths. (black circles: medians, an irradiance of 0.1 mW mm^{-2} was kept constant for all wavelengths, $n = 6$ cells). (f) Schematic drawing illustrating control of 2 neurons expressing either somBiPOLES (red) or a blue-light-sensitive ChR (blue). (g) Left: Cre-On/Cre-Off strategy to achieve mutually exclusive expression of CheRiff-mScarlet in CA1 pyramidal neurons and somBiPOLES in VIP-positive GABAergic neurons. Both cell types innervate OLM interneurons in CA1. Right: Example maximum-intensity projection images of 2-photon stacks showing expression of somBiPOLES in VIP-interneurons (top) and CheRiff-mScarlet in the pyramidal layer of CA1 (bottom). (h) IC-recordings demonstrating mutually exclusive spiking of somBiPOLES- and CheRiff-expressing neurons under red or blue illumination. (i) Postsynaptic whole-cell voltage-clamp recordings from an OLM cell at indicated membrane voltages showing EPSCs and IPSCs upon blue- and red-light pulses, respectively. Right: quantification of blue- and red-light-evoked PSCs and their reversal potential. Symbols show mean \pm SEM, $n_{460 \text{ nm}} = 8$ cells, $n_{635 \text{ nm}} = 7$ cells, lines: linear regression fit, $R^2 = 0.06$ and 0.20 for blue and red light, respectively. The data presented in this figure are provided in the Source Data file.

Bidirectional neuronal control using dual-laser 2-photon holography

Two-photon holographic excitation enables spatially localized photostimulation of multiple neurons with single-cell resolution in scattering tissue¹. We evaluated the feasibility of bidirectional control of single neurons by 2-photon holographic excitation (Supplementary Fig. 10a) in hippocampal organotypic slices virally transduced with somBiPOLES expressed from a CaMKII promoter. Single-photon excitation confirmed high potency of somBiPOLES using this expression strategy (Supplementary Fig. 11). The 2-photon action spectrum of somBiPOLES was explored by measuring the peak photocurrents (I_p) at a range of holding potentials (-80 to -55 mV) and excitation wavelengths (850 to 1100 nm). Similar to single-photon excitation, blue-shifted wavelengths ($\lambda_{ex} < 980$ nm) generated large photocurrents, apparently dominated by the flow of chloride ions (outward chloride currents below the chloride Nernst potential and inward chloride currents above the chloride Nernst potential, Fig. 5a-c, Supplementary Fig. 10b). Red-shifted wavelengths ($\lambda_{ex} > 980$ nm) generated photocurrents, which appeared to be dominated by the flow of protons and cations across the membrane (inward currents at physiological neuronal membrane potentials, Fig. 5a-c, Supplementary Fig. 10b). Since 920 nm and 1100 nm illumination generated the largest magnitudes of inhibitory and excitatory photocurrents respectively, these wavelengths were used to evaluate whether neuronal activity could be reliably suppressed or evoked in neurons expressing somBiPOLES. Action potentials could be reliably evoked using short (5 ms) exposure to 1100 nm light (power density: $0.44 \text{ mW}/\mu\text{m}^2$), with latency (19.9 ± 6.3 ms) and jitter (2.5 ± 1.5 ms) (Fig. 5d, Supplementary Fig. 10c) comparable to literature values for Chrimson³¹. 5 ms pulses were also able to induce high-fidelity trains of APs with frequencies up to 20 Hz (Supplementary Fig. 10d). It is likely that shorter latency and jitter (and consequently higher rates of trains of APs) could be achieved by replacing the stimulation laser by one with optimized pulse parameters, in particular, higher peak energy³². 920 nm excitation effectively inhibited neural activity, increasing the rheobase of AP firing at power densities above $0.1 \text{ mW } \mu\text{m}^{-2}$ (Fig. 5e). It further enabled temporally precise elimination of single electrically evoked APs (Supplementary Fig. 10e) and silencing of neuronal activity over sustained (200 ms) periods (Fig. 5f). Finally, we demonstrate two-photon, bidirectional control of neurons by co-incident illumination of appropriately titrated 920 nm and 1100 nm light (Fig. 5g). Thus, somBiPOLES is suitable for dual-color 2-photon holographic manipulation of neuronal activity with cellular resolution with standard lasers typically used for two-photon imaging.

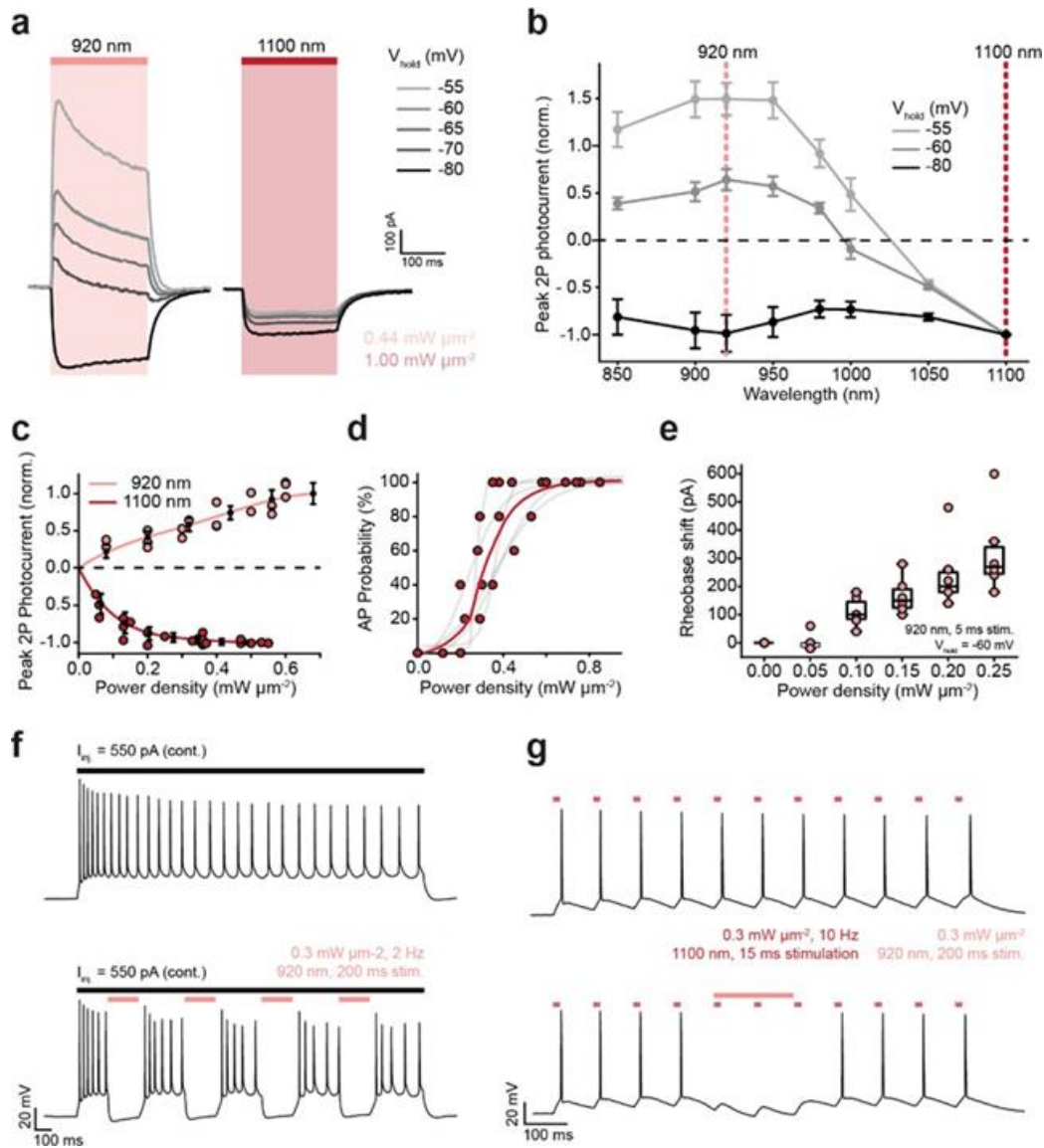


Figure 5. Bidirectional control of neuronal activity with somBiPOLES using dual-color 2-photon holography. (a-c) Voltage clamp (VC) characterization of somBiPOLES in CA1 pyramidal cells. **(a)** Representative photocurrent traces at different holding potentials, obtained by continuous 200 ms illumination of 920 and 1100 nm at constant average power density (0.44 and 1.00 $\text{mW } \mu\text{m}^{-2}$). **(b)** Peak photocurrent as a function of wavelength at different holding potentials (mean \pm SEM, $n = 5$). Data acquired with a constant photon flux of 6.77×10^{26} photons $\text{s}^{-1}\text{m}^{-2}$. Dashed lines indicate 920 and 1100 nm respectively; the wavelengths subsequently utilized for photo-stimulation and inhibition. **(c)** Peak photocurrent as a function of incident power density at a holding potential of -60 mV (mean \pm SEM, 920 nm, $n = 4$; 1100 nm, $n = 5$). **(d-g)** Current clamp (IC) characterization of somBiPOLES in CA1 pyramidal cells. **(d)** Probability of photoevoked action potentials under 1100 nm illumination for 5 ms ($n = 5$, red: average, gray: individual trials). **(e)** Characterization of the efficacy of silencing somBiPOLES expressing neurons under 920-nm illumination by co-injection of current (Box: median, 1st – 3rd quartile, whiskers: 1.5x inter quartile range, $n = 5$). **(f)** Representative voltage traces demonstrating sustained neuronal silencing of neurons by two-photon excitation of somBiPOLES at 920 nm. Upper trace (control): 550 pA current injected (illustrated by black line), no light. Lower trace: continuous injection of 550 pA current, 0.3 $\text{mW } \mu\text{m}^{-2}$, 920 nm, 2 Hz, 200 ms illumination. **(g)** Two-photon, bidirectional, control of single neurons demonstrated by co-incident illumination of 920 nm and 1100 nm light. Upper trace: 10 Hz spike train evoked by 15 ms pulses of 1100 nm light. Lower trace: optically induced action potentials shunted using a single, 200 ms pulse of 920 nm light. The data presented in this figure are provided in the Source Data file.

Considering the reliable performance of BiPOLES in pyramidal neurons we next tested its applicability in the invertebrate model systems *C. elegans* and *D. melanogaster* as well as mice and ferrets, representing vertebrate model systems.

Bidirectional control of motor activity in C. elegans

We expressed BiPOLES in cholinergic motor neurons of *C. elegans* to optically control body contraction and relaxation. Illumination with red light resulted in body-wall muscle contraction and effective body-shrinkage, consistent with motor neuron activation. Conversely, blue light triggered body extension, indicative of muscle relaxation and thus, cholinergic motor neuron inhibition (Fig. 6b). Maximal body length changes of +3% at 480 nm and -10% at 560-600 nm and reversal of the effect between 480-520 nm were consistent with the inhibitory and excitatory action spectrum of BiPOLES (Fig. 6b, Supplementary Fig. 12a). The light effects on body length required functional BiPOLES as light did not affect body length in the absence of all-*trans* retinal (ATR, Fig. 6b). Previous strategies for bidirectional motor control in *C. elegans* using ChR2(HR) and NpHR did not show body contraction and elongation in the same animal³³. Therefore, we tested this directly with light conditions similar to those used for BiPOLES activation. Excitation with blue light resulted in 5% body length decrease, while activation of NpHR at its peak wavelength (575 nm) failed to induce significant changes in body length (Supplementary Fig. 12b). Thus, BiPOLES expands the possibilities for bidirectional control of neuronal activity in *C. elegans* beyond what is achievable with currently available tools.

Bidirectional control of motor activity and nociception in D. melanogaster

Next, we demonstrate bidirectional control of circuit function and behavior with BiPOLES in *Drosophila melanogaster*. *GtACR2* and *CsChrimson* were previously used in separate experiments to silence and activate neuronal activity, respectively¹⁰. In contrast, rhodopsin pump functionality is strongly limited in this organism^{10,11} and bidirectional control of neuronal activity has not been achieved. We therefore expressed BiPOLES in glutamatergic motor neurons of *D. melanogaster* larvae (Fig. 6c). Illumination with blue light led to muscle relaxation and concomitant elongation (Fig. 6d). Change in body length was similar to animals expressing *GtACR2* alone (Supplementary Fig. 12c). Importantly, *GtACR2* activation in BiPOLES overrides blue-light evoked *Chrimson* activity and thereby eliminates blue-light excitation of neurons, as observed with *CsChrimson* alone (Supplementary Fig. 12c). Conversely, red illumination of BiPOLES expressing larvae triggered robust muscle contraction and corresponding body length reduction (Fig. 6d). Thus, BiPOLES facilitates bidirectional optogenetic control of neuronal activity in *D. melanogaster* which was not achieved previously.

We further tested BiPOLES functionality in a more sophisticated *in vivo* paradigm expressing it in key modulatory neurons (dorsal pair *llp7* neurons, *Dp7*) of the mechanonociceptive circuit. *Dp7* neurons naturally exert bidirectional control of the larval escape response to noxious touch depending on their activation level³⁴ (Fig. 6e). Acute BiPOLES-dependent silencing of *Dp7* neurons with blue light strongly decreased the rolling escape (Fig. 6f), consistent with previously

shown chronic silencing of these neurons³⁴. In turn, red light illumination of the same animals enhanced escape responses upon noxious touch showing that BiPOLES activation in Dp7 neurons can acutely tune their output and thus the corresponding escape response (Fig. 6f). BiPOLES activation in Dp7 neurons showed a similar ability to block or enhance nociceptive behavior as *GtACR2* or *CsChrimson*, respectively, while preventing Chrimson-dependent activation with blue light (Supplementary Fig. 12d, e). Taken together, BiPOLES allows robust, acute, and bidirectional manipulation of neuronal output and behavior in *Drosophila melanogaster* *in vivo*.

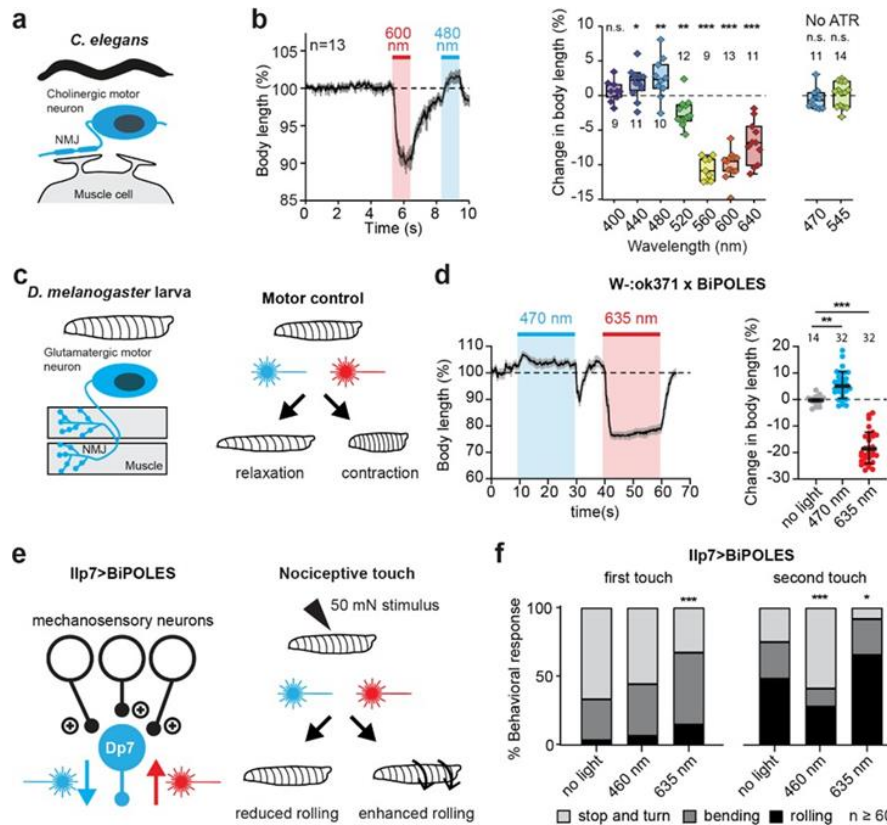


Figure 6. BiPOLES allows bidirectional modulation of neuronal activity in *C. elegans* and *D. melanogaster*. (a) BiPOLES expressed in cholinergic neurons of *C. elegans* enables bidirectional control of body contraction and relaxation. Scheme of BiPOLES-expressing cholinergic motor neuron innervating a muscle cell. (b) Left: Temporal dynamics of relative changes in body length upon illumination with 600 and 480 nm light (mean \pm SEM, 1.1 mW mm⁻², n = 13 animals). Right: Spectral quantification of maximal change in body length, compared is the body length before to during light stimulation (seconds 0-4 vs. seconds 6-9, see Supplementary fig. 12a; Box: median, 1st – 3rd quartile, whiskers: 1.5x inter quartile range, two-way ANOVA (Sidak's multiple comparisons test), p values: 400 nm (n = 9 animals): 0.99, 440 nm (n = 12): 0.049, 480 nm (n = 10): 0.007, 520 nm (n = 12): 0.002, 560 nm (n = 9): < 0.0001, 600 nm (n = 13): < 0.0001, 640 nm (n = 11): < 0.0001, no ATR 470 nm (n = 11): 0.24, no ATR 545 nm (n = 14): 0.78). Experiments in absence of all-trans retinal were done with 470/40 nm and 545/30 nm bandpass filters. (c) BiPOLES expressed in glutamatergic neurons of *D. melanogaster* larvae enables bidirectional control of body contraction and relaxation. Scheme of BiPOLES-expressing glutamatergic motor neuron innervating muscle fibers. (d) Left: Temporal dynamics of relative changes in body length upon illumination with 470 (17 μ W mm⁻², n = 32 animals) and 635 nm light (25 μ W mm⁻², n = 32). Right: Quantification of maximal change in body length (mean \pm SEM, no light = 14, 470nm = 32, 635nm = 32, **p = 0.0152, ***p = 0.0005, one-way ANOVA with Dunnett's multiple comparisons test). (e) BiPOLES- dependent manipulation of Dp7 neurons in the *Drosophila* larval brain (Ilp7-Gal4>UAS-BiPOLES) and the resulting change in nociceptive escape behavior following a 50 mN noxious touch. (f) Behavioral response after the first and second mechanical stimulus under blue light (470 nm, 1.7 mW mm⁻²) or red light (635 nm, 2.5 mW mm⁻²) illumination compared to no light. n = 61 animals *p = 0.034, ***p = 0.0005 (first touch) and 0.0007 (second touch), X²-test. The data presented in this figure and details on the statistical analysis are provided in the Source Data file.

All-optical excitation and inhibition of Locus Coeruleus in mice

To further extend the applications of BiPOLES to vertebrates, we generated various conditional and non-conditional viral vectors, in which the expression of the fusion construct is regulated by different promoters (see Methods, Table 2). Using these viral vectors, we sought to test BiPOLES and somBiPOLES in the mammalian brain. To this end, we conditionally expressed somBiPOLES in TH-Cre mice, targeting Cre-expressing neurons in the Locus Coeruleus (LC) (Fig. 7a). Orange illumination (594 nm) through an optical fiber implanted bilaterally above LC reliably triggered transient pupil dilation, indicative of LC-mediated arousal³⁵ (Fig. 7b-d). Pupil dilation was evident already at 0.7 mW at the fiber tip and gradually increased with increasing light power (Supplementary Fig. 13a). Light-mediated pupil dilation was reverted immediately by additional blue light (473 nm) during the orange-light stimulation, or suppressed altogether when blue-light delivery started before orange-light application (Fig. 7b-d), suggesting that orange-light-induced spiking of somBiPOLES-expressing neurons in LC was efficiently shunted. Illumination of the LC in wt-animals did not influence pupil dynamics (Supplementary Fig. 13b). Thus, LC-neurons were bidirectionally controlled specifically in somBiPOLES expressing animals.

We estimated the brain volume accessible to reliable activation and inhibition with somBiPOLES using Monte-Carlo simulations of light propagation¹⁶ under the experimental settings used for the LC-manipulations described above (Supplementary Fig. 14). Based on the light parameters required for neuronal excitation and inhibition determined in Fig. 3, and assuming 1 mW of 473 nm and 10 mW of 593 nm at the fiber tip, we estimate that reliable bidirectional control of neuronal activity can be achieved over a distance of >1.5 mm in the axial direction below the fiber tip (Supplementary Fig. 14c).

Manipulation of neocortical excitation/inhibition ratio in ferrets

Finally, we applied BiPOLES to bidirectionally control excitation/inhibition (E/I) ratio in the mammalian neocortex. Therefore, we generated a viral vector using the minimal *Dlx* promoter³⁶ (mDlx) to target GABAergic neurons in ferret secondary visual cortex (V2). Functional characterization in GABAergic neurons *in vitro* confirms all-optical spiking and inhibition of GABAergic neurons with mDlx-BiPOLES (Supplementary Fig. 15). Thus, we injected mDlx-BiPOLES in ferret V2 to modulate E/I-ratio during sensory processing (Fig. 7e). Extracellular recordings obtained from linear silicon probes in V2 of isoflurane-anesthetized ferrets provided evidence for modulation of cortical activity by shifts in E/I ratio (Fig. 7f, g). Blue light led to an increase in baseline activity, consistent with deactivation of inhibitory, GABAergic neurons (Fig. 7f, g). Activation of GABAergic cells by red light did not further decrease the low cortical baseline activity, but significantly reduced cortical responses triggered by sensory stimuli (Fig. 7f, g). Although effects of blue light on evoked spiking were not significant in the average data, we obtained clear evidence in individual recordings that blue light could enhance late response components (Fig. 7f), confirming a disinhibitory effect. Overall, these data suggest that BiPOLES is efficient in bidirectional control of inhibitory mechanisms, demonstrating its applicability for the control of E/I shifts in the cortical microcircuit *in vivo*.

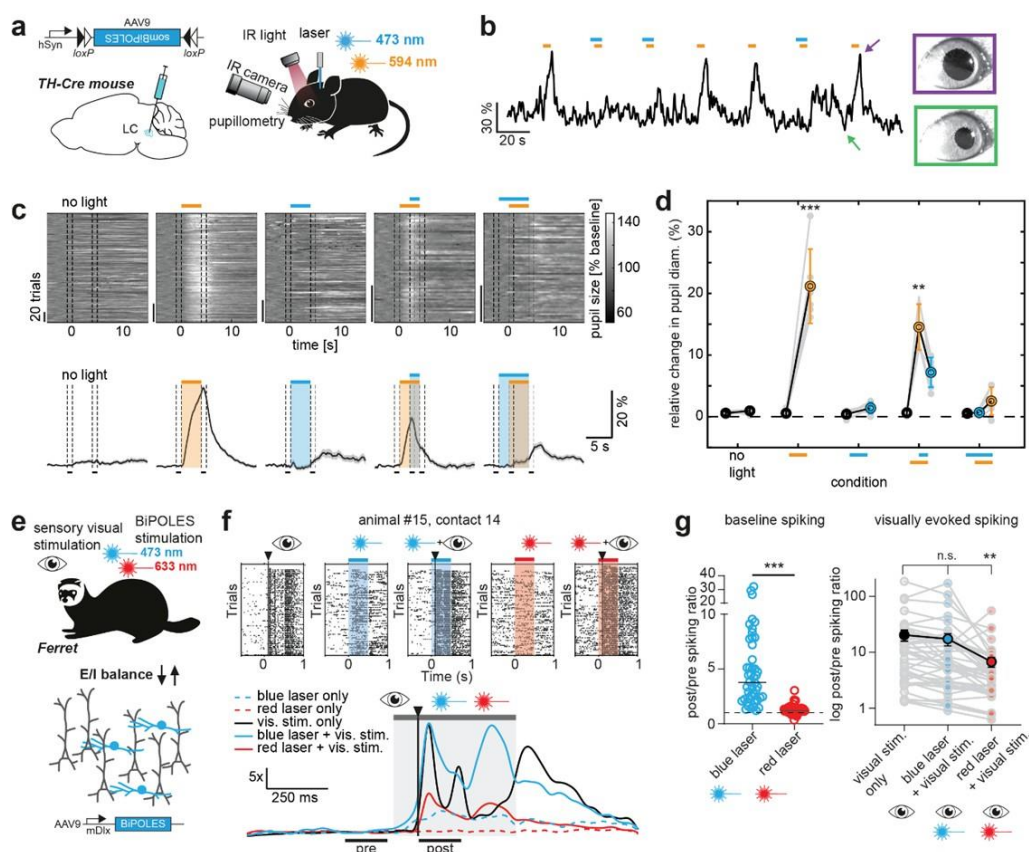


Figure 7. BiPOLES and somBiPOLES allow bidirectional modulation of neuronal activity in mice and ferrets. (a) Conditional expression of somBiPOLES in Cre-positive neurons of the TH-Cre mouse to modulate pupil dilation. **(b)** Relative pupil diameter in single trials. Orange and blue bars indicate time of illumination with 594 (orange) and 473 nm (blue), respectively. Arrows indicate positions of the two example images of the eye. **(c)** Quantification of normalized pupil size in one animal under various stimulation conditions for somBiPOLES as indicated. Top: single trials. Bottom: mean \pm SEM. Dashed lines show time windows used for quantification in the plot on the right. **(d)** Quantification of relative pupil size ($n = 6$ mice; One-way analysis of variance; $F = 61.67$, $p = 1.36 \times 10^{-12}$; Tukey's multiple comparison test: $**p = 0.0028$, $***: p < 0.0001$). **(e)** Modulation of GABAergic neurons (blue) in ferret secondary visual cortex (area 18) with mDlx-BiPOLES. Red (633 nm) or blue (473 nm) laser light was used to (de-)activate interneurons with or without a following 10-ms visual flash (white LED; Osram OSLO Compact) to the ferret's right eye. **(f)** Example neuronal spiking responses at one contact of the linear probe ($\sim 700 \mu\text{m}$ depth) under indicated stimulation conditions Top: Raster-plots of the visual stimulus alone, blue laser (+visual), red laser (+visual) conditions. Bottom: Normalized to 'pre'-phase averaged spike-density plot ($\sigma = 20$ ms) of each indicated condition. Gray area: laser-on epoch; black vertical line: visual stimulus onset. Black horizontal lines indicate the 200 ms pre- and post-stim analysis epochs to compute the results in (g). Note the rate-increase after the onset of the blue laser before the onset of the visual stimulus and the reduced answer after red laser illumination. **(g)** Spike-rate ratio of post vs pre-laser-stimulus epoch. Left: quantification of laser-mediated impact on baseline spiking rate (no visual stim.). Right: quantification of the spike-rate change of the same units during only visual and laser+visual stimulation. ($n = 46$ contacts showing visual responses from 3 animals, $**p = 0.0046$, $***p < 0.0001$). The data presented in this figure and details on the statistical analysis are provided in the Source Data file.

Discussion

In summary, BiPOLES is a performance-optimized fusion construct composed of a red-light-activated cation- and a blue-light-activated anion-selective ChR. BiPOLES serves as an optogenetic tool for potent excitation and inhibition of the same neurons with red and blue light, respectively. In addition, it can be applied for exclusive red-light activation of a neuronal subpopulation in multicolor experiments, and for locally defined optical tuning of the membrane voltage between the Nernst potential for chloride and the action potential threshold.

BiPOLES performs reliably in invertebrate and vertebrate model systems, showing potent, bidirectional modulation in the *C. elegans* motor system, the *D. melanogaster* motor and nociceptive systems and the ferret visual cortex. Addition of the soma-targeting signal from the mammalian potassium channel Kv2.1 yielded somBiPOLES, leading to further enhancement of trafficking to the plasma membrane at the soma and proximal dendrites while avoiding localization to distal dendrites and axons, as previously shown for individually expressed microbial rhodopsins²⁷⁻²⁹. Thus, eliminating the risk of inadvertent blue-light mediated depolarization of axons^{28,37} while improving bidirectional optogenetic manipulation of the somatodendritic compartment somBiPOLES is optimized for applications in mammalian systems.

Combining cation and anion channels of overlapping action spectra requires careful consideration of the electrochemical conditions of the neuronal membrane. Since the resting membrane potential is close to the Nernst potential of chloride, anion channels displaying large unitary conductance are needed in order to efficiently shunt depolarizing currents of the red-shifted cation channel, which, in turn, needs to be potent enough to reliably trigger action potentials. Thus, photocurrent amplitudes and spectral sensitivity of the two opsins need to match the aforementioned conditions in order to both reliably silence and drive neuronal activity. If the red-shifted excitatory

opsin shows too large, blue-light sensitive photocurrents, it may compromise the silencing capacity of the anion channel. Conversely, if the action spectrum of the blue-light sensitive anion channel extends too far towards longer wavelengths, efficient red-light evoked spiking may get impaired. For the molecular engineering of BiPOLES we focused on a large spectral separation of the anion and the cation conductance. Minimizing the optical cross-talk of both channels favors inhibitory conductance under blue light illumination and increases both the light intensity range and the spectral range that allows exclusive activation of the red shifted cation channel. Due to the large spectral separation, BiPOLES can be controlled with two simple light sources, such as LEDs, without the requirement of sophisticated spectral control, making its use straightforward. The GtACR2-L4-ChRmine-construct might be an interesting alternative if spectrally narrow light sources, such as lasers, are available, because it reaches peak depolarizing currents 60 nm blue-shifted compared to BiPOLES. Thus, inhibition and excitation can be achieved with 430-470 nm and 530-550 nm (Fig. 1f) providing an additional spectral window in the red, that can be used for a third optogenetic actuator or sensor. Finally, a seemingly trivial but equally important advantage of all the tandem systems we present here is their modular architecture allowing easy tailoring of fusion constructs fulfilling specific experimental requirements.

Noteworthy, BiPOLES does not represent the first optogenetic tool for bidirectional control of neuronal activity. Different combinations of the excitatory blue-light-sensitive ChR2 and orange-light-sensitive inhibitory ion pumps such as NpHR, bR, or Arch3.0 were generated previously^{2,4,6}. However, among all these variants, only the combination of ChR2 and NpHR (i.e. eNPAC and eNPAC2.0) was successfully used to address neuroscientific questions in mice⁶⁻⁹. BiPOLES will significantly expand the possibilities of bidirectional neuronal manipulations, since, aside from efficiently expressing in a wide array of different model systems, it also features a number of additional advantages: First, combining two potent channels, rather than a pump and a channel, provides a more balanced ionic flux per absorbed photon for the inhibitory and excitatory rhodopsin. This results in a high operational light sensitivity for both excitation and inhibition by orange and blue light, respectively. In contrast, high irradiance and expression levels are required for the ion pumps that only transport one charge per absorbed photon. Second, due to the use of two channels, BiPOLES-mediated photocurrents do not actively move ions against their gradients, which can cause adverse side-effects³⁷, but rather fixes the neuronal membrane voltage anywhere between the reversal potential of GtACR2 and Chrimson. The membrane voltage can be tuned depending on the ratio of blue/red light or a by a single light source tuned to wavelengths between the absorption peaks of GtACR2 and Chrimson. Third, inverting the color of the excitatory and inhibitory opsin, compared to previous tools, restricts optical excitation in BiPOLES-expressing cells exclusively to the orange/red spectrum. The inverted color-scheme enables scale-free and independent spiking of two neuronal populations in combination with a second, blue-light-sensitive ChR, expressed in a second population of neurons, as the blue-light-activated, inhibitory channel GtACR2 potentially shunts Chrimson-mediated, blue-light-activated excitatory photocurrents. Other applications could employ multiplexing with blue-light sensitive cyclases³⁸ or genetically encoded activity-indicators that

require blue light for photoconversion^{39,40}. Fourth, compared to the first generation of tandem constructs, BiPOLES was optimized for membrane trafficking and especially the somBiPOLES variant shows strongly improved membrane expression in mammalian neurons, enabling reliable and potent optogenetic spiking and inhibition even in deep brain regions *in vivo*. One additional reason for the superior membrane expression of BiPOLES compared to other rhodopsin-tandems might be the absence of N-terminal, extracellular cysteine residues, which are involved in disulfide bond formation and thus dimerization in all structurally described ChRs⁴¹⁻⁴⁴. The absence of N-terminal cysteines may avoid heteromeric protein networks and undesired clustering of the fused tandem-rhodopsins. Fifth, soma-targeted BiPOLES allows efficient and reliable bidirectional control of neuronal spiking over a wide range of light intensities. This is important for *in vivo* applications in the mammalian brain, where light scattering and absorption lead to an exponential fall-off of the irradiance over distance¹⁷. The color scheme in somBiPOLES in combination with the large conductance of *GtACR2* and its absence from axon terminals enables potent and reliable silencing with blue light over a wide range of intensities. Potential cross-activation of Chrimson by high blue light intensities did not compromise neuronal silencing in pyramidal neurons. Similarly, due to the red-shifted absorption of Chrimson, neuronal spiking can be efficiently achieved with orange light. somBiPOLES reliably mediates silencing and activation at modest intensities of blue and orange light far away from the fiber tip, while maintaining its wavelength-specificity under high-intensity irradiance, as typically present directly under the fiber tip. Thus, somBiPOLES holds the potential to manipulate neuronal activity in large brain areas with single-photon illumination (Supplementary Fig. 14c). Finally, a fusion-protein of two potent channels with opposite charge selectivity targeted to the somatodendritic compartment and displaying a local one-to-one expression ratio in the plasma membrane, enables temporally precise bidirectional control of neuronal activity at single-cell resolution using 2-photon excitation. In contrast to widefield illumination with visible light, 2-photon excitation in combination with soma-targeted opsins allows optogenetic control with single-cell resolution⁴⁵⁻⁴⁷. Bidirectional optogenetic control in the same cells has not been achieved with 2-photon excitation, so far; partially due to the low quantum efficiency of rhodopsin pumps, which limits their 2-photon activation. In contrast, the large conductance of the two channels improves their efficacy with respect to the number of transported ions per absorbed photon, and their presence at equal stoichiometry anywhere on the membrane ensures reliable and reproducible generation of anion- and/or cation currents, which is particularly important under locally confined 2-photon excitation.

In principle, also multicistronic vectors encoding both opsins under a single promoter using either an internal ribosomal entry site (IRES)⁴⁸ or a 2A ribosomal skip sequence allow expression of both ion channels at a fixed ratio from a single AAV vector^{3,7}. However, with both of these strategies neither co-localized nor stoichiometric membrane expression of both channels is guaranteed since both channels might get differentially targeted and distributed in the plasma membrane. This may not pose a limitation for experiments that require bidirectional control of large numbers of cells where precise control of single-cell activity or sub-cellular ion gradients

is not so crucial. BiPOLES as a covalently linked fusion protein displays a fixed expression of both opsins at a 1:1 stoichiometry anywhere in the membrane and membrane trafficking or degradation of both opsins occur at identical rates, preserving excitatory and inhibitory currents at a fixed ratio in all expressing cells. A fixed stoichiometry anywhere in the cell membrane is important if local, subcellular activation of the opsins is required, such as during 2-photon excitation or when a fixed ratio of cation and anion conductance is desired between different neurons or in particular neuronal compartments, such as single dendrites or dendritic spines.

Notably, BiPOLES employs an anion channel for optogenetic silencing and therefore relies on the extra- and intracellular chloride concentration. In the case of a depolarized chloride Nernst potential, opening of the anion channel may produce depolarizing currents, which can trigger action potentials or neurotransmitter release⁴⁹. Unlike for rhodopsin pumps, efficient silencing consequently requires low cytosolic chloride concentrations and is therefore limited in neurons or cellular compartments with a depolarized Nernst potential for chloride, such as immature neurons or axon terminals. Given these caveats, BiPOLES may not be suitable for bidirectional control of developing neurons or presynaptic boutons. In this case, silencing may be more efficient with rhodopsin pumps, despite their own limitations^{37,49} or with G-protein coupled rhodopsins^{50,51}. As with any optogenetic application, neurophysiological parameters need to be considered by the experimenter, guiding the appropriate choice of the tool suitable to address the specific experimental requirements.

Since BiPOLES can be used to spike or inhibit the same population of mature neurons *in vivo*, a number of previously inaccessible questions can be addressed. During extracellular recordings, BiPOLES may be useful for optogenetic identification (optotagging) with red light⁵² and optogenetic silencing of the same neurons. This will permit verification of the identity of silenced neurons by their spiking profiles. Moreover, in combination with a second, blue-light sensitive ChR, BiPOLES can be used to map local networks of spatially intermingled neurons. For example, expressed in distinct types of molecularly defined GABAergic neurons, connectivity of these neurons to a postsynaptic target cell can be evaluated. Additional applications for BiPOLES may encompass bidirectional control of engram neurons⁵³ to test both necessity and sufficiency of a particular set of neurons for memory retrieval or switching the valence of a particular experience by inhibiting or activating the same or even two distinct populations of neuromodulatory neurons. In principle, this could even be achieved with cellular resolution using 2-photon holography. Due to its utility for a wide range of research questions, its versatile functionality and its applicability in numerous model systems, as demonstrated in this study, BiPOLES fills an important gap in the optogenetic toolbox and might become the tool of choice to address a number of yet inaccessible problems in neuroscience.

Methods

Molecular Biology

For HEK-cell expression, the coding sequences of Chrimson (KF992060.1), CsChrimson (KJ995863.2) from *Chlamydomonas noctigama*¹², ChRmine from *Rhodomonas lens* although

initially attributed to *Tiarina fusus*^{22,25} (Addgene #130997), *bReaChES20*, *iC++* (Addgene #98165)¹⁹, *Aurora* (Addgene #98217)¹¹, *GtACR1* (KP171708) and *GtACR2* (KP171709) from *Guillardia theta*¹⁸ as well as the blue shifted Arch3.0 mutant M128A/S151A/A225T herein described as ArchBlue26 were cloned together with mCerulean354 and a trafficking signal (ts) from the Kir 2.1 channel⁴ into a pCDNA3.1 vector containing the original opsin tandem cassette2 with a linker composed of eYFP and the first 105 N-terminal amino acids of the rat gastric H+/K+-ATPase beta subunit (β HK, NM_012510.2), kindly provided by Sonja Kleinlogel (University of Bern, CH). For direct comparison also the bicistronic tool eNPAC2.06 – kindly provided by Karl Deisseroth (Stanford University, CA) - was cloned into the same backbone. Site-directed mutagenesis to introduce the f-Chrimson and vf-Chrimson mutations Y261F, S267M and K176R²¹ was performed using the QuickChange Site-Directed Mutagenesis Kit (Agilent Technologies, Santa Clara, CA) according to the manufacturers' instructions.

For neuronal expression, the insert consisting of *GtACR2*-ts-mCerulean3- β HK-Chrimson was cloned into an AAV2-backbone behind a human synapsin (hSyn) promoter (pAAV-hSyn-BiPOLES-mCerulean; Addgene #154944). A soma-targeted, membrane-trafficking optimized variant was generated by fusing an additional trafficking signal from the potassium channel Kv2.1²⁷ to the C-terminus of Chrimson (pAAV-hSyn-somBiPOLES-mCerulean; Addgene #154945). For expression in GABAergic neurons, BiPOLES and somBiPOLES were cloned into an AAV2-backbone behind the minimal *Dlx* (mDlx) promoter³⁶ resulting in pAAV-mDlx-BiPOLES-mCerulean (Addgene #154946) and pAAV-mDlx-somBiPOLES-mCerulean (Addgene #154947). For expression in projection neurons, somBiPOLES was cloned into an AAV2-backbone behind the minimal CaMKII promoter⁵⁵ resulting pAAV-CaMKII-somBiPOLES-mCerulean (Addgene #154948). Double-floxed inverted open reading frame variants of BiPOLES and somBiPOLES were generated by cloning these inserts in antisense direction behind the *Ef1alpha* or hSyn promoter, flanked by two loxP and lox2272 sites (*Ef1a-DIO-BiPOLES-mCerulean*, Addgene #154949; *hSyn-DIO-BiPOLES-mCerulean*, Addgene #154950; *hSyn-DIO-somBiPOLES-mCerulean*, Addgene #154951). Note that in all constructs the mCerulean3-tag is fused between *GtACR2*-ts and β HK-Chrimson and therefore part of BiPOLES. We nonetheless chose to add "mCerulean" to the plasmid names to remind the reader of the presence of a cyan fluorophore in BiPOLES. BiPOLES stands for "Bidirectional Pair of Opsins for Light-induced Excitation and Silencing". Sequences of all primers used for cloning and sequences of DNA-inserts used in this study are provided in a separate list (Supplementary Data 1).

Patch-Clamp experiments in HEK293 cells

⁵⁶Fusion constructs were expressed under the control of a CMV-promotor in HEK293 cells that were cultured in Dulbecco's Modified Medium (DMEM) with stable glutamine (Biochrom, Berlin, Germany), supplemented with 10% (v/v) fetal bovine serum (FBS Superior; Biochrom, Berlin, Germany), 1 μ M all-*trans* retinal, and 100 μ g ml⁻¹ penicillin/streptomycin (Biochrom, Berlin, Germany). Cells were seeded on poly-lysine coated glass coverslips at a concentration of 1 x 10⁵

cells ml^{-1} and transiently transfected using the FuGENE® HD Transfection Reagent (Promega, Madison, WI) two days before measurement.

Patch-clamp experiments were performed in transgene expressing HEK293 cells two days after transfection⁵⁶. Patch pipettes were prepared from borosilicate glass capillaries (G150F-3; Warner Instruments, Hamden, CT) using a P-1000 micropipette puller (Sutter Instruments, Novato, CA) and subsequently fire polished. Pipette resistance was between 1.2 and 2.5 M Ω . Single fluorescent cells were identified using an Axiovert 100 inverted microscope (Carl Zeiss, Jena, Germany). Monochromatic light (± 7 nm) was provided by a Polychrome V monochromator (TILL Photonics, Planegg, Germany) or by a pE-4000 CoolLED system (CoolLED, Andover, UK) for light titration experiments. Light intensities were attenuated by a motorized neutral density filter wheel (Newport, Irvine, CA) for equal photon flux during action spectra recordings. Light pulses of the Polychrome V were controlled by a VS25 and VCM-D1 shutter system (Vincent Associates, Rochester, NY). Recordings were done with an AxoPatch 200B amplifier (Molecular Devices, Sunnyvale, CA) or an ELV-03XS amplifier (npi Electronics, Tamm, Germany), filtered at 2 kHz and digitized using a DigiData 1440A digitizer (Molecular Devices, Sunnyvale, CA) at a sampling rate of 10 kHz. The reference bath electrode was connected to the bath solution via a 140 mM NaCl agar bridge. Bath solutions contained 140 mM NaCl, 1 mM KCl, 1 mM CsCl, 2 mM CaCl₂, 2 mM MgCl₂ and 10 mM HEPES at pH_e 7.2 (with glucose added up to 310 mOsm). Pipette solution contained 110 mM NaGluconate, 1 mM KCl, 1 mM CsCl, 2 mM CaCl₂, 2 mM MgCl₂, 10 mM EGTA and 10 mM HEPES at pH_i 7.2 (glucose added up to 290 mOsm). All light intensities were measured in the object plane using a P9710 optometer (Gigahertz-Optik, Türkenfeld, Germany) and normalized to the water Plan-Apochromat 40x/1.0 differential interference contrast (DIC) objective illuminated field (0.066 mm²). The irradiance was 2.7 mW mm⁻² at 650 nm, 3.5 mW mm⁻² at 600 nm, 4.2 mW mm⁻² at 530 nm, 5.7 mW mm⁻² at 490 nm and 5.2 mW mm⁻² at 450 nm. All electrical recordings were controlled by the pCLAMP™ software (Molecular Devices, Sunnyvale, CA). All whole-cell recordings had a membrane resistance of at least 500 M Ω (usual >1 G Ω) and an access resistance below 10 M Ω .

		irradiance (mW mm ⁻²)					
		0.001	0.01	0.1	1	10	100
wavelength (nm)	365	1.84E+18	1.84E+19	1.84E+20	1.84E+21	1.84E+22	1.84E+23
	385	1.94E+18	1.94E+19	1.94E+20	1.94E+21	1.94E+22	1.94E+23
	405	2.04E+18	2.04E+19	2.04E+20	2.04E+21	2.04E+22	2.04E+23
	435	2.19E+18	2.19E+19	2.19E+20	2.19E+21	2.19E+22	2.19E+23
	460	2.32E+18	2.32E+19	2.32E+20	2.32E+21	2.32E+22	2.32E+23
	470	2.37E+18	2.37E+19	2.37E+20	2.37E+21	2.37E+22	2.37E+23
	490	2.47E+18	2.47E+19	2.47E+20	2.47E+21	2.47E+22	2.47E+23
	525	2.65E+18	2.65E+19	2.65E+20	2.65E+21	2.65E+22	2.65E+23
	550	2.77E+18	2.77E+19	2.77E+20	2.77E+21	2.77E+22	2.77E+23
	580	2.92E+18	2.92E+19	2.92E+20	2.92E+21	2.92E+22	2.92E+23
	595	3E+18	3E+19	3E+20	3E+21	3E+22	3E+23
	630	3.18E+18	3.18E+19	3.18E+20	3.18E+21	3.18E+22	3.18E+23
	660	3.33E+18	3.33E+19	3.33E+20	3.33E+21	3.33E+22	3.33E+23

Table 1: Photon flux given as number of photons sec⁻¹ m⁻²

Preparation of organotypic hippocampal slice cultures

All procedures were in agreement with the German national animal care guidelines and approved by the independent Hamburg state authority for animal welfare (Behörde für Justiz und Verbraucherschutz). They were performed in accordance with the guidelines of the German Animal Protection Law and the animal welfare officer of the University Medical Center Hamburg-Eppendorf. Organotypic hippocampal slices were prepared from Wistar rats or VIP-IRES-Cre mice of both sexes (Jackson-No. 031628) at post-natal day 5-7⁵⁷. Dissected hippocampi were cut into 350 µm slices with a tissue chopper and placed on a porous membrane (Millicell CM, Millipore). Cultures were maintained at 37°C, 5% CO₂ in a medium containing 80% MEM (Sigma M7278), 20% heat-inactivated horse serum (Sigma H1138) supplemented with 1 mM L-glutamine, 0.00125% ascorbic acid, 0.01 mg ml⁻¹ insulin, 1.44 mM CaCl₂, 2 mM MgSO₄ and 13 mM D-glucose. No antibiotics were added to the culture medium.

Transgene delivery for single-photon experiments

For transgene delivery in organotypic slices, individual CA1 pyramidal cells were transfected by single-cell electroporation⁵⁸ between DIV 14-16⁵⁸. Except for pAAV-hSyn-eNPAC2.0, which was used at a final concentration of 20 ng µl⁻¹, all other plasmids, namely pAAV-hSyn-BiPOLES-mCerulean, pAAV-hSyn-somBiPOLES-mCerulean, pAAV-hSyn-Chrimson-mCerulean, and pAAV-hSyn-somGtACR2-mCerulean were used at a final concentration of 5 ng µl⁻¹ in K-gluconate-based solution consisting of (in mM): 135 K-gluconate, 10 HEPES, 4 Na₂-ATP, 0.4 Na-GTP, 4 MgCl₂, 3 ascorbate, 10 Na₂-phosphocreatine (pH 7.2). A plasmid encoding hSyn-mKate2 or hSyn-mCerulean (both at 50 ng µl⁻¹) was co-electroporated with the opsin-mCerulean or eNPAC2.0 plasmids, respectively, and served as a morphology marker. An Axoporation 800A (Molecular Devices) was used to deliver 50 hyperpolarizing pulses (-12 V, 0.5 ms) at 50 Hz. During electroporation slices were maintained in pre-warmed 37°C) HEPES-buffered solution (in mM): 145 NaCl, 10 HEPES, 25 D-glucose, 2.5 KCl, 1 MgCl₂ and 2 CaCl₂ (pH 7.4, sterile filtered). In

some cases, slice cultures were transduced with adeno-associated virus (see Table 2 for details) at DIV 3-5⁵⁹. The different rAAVs were locally injected into the CA1 region using a Picospritzer (Parker, Hannafin) by a pressurized air pulse (2 bar, 100 ms) expelling the viral suspension into the slice. During virus transduction, membranes carrying the slices were kept on pre-warmed HEPES-buffered solution.

Adeno-associated virus (AAV9)	Titer used for transduction of hippocampal organotypic slice cultures (vg/ml)	Addgene plasmid reference
mDlx-BiPOLES-mCerulean	2.8×10^{13}	154946
hSyn-DIO-BiPOLES-mCerulean	7.0×10^{13}	154950
hSyn-DIO-somBiPOLES-mCerulean	3.4×10^{13}	154951
CaMKIIa(0.4)-somBiPOLES-mCerulean	2.5×10^{13}	154948
CaMKIIa(0.4)-DO-CheRiff-ts-mScarlet-ER	8.15×10^{11}	n.a.
mDlx-H2B-EGFP	2.8×10^{10}	n.a.
CaMKIIa-Cre	3.0×10^{12}	n.a.

Table 2: List of adeno-associated viral vectors used for experiments in organotypic hippocampal slices.

Viruses were transduced at the indicated titers. n.a.: not applicable.

Preparation of organotypic hippocampal slice cultures for two-photon holographic stimulation of somBiPOLES

All experimental procedures were conducted in accordance with guidelines from the European Union and institutional guidelines on the care and use of laboratory animals (council directive 2010/63/EU of the European Union). Organotypic hippocampal slices were prepared from mice (Janvier Labs, C57Bl6J) at post-natal day 8 (P8). Hippocampi were sliced into 300 μ m thick sections in a cold dissecting medium consisting of GBSS supplemented with 25 mM D-glucose, 10 mM HEPES, 1 mM Na-Pyruvate, 0.5 mM α -tocopherol, 20 nM ascorbic acid and 0.4% penicillin/streptomycin (5000 U ml⁻¹). Slices were placed onto a porous membrane (Millicell CM, Millipore) and cultured at 37°C, 5% CO₂ in a medium consisting of 50% Opti-MEM (Fisher 15392402), 25% heat-inactivated horse serum (Fisher 10368902), 24% HBSS and 1% penicillin/streptomycin (5000 U ml⁻¹). This medium was supplemented with 25 mM D-glucose, 1 mM Na-Pyruvate, 20 nM ascorbic acid and 0.5 mM α -tocopherol. After three days in-vitro, the medium was replaced with one containing 82% neurobasal-A, 15% heat-inactivated horse serum (Fisher 11570426), 2% B27 supplement (Fisher, 11530536), 1% penicillin/streptomycin (5000 U ml⁻¹), which was supplemented with 0.8 mM L-glutamine, 0.8 mM Na-Pyruvate, 10 nM

ascorbic acid and 0.5 mM α -tocopherol. This medium was removed and replaced once every 2-3 days.

Slices were transduced with AAV9-CaMKII-somBiPOLES-mCerulean at DIV 3 by bulk application of 1 μ l of virus (final titer: 2.5×10^{13} vg ml⁻¹) per slice. Experiments were performed between DIV 13-17.

Slice culture electrophysiology with single-photon stimulation

At DIV 19-21, whole-cell patch-clamp recordings of transfected or virus-transduced CA1 pyramidal or GABAergic neurons were performed. Experiments were done at room temperature (21-23°C) under visual guidance using a BX 51WI microscope (Olympus) equipped with Dodt-gradient contrast and a Double IPA integrated patch amplifier controlled with SutterPatch software (Sutter Instrument, Novato, CA). Patch pipettes with a tip resistance of 3-4 MW were filled with intracellular solution consisting of (in mM): 135 K-gluconate, 4 MgCl₂, 4 Na₂-ATP, 0.4 Na-GTP, 10 Na₂-phosphocreatine, 3 ascorbate, 0.2 EGTA, and 10 HEPES (pH 7.2). Artificial cerebrospinal fluid (ACSF) consisted of (in mM): 135 NaCl, 2.5 KCl, 2 CaCl₂, 1 MgCl₂, 10 Na-HEPES, 12.5 D-glucose, 1.25 NaH₂PO₄ (pH 7.4). In experiments where synaptic transmission was blocked, 10 μ M CPPene, 10 μ M NBQX, and 100 μ M picrotoxin (Tocris, Bristol, UK) were added to the recording solution. In experiments analyzing synaptic inputs onto O-LM interneurons, ACSF containing 4 mM CaCl₂ and 4 mM MgCl₂ was used to reduce the overall excitability. Measurements were corrected for a liquid junction potential of -14,5 mV. Access resistance of the recorded neurons was continuously monitored and recordings above 30 M Ω were discarded. A 16 channel LED light engine (CoolLED pE-4000, Andover, UK) was used for epifluorescence excitation and delivery of light pulses for optogenetic stimulation (ranging from 385 to 635 nm). Irradiance was measured in the object plane with a 1918 R power meter equipped with a calibrated 818 ST2 UV/D detector (Newport, Irvine CA) and divided by the illuminated field of the Olympus LUMPLFLN 60XW objective (0.134 mm²).

For photocurrent density measurements in voltage-clamp mode CA1 cells expressing BiPOLES, somBiPOLES, Chrimson or somGtACR2 were held at -75 or -55 mV to detect inward (cationic) or outward (anionic) currents elicited by red (635 nm, 20 ms, 1 and 10 mW mm⁻²) and blue light (490 nm, 100 ms, 10 mW mm⁻²), respectively. For each cell, the peak photocurrent amplitude (in pA) was divided by the cell membrane capacitance (in pF) which was automatically recorded by the SutterPatch software in voltage-clamp mode ($V_{\text{hold}} = -75$ mV).

In current-clamp experiments holding current was injected to maintain CA1 cells near their resting membrane potential (-75 to -80 mV). To assess the suitability of BiPOLES and somBiPOLES as dual-color neuronal excitation and silencing tools, alternating pulses of red (635 nm, 20 ms, 10 mW mm⁻²), blue (490 nm, 100 ms, 10 mW mm⁻²) and a combination of these two (onset of blue light 40 ms before red light) were delivered to elicit and block action potentials. For eNPAC2.0 alternating pulses of blue (470 nm, 20 ms, 10 mW mm⁻²), yellow (580 nm, 100 ms, 10 mW mm⁻²) and a combination of these two (onset of yellow light 40 ms before blue

light) were used.

In experiments determining the spiking probability of somBiPOLES and Chrimson under illumination with light of different wavelengths (470, 595 and 635 nm), a train of 20 light pulses (5 ms pulse duration) was delivered at 5 Hz. For each wavelength, irradiance values from 0.1 to 100 mW mm⁻² were used. For comparisons with eNPAC2.0, only light of 470 nm was used, which is the peak activation wavelength of ChR2(HR). AP probability was calculated by dividing the number of light-triggered APs by the total number of light pulses.

To compare the irradiance threshold needed to spike CA1 cells with BiPOLES, somBiPOLES, eNPAC2.0, Chrimson, and CheRiff across different wavelengths, 470, 525, 595 and 635 nm light ramps going from 0 to 10 mW mm⁻² over 1 s were delivered in current-clamp mode. In the case of BiPOLES and somBiPOLES the blue light ramp went up to 100 mW mm⁻² to rule out that very high blue-light irradiance might still spike neurons. The irradiance value at the time of the first spike was defined as the irradiance threshold (in mW mm⁻²) needed to evoke action potential firing.

To measure the ability of BiPOLES, somBiPOLES, and som*Gt*ACR2 to shift the rheobase upon blue-light illumination, depolarizing current ramps (from 0–100 to 0–900 pA) were injected into CA1 neurons in the dark and during illumination with 490 nm light at irradiance values ranging from 0.001 to 100 mW mm⁻². The injected current at the time of the first spike was defined as the rheobase. The relative change in the number of ramp-evoked action potentials (APs) was calculated counting the total number of APs elicited during the 9 current ramp injections from 0–100 to 0–900 pA) for each irradiance and normalized to the number of APs elicited in the absence of light. The same experiment was conducted for eNPAC2.0, but using 580 nm light ranging from 0.01 to 100 mW mm⁻². Statistical significance was calculated using Friedman test.

To optically clamp the neuronal membrane potential using somBiPOLES, simultaneous illumination with blue and orange light at varying ratios was used. In current-clamp experiments, 470 and 595 nm light ramps (5 s) of opposite gradient (1 to 0 mW mm⁻² and 0 to 1 mW mm⁻², respectively) were applied. Alternatively, optical clamping of the membrane potential was achieved by tuning a single wavelength between 385 and 660 nm (2 s light pulses, 0.1 mW mm⁻²). Voltage traces were median-filtered to remove orange/red-light-mediated spikes and reveal the slow change in membrane voltage during illumination.

For independent optogenetic activation of two distinct populations of neurons, organotypic slice cultures from VIP-Cre mice were transduced with 2 adeno-associated viral vectors: 1, a double-floxed inverted open reading frame (DIO) construct encoding somBiPOLES (hSyn-DIO-somBiPOLES-mCerulean, see Table 2 for details) to target VIP-positive interneurons, and 2, a double-floxed open reading frame (DO) construct encoding CheRiff (hSyn-DO-CheRiff-ts-mScarlet-ER, see Table 2 for details) to target CA1 pyramidal neurons and exclude expression in VIP-positive cells. Synaptic input from these two populations was recorded in VIP-negative stratum-oriens GABAergic neurons (putative O-LM cells). In CA1, O-LM neurons receive innervation both from local CA1 pyramidal cells and VIP-positive GABAergic neurons⁶⁰. To

facilitate identification of putative GABAergic post-synaptic neurons in stratum oriens, slices were transduced with an additional rAAV encoding mDlx-H2B-EGFP. In the absence of synaptic blockers light-evoked EPSCs and IPSCs were recorded while holding the postsynaptic cell at different membrane potentials (-80, -65, -55, -45 and 6 mV) in whole-cell voltage clamp mode. A blue (460 nm, 0.03 - 84.0 mW mm⁻²) and a red (635 nm, 6.0 – 97.0 mW mm⁻²) light pulse were delivered 500 ms apart from each other through a Leica HC FLUOTAR L 25x/0.95 W VISIR objective.

To functionally assess the putative expression of somBiPOLES in the axon terminals of CA3 pyramidal cells, slice cultures were transduced with an AAV9 encoding for CaMKIIa(0.4)-somBiPOLES-mCerulean (see Table 2 for details). Red-light evoked EPSCs were recorded in postsynaptic CA1 cells during local illumination either in CA3 at the somata (two light pulses of 5 ms delivered 40 ms apart using a fiber-coupled LED (400 μm fiber, 0.39 NA, 625 nm, Thorlabs) controlled by a Mightex Universal 4-Channel LED Driver (1.6 mW at fiber tip), or in CA1 at axon terminals of somBiPOLES-expressing CA3 cells (two light pulses of 5 ms delivered 40 ms apart through the 60x microscope objective, 635 nm, 50 mW mm⁻²). Axonal light stimulation was done in the presence of tetrodotoxin (TTX, 1 μM) and 4-aminopyridine (4-AP, 100 μM) to avoid antidromic spiking of CA3 cells.

To determine the high-frequency spiking limit with somBiPOLES, action potentials were triggered in CA1 cells at frequencies ranging from 10 to 100 Hz using 40 light pulses (595 nm, 3 ms pulse width, 10 mW mm⁻²). AP probability was calculated by dividing the number of light-triggered APs by the total number of light pulses.

To characterize the spectral activation of BiPOLES, eNPAC2.0. and som *GtACR2*, photocurrents were recorded from CA1 cells in voltage-clamp mode in response to 500 ms illumination with various wavelengths (from 385 to 660 nm, 10 mW mm⁻²). BiPOLES- and som *GtACR2*-expressing cells were held at a membrane voltage of -55 mV, more positive than the chloride Nernst potential, to measure light-mediated outward chloride currents. Photocurrent recordings from eNPAC2.0-expressing cells were done at a holding voltage of -75 mV. For BiPOLES and eNPAC2.0 the photocurrent ratio between excitatory and inhibitory photocurrents was calculated in each cell by dividing the amplitude of the photocurrents evoked by 490/595 nm (for BiPOLES) and 460/580nm (for eNPAC2.0).

Passive and active membrane parameters were measured in somBiPOLES-expressing and non-transduced, wild-type CA1 pyramidal cells. Resting membrane potential, membrane resistance and capacitance were automatically recorded by the SutterPatch software in voltage-clamp mode ($V_{\text{hold}} = -75$ mV) in response to a voltage test pulse of 100 ms and -5 mV. The number of elicited action potentials were counted in response to a somatic current injection of 300 pA in current-clamp mode (0 pA holding current). For the 1st elicited AP, the voltage threshold, peak and amplitude were measured.

Slice culture immunohistochemistry and confocal imaging

The subcellular localization of BiPOLES and somBiPOLES in hippocampal neurons was assessed 20 days after virus transduction (AAV9-hSyn-DIO-BiPOLES-mCerulean + CaMKIIa-Cre, and CaMKIIa(0.4)-somBiPOLES-mCerulean, respectively. See Table 2 for details). Hippocampal organotypic slice cultures were fixed in a solution of 4% (w/v) paraformaldehyde (PFA) in PBS for 30 min at room temperature (RT). Next, slices were washed in PBS (3 x 10 min), blocked for 2 h at RT (10% [v/v] normal goat serum [NGS] in 0.3% [v/v] Triton X-100 containing PBS) and subsequently incubated for 48 h at 4°C with a primary antibody against GFP to amplify the mCerulean signal (chicken, anti-GFP, Invitrogen, A10262, Lot 1972783) at 1:1000 in carrier solution (2% [v/v] NGS, in 0.3% [v/v] Triton X-100 containing PBS). Following 3 rinses of 10 min with PBS, slices were incubated for 3 h at RT in carrier solution (same as above) with an Alexa Fluor® dye-conjugated secondary antibody (goat, anti-chicken Alexa-488, Invitrogen; A11039, Lot 2079383, 1:1000). Slices were washed again, transferred onto glass slides and mounted for visualization with Shandon Immu-Mount (Thermo Scientific; 9990402).

Confocal images were acquired using a laser-scanning microscope (Zeiss, LSM 900) equipped with a 40x oil-immersion objective lens (Zeiss EC Plan-Neofluar 40x/1.3 oil). Excitation/emission filters were appropriately selected for Alexa 488 using the dye selection function of the ZEN software. The image acquisition settings were optimized once and kept constant for all images within an experimental data set. Z-stack images were obtained using a 1 µm z-step at a 1024 x 1024-pixel resolution scanning at 8 µs per pixel. Fiji61 was used to quantify fluorescence intensity values along a line perpendicular to the cell equator and spanning the cell diameter. For each cell, grey values above 80% of the maximum intensity were distributed in 10 bins according to their location along the line.

Slice culture two-photon imaging

Neurons in organotypic slice cultures (DIV 19-21) were imaged with two-photon microscopy to check for the live expression of hSyn-DIO-somBiPOLES-mCerulean, CaMKIIa(0.4)-DO-CheRiff-ts-mScarlet-ER, mDlx-BiPOLES-mCerulean and CaMKIIa(0.4)-somBiPOLES-mCerulean. The custom-built two-photon imaging setup was based on an Olympus BX-51WI upright microscope upgraded with a multiphoton imaging package (DF-Scope, Sutter Instrument), and controlled by ScanImage 2017b software (Vidrio Technologies). Fluorescence was detected through the objective (Leica HC FLUOTAR L 25x/0.95 W VISIR) and through the oil immersion condenser (numerical aperture 1.4, Olympus) by two pairs of GaAsP photomultiplier tubes (Hamamatsu, H11706-40). Dichroic mirrors (560 DXCR, Chroma Technology) and emission filters (ET525/70m-2P, ET605/70m-2P, Chroma Technology) were used to separate cyan and red fluorescence. Excitation light was blocked by short-pass filters (ET700SP-2P, Chroma Technology). A tunable Ti:Sapphire laser (Chameleon Vision-S, Coherent) was set to 810 nm to excite mCerulean on BiPOLES and somBiPOLES. An Ytterbium-doped 1070-nm pulsed fiber laser (Fidelity-2, Coherent) was used at 1070 nm to excite mScarlet on CheRiff. Maximal intensity projections of z-stacks were generated with Fiji61.

Electrophysiology for two-photon photostimulation of somBiPOLES

At DIV 13-17, whole-cell patch-clamp recordings of somBiPOLES-infected excitatory neurons were performed at room temperature (21 - 23°C). An upright microscope (Scientifica, SliceScope) was equipped with an infrared (IR) source (Thorlabs, M1050L4), oblique condenser, microscope objective (Nikon, CFI APO NIR, 40X, 0.8 NA), tube lens (Thorlabs, AC508-300-B) and an CMOS camera (Point Grey, CM3-U3-31S4M-CS) to collect IR light transmitted through the sample. Recordings were performed using an amplifier (Molecular Devices, Multiclamp 700B), a digitizer (Molecular Devices, Digidata 1550B) at a sampling rate of 10 kHz and controlled using pCLAMP11 (Molecular Devices). During experimental sessions, slice cultures were perfused with artificial cerebrospinal fluid (ACSF) comprised of 125 mM NaCl, 2.5 mM KCl, 1.5 mM CaCl₂, 1 mM MgCl₂, 26 mM NaHCO₃, 0.3 mM ascorbic acid, 25 mM D-glucose, 1.25 mM NaH₂PO₄. Synaptic transmission was blocked during all experiments by addition of 1 μM AP5 (Abcam, ab120003), 1 μM NBQX (Abcam, ab120046), and 10 μM picrotoxin (Abcam, ab120315) to the extracellular (recording) solution. Continuous aeration of the recording solution with 95% O₂ and 5% CO₂, resulted in a final pH of 7.4. Patch pipettes with a tip resistance of 4-6 MΩ were filled with intracellular solution consisting of 135 mM K-gluconate, 4 mM KCl, 4 mM Mg-ATP, 0.3 mM Na-GTP, 10 mM Na₂-phosphocreatine and 10 mM HEPES (pH 7.35). Only recordings with an access resistance below 30 MΩ were included in subsequent analysis.

During experiments performed using whole-cell voltage clamp, neurons were held at -60 mV (the average resting potential of neurons in hippocampal organotypic slices). The soma of each patched neuron was precisely positioned in the center of the field of view. When recording the photocurrent as a function of membrane potential (holding potentials: -80, -70, -65, -60, -55 mV), neurons were temporarily held at each holding potential 5 s before and after photostimulation. For data presented in Fig. 5a-d, two-photon photoactivation was performed by continuous, 200 ms, illumination of each patched neuron using a 12-μm-diameter holographic spot (wavelengths: 850, 900, 920, 950, 980, 1000, 1050, 1100 nm), which was precisely positioned in the center of the field of view. Data presented in Fig 7d-g was acquired in current clamp experiments. Where necessary, current was injected to maintain neurons at the resting membrane potential (-60 mV). The ability of two-photon holographic excitation to evoke action potentials was first assessed using a protocol consisting of 5, 5 ms pulses of 1100 nm light for power densities ranging between 0.16 – 1.00 mW μm⁻². The latency and jitter of light-evoked action potentials, respectively defined as the mean and standard deviation of the time between the onset of stimulation to the peak of the action potential, were measured using an identical protocol. Trains of light pulses with frequencies between (2 – 30 Hz) were used to verify that trains of action potentials could be reliably induced using 5 ms 1100 nm illumination. The potency of two-photon inhibition was evaluated by measuring the rheobase shift induced by 920 nm illumination. Depolarizing current was injected for 5 ms into recorded neurons (from 0 - 1.2 nA in steps of 20 pA). The protocol was topped when action potentials were observed for 3 consecutive current steps. The rheobase was defined as the amount of current injected to evoke the first of these 3 action potentials. The rheobase shift was measured by repeating the protocol with co-incident, 5 ms, illumination of the neuron with a 920 nm holographic spot (power densities between 0.05 - 0.25 mW μm⁻²). Co-incident trains of light pulses (15 ms) and injected current (10 ms) with frequencies between (2 - 30 Hz) were used to verify

that two-photon inhibition could precisely and reliably eliminate single spikes. Sustained neuronal silencing by two-photon excitation of somBiPOLES under 920 nm illumination was characterized by continuously injecting current above the rheobase for 1 s. The protocol was repeated with 200 ms co-incident illumination using a 920 nm holographic spot (power densities between 0.05 - 0.3 mW μm^{-2}).

Two-photon, bidirectional, control of single neurons was demonstrated by co-incident illumination of titrated 920 nm and 1100 nm light. A 10-Hz train of 15 ms pulses of 1100 nm light was used to evoke a train of action potentials which were shunted using a continuous 200 ms pulse of 920 nm light.

Two-photon photostimulation of somBiPOLES in hippocampal organotypic slices

Two-photon photostimulation was performed using a tunable femtosecond laser (Coherent Discovery, 80 MHz, 100 fs, tuned between 850 – 1100 nm). A schematic diagram of the experimental setup is presented in Supplementary Fig. 10. A telescope formed of two lenses (L1 (Thorlabs, AC508-100-B) and L2 (Thorlabs, AC508-400-B)) expanded the beam onto a Spatial Light Modulator (SLM, Hamamatsu, LCOS 10468-07, 600 x 800 pixels, 20 μm pitch). In the schematic diagram, the reflective SLM is shown as transmissive for illustrative purposes. The SLM, controlled using custom-built software⁶², was used to modulate the phase of the beam. Holograms designed to generate 12 μm holographic spots at the focal plane of the microscope were computed using an iterative Gerchberg-Saxton algorithm⁶³. The zeroth diffraction order from the SLM was removed using a physical beam block. The modulated field was relayed and de-magnified using a pair of telescopes (formed of lenses L3 Thorlabs, AC508-750-B), L4 (Thorlabs, AC508-750-B), L5 (Thorlabs, AC508-500-B) and L6 (Thorlabs, AC508-300-B)) to fill the back-aperture of the microscope objective (Nikon, CFI APO NIR, 40X, 0.8 NA) which projected the holograms onto the focal plane. Phase masks were calculated such that holographic spots for light of different wavelengths overlapped laterally and axially. The anti-reflective coating of the lenses used is optimized for wavelengths 650 - 1050 nm, and losses incurred at 1100 nm result in the system being power limited at this wavelength. Hence, spectral characterisation was performed by normalizing the power density at all wavelengths to the maximum transmitted at 1100 nm. The power incident on the sample plane was adjusted using a high-speed modulator (Thorlabs, OM6NH/M), which was calibrated for each experimental session for each wavelength used, to ensure a photon flux of 6.77×10^{26} photons $\text{s}^{-1} \text{m}^{-2}$ for all data presented in Fig. 5a. All powers were measured in the object plane using a power meter (Thorlabs, S121C). This experimental configuration was used for all data presented in Fig. 5a, along with all data acquired using 1100 nm illumination. Two-photon inhibition was performed using a femtosecond laser with fixed wavelength (Spark Alcor, 80 MHz, 100 fs, 920 nm) which was combined with the beam from the tunable laser using a dichroic mirror (Thorlabs, DMLP950R). A liquid crystal variable retarder (Thorlabs, LCC1111-B) and polarizing beam splitter (Thorlabs, PBS253) were combined to modulate the maximum power of the fixed 920 nm beam independently of that of the tunable laser. The power densities used in each experiment are specified alongside the relevant data in Fig. 5 and Supplementary Fig. 10.

Transgenic C. elegans lines and transgenes

The strain ZX417 (zxEx34[punc17::NpHR-ECFP;punc17::CHOP-2(H134R)::eYFP;rol-6]) was generated by injection of plasmid DNA (plasmids pRF4 (rol-6d), punc-17::NpHR-eCFP, and punc-

17::Chr2(H134R)-eYFP; each at 80 ng/μl) into the germline of *C. elegans* wildtype hermaphrodites. Transgenic animals were picked from the F1 generation and one line (ZX417) was selected out of several transgenic F2 lines for further experiments 33. For expression in cholinergic neurons of *C. elegans*, BiPOLES (GtACR2::ts::mCerulean3::βHK::Chrimson) was subcloned into the punc-17 vector RM#348p (a gift from Jim Rand) via Gibson Assembly based on the plasmid CMV_GtACR2_mCerulean_βHK_Chrimson, using the restriction enzyme NheI and the primers ACR2_Chrimson_fwd (5'-atcttcaggaggacccttggATGGCATCACAGGTCGTC-3') and ACR2_Chrimson_rev (5'-ataccatggtaccgtcgacgTCACACTGTGTCCTCGTC-3'), resulting in the construct pAB26. The respective transgenic strain ZX2586 (wild type; zxEx1228[punc-17::GtACR2::ts::mCerulean3::βHK::Chrimson; pelt-2::GFP]), was generated via microinjection⁶⁴ of both 30 ng μl⁻¹ plasmid and co-marker plasmid DNA pelt-2::GFP. Animals were cultivated on nematode growth medium (NGM), seeded with *E. coli* OP-50 strain, in 6 cm petri dishes. To obtain functional rhodopsins in optogenetic experiments, the OP-50 bacteria were supplemented with all-trans retinal ATR (0.25 μl of a 100 mM stock (in ethanol) mixed with 250 μl OP-50 bacterial suspension).

C. elegans stimulation and behavioral experiments

For body-length measurements, L4 stage transgenic animals were cultivated on ATR plates overnight. Video analysis of light-stimulation protocols provided information on depolarized and hyperpolarized states, based on contracted or relaxed body-wall muscles (BWMs)⁶⁵. Prior to experiments, animals were singled on plain NGM plates to avoid imaging artefacts. They were manually tracked with an Axio Scope.A1 microscope (Zeiss, Germany), using a 10x objective (Zeiss A-Plan 10x/0,25 Ph1 M27) and a Powershot G9 digital camera (Canon, USA). For light-stimulation of optogenetic tools, transgenic worms were illuminated with 5 s light pulses at 1.1 mW mm⁻² of different wavelengths as indicated in Fig. 6d (monochromatic light source, Polychrome V, Till Photonics or 100W HBO mercury lamp with 470/40 ET Bandpass or 575/40 ET Bandpass filters, AHF Analysentechnik), controlled via an Arduino-driven shutter (Sutter Instrument, USA). Videos were processed and analyzed using a custom written MATLAB script⁶⁶ (MathWorks, USA). For the analysis of data, the animals' body length was normalized to the recording period prior to illumination.

Transgenic D. melanogaster lines and transgenes

BiPOLES-mCerulean cDNA was cloned via blunt-end ligation into pJFRC7⁶⁷. BILOES was cut with BamHI/HindIII and the vector was cut with NotI/XbaI. A transgenic line inserted into the attP2 site on the 3rd chromosome⁶⁸ was generated by phiC31-mediated site-specific transgenesis (FlyORF Injection Service, Zurich, Switzerland). A Gal4 line expressing in glutamatergic neurons including motor neurons (*OK371-Gal4¹¹*) was used for locomotion experiments, a Dp7-expressing line (*Ilp7-Gal4³⁴*) was used for mechanonociception experiments.

Locomotion and mechanonociception assays in D. melanogaster larvae

D. melanogaster larvae were staged in darkness on grape agar plates and fed with yeast paste containing 5 mM all-trans-retinal. Third instar larvae (96 h ± 2 h after egg laying) were used for all experiments.

For locomotion and body length analyses, animals were carefully transferred under minimum red light conditions to a 2% agar film on a FTIR (frustrated total internal reflection) based tracking system (FIM, University of Münster)⁶⁹. Five freely moving larvae/trial were video- captured and stimulated with 470nm (17 μ W mm⁻²) or 635nm (25 μ W mm⁻²) light (CoolLED PE4000) for activation of BiPOLES. Animal locomotion was tracked with 10 frames per s for up to 70 s and then body length was analyzed using the FIMtracking software (FIM, University of Münster). For analysis, only animals displaying continuous locomotion before the light stimulus were kept. Larval body length was analyzed over time and was displayed with a 1 s moving average. The body length was normalized to the average of the first 5 s of recording. Relative body length changes during the experiment were then analyzed and plotted.

For mechanonociception, staged larvae were placed on 2% agar plates with a 1 ml water film added. Experiments were performed under minimum light conditions (no activation) with calibrated von-Frey-filaments (50 mN). For activation of BiPOLES, larvae were illuminated during the assay with either 470 nm (17 μ W mm⁻²) or 635 nm (25 μ W mm⁻²). Larvae were stimulated twice on mid-abdominal segments (a3–a6) within 2 s. Behavioral responses (stop and turning, bending, rolling) were noted, analyzed and plotted. Staging and experiments were done in a blinded and randomized fashion.

Modulation of noradrenergic neurons in the mouse locus coeruleus

Animals: All procedures were in agreement with the German national animal care guidelines and approved by the Hamburg state authority for animal welfare (Behörde für Justiz und Verbraucherschutz) and the animal welfare officer of the University Medical Center Hamburg-Eppendorf. Experiments were performed on mice of either sex between 2.5 and 4 months of age at the start of the experiment. Mice were obtained from The Jackson Laboratory, bred and maintained at our own colony (12/12h light-dark cycle, 22°C room temperature, ~40% relative humidity, food and water ad libitum). Transgenic mice expressing Cre recombinase in tyrosine hydroxylase positive neurons (TH-Cre, Stock No: 008601)⁷⁰ were injected with a suspension of rAAV9 viral particles encoding hSyn-DIO-somBiPOLES to target Cre-expressing neurons in the locus coeruleus. Control experiments were performed in non-injected wildtype littermates.

Virus injection and implantation of optic fibers: General anesthesia and analgesia was achieved by intraperitoneal injections of midazolam/medetomidine/fentanyl (5.0/0.5/0.05 mg kg⁻¹, diluted in NaCl). After confirming anesthesia and analgesia by absence of the hind limb withdrawal reflex, the scalp of the animal was trimmed and disinfected with Iodide solution (Betaisodona; Mundipharma, Germany). The animal was placed on a heating pad to maintain body temperature, fixed in a stereotactic frame, and eye ointment (Vidisic; Bausch + Lomb, Germany) was applied to prevent drying of the eyes. To bilaterally access the LC, an incision (~1 cm) was made along the midline of the scalp, the skull was cleaned, and small craniotomies were drilled -5.4 mm posterior and \pm 1 mm lateral to Bregma. 0.4 μ l of virus suspension were injected into each LC (-3.6 mm relative to Bregma) at a speed of ~100-200 nl min⁻¹ using a custom-made air pressure system connected to a glass micropipette. After each

injection, the micropipette was left in place for a minimum of 5 minutes before removal. After virus injection, cannulas housing two ferrule-coupled optical fibers (200 μm core diameter, 0.37 NA, 4 mm length) spaced 2 mm apart (TFC_200/245-0.37_4mm_TS2.0_FLT; Doric Lenses, Canada) were inserted just above the injection site to a depth of -3.5 mm relative to Bregma using a stereotactic micromanipulator.

The implant, as well as a headpost for animal fixation during the experiment, were fixed to the roughened skull using cyanoacrylate glue (Pattex; Henkel, Germany) and dental cement (Super Bond C&B; Sun Medical, Japan). The incised skin was glued to the cement to close the wound. Anesthesia was antagonized by intraperitoneally injecting a cocktail of atipamezole/flumazenil/buprenorphine (2.5/0.5/0.1 mg kg⁻¹, diluted in NaCl). Carprofen (4 mg kg⁻¹) was given subcutaneously for additional analgesia and to avoid inflammation. In addition, animals received meloxicam mixed into softened food for 3 days after surgery.

Optogenetic stimulation: 4 - 6 weeks after surgery, mice were habituated to head fixation and placement in a movement-restraining plastic tube for at least one session. Bilateral optogenetic stimulation of LC neurons was achieved by connecting the fiber implant to a 1x2 step-index multimode fiber optic coupler (200 μm core diameter, 0.39 NA; TT200SL1A, Thorlabs, Germany) in turn connected to a laser combiner system (LightHUB; Omicron, Germany) housing a 473 nm (LuxX 473-100; Omicron, Germany) and a 594 nm diode laser (Obis 594 nm LS 100 mW; Coherent, Germany) for activation the GtACR2 and Chrimson components of somBiPOLES, respectively. Coupling to the implant was achieved with zirconia mating sleeves (SLEEVE_ZR_1.25; Doric lenses, Canada) wrapped with black tape to avoid light emission from the coupling interface. Following a habituation period of ~3 min after placing in the setup, stimuli were generated and presented using custom-written MATLAB scripts (MathWorks, US) controlling a NI-DAQ-card (PCIe-6323; National Instruments, US) to trigger the lasers via digital input channels. For activation of Chrimson, pulse trains (594 nm, ~10 mW at each fiber end, 20 ms pulse duration, 20 Hz repetition rate) of 4 s duration were presented, while GtACR2 was activated by continuous illumination (473 nm, ~10 mW at each fiber end) of 2 - 6 seconds duration. 30 - 40 trials of 473 nm pulses, 594 nm pulse trains, and combinations thereof, were presented at an inter-train-interval of 20 - 30 seconds in each session.

Data acquisition: A monochrome camera (DMK 33UX249; The Imaging Source, Germany) equipped with a macro objective (TMN 1.0/50; The Imaging Source, Germany) and a 780 nm long-pass filter (FGL780; Thorlabs, Germany) was pointed towards one eye of the mouse. Background illumination was provided with an infrared spotlight (850 nm), while a UV LED (395 nm; Nichia, Japan) was adjusted to maintain pupil dilation of the mouse at a moderate baseline level. Single frames were triggered at 30 Hz by an additional channel of the NI-DAQ-card that controlled optogenetic stimulation, and synchronization was achieved by simultaneous recording of all control voltages and their corresponding timestamps.

Data analysis: Pupil diameter was estimated using a custom-modified, MATLAB-based algorithm developed by McGinley et al⁷¹. In short, an intensity threshold was chosen for each recording to roughly

separate between pupil (dark) and non-pupil (bright) pixels. For each frame, a circle around the center of mass of putative pupil pixels and with an area equivalent to the amount of pupil pixels was then calculated, and putative edge pixels were identified by canny edge detection. Putative edge pixels that were more than 3 pixels away from pixels below the threshold (putative pupil) or outside an area of $\pm 0.25 - 1.5$ times the diameter of the fitted circle were neglected. Using least-squares regression, an ellipse was then fit on the remaining edge pixels, and the diameter of a circle of equivalent area to this ellipse was taken as the pupil diameter. Noisy frames (e.g. no visible pupil due to blinking or blurry pupil images due to saccades of the animal) were linearly interpolated, and the data was low-passed filtered (< 3 Hz; 3rd order Butterworth filter). Pupil data was segmented from 5 s before to 15 s after onset of each stimulus and normalized to the median pupil diameter of the 5 s preceding the stimulus onset, before individual trials were averaged. Randomly chosen segments of pupil data of the same duration served as a control. The difference in median pupil diameter one second before and after stimulation (as indicated in Fig. 7c) was used to calculate potential changes in pupil diameter for each condition. Statistical significance was calculated using one-way analysis of variance and Tukey's post-hoc multiple comparison tests.

In-vivo recordings from ferret visual cortex

Data were collected from 3 adult female ferrets (*Mustela putorius*). All experiments were approved by the independent Hamburg state authority for animal welfare (Behörde für Justiz und Verbraucherschutz) and were performed in accordance with the guidelines of the German Animal Protection Law and the animal welfare officer of the University Medical Center Hamburg-Eppendorf.

For injection of rAAV9 viral particles encoding mDlx-BiPOLES-mCerulean (see table 1) animals were anesthetized with an injection of ketamine (15 mg kg⁻¹), medetomidine (0.02 mg kg⁻¹), midazolam (0.5 mg kg⁻¹) and atropine (0.15 mg kg⁻¹). Subsequently, they were intubated and respirated with a mixture of 70:30 N₂/O₂ and 1-1.5% isoflurane. A cannula was inserted into the femoral vein to deliver a bolus injection of enrofloxacin (15 mg kg⁻¹) and rimadyl (4 mg kg⁻¹) and, subsequently, continuous infusion of 0.9% NaCl and fentanyl (0.01 mg kg⁻¹ h⁻¹). Body temperature, heart rate and end-tidal CO₂ were constantly monitored throughout the surgery. Before fixing the animal's head in the stereotaxic frame, a local anesthetic (Lidocaine, 10%) was applied to the external auditory canal. The temporalis muscle was folded back, such that a small craniotomy (\varnothing : 2.5mm) could be performed over the left posterior cortex and the viral construct was slowly (0.1 μ l min⁻¹) injected into secondary visual cortex (area 18). The excised piece of bone was put back in place and fixed with tissue-safe silicone (Kwikcast; WPI). Also, the temporalis muscle was returned to its physiological position and the skin was closed. After the surgery the animals received preventive analgesics (Metacam, 0.1 mg) and antibiotics (Enrofloxacin, 15 mg kg⁻¹) for ten days.

After an expression period of at least 4 weeks, recordings of cortical signals were carried out under isoflurane anesthesia. Anesthesia induction and maintenance were similar to the procedures described above, except for a tracheotomy performed to allow for artificial ventilation of the animal over an extended period. The i.v. infusion was supplemented with pancuronium bromide (6 μ g kg⁻¹ h⁻¹) to prevent slow ocular drifts. To keep the animal's head in a stable position throughout the placement of

recording electrodes and the measurements, a headpost was fixed with screws and dental acrylic to the frontal bone of the head. Again, the temporalis muscle was folded back and a portion of the cranial bone was resected. The dura was removed before introducing an optrode with 32 linearly distributed electrodes (A1x32-15mm-50(100)-177, NeuroNexus Technologies) into the former virus-injection site (area 18). The optrode was manually advanced via a micromanipulator (David Kopf Instruments) under visual inspection until the optic fiber was positioned above the pial surface and the uppermost electrode caught a physiological signal, indicating that it had just entered the cortex. During electrophysiological recordings the isoflurane level was maintained at 0.7%. To ensure controlled conditions for sensory stimulation, all experiments were carried out in a dark, sound-attenuated anechoic chamber (Acoustair, Moerkapelle, Netherlands). Visual stimuli were created via an LED placed in front of the animal's eye. In separate blocks, 150 laser stimuli of different colors ('red', 633nm LuxXplus and 'blue', 473nm LuxXplus, LightHub-4, Omicron) were applied through the optrode for 500 ms, each, at a variable interval of 2.5-3 seconds. Randomly, 75 laser stimuli were accompanied by a 10ms LED-flash, starting 100ms after the respective laser onset. For control, one block of 75 LED-flashes alone were presented at comparable interstimulus intervals.

Electrophysiological signals were sampled with an AlphaLab SnR recording system (Alpha Omega Engineering, Nazareth, Israel) or with a self-developed neural recording system based on INTAN digital head-stages (RHD2132, Intantech). Signals recorded from the intracortical laminar probe were band-pass filtered between 0.5 Hz and 7.5 kHz and digitized at 22-44 kHz or 25 kHz, respectively. All analyses of neural data presented in this study were performed offline after the completion of experiments using MATLAB scripts (MathWorks). To extract multiunit spiking activity (MUA) from broadband extracellular recordings, we high-pass filtered signals at 500Hz and detected spikes at negative threshold (>3.5 SD)⁷⁴.

Data availability

Source data are provided with this paper. All data generated in this study are provided in the Source Data file.

Acknowledgements

We thank Stefan Schillemeit and Tharsana Tharmalingam for excellent technical assistance, Mathew McGinley and Peter Murphy for help with pupil analysis and Sonja Kleinlogel for providing plasmids carrying the original opsin tandem. We also thank Karl Deisseroth and Charu Ramakrishnan for providing the plasmids and coding sequences of bReaChES and eNPAC2.0, as well as for providing the ChRmine plasmid and coding sequence in advance of publication. We further thank Jonas Wietek for providing ACR plasmids and for discussions at an early phase of the project. Ingke Braren of the UKE Vector Facility produced AAV vectors. This work was supported by the German Research Foundation, DFG (SPP1926, FOR2419/P6, SFB936/B8 to J.S.W., SFB936/A2 and SPP2041/EN533/15-1 to A.K.E., SPP1926 and SFB1315 to P.H., SFB807/P11 to A.C.F.B. & A.G.), the 'Agence Nationale de la Recherche' (CE16-2019 HOLOPTOGEN, CE16-0021 SLALLOM, ANR-10-LABX-65 LabEx LIFESENSES, and ANR-18-IAHU-01 *IHU FOReSIGHT to V.E.), the AXA research foundation and the European Research Council (ERC2016-StG-714762 to J.S.W., HOLOVIS-AdG to V.E., Stardust H2020 767092 to P.H.). Peter Hegemann is a Hertie Professor and supported by the Hertie Foundation.

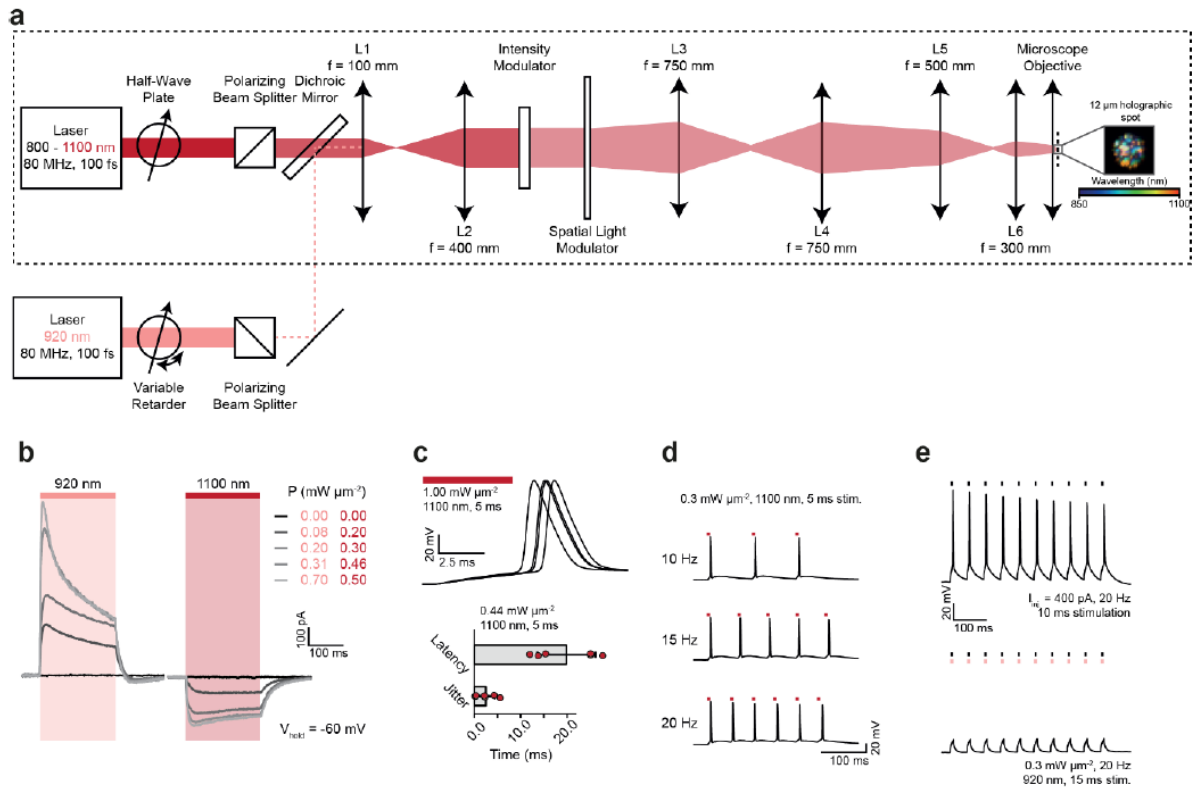
Author contributions

Conceptualization: JV, SRR, PH, JSW; Investigation: JV, SRR, AD, FP, RS, FT, ACFB, IB, FZ, NZ, JA, SA, KS, JSW; Data Curation: JV, SRR, AD, FP, RS, FT, ACFB, JA; Analysis: JV, SRR, AD, FP, RS, FT, ACFB, IB, FZ, JA, JSW; Software: AD, FP; Supervision: EP, AG, PS, VE, AKE, PH, JSW; Funding acquisition: EP, AG, PS, VE, AKE, PH, JSW; Project administration: PH, JSW; Writing: JV, SRR, FP, RS, JSW with contributions from all authors.

References

- 1 Chen, I. W., Papagiakoumou, E. & Emiliani, V. Towards circuit optogenetics. *Curr Opin Neurobiol* **50**, 179-189, doi:10.1016/j.conb.2018.03.008 (2018).
- 2 Kleinlogel, S. *et al.* A gene-fusion strategy for stoichiometric and co-localized expression of light-gated membrane proteins. *Nat Methods* **8**, 1083-1088, doi:10.1038/nmeth.1766 (2011).
- 3 Tang, W. *et al.* Faithful expression of multiple proteins via 2A-peptide self-processing: a versatile and reliable method for manipulating brain circuits. *J Neurosci* **29**, 8621-8629, doi:10.1523/JNEUROSCI.0359-09.2009 (2009).
- 4 Gradinaru, V. *et al.* Molecular and cellular approaches for diversifying and extending optogenetics. *Cell* **141**, 154-165, doi:10.1016/j.cell.2010.02.037 (2010).
- 5 Gradinaru, V. *et al.* Targeting and readout strategies for fast optical neural control in vitro and in vivo. *J Neurosci* **27**, 14231-14238, doi:10.1523/JNEUROSCI.3578-07.2007 (2007).
- 6 Carus-Cadavieco, M. *et al.* Gamma oscillations organize top-down signalling to hypothalamus and enable food seeking. *Nature* **542**, 232-236, doi:10.1038/nature21066 (2017).
- 7 Rashid, A. J. *et al.* Competition between engrams influences fear memory formation and recall. *Science* **353**, 383-387, doi:10.1126/science.aaf0594 (2016).
- 8 Vesuna, S. *et al.* Deep posteromedial cortical rhythm in dissociation. *Nature* **586**, 87-94, doi:10.1038/s41586-020-2731-9 (2020).
- 9 Heikenfeld, C. *et al.* Prefrontal - subthalamic pathway supports action selection in a spatial working memory task. *Scientific reports* **10**, 10497, doi:10.1038/s41598-020-67185-1 (2020).
- 10 Mohammad, F. *et al.* Optogenetic inhibition of behavior with anion channelrhodopsins. *Nat Methods* **14**, 271-274, doi:10.1038/nmeth.4148 (2017).
- 11 Wietek, J. *et al.* Anion-conducting channelrhodopsins with tuned spectra and modified kinetics engineered for optogenetic manipulation of behavior. *Scientific reports* **7**, 14957, doi:10.1038/s41598-017-14330-y (2017).
- 12 Klapoetke, N. C. *et al.* Independent optical excitation of distinct neural populations. *Nat Methods* **11**, 338-346, doi:10.1038/nmeth.2836 (2014).
- 13 Yizhar, O. *et al.* Neocortical excitation/inhibition balance in information processing and social dysfunction. *Nature* **477**, 171-178, doi:10.1038/nature10360 (2011).
- 14 Akerboom, J. *et al.* Genetically encoded calcium indicators for multi-color neural activity imaging and combination with optogenetics. *Front Mol Neurosci* **6**, 2, doi:10.3389/fnmol.2013.00002 (2013).
- 15 Erbguth, K., Prigge, M., Schneider, F., Hegemann, P. & Gottschalk, A. Bimodal activation of different neuron classes with the spectrally red-shifted channelrhodopsin chimera C1V1 in *Caenorhabditis elegans*. *PLoS one* **7**, e46827, doi:10.1371/journal.pone.0046827 (2012).
- 16 Stujenske, J. M., Spellman, T. & Gordon, J. A. Modeling the Spatiotemporal Dynamics of Light and Heat Propagation for In Vivo Optogenetics. *Cell reports* **12**, 525-534, doi:10.1016/j.celrep.2015.06.036 (2015).
- 17 Yizhar, O., Fenno, L. E., Davidson, T. J., Mogri, M. & Deisseroth, K. Optogenetics in neural systems. *Neuron* **71**, 9-34, doi:10.1016/j.neuron.2011.06.004 (2011).
- 18 Govorunova, E. G., Sineshchekov, O. A., Janz, R., Liu, X. & Spudich, J. L. NEUROSCIENCE. Natural light-gated anion channels: A family of microbial rhodopsins for advanced optogenetics. *Science* **349**, 647-650, doi:10.1126/science.aaa7484 (2015).
- 19 Berndt, A. *et al.* Structural foundations of optogenetics: Determinants of channelrhodopsin ion selectivity. *Proc Natl Acad Sci U S A* **113**, 822-829, doi:10.1073/pnas.1523341113 (2016).
- 20 Rajasethupathy, P. *et al.* Projections from neocortex mediate top-down control of memory retrieval. *Nature* **526**, 653-659, doi:10.1038/nature15389 (2015).
- 21 Mager, T. *et al.* High frequency neural spiking and auditory signaling by ultrafast red-shifted optogenetics. *Nat comm* **9**, 1750, doi:10.1038/s41467-018-04146-3
- 22 Marshel, J. H. *et al.* Cortical layer-specific critical dynamics triggering perception. *Science* **365**, doi:10.1126/science.aaw5202 (2019).
- 23 Batabyal, S., Cervenka, G., Ha, J. H., Kim, Y. T. & Mohanty, S. Broad-Band Activatable White-Opsin. *PLoS one* **10**, e0136958, doi:10.1371/journal.pone.0136958 (2015).
- 24 Bansal, H., Gupta, N. & Roy, S. Theoretical Analysis of Low-power Bidirectional Optogenetic Control of High-frequency Neural Codes with Single Spike Resolution. *Neuroscience* **449**, 165-188, doi:10.1016/j.neuroscience.2020.09.022 (2020).
- 25 Sineshchekov, O. A. *et al.* Conductance Mechanisms of Rapidly Desensitizing Cation Channelrhodopsins from Cryptophyte Algae. *mBio* **11**, doi:10.1128/mBio.00657-20 (2020).
- 26 Sudo, Y. *et al.* A blue-shifted light-driven proton pump for neural silencing. *J Biol Chem* **288**, 20624-20632, doi:10.1074/jbc.M113.475533 (2013).
- 27 Lim, S. T., Antonucci, D. E., Scannevin, R. H. & Trimmer, J. S. A novel targeting signal for proximal clustering of the Kv2.1 K⁺ channel in hippocampal neurons. *Neuron* **25**, 385-397, doi:10.1016/s0896-6273(00)80902-2 (2000).
- 28 Mahn, M. *et al.* High-efficiency optogenetic silencing with soma-targeted anion-conducting channelrhodopsins. *Nat comm* **9**, 4125, doi:10.1038/s41467-018-06511-8 (2018).
- 29 Messier, J. E., Chen, H., Cai, Z. L. & Xue, M. Targeting light-gated chloride channels to neuronal somatodendritic domain reduces their excitatory effect in the axon. *eLife* **7**, doi:10.7554/eLife.38506 (2018).
- 30 Hochbaum, D. R. *et al.* All-optical electrophysiology in mammalian neurons using engineered

- microbial rhodopsins. *Nat Methods* **11**, 825-833, doi:10.1038/nmeth.3000 (2014).
- 31 Mardinly, A. R. *et al.* Precise multimodal optical control of neural ensemble activity. *Nat Neurosci* **21**, 881-893, doi:10.1038/s41593-018-0139-8 (2018).
- 32 Ronzitti, E. *et al.* Submillisecond Optogenetic Control of Neuronal Firing with Two-Photon Holographic Photoactivation of Chronos. *J Neurosci* **37**, 10679-10689, doi:10.1523/JNEUROSCI.1246-17.2017 (2017).
- 33 Zhang, F. *et al.* Multimodal fast optical interrogation of neural circuitry. *Nature* **446**, 633-639, doi:10.1038/nature05744 (2007).
- 34 Hu, C. *et al.* Sensory integration and neuromodulatory feedback facilitate *Drosophila* mechanonociceptive behavior. *Nat Neurosci* **20**, 1085-1095, doi:10.1038/nn.4580 (2017).
- 35 Breton-Provencher, V. & Sur, M. Active control of arousal by a locus coeruleus GABAergic circuit. *Nat Neurosci* **22**, 218-228, doi:10.1038/s41593-018-0305-z (2019).
- 36 Dimidschstein, J. *et al.* A viral strategy for targeting and manipulating interneurons across vertebrate species. *Nat Neurosci* **19**, 1743-1749, doi:10.1038/nn.4430 (2016).
- 37 Mahn, M., Prigge, M., Ron, S., Levy, R. & Yizhar, O. Biophysical constraints of optogenetic inhibition at presynaptic terminals. *Nat Neurosci* **19**, 554-556, doi:10.1038/nn.4266 (2016).
- 38 Stierl, M. *et al.* Light modulation of cellular cAMP by a small bacterial photoactivated adenylyl cyclase, bPAC, of the soil bacterium *Beggiatoa*. *J Biol Chem* **286**, 1181-1188, doi:10.1074/jbc.M110.185496 (2011).
- 39 Moeyaert, B. *et al.* Improved methods for marking active neuron populations. *Nat comm* **9**, 4440, doi:10.1038/s41467-018-06935-2 (2018).
- 40 Perez-Alvarez, A. *et al.* Freeze-frame imaging of synaptic activity using SynTagMA. *Nat comm* **11**, 2464, doi:10.1038/s41467-020-16315-4 (2020).
- 41 Kato, H. E. *et al.* Crystal structure of the channelrhodopsin light-gated cation channel. *Nature* **482**, 369-374, doi:10.1038/nature10870 (2012).
- 42 Volkov, O. *et al.* Structural insights into ion conduction by channelrhodopsin 2. *Science* **358**, doi:10.1126/science.aan8862 (2017).
- 43 Oda, K. *et al.* Crystal structure of the red light-activated channelrhodopsin Chrimson. *Nat comm* **9**, 3949, doi:10.1038/s41467-018-06421-9 (2018).
- 44 Kim, Y. S. *et al.* Crystal structure of the natural anion-conducting channelrhodopsin GtACR1. *Nature* **561**, 343-348, doi:10.1038/s41586-018-0511-6 (2018).
- 45 Baker, C. A., Elyada, Y. M., Parra, A. & Bolton, M. M. Cellular resolution circuit mapping with temporal-focused excitation of soma-targeted channelrhodopsin. *eLife* **5**, doi:10.7554/eLife.14193 (2016).
- 46 Forli, A. *et al.* Two-Photon Bidirectional Control and Imaging of Neuronal Excitability with High Spatial Resolution In Vivo. *Cell reports* **22**, 3087-3098, doi:10.1016/j.celrep.2018.02.063 (2018).
- 47 Shemesh, O. A. *et al.* Temporally precise single-cell-resolution optogenetics. *Nat Neurosci* **20**, 1796-1806, doi:10.1038/s41593-017-0018-8 (2017).
- 48 Douin, V. *et al.* Use and comparison of different internal ribosomal entry sites (IRES) in tricistronic retroviral vectors. *BMC Biotechnol* **4**, 16, doi:10.1186/1472-6750-4-16 (2004).
- 49 Wiegert, J. S., Mahn, M., Prigge, M., Printz, Y. & Yizhar, O. Silencing Neurons: Tools, Applications, and Experimental Constraints. *Neuron* **95**, 504-529, doi:10.1016/j.neuron.2017.06.050 (2017).
- 50 Mahn, M. *et al.* Efficient optogenetic silencing of neurotransmitter release with a mosquito rhodopsin. *Neuron* **109**, 1621-1635 e1628, doi:10.1016/j.neuron.2021.03.013 (2021).
- 51 Copits, B. A. *et al.* A photoswitchable GPCR-based opsin for presynaptic inhibition. *Neuron*, doi:10.1016/j.neuron.2021.04.026 (2021).
- 52 Lima, S. Q., Hromadka, T., Znamenskiy, P. & Zador, A. M. PINP: a new method of tagging neuronal populations for identification during in vivo electrophysiological recording. *PLoS one* **4**, e6099, doi:10.1371/journal.pone.0006099 (2009).
- 53 Ramirez, S. *et al.* Creating a false memory in the hippocampus. *Science* **341**, 387-391, doi:10.1126/science.1239073 (2013).
- 54 Markwardt, M. L. *et al.* An improved cerulean fluorescent protein with enhanced brightness and reduced reversible photoswitching. *PLoS one* **6**, e17896, doi:10.1371/journal.pone.0017896 (2011).
- 55 Dittgen, T. *et al.* Lentivirus-based genetic manipulations of cortical neurons and their optical and electrophysiological monitoring in vivo. *Proc Natl Acad Sci U S A* **101**, 18206-18211, doi:10.1073/pnas.0407976101 (2004).
- 56 Grimm, C., Vierock, J., Hegemann, P. & Wietek, J. Whole-cell Patch-clamp Recordings for Electrophysiological Determination of Ion Selectivity in Channelrhodopsins. *J Vis Exp*, doi:10.3791/55497 (2017).
- 57 Gee, C. E., Ohmert, I., Wiegert, J. S. & Oertner, T. G. Preparation of Slice Cultures from Rodent Hippocampus. *Cold Spring Harbor protocols* 2017, pdb prot094888, doi:10.1101/pdb.prot094888 (2017).
- 58 Wiegert, J. S., Gee, C. E. & Oertner, T. G. Single-Cell Electroporation of Neurons. *Cold Spring Harbor protocols* 2017, pdb prot094904, doi:10.1101/pdb.prot094904 (2017).



Supplementary Fig. 10. Design of the dual-laser 2-photon holography setup. (a) A schematic diagram of the experimental setup used for two-photon photo-stimulation and inhibition using holography. The optical path indicated by the black, dashed rectangle was used to acquire all data presented in Fig. 5. The system was aligned at the central wavelength (980 nm), but holograms at all wavelengths were co-aligned laterally and axially as demonstrated in the inset. Double-headed arrows are used to illustrate lenses, denoted by L, with focal lengths denoted by f. The reflective Spatial Light Modulator (SLM) is shown as transmissive for illustrative purposes. The photoinhibition beam (920 nm) was combined with the beam from the tunable laser using a dichroic mirror. The precise details of each optical component can be found in the main text. (b) Representative photocurrent traces at a range of different average power densities, obtained by continuous 200 ms illumination of 920 and 1100 nm at a holding potential of -60 mV. (c) Top: Representative traces of photo-evoked action potentials. Bottom: Mean latency and jitter calculated as the average of 5 trials in different neurons. Error bars represent the standard deviation across trials. (d) Representative photo evoked trains of action potentials under 1100-nm illumination at different stimulation frequencies. (e) Demonstration of precise elimination of single action potentials using short (15 ms) pulses of 920 nm light. Upper trace (control): electrically induced 20 Hz spike train by 10 ms injection of 400 pA current. Lower trace: suppression of electrically induced action potentials by co-incident illumination of 15 ms pulses of 920 nm light. The data presented in this figure are provided in the Source Data file.

4. Discussion

In this work, in collaboration with the laboratories of Peter Hegemann and J. Simon Wiegert, I characterized a new construct, BiPOLES, under two-photon CGH excitation. We showed that, in neurons expressing the construct, it was possible to reliably and precisely evoke single and trains of action potentials with 1100 nm illumination. The use of 920 nm light allowed to reliably inhibit current-induced and photo-evoked action potentials. To my knowledge, this was the first demonstration of bidirectional control of neuronal activity using two-photon excitation.

The BiPOLES construct used two complementary rhodopsins to photo-activate and -inhibit neurons: Chrimson and GtACR2 respectively. Chrimson, as well as its faster variants fast-Chrimson (f-Chrimson) and very-fast-Chrimson (vf-Chrimson) (*Mager et al. 2018*), is the most red-shifted excitatory rhodopsin in the optogenetic toolbox with a peak activation at 600 nm under 1P excitation (*Klapoetke et al. 2014*). GtACR2, on the other hand, is the most blue-shifted inhibitory anion conducting channelrhodopsin, with a peak activation at 470nm under 1P excitation (*Govorunova et al. 2015*). Although they display the largest spectral separation possible, their respective action spectra overlap slightly under 1P excitation. Since the excitation spectra of rhodopsins are even broader under 2P excitation, the spectral overlap between Chrimson and GtACR2 is even greater in this condition. Another point is the fact that GtACR2 generates photocurrents of higher amplitude than Chrimson, when illuminated with their respective optimal wavelength. As a result, it was only possible to photo-evoked action potentials in BiPOLES-expressing neurons under 1100 nm illumination. This forbids the use of ultrashort pulsed lasers with a low repetition rate and high peak energy, that typically have a fixed output at 1030 – 1040 nm. Indeed, at these wavelengths, GtACR2 is still activated, resulting in an efficient shunting of the depolarization that is generated by the Chrimson photocurrent.

a. Other possible combinations

i. Using ChRmine, a more potent excitatory rhodopsin

One possibility to overcome this issue would be to switch the excitatory rhodopsin to one that is more potent in this wavelength range; the cation channelrhodopsin ChRmine may be a good candidate (*Marshel et al. 2019*). Although its peak action spectrum is less red-shifted than that of Chrimson and may generate more crosstalk when combined with GtACR2, its single channel conductance is higher, and it is still well activated by red light, resulting in significantly higher photocurrents than Chrimson. Thus, it may be possible to photo-evoked action potentials at 1040 nm.

In the published paper [Fig. 1 and Supplementary Fig. 1], the GtACR2-L4-ChRmine-eYFP construct was characterized under 1P illumination. We also characterized its properties under 2P illumination. Specifically, to test the construct under 2P excitation, I first expressed it in CHO cells, via transient

transfection and patched the expressing cells in the whole-cell voltage-clamp configuration to record photocurrents evoked under illumination at different wavelengths with equal photon flux [Figure II.4.1].

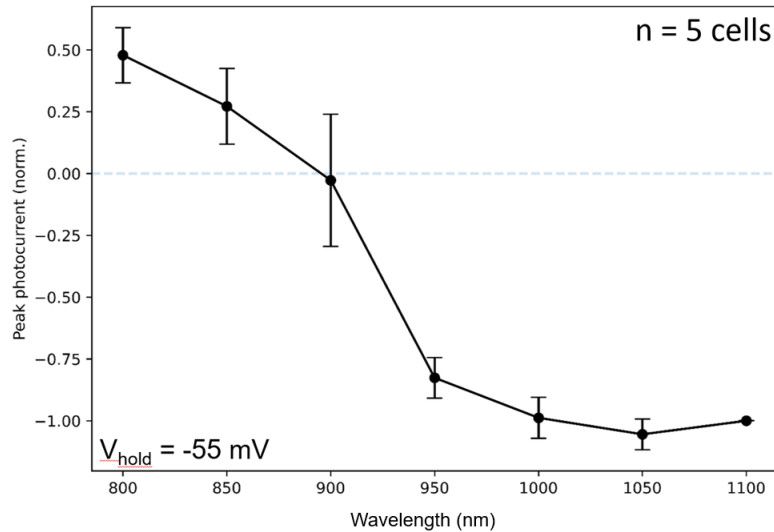


Figure II.4.1. Peak photocurrent as a function of wavelength at a holding potential of -55 mV. Data recorded in CHO cells and acquired with a constant photon flux of 6.77×10^{26} photons $s^{-1}m^{-2}$. (mean \pm SEM, n = 5).

Using this construct, outward and inward photocurrents could be elicited under 2P illumination. As expected from the action spectra of both rhodopsins, the photocurrent reversal wavelength was shifted toward blue wavelengths compared to BiPOLES (≈ 900 nm for GtACR2-L4-ChRmine-eYFP vs. ≈ 1025 nm for BiPOLES at a holding potential of -55 mV), with the induction of outward photocurrents mainly driven by GtACR2 with illumination at $\lambda < 900$ nm. Consistent with our hypothesis, high inward photocurrents, driven by ChRmine, were induced under illumination at $\lambda > 900$ nm with a peak current at 1050 nm.

These results were obtained at a membrane potential of -55 mV, which is further away from the chloride Nernst potential than the resting membrane potential of neurons ($V_m \approx -75$ mV), for which we expect a smaller amplitude of the GtACR2-driven photocurrent. To verify if this is the case, we expressed the construct in organotypic hippocampal neurons by bulk infection with AAV9-hSyn-GtACR2-L4-ChRmine-eYFP (final titer: 5.06×10^{14} vg/ml). Expressing neurons were patched in the whole-cell voltage-clamp configuration ($V_{\text{hold}} = -75$ mV) and photocurrents evoked under illumination at different wavelengths (850 – 1100 nm) and at equal photon flux (6×10^{26} photons $s^{-1}m^{-2}$) were recorded [Figure II.4.2].

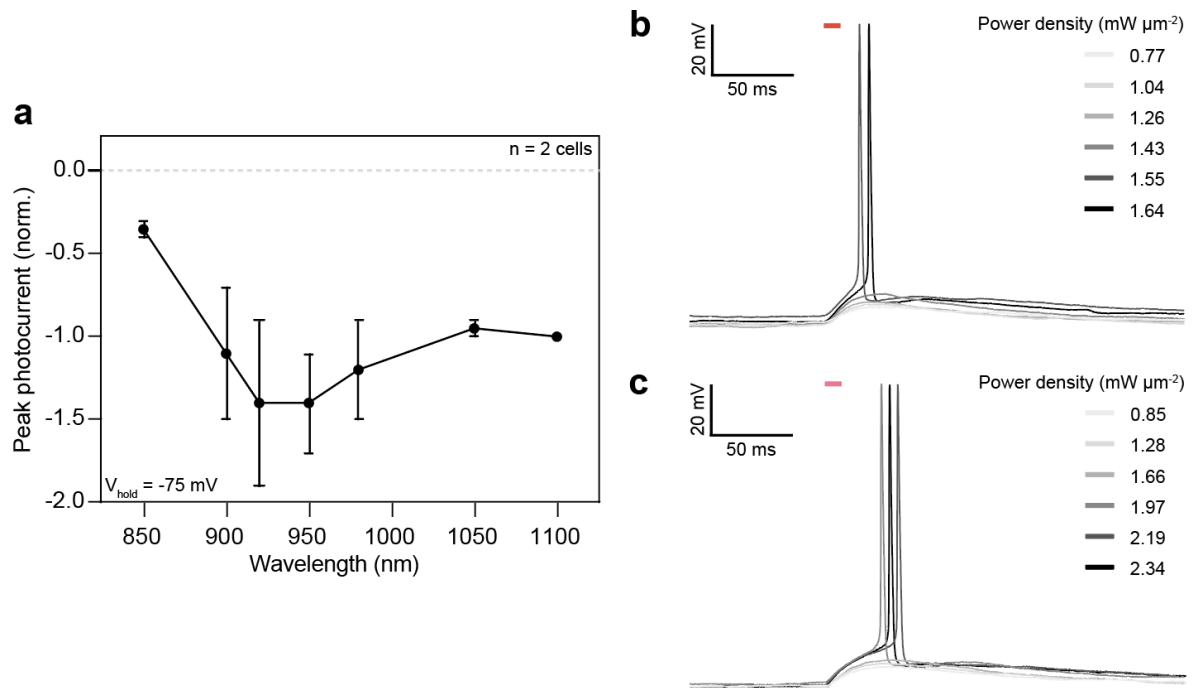


Figure II.4.2. Two-photon characterization of GtACR2-L4-ChRmine-eYFP in organotypic hippocampal slices. (a) Peak photocurrent as a function of wavelength at a holding potential of -75 mV. Data recorded in organotypic hippocampal slices infected with AAV9-hSyn-GtACR2-L4-ChRmine-eYFP (final titer: 5.06×10^{14} vg/ml) and acquired with a constant photon flux of 6×10^{26} photons $\text{s}^{-1}\text{m}^{-2}$. (mean \pm SEM, $n = 2$). **(b)** Representative trace of photo-evoked action potentials under holographic illumination ($\lambda = 1040$ nm, 5 ms duration). **(c)** Representative trace of photo-evoked action potentials under holographic illumination ($\lambda = 920$ nm, 5 ms duration).

As expected, the amplitude of GtACR2-driven photocurrents was significantly reduced at this holding potential, even at the peak absorption wavelength of the inhibitory rhodopsin (920 – 940 nm). The photocurrents generated by ChRmine were greater than those of GtACR2, resulting in a net inward current at all wavelengths tested [Figure II.4.2, a]. Consequently, we were unable to silence expressing neurons at 920 nm.

ii. Replacing the chloride rhodopsin with a potassium rhodopsin

To solve the limitations mentioned above, one could engineer a ChRmine variant with a spectrum shifted towards longer wavelengths while maintaining its high conductance or shift the spectrum of GtACR2 to shorter wavelengths, or to replace GtACR2 with a more efficient rhodopsin. The recently discovered potassium channelrhodopsins (*Govorunova et al. 2022; Vierock et al. 2022*) could be a good alternative. Indeed, the use of chloride channels to silence neurons is limited to cells or compartments with a low cytosolic chloride concentration. This means that the BiPOLES configuration using GtACR2 cannot be used for bidirectional control of neurons in early developmental stages or in axon terminals, where the cytosolic Cl^- concentration is high. Moreover, even in mature neurons, the chloride Nernst potential E_{Cl} is closer to the resting membrane potential V_m than the potassium Nernst potential E_K . Thus, the risk of depolarizing the cell when trying to silence it would be significantly smaller with potassium channels.

To date, only a small number of potassium channelrhodopsins have been discovered. Among them, HcKCR1 and HcKCR2 display a red-shifted action spectrum with peak absorptions around 1040 nm for the former and 1000 nm for the latter (*Govorunova et al. 2022*). WiChR, the most recent potassium channelrhodopsin published to date, is slightly more blue-shifted with a peak around 940 – 980 nm, with high photocurrent, and therefore may appear as a good candidate to replace GtACR2, but its spectrum may be too broad for its use in a BiPOLES construct. In fact, the rhodopsin shows more than 75 % activation in the range of 900 – 1050 nm and was proven to efficiently inhibit current-induced action potentials at 1030 nm (*Vierock et al. 2022*).

All of the possible variants listed above use a red-shifted excitatory rhodopsin and a blue-shifted inhibitory rhodopsin. This new combination is highly advantageous when performing 1P, dual-color excitation of genetically distinct but spatially intermixed neuronal populations [Figure 4f of the publication] compared to previous constructs such as eNPAC, since it confines the excitation of BiPOLES to the orange-red band of the spectrum, allowing the use of a second, blue-light activated excitatory rhodopsin in another neuronal population without crosstalk. However, the use of 2P excitation, with its exquisite spatial and lateral resolution, eliminates this issue. Thus, it may also be possible to combine a red-shifted inhibitory rhodopsin with a blue-shifted excitatory rhodopsin. A promising combination here could be the red-shifted potassium channelrhodopsin HcKCR1 combined with the most blue-shifted excitatory rhodopsin PsChR (*Govorunova et al. 2013*). The 2P action spectrum of PsChR exhibits a peak at 850 nm with a low activation at wavelengths above 1000 nm (< 10 % of the peak photocurrent). In contrast, HcKCR1 is most activated at 1040 nm with only 10 % of its maximum sensitivity at 850 nm. Since Ti:Sapphire lasers displays a maximum power output between 800 – 900 nm, this combination may allow to increase further the maximum number of cells that could be probed simultaneously.

b. Perspectives

To my knowledge, BiPOLES is the only tool that provides a fixed ratio of expression of excitatory and inhibitory rhodopsins for bidirectional control of neuronal activity and performs well under 2P excitation.

The spectral overlap of Chrimson and GtACR2 restricted the photoactivation of the construct to 1100 nm illumination only. Since the most widely used 2P laser sources (Ti:Sapphire and ytterbium-doped fiber lasers) do not deliver high powers at this wavelength, in our case, it was only possible to elicit action potentials in one cell at a time. However, more cells could be targeted simultaneously using more complex laser sources and/or using the recently developed ultra-Fast Light Targeting (FLiT) approach (*Faini et al. 2023*). This technique, by rapidly scanning the laser beam across a divided SLM

screen that displays H different holograms, enables to change the pattern of photostimulation significantly faster than what is achievable by the refreshing rate of the SLM. This could increase from \sqrt{H} to H times the number of achievable targets, where H can go up to 25 – 30.

By combining this construct with an indicator of activity, it could be possible to identify neurons responding to a sensory stimulus and record their activity pattern, even in freely moving animals a flexible two-photon fiberscope (2P-FENDO) (*Accanto et al. 2023*) and in deep structures of the brain by implanting GRIN lenses. Replaying this activity using BiPOLES, probing the roles of specific cells in the identified network by photo-activating them and -inhibiting them, modifying their patterns of activity by increasing or decreasing their firing frequency for example would allow a better understanding of the mechanisms underlying the sensory perception.

III. CHAPTER 2: Results – Scanless two-photon voltage imaging

In this chapter, I will present the second part of my PhD work that consisted in demonstrating the use of two-photon scanless excitation for the optical readout of the neuronal activity, using voltage indicators. The paper is currently under review at Nature Communications. The project was supervised by Eirini Papagiakoumou and Valentina Emiliani. My role was to conceptualize the experiments on the biological side, prepare and optimize the different samples, record data and analyze the electrophysiological data. The optical setup and the optics side of the experiments, as well as the analysis of the imaging data has been conceptualized and performed by Ruth Sims, a post-doc from the lab. The experiments were performed by the both of us, except for the experiments for the last figure, which were performed by Ruth Sims and Christiane Grimm, another post-doc, on samples provided by Aysha Mohamed-Lafirdeen.

This chapter starts with a brief state of the art on the different approaches used for single- and two-photon voltage imaging. The submitted manuscript is then presented (for supplementary materials see: Annex or [publication](#)), followed by unpublished data recorded at 1030 nm.

1. State of the art

a. Single-photon voltage imaging

The field of voltage imaging emerged in 1968 with the first optical recordings of action potentials by Tasaki et al. (*Tasaki et al. 1968*), quickly followed by the report of the discovery of the merocyanin 540 dye that allowed single-shot recordings (*Cohen et al. 1974*). Since then, extraordinary efforts have been made to develop better probes and to optimize the optical approaches for detecting neuronal activity.

Due to the inherent challenges of voltage imaging in terms of SNR and acquisition rates required to image fast electrical events in neurons, 1P widefield excitation has been the gold standard approach to perform voltage imaging. In most cases, the excitation axis consists of widefield illumination (where the entire sample is illuminated) generated by an LED or a fluorescent lamp (*Jin et al. 2012; Hochbaum et al. 2014; Piatkevich et al. 2018*), while the detection axis is typically comprised of a scientific complementary metal oxide semiconductor (sCMOS) based camera. This detector is based on a small silicon chip (on the order of centimeters) divided up into millions of tiny pixels that can store photons during exposure time, and whose signals can be amplified in parallel during readout. It has the advantage of being fast (up to 500 Hz for a full frame acquisition), with low read-noise and a good dynamic range.

With 1P excitation and bright indicators, this configuration does not require high powers to obtain a good signal (a few nW to a few μW per μm^2) and has been used to monitor the neuronal activity of cell population at the mesoscopic level, *in vivo*. Using this approach, scientists have been able to analyze cortical circuit dynamics (Ferezou, Bolea, and Petersen 2006) (including excitation and inhibition) or study intracortical functional connections (Lim, LeDue, and Murphy 2015). However, imaging with cellular resolution has been limited by the lack of axial confinement inherent to 1P excitation, which can result in a significant amount of background fluorescence, especially in thick and densely labeled samples. This, in turn, can lead to a reduced $\Delta F/F_0$, potentially making it difficult to image events of small amplitude.

Several genetic approaches have been utilized to address this problem. The addition of a trafficking motif from the soma-localized Kv2.1 channel allows the expression of the voltage indicator to be restricted to the soma, effectively reducing the background fluorescence that would otherwise originate from the neuropils (Adam et al. 2019a). Other approaches have focused on achieving a sparse expression of the indicator. By using specific promoters or transgenic Cre lines to target naturally sparse cell populations (Gong et al. 2015), or by controlling voltage indicator expression via the titratable activity of destabilized Cre (C. Song et al. 2017), it has been possible to strongly reduce the background fluorescence emanating from cells located above and below the focal plane.

Another method has used the application of patterned illumination. Here, the light from a visible source (LED or laser) is shaped using SLMs for holographic light patterning (Foust et al. 2015; Tanese et al. 2017; Fan et al. 2020a) or a digital micromirror device (DMD) (Adam et al. 2019a; Xiao et al. 2021b), which consists of a micromirror array whose mirrors can be turned on and off to shape the light. The light can then be directed to a specific region of interest (a neuron, a dendrite, a spine), allowing background fluorescence to be significantly reduced.

Using 1P patterned light and/or sparse staining, scientists have been able to record membrane potential changes at near cellular resolution *in vitro* in superficial layers (Kannan et al. 2018; Quicke et al. 2019; Filipis et al. 2023), but also *in vivo* in a variety of organisms such as rodents (Hochbaum et al. 2014; Adam et al. 2019a; Fan et al. 2020a; Kannan et al. 2022), drosophila (Gong et al. 2015; Kannan et al. 2018; Abdelfattah et al. 2019b), zebrafish (Piatkevich et al. 2018; Abdelfattah et al. 2019b) or *C. elegans* (Azimi Hashemi et al. 2019), at depths up to 230 μm .

However, the use of 1P excitation has limited this approach to transparent samples, shallow depths or sparse cell populations. These limitations could be overcome by using 2P imaging approaches, although this also requires facing additional challenges as described in the following section.

b. Two-photon voltage imaging

The main challenges related to the use of 2P excitation come from the small 2P cross section of fluorescent molecules, which is ≈ 40 GM for the GFP-based indicators (*Drobizhev et al. 2011*). As a comparison, the 2P cross-section of the channelrhodopsin ChR2 is 260 GM (*Rickgauer and Tank 2009*). This property, combined with the limited number of proteins localized on the membrane, and the fast kinetics of events to be detected required finding alternative solutions to the use of conventional scanning microscopy: increase the acquisition speed at the cost of the size of the FOV, or maintain a large FOV by reducing the acquisition rate, increasing the size of the excitation volume or using newly developed light multiplexing approaches.

Specifically, the first demonstration of voltage imaging with 2P excitation in 2008 has used a conventional scanning approach with galvanometric mirrors to record action potentials from mouse nerve terminals (*Fisher et al. 2008*). For this, the FOV had to be reduced to a line as small as $0.5 \mu\text{m}$ to collect enough signal at kilohertz acquisition rates. Other studies, *in vivo*, have focused on maintaining a large FOV by reducing the acquisition rate down to < 10 Hz to image cell population responses to long stimuli ($0.5 - 2$ s), with a loss of cellular and temporal resolution (*Ahrens et al. 2012; Störace et al. 2015*). The use of resonant scanning has increased the acquisition speed of large FOVs (hundreds μm^2) to video rate (≈ 30 Hz) (*Akemann et al. 2013*), but it is still insufficient to record fast neuronal activity.

To overcome this problem, more sophisticated optical methods have been utilized to perform voltage imaging with 2P excitation. Random access multiphoton (RAMP) microscopy is one of them (*Iyer, Hoogland, and Saggau 2006*). By rapidly displacing the diffraction limited spot across pre-determined positions of interest, this technique increases the acquisition rates up to several kHz without significantly reducing the FOV, thus allowing recordings from spatially separated neuronal compartments to optically report action potential backpropagation (*Chamberland et al. 2017*), or recordings from multiple cells simultaneously (*B. Li et al. 2020*). However, the inherently short dwell time necessary to achieve such acquisition speed limits the number of photons that can be detected from a diffraction-limited spot. Moreover, since the excitation volume is small, and the signal of interest comes only from the thin plasma membrane of expressing cells, this approach is highly sensitive to sample motion, a phenomenon that occurs *in vivo* when the animal breathes or moves, and which can shift the FOV of a few micrometers. This, combined with PMT detection, can generate important artifacts, especially when using negative-going indicators, where the decrease of fluorescence due to motion could be mistaken for a depolarization of the membrane potential.

More recently, the ultrafast local volume excitation (ULoVE) approach has been developed (*Villette et al. 2019*) to increase the excitation efficiency. With ULoVE, the diffraction-limited spot used in classical RAMP microscopy is replaced by a holographically generated volume of excitation that is rapidly scanned across predetermined positions. Because the size of the excitation volume can be tuned, this technique allows more photons to be detected at a given position and to minimize motion artifacts. Combined with the GEVI ASAP3, the authors were able to demonstrate recordings of subthreshold activity and action potentials in deep layers of the cortex (L5) in awake mice (*Villette et al. 2019*). More recently, this technique has also been combined with the latest indicator JEDI-2P where sustained recordings (45 minutes) were performed *in vivo* in Layers 2/3 and 5 at depths up to 430 μm (Zhuohe Liu et al. 2022a). However, because the excitation volume is larger than the plasma membrane, some signal that does not originate from the region of interest may be integrated by the PMT. In this situation, F_0 will increase, but not ΔF , thus reducing the $\Delta F/F_0$ and potentially missing events of smaller amplitude. Moreover, this approach requires sparse labelling of the sample to minimize the possible crosstalk between signals coming from two adjacent cells.

Other approaches include the free-space angular-chirp-enhanced delay (FACED) technique (Wu et al. 2020b), or the use of a spatiotemporal multiplexed ultrafast resonance frame-scanning (SMURF) 2P microscope (*Platasa et al. 2023*). In the FACED configuration, a pair of nearly parallel mirrors is used to form an array of spatially separated and temporally delayed beams that can be scanned in parallel across a defined FOV. This approach has been used for 2P voltage imaging of supra- and subthreshold activity of multiple neurons in response to visual stimulation, in a FOV of 50 x 250 μm^2 and at depths up to 300 μm , *in vivo*, in awake mice (Wu et al. 2020b). In the SMURF configuration, spatially multiplexing the laser beam generates multiple beamlets that are also temporally delayed and used to image a defined FOV at kilohertz frame rates. Combined with the positive-going indicators SpikeyGi and SpikeyGi2, this technique allowed *in vivo*, kilohertz rate, 2P voltage imaging of > 100 neurons simultaneously over a FOV of 400 x 400 μm^2 . However, achieving this required sending a total power of \approx 480 mW (30 mW per beamlet), which is significantly above the heating threshold of 200 mW that is commonly established for 2P microscopy (*Podgorski and Ranganathan 2016*). Moreover, both techniques scan the entire FOV, commonly including regions that do not contain cells, at a cost of the temporal resolution of the signal coming from the regions of interest.

The techniques described above all rely on a scanning approach and on PMT detection. Although they are very efficient and have yielded spectacular results, allowing 2P voltage imaging at kilohertz rates of multiple targets *in vivo* and in some cases, deep into the mouse cortex, they remain technically extremely challenging. Indeed, their sophisticated and/or bespoke nature renders them difficult to implement in a biological laboratory without sufficient expertise in optics. Moreover, they have not

yet been shown to be compatible with 2P optogenetics, which would be required for all-optical experiments.

2. Paper: submitted version

Scanless two-photon voltage imaging

Ruth R. Sims*¹, Imane Bendifallah*¹, Christiane Grimm¹, Aysha Mohamed-Lafirdeen¹, Xiaoyu Lu², François St-Pierre^{2,3,4}, Eirini Papagiakoumou^{1§}, and Valentina Emiliani^{1§}

¹Institut de la Vision, Sorbonne Université, INSERM, CNRS, F-75012 Paris, France

²Systems, Synthetic, and Physical Biology Program, Rice University, Houston, TX, USA

³Department of Neuroscience and Department of Biochemistry and Molecular Biology, Houston, TX, USA

⁴Department of Electrical and Computer Engineering, Rice University, Houston, TX, USA

*Equal contribution

§valentina.emiliani@inserm.fr

§eirini.papagiakoumou@inserm.fr

Keywords: Two-photon microscopy, voltage imaging, temporal focusing, optogenetics, computer-generated holography

Abstract

Parallel light-sculpting methods have been used to perform scanless two-photon photostimulation of multiple neurons simultaneously during all-optical neurophysiology experiments. We demonstrate that scanless two-photon excitation also enables high-resolution, high-contrast, voltage imaging by efficiently exciting fluorescence in a large fraction of the cellular soma. We present a thorough characterisation of scanless two-photon voltage imaging using existing parallel approaches and lasers with different repetition rates. We demonstrate voltage recordings of high frequency spike trains and sub-threshold depolarizations in intact brain tissue from neurons expressing the soma-targeted genetically encoded voltage indicator JEDI-2P-kv. Using a low repetition-rate laser, we perform recordings from up to ten neurons simultaneously. Finally, by co-expressing JEDI-2P-kv and the channelrhodopsin ChroME-ST in neurons of hippocampal organotypic slices, we perform single-beam, simultaneous, two-photon voltage imaging and photostimulation. This enables in-situ validation of the precise number and timing of light evoked action potentials and will pave the way for rapid and scalable identification of functional brain connections in intact neural circuits.

Introduction

Deciphering the logic and syntax of neural computation is a central goal in neuroscience and requires methods to record (read-out) and manipulate (write-in) the activity of individual neurons. Electrophysiological methods have proven instrumental towards achieving this goal since they can read and write neural activity with high fidelity. However, while extracellular probes can record from large populations, they have limited spatial resolution and cannot excite or inhibit specific neurons. In contrast, whole-cell patch-clamp methods can manipulate and record the electrical activity of targeted neurons but are hard to achieve *in vivo* even for a handful of neurons simultaneously and are unsuitable for longitudinal (chronic) studies. Furthermore, all electrophysiological methods have limited access to smaller cellular compartments of neurons (such as axons, distal dendrites, spines and boutons). These limitations have stimulated the development of a plethora of minimally invasive photonic approaches, combining advanced optical methods with light-sensitive proteins, such as genetically encoded fluorescent indicators and optogenetic actuators, for recording and manipulating neural activity, respectively¹⁻³.

In the nervous system, calcium ions regulate a broad range of processes and generate versatile intracellular signals⁴. Since action potentials lead to a large elevation of intracellular calcium, which can last an order of magnitude longer than the action potentials themselves⁵, the developments of synthetic⁶ and genetically encoded⁷ fluorescent calcium indicators (GECIs) capable of reporting changes in intracellular calcium were extremely important scientific breakthroughs. GECIs can be targeted to sub-cellular compartments and specific cell types^{8,9}. Their long-term expression in intact tissues and organisms² enables the repeated observation of individual cells. Calcium transients last significantly longer than the underlying voltage fluctuations, facilitating the detection of neural activity, but also limiting the quantification of spike firing rate and timing. Furthermore, GECIs are not well-suited for detecting sub-threshold voltage changes and hyperpolarizations resulting from synaptic and neuromodulatory inputs¹⁰.

Voltage indicators, which generate optical signals whose magnitude varies as a function of membrane potential, promise to address many of the aforementioned limitations of GECIs¹¹. Following the first optical recordings of membrane potential with a synthetic dye¹², voltage-sensitive indicators have undergone continual advancements, including improved synthetic dyes¹³, genetically encoded voltage indicators (GEVIs) and hybrid GEVIs¹⁴. However, detecting voltage spikes with GEVIs requires millisecond-timescale imaging, two orders of magnitude faster than generally required for GECIs. This technical challenge has limited the broad adoption of GEVIs for population imaging with cellular resolution.

The majority of voltage imaging experiments have relied on widefield, one-photon (1P) illumination and detection. The resulting mesoscopic observations of population activity have enabled investigation of the functional organisation and dynamics of cell-type specific excitatory and inhibitory cortical circuits^{15,16}. The lack of optical sectioning of 1P widefield microscopy has been overcome using sparse labelling strategies¹⁷ or sculpted illumination¹⁸⁻²¹. However, these strategies are not suitable for

multitarget voltage imaging in densely labelled scattering samples with cellular resolution, such as mammalian in-vivo preparations.

In principle, the optical sectioning inherent to two-photon excitation can be used to overcome these problems²², and two-photon laser scanning microscopy (2P-LSM) is commonly used to perform calcium imaging in scattering tissue²³. However, the acquisition rate of conventional 2P-LSM is limited and millisecond transients such as action potentials can only be detected by drastic reduction of the field of view^{24–27}. As a result, several specialised scanning-based techniques have been developed to image neural activity across larger areas at kilohertz rates^{28–35} and have yielded spectacular results, such as recording the voltage dynamics of cortical neurons in layer 5 in awake behaving mice. However, these methods are extremely technically demanding, have thus far been limited to imaging a few cells simultaneously, and have not yet been demonstrated to be compatible with two-photon optogenetics, as required for two-photon, all-optical neurophysiology experiments.

Here, we propose an alternative approach for high-contrast, high-resolution, voltage imaging in densely labelled samples that is compatible with simultaneous two-photon optogenetic stimulation. Our method leverages existing scanless two-photon excitation approaches^{36–39} and the recently developed soma-targeted GEVI JEDI-2P-kv⁴⁰. We demonstrate that, in combination with temporal focusing (TF)^{41–43}, the three light-sculpting approaches commonly used for scanless two-photon photoactivation — Generalised Phase Contrast (GPC)^{36,38}, low numerical aperture (NA) Gaussian beams (such as 3D-SHOT)^{39,44} and Computer-Generated Holography (CGH)^{45,46}— enable voltage imaging in mammalian cells. By performing simultaneous imaging and electrophysiology, we provide a thorough quantitative comparison of these illumination modalities. Next, by viral expression of JEDI-2P-kv in mouse hippocampal organotypic slices, we show that 2P-TF-GPC enables high spatiotemporal resolution voltage imaging of neural activity in extremely densely labelled preparations. We further demonstrate the detection of high-frequency spike trains and subthreshold membrane depolarizations with amplitudes on the order of excitatory postsynaptic potentials (PSPs). Capitalising on the overlapping spectra of JEDI-2P-kv and the channelrhodopsin ChroME-ST⁴⁴, we demonstrate simultaneous two-photon voltage imaging and photostimulation in multiple cells. This approach enables *in-situ* characterisation of the light-induced spiking properties of a population of neurons. Collectively, these results pave the way for studying neural function with two-photon all-optical neurophysiology in highly-scattering, densely labelled preparations.

Results

Scanless two-photon voltage imaging with sculpted, temporally focused excitation

The optical setup (Figure 1a, Supplementary Figure 1 and Table S1) was comprised of two independent excitation paths, one designed to generate temporally focused (TF) Generalized Phase Contrast (GPC) patterns^{36,38} or low NA Gaussian spots (similar to 3D-SHOT³⁹), and the second for TF-Computer Generated Holography (CGH)³⁷. These paths were combined prior to the microscope objective with a polarising beam splitter. Each excitation path was designed to generate temporally focused spots with dimensions matching the typical size of a neuronal soma (12 μm lateral full width at half maximum

(FWHM) and $\sim 9 \mu\text{m}$ axial FWHM for all modalities (Figure 1b, c, Supplementary Note 2, Supplementary Figures 2-5)). The fluorescence from $1 \mu\text{m}$ microspheres excited with a $12 \mu\text{m}$ GPC spot was recorded and found to have an axial FWHM of $3.7 \mu\text{m}$ demonstrating sub-cellular axial resolution (Figure 1c, right panel). In all cases, emitted fluorescence was detected by an sCMOS camera, effective pixel size $0.1625 \mu\text{m}$. The nominal field of excitation of each of the light sculpting approaches was $250 \times 250 \mu\text{m}^2$ ^{36,47,48}. However, the effective imaging field of view was limited in one dimension by the number of sCMOS rows readout simultaneously at a given acquisition rate (see Methods). The system was equipped with three different laser sources, two high repetition rate oscillators (as commonly used for two-photon laser scanning microscopy; 80 MHz, 920 or 940 nm, 100 fs, 12.5 nJ and 50 nJ pulse energies) and a third low repetition rate, high pulse energy laser (250 kHz, 940 nm, 100 fs, up to 2.5 μJ energy per pulse).

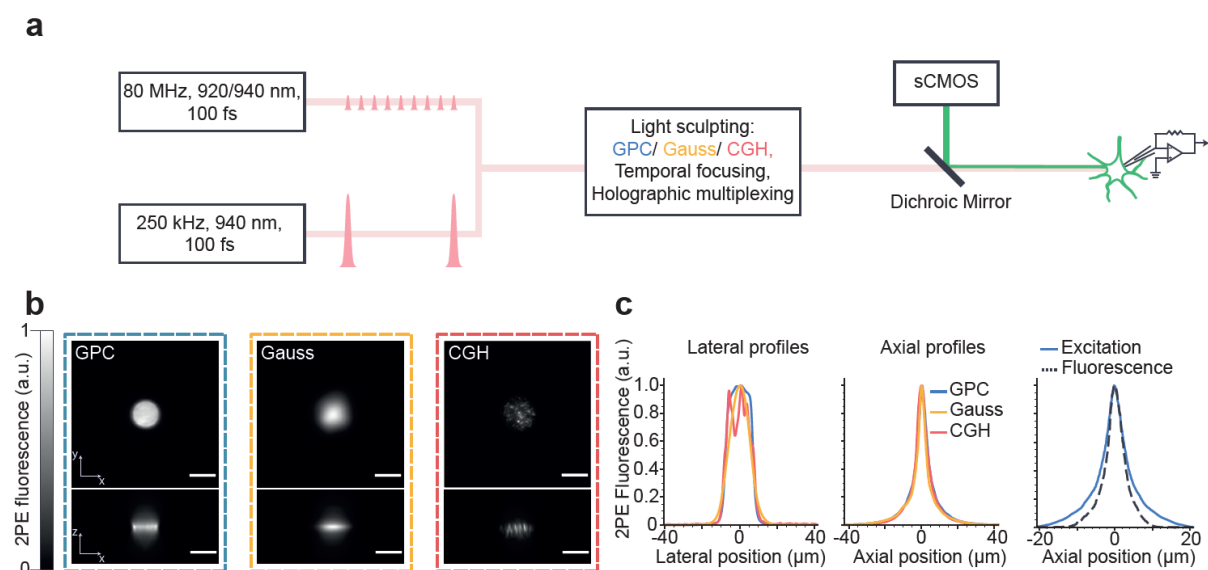


Figure 1. Schematic and characterization of the optical setup developed for scanless two-photon voltage imaging. (a) Summary of the optical setup designed to generate $12 \mu\text{m}$ (Full Width Half Maximum), temporally focused, Gaussian, Generalised Phase Contrast (GPC) and holographic (CGH) spots. The setup was equipped with three lasers, two of them delivering nJ-pulse energies at 80 MHz (Coherent Discovery, 1 W, 80 MHz, 100 fs tuned to 920, 940 or 1030 nm; Spark Alcor, 4 W, 80 MHz, 100 fs, 920 nm) and the third a custom Optical Parametric Amplifier (OPA) pumped by an amplified fibre laser, with fixed wavelength output (Amplitude Satsuma Niji, 0.5-0.6 W, 250 kHz, 100 fs, 940 nm). Fluorescence signals were acquired using an sCMOS camera. The microscope was equipped for electrophysiology patch-clamp recordings. (b) Lateral and axial cross sections of two-photon excited fluorescence generated with Gaussian (yellow), GPC (blue) and GCH (red) beams, as indicated in the legend. Scale bars represent $10 \mu\text{m}$. (c) Lateral and axial profiles of two-photon excited fluorescence generated with each excitation modality, and the corresponding system response, demonstrating single-cell resolution.

We compared the performance of three excitation modalities (2P-TF-GPC, 2P-TF-Gaussian and 2P-TF-CGH) for scanless two-photon voltage imaging using a high repetition rate laser source, as typically used for conventional 2P-LSM. We transiently expressed a recently developed, negative-going, voltage indicator optimised for two-photon excitation (JEDI-2P-kv⁴⁰), in mammalian (CHO) cells (Figure 2a). We controlled the membrane potential of individual cells using whole-cell patch-clamp electrophysiology and simultaneously performed two-photon voltage imaging. We used three different protocols, hereafter named 1, 2 and 3 (Figure 2b), to test the feasibility of scanless two-photon voltage imaging and to assess the advantages and disadvantages of each parallel approach.

Protocol 1 was used to quantify the voltage sensitivity of fluorescence of cells expressing JEDI-2P-kv. The responses of patched cells to three 100 ms, 100 mV voltage steps were recorded at 100 Hz under continuous illumination (power density: $0.88 \text{ mW } \mu\text{m}^{-2}$, 100 mW per cell) for 3 seconds. Voltage responses were clearly observed as a decrease in fluorescence with 2P-TF-GPC, 2P-TF-Gaussian and 2P-TF-CGH (Figure 2b, left panel). For most cells, we observed variability between the response amplitude measured at different membrane locations. Since differences in voltage responsivity of the fluorescence originating from different portions of the membrane were random, this is plausibly due to differences in plasma membrane trafficking and protein folding.

All data acquired using protocol 1 ($n = 41$ cells) were pooled and used to establish and validate an analysis pipeline capable of automatically identifying and segmenting neurons and of detrending the optical traces (Supplementary Figure 6). Due to the similarities between the data obtained with scanless two-photon voltage imaging and single photon voltage imaging with widefield detection, it was possible to develop an analysis pipeline based on existing open-source packages. Compared with results obtained by calculating the unweighted mean of all pixels within segmented cells, the regression-based pixel weighting algorithm^{14,49–51} (Methods, Supplementary Note 3), which improved segmentation, was found to increase $-\% \Delta F/F_0$ for all modalities (33.8 ± 9.5 vs. 43 ± 11.7 , mean \pm s.d., $p < 0.00001$, $n=41$, Supplementary Figure 7b), resulting in values in accordance with those previously reported⁴⁰. No significant difference in SNR (signal amplitude divided by the standard deviation of the baseline signal) was found between the two approaches (59.4 ± 30.2 vs. 59.6 ± 31.3 , $p = 0.9158$, $n=41$, Supplementary Figure 7c), a result of the fact that the improved segmentation contained approximately half of the pixels of the initial segmentation (16263 ± 2180 vs. 8962 ± 2676 , $p < 0.00001$, $n=41$, Supplementary Figure 7d). However, the location of these pixels coincided with the exterior cell membrane (Supplementary Figure 7d, inset), the most voltage-sensitive, which compensated for the effective reduction in photon count. We found that the final traces generated using the weighted pixel mask exhibited slightly more photobleaching than the traces generated with the original segmentation (0.82 ± 0.02 vs. 0.80 ± 0.03 , $p < 0.00001$, $n=41$, Supplementary Figure 7e). This is likely the result of two factors. Firstly, responsive pixels imaged with high contrast are more likely to be retained in the second segmentation step. These pixels are those where the cellular equator coincided with the focal plane, where the excitation power density (and presumably photobleaching) is highest. Secondly, the voltage responsive fluorophores are more likely to be tethered to the membrane, less mobile and hence more susceptible to photobleaching.

Having established the analysis pipeline, we then compared the three excitation modalities (Supplementary Figure 8). 2P-TF-GPC, 2P-TF-Gaussian and 2P-TF-CGH were all found to be suitable for scanless two-photon voltage imaging. Data obtained with 2P-TF-CGH exhibited the highest signal-to-noise ratio (81.6 ± 35.3 , $n = 15$), almost double that of 2P-TF-GPC (48.5 ± 19.2 , $p = 0.00222$, $n = 17$) and 2P-TF-Gaussian (43.9 ± 20.3 , $p = 0.00608$, $n = 9$). We hypothesised this was because the high spatial density of photons in speckle grains results in more efficient two-photon excitation. This hypothesis was confirmed by simulations (Supplementary Note 2, Supplementary Figure 5).

Since the high density of photons in speckles also increase the likelihood of non-linear photophysics (for instance photobleaching⁵²), we designed and used a different protocol (Protocol 2) to investigate the extent of these non-linear effects as a function of the excitation power density (0.66 – 1.55 mW μm^{-2} corresponding to 75 – 175 mW per cell). Protocol 2 consisted of three 100 ms, 100 mV voltage steps, 200 ms illumination pulses centred on each voltage step, and 2.5 s inter-pulse intervals (Figure 2b, middle panel). For all modalities, the baseline fluorescence (F_0) increased quadratically as a function of power density (Figure 2c, first panel), as expected with two-photon illumination and indicating that fluorescence excitation was not saturated at any of the powers used. Furthermore, the SNR increased linearly as a function of power density (Figure 2c, second panel, $R^2 = 0.999$ (2P-TF-GPC), $R^2 = 0.995$ (2P-TF-Gaussian), $R^2 = 0.998$ (2P-TF-CGH)), confirming that experiments were performed in the shot-noise limited regime rather than being limited by the read noise of the detector. On this basis, all SNR estimates stated hereafter were calculated as $\text{SNR} = (-\Delta F/F_0)\sqrt{F_0}$ ⁵³.

The SNR of the responses to 100 mV steps (Protocol 2) was higher at all excitation power densities with 2P-TF-CGH than with 2P-TF-GPC or 2P-TF-Gaussian, (Figure 2c, second panel, Supplementary Figure 9a), though the 2P-TF-CGH fluorescent transients exhibited a systematically lower average $-\Delta F/F_0$ than when using 2P-TF-GPC. This difference increased as a function of power density (Figure 2c, third panel, Supplementary Figure 9b). Photostability, defined as the ratio between the integral of the baseline fluorescent trace to $F_0 \cdot n_t$ where F_0 represents the fluorescence in the first frame and n_t the number of baseline fluorescence timepoints (schematic diagram, Figure 2c, fourth panel, inset), decreased as a function of excitation power in all cases (Figure 2c, fourth panel). No significant difference was observed between the different modalities (Supplementary Figure 9c). Photorecovery, quantified as the ratio of fluorescence after dark intervals to the original fluorescence (schematic diagram, Figure 2c, fourth panel, inset), was over 97% following 2.5 s dark inter-pulse intervals when excited with 2P-TF-Gaussian and 2P-TF-GPC, which is consistent with previous observations⁵⁴. In the case of 2P-TF-CGH, the photorecovery decreased as a function of excitation power density and was lower than the other modalities (<95% for power densities greater than 0.88 mW μm^{-2} (100 mW per cell), $p=0.01$, Figure 2c, fifth panel, Supplementary Figure 9d).

Finally, we used protocol 3 (Figure 2b, right panel) to assess the detection of short, action-potential like transients with scanless two-photon voltage imaging. Cells were illuminated continuously for 500 ms (power density: 1.33 mW μm^{-2} , corresponding to 150 mW per cell) and the fluorescence response to a 20 Hz train of 10 rectangular pulses (100 mV amplitude, 3 ms duration) was recorded with a 1 kHz acquisition frequency (see Methods). The transients recorded using 2P-TF-GPC, 2P-TF-Gaussian and 2P-TF-CGH, had $-\Delta F/F_0$ values of $45 \pm 14 \%$, $42 \pm 16 \%$ and $26 \pm 6 \%$ ($n = 8-11$) respectively (Supplementary Figure 10b). For all modalities, the average SNR was greater than 11, demonstrating that action-potential-like signals can be reliably detected in single trials with scanless two-photon voltage imaging. As per data presented in supplementary figures 10c and d, the highest SNR data was acquired using 2P-TF-CGH (20.5 ± 6.2 compared with 13.9 ± 3.6 (2P-TF-GPC) and 11.5 ± 4.1 (2P-TF-Gaussian), $n = 8-11$), at the cost of lower photostability (0.86 ± 0.07 (2P-TF-CGH) versus 0.92 ± 0.08 (2P-TF-GPC) and 0.89 ± 0.12 (2P-TF-Gaussian), $n = 8-11$).

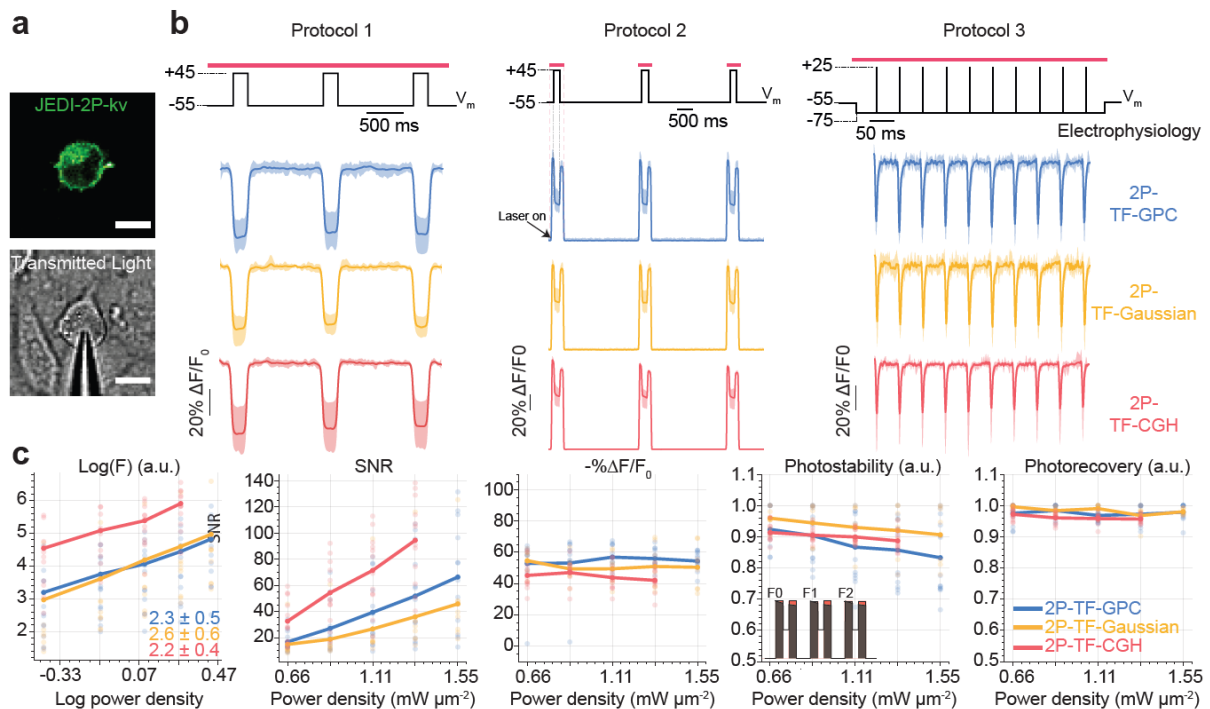


Figure 2. In-vitro electrophysiological characterisation of scanless two-photon voltage imaging in cultured CHO cells. (a) Confocal image of a JEDI-2P-kv expressing CHO cell (upper) and transmitted light image of a patched CHO cell (lower). Scale bars represent 10 μm . (b) Data from three protocols used to test the performance of each of the three different parallel illumination modalities for two-photon voltage imaging. Responses are reported as the fluorescence change (ΔF) normalized by the baseline fluorescence (F_0), expressed as a percentage of the baseline fluorescence ($\% \Delta F/F_0$). The average trace and 95 percent confidence interval from all cells imaged with each modality are plotted (blue – GPC, yellow – Gaussian, red – CGH). The corresponding electrophysiology control signals are plotted in black. The red bar above the electrophysiology trace indicates the illumination epoch. (c) Quantification of data for all cells from protocol 2. Log(F), SNR, $-\% \Delta F/F_0$, photobleaching and photorecovery are plotted as a function of power density (power density: 0.66 – 1.55 $\text{mW } \mu\text{m}^{-2}$, 75 – 175 mW per cell, $n = 8 - 13$), see also Supplementary Figure 9. Each point represents a measurement from an individual cell. The mean is plotted for each condition. Photostability is defined as the ratio between the integral of the baseline fluorescent trace to $F_0 \cdot n t$ where F_0 represents the fluorescence in the first frame and $n t$ the number of baseline fluorescence timepoints (see schematic diagram, fourth panel, inset). Photorecovery is defined as the average ratio of the fluorescence prior to the 100-mV depolarization in each illumination epoch (for instance F_1/F_0 as defined in the schematic diagram, fourth panel, inset). All data was acquired with laser A tuned to 940 nm and camera A (See Supplementary Figure 1 and Supplementary Tables 1 and 2).

Overall, these results confirm that 2P-TF-GPC, 2P-TF-Gaussian and 2P-TF-CGH can successfully be applied to scanless two-photon voltage imaging, albeit with different advantages and limitations. Since the SNR of data acquired using 2P-TF-CGH was significantly higher than for 2P-TF-Gaussian or 2P-TF-GPC, we consider it the optimal modality for imaging large numbers of cells simultaneously, for short periods, with a given incident power. For prolonged recordings (continuous illumination for hundreds of milliseconds or more) of neurons labelled with JEDI-2P-kv, we would recommend 2P-TF-GPC or 2P-TF-Gaussian, since we observed lower photobleaching and higher photorecovery with these methods than with 2P-TF-CGH. Although no significant performance differences were found between 2P-TF-Gaussian and 2P-TF-GPC (Figure 2c, Supplementary Figures 8 and 9), 2P-TF-Gaussian requires higher power at the laser output for a given SNR. Specifically, uniform illumination of the somal membrane was achieved with 2P-TF-Gaussian by expanding and subsequently cropping the beam (Supplementary Note 2, Supplementary Figure 4) and thus was ~ 3 times less power-efficient than 2P-

TF-GPC⁵⁴. However, it is perhaps the simplest approach to implement, and hence a good solution given a sufficiently powerful laser source.

Scanless voltage imaging of neural activity in hippocampal organotypic slices with two-photon, temporally focused Generalized Phase Contrast

We set out to identify the imaging conditions (specifically the power densities and acquisition rates) required to observe neural activity ranging from high-frequency spike trains to sub-threshold depolarizations in densely labelled samples. We also aimed to determine whether the necessary imaging conditions perturb neural activity or otherwise impact cellular physiology. We performed simultaneous 2P-TF-GPC imaging and whole cell-patch clamp recordings of granule cells located in the dentate gyrus (DG) of organotypic slices bulk-transduced with JEDI-2P-kv (see Methods). Expression of JEDI-2P-kv in the granule cells of the DG was well localised to the plasma membrane, with no evidence of intracellular aggregation (Figure 3a). Even though granule cells are extremely closely packed in DG, due to the optical sectioning conferred by temporally focused, targeted illumination, we were able to image individual neurons with high-contrast and high-resolution in this challenging preparation (Figure 3b).

Using protocol 1, we confirmed we could detect 100 mV depolarizations in densely labelled, scattering organotypic slices with comparable $-\% \Delta F/F_0$ (43 ± 8) to that obtained in CHO cells (51 ± 11) ($n > 15$ cells, accounting for differences in the resting potential between neurons and CHO cells, Supplementary Figures 11 and 12). No significant difference was observed in SNR (69 ± 25 (CHO), 50 ± 30 (organotypic slices), $n > 15$ cells, Supplementary Figure 12e) or photostability between results obtained in hippocampal organotypic slices and CHO cells. The effective lateral and axial resolution of the scanless two-photon imaging system, quantified as the relative $\Delta F/F_0$ of an electrically evoked spike as a function of the distance between the excitation spot and the soma, was found to be approximately isotropic and of similar dimensions to the neuronal soma ($14 \mu\text{m}$ lateral and $13 \mu\text{m}$ axial FWHM, Supplementary Figure 12h), confirming the cellular resolution of scanless two-photon voltage imaging.

Next, we recorded the fluorescence from patched cells while 50 action potentials (APs) were evoked electrically by injection of current (700 - 900 pA, 2 ms) into the soma at a rate of 1 Hz. Electrically evoked APs were imaged with 3 different acquisition rates: 500 Hz, 750 Hz, and 1 kHz (corresponding to per-frame exposure times of 2, 1.33 and 1 ms respectively) as previously used for 1P widefield voltage imaging⁵⁵. In all conditions, individual APs could clearly be identified from single trials in the raw fluorescence traces (representative traces for single cells plotted in Figure 3c, power density: $1.11 \text{ mW } \mu\text{m}^{-2}$, corresponding to 125 mW per cell). Putative APs were identified by template matching, based on the most prominent peaks originally identified in each fluorescence trace⁵⁰. The 1 kHz recordings exhibited a higher $-\% \Delta F/F_0$ than 500 Hz recordings across all powers (30.5 ± 2.2 vs 25.7 ± 1.2 , $n > 5$ cells, Figure 3d). However, consistent with previous reports¹⁷, higher SNR was achieved with 500 Hz recordings than for 1 kHz (for example for $0.66 \text{ mW } \mu\text{m}^{-2}$ (75 mW per cell): 14.2 ± 0.3 vs 11.9 ± 0.3 , Figure 3d), because the increase in the number of photons collected per action potential more than compensated for the reduced $-\% \Delta F/F_0$.

Having established that it was possible to record APs with high SNR in single trials at different acquisition rates, we next tested whether we could also monitor individual spikes within high-frequency trains of action potentials (such as bursts) under these conditions. We observed that an acquisition rate of 500 Hz was sufficient to track individual APs in trains with frequencies up to 100 Hz (Figure 3e, Supplementary Figure 13) and using power densities as low as $0.66 \text{ mW } \mu\text{m}^{-2}$ (75 mW per cell). As a result of increased SNR recordings with lower acquisition rates, at low power densities, the detection probability (fraction of correctly identified APs) was higher (Figure 3f). Note that the difference in SNR between results presented in Figure 3d and Figure 3f is the result of using different cameras and different excitation wavelengths, as specified in the Methods and Supplementary Tables 1 and 2. However, an acquisition rate of 500 Hz was insufficient for robustly tracking spikes in 125 Hz trains due to a reduction in $-\% \Delta F/F_0$ (Supplementary Figure 13b), which led to a deterioration in detection probability and fluorescence response compared with the data acquired at 1 kHz at power densities $\geq 0.66 \text{ mW } \mu\text{m}^{-2}$ (corresponding to 75 mW per cell, Figure 3f, Supplementary Figure 13). For all power densities $> 0.66 \text{ mW } \mu\text{m}^{-2}$ (75 mW per cell) sub-millisecond precision of AP timing estimation was obtained, as measured with respect to the electrophysiology trace (Figure 3f).

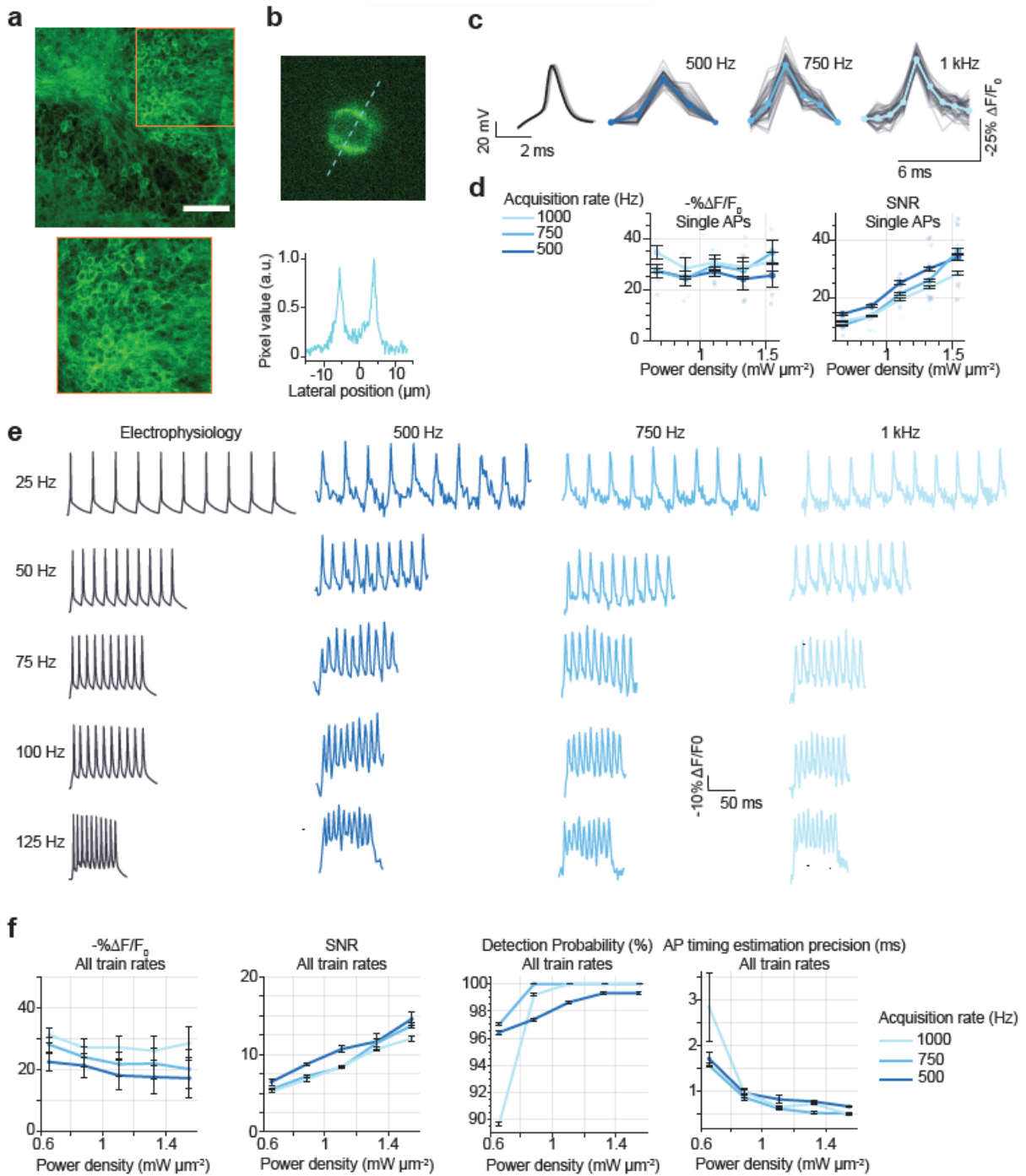


Figure 3. Recording electrically evoked single action potentials and high-frequency spike trains in JEDI-2P-kv expressing hippocampal organotypic slices with 2P-TF-GPC. (a) Upper: confocal image of a representative organotypic slice bulk-infected with JEDI-2P-kv. Scale bar represents 75 μm . Lower: zoom (x2) of densely expressing region where data was recorded. (b) Upper: representative single frame from data acquired with TF-GPC (1 ms exposure time), Lower: line-profile through the image (indicated by the dashed line) demonstrating that single cells are imaged with high-contrast in densely labelled samples with 2P-TF-GPC. (c) Electrically induced and recorded action potentials (left) and optically recorded (right) were resolved in single trials using 2P-TF-GPC at different acquisition rates. Individual trials are plotted in grey. The average trace across all trials is plotted in a different shade of blue corresponding to each acquisition rate (500 Hz, 750 Hz and 1 kHz, as labelled). Power density: $1.1 \text{ mW } \mu\text{m}^{-2}$ (125 mW per cell). (d) $-\% \Delta F/F_0$ and SNR plotted as a function of power density in different shades of blue for different acquisition rates (see legend). Error bars represent the standard error of measurements across all cells ($n = 4-6$). Individual points represent the average value over 50 action potentials for individual cells. All data were acquired using laser A tuned at 940 nm, and camera A (See Supplementary Figure 1 and Supplementary Tables 1 and 2). (e) Representative fluorescence traces recorded from individual cells to different rates of electrically evoked spike trains recorded at the different acquisition rates of 500 Hz, 750 Hz and 1 kHz corresponding to 2 ms, 1,33 ms and 1 ms exposure time (power density: $1.1 \text{ mW } \mu\text{m}^{-2}$, 125 mW per cell). A representative trace of electrically evoked spike trains is also plotted in black (left). (f) $-\% \Delta F/F_0$, SNR, action potential detection probability and precision of action potential timing estimation (defined as the jitter in timing estimation for all identified action potentials relative to the corresponding electrophysiological recordings) plotted as a function of power density for different acquisition rates (500 Hz, 750 Hz, and 1 kHz, see legend). A lower value indicates superior timing estimation. Data plotted for all train rates ($n = 2-5$). All data were acquired using laser B fixed at 920 nm, and camera B (See Supplementary Figure 1 and Supplementary Tables 1 and 2).

We next examined whether these conditions (power density: $1.11 \text{ mW } \mu\text{m}^{-2}$, corresponding to 125 mW per cell, 1 kHz acquisition rate) were also suitable for imaging sub-threshold changes in membrane potential. To emulate excitatory PSPs, patched cells were clamped to -75 mV , while the membrane potential was varied in 0.5 mV steps from 0 to 2.5 mV for 20 ms . This protocol was repeated 50 times. Since it was not possible to detect these transients from individual recordings (Figure 4a, b, $n=6$), we averaged data from different trials to improve SNR. Averaging data from 25 repeats was sufficient to stabilise the magnitude of the fluorescence transient ($-\% \Delta F/F_0$) for a given depolarization (Figure 4a, c) and to increase the SNR above 1 for all depolarizations larger than 0.5 mV (Figure 4d).

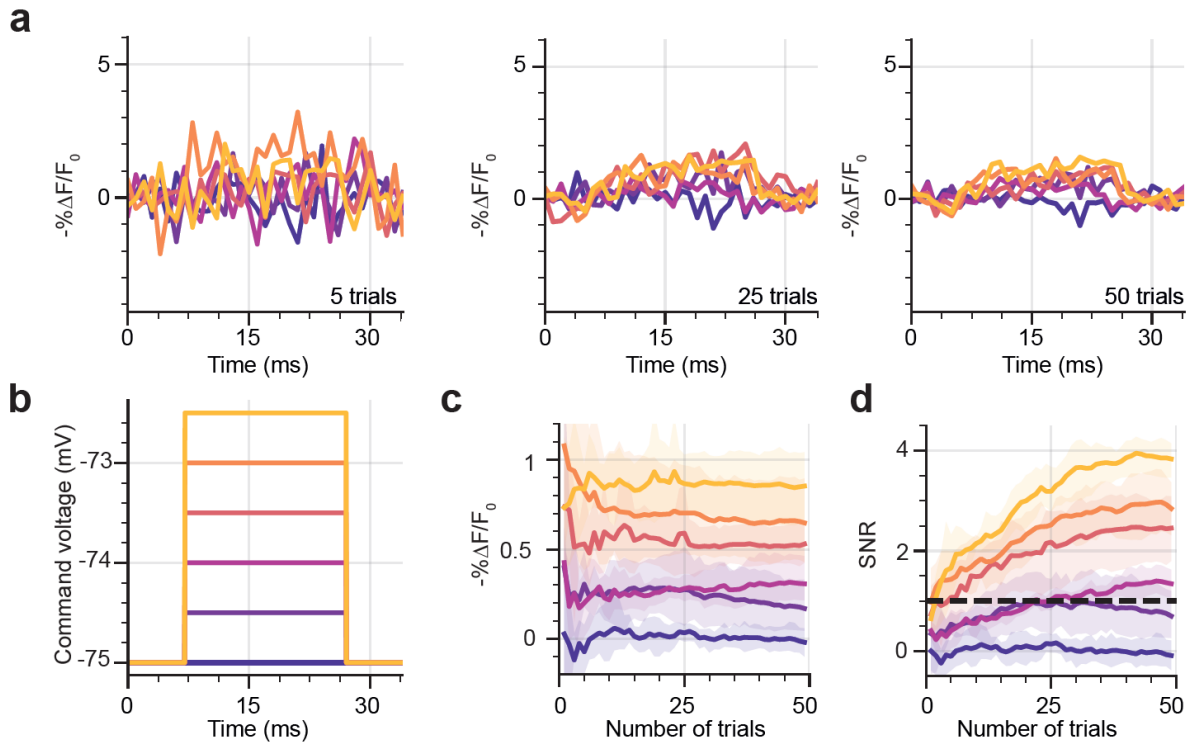


Figure 4. Recording sub-threshold depolarizations in JEDI-2P-kv expressing hippocampal organotypic slices using 2P-TF-GPC. (a) Average fluorescence traces recorded from neurons after 5, 25 and 50 trials for different magnitudes of sub-threshold depolarizations ranging between 0 and 2.5 mV. Sub-threshold depolarisations < 2.5 mV cannot be reliably resolved in single trials using 2P-TF-GPC and JEDI-2P-kv, however after 25 trials depolarisations greater than or equal to 1 mV can be resolved. Traces were recorded with a 1 ms exposure time and $1.1 \text{ mW } \mu\text{m}^{-2}$ (125 mW per cell). (b) Command voltage steps used to change the membrane potential of patched neurons. (c) Average $-\% \Delta F/F_0$ and (d) SNR of the fluorescence response to different sub-threshold changes of membrane potential plotted as a function of number of repeats. The 95% confidence interval is also plotted (shaded region). All data ($n = 6$) were acquired using laser B fixed at 920 nm and camera B (See Supplementary Figure 1 and Supplementary Tables 1 and 2).

Next, we tested the capability of scanless two-photon voltage imaging to record spontaneous network activity, a fundamental feature of developing neural circuits⁵⁶. We performed simultaneous electrophysiological (whole cell patch clamp, (current clamp)) and fluorescence recordings (2P-TF-GPC, power density: $1.33 \text{ mW } \mu\text{m}^{-2}$ (150 mW per cell), 1 kHz acquisition rate) of spontaneous activity from neurons in hippocampal organotypic slices which exhibited a range of different resting potentials ($n > 10$ cells; 5 slices). We were able to observe several hallmarks of spontaneously generated activity, large slow depolarizations, bursts of action potentials, rhythmic sub-threshold depolarizations and hyperpolarizations (Figure 5 and Supplementary Figure 14). These results confirmed the capability of scanless two-photon voltage imaging for high temporal precision, single trial recordings of action potentials and sub-threshold events, even though the sensitivity curve of JEDI-2P-kv is not optimized for sub-threshold recordings. Collectively, the results presented in Figures 3-5 parameterize the necessary imaging conditions required to detect neural activity with sufficient SNR using scanless two-photon voltage imaging.

To test the robustness of our approach for long-term recordings, we repeated the same protocol (2P-TF-GPC, 30 s continuous illumination, $1.33 \text{ mW } \mu\text{m}^{-2}$ (150 mW per cell), 1 kHz acquisition rate), for a

maximum recording time of 20 minutes. Due to limitations of the prototype experimental configuration (primarily data transfer rates), there was a dark period (<10 seconds) between consecutive acquisitions. To increase the duty cycle of the recordings, we reduced the acquisition speed to 500 Hz which enabled us to perform longer continuous recordings with a shorter dark period of <5 seconds (2P-TF-GPC, 1 min continuous illumination, $1.33 \text{ mW } \mu\text{m}^{-2}$ (150 mW per cell), 500 Hz acquisition rate). As indicated by the data presented in Supplementary Figure 15, we were able to record spontaneous activity from single neurons for a maximum recording time of 20 minutes without a significant decrease in SNR (Supplementary Figure 15b). The imaging period was primarily limited by axial sample drift which decreased the SNR (data not shown), but could be overcome in future experiments with a tandem construct containing the voltage indicator and a spectrally shifted, fluorescent reporter used to track the sample drift and to dynamically update the co-ordinates of the multiplexed spots.

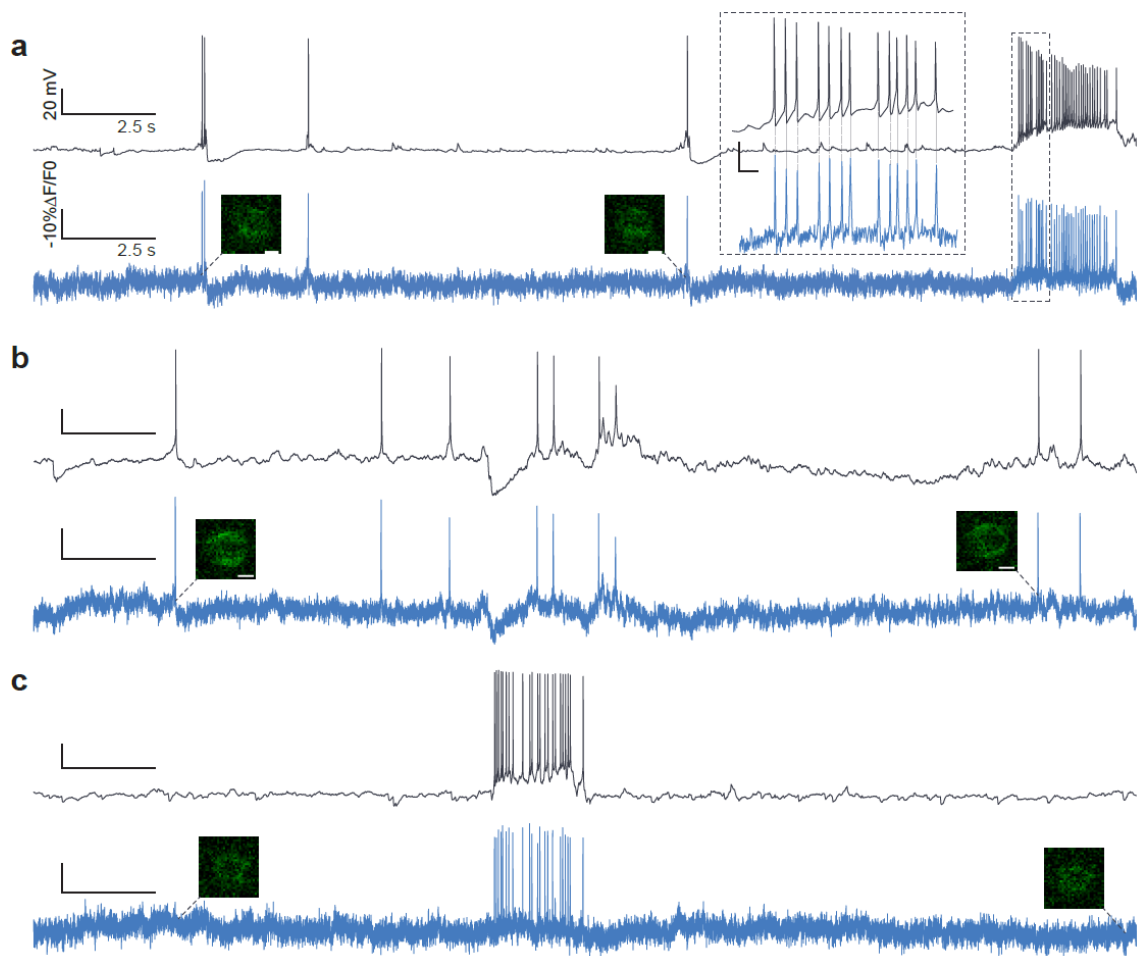


Figure 5. Recording spontaneous neural activity in JEDI-2P-kv expressing hippocampal organotypic slices using 2P-TF-GPC. (a-c) Simultaneous current clamp (upper, black) and fluorescence recordings (lower, blue) of spontaneous activity in neurons from hippocampal organotypic slices over a continuous 30 s recording period. Single imaging frames are shown close to the beginning and end of each recording. Scale bars represent $5 \mu\text{m}$. Inset, (a) zoomed in portion of the electrophysiological and fluorescence traces. Corresponding action potentials in the electrophysiological and fluorescence traces (average rate: 17 Hz) is indicated by the dashed lines. (Power density: $1.33 \text{ mW } \mu\text{m}^{-2}$, 150 mW per cell, 1 kHz acquisition rate). All data was acquired using laser A tuned to 940 nm and camera A (See Supplementary Figure 1 and Supplementary Tables 1 and 2).

Having established the conditions necessary to observe neural activity ranging from high-frequency trains of action potentials to sub-threshold membrane potential depolarizations, we next investigated whether such imaging conditions induced physiological perturbations. There are two main sources of light-induced perturbations. The first is heating, due to linear absorption of the infrared light (mostly by water), which has been reported to affect ion channel conductances⁴⁵ and action potential waveforms⁴⁶. The second is non-linear photodamage, due to higher order light-matter interactions which occur because of high instantaneous photon density in the focal volume and can ultimately induce apoptosis and cell ablation^{47–49}. We performed experiments (10 ms strobed illumination, 50 cycles, 1 Hz, total illumination time 500 ms, >15 cells per region, targeted sequentially: identical to the protocol used to detect APs (Figure 3b-c)) at power densities we found necessary to observe neural activity with sufficient SNR and above ($0.66 - 1.55 \text{ mW } \mu\text{m}^{-2}$, corresponding to 75 – 175 mW per cell). Following these experiments, we used immunohistochemistry to detect heat-shock proteins (anti-HSP70/72 immunostaining) and activation of apoptotic pathways (anti-activated-Caspase-3 immunostaining). Fixed slices were imaged using confocal microscopy. No difference in fluorescence intensity was observed between any of the illumination powers used and the control slices (not illuminated) in the case of Caspase-3 (Supplementary Figure 16a). In contrast, we observed that levels of anti-HSP increased as a function of excitation power above $1.1 \text{ mW } \mu\text{m}^{-2}$ (125 mW per cell), which indicates that the physiological damage induced by the high repetition rate laser sources, is predominantly heating. Since the damage threshold of $1.1 \text{ mW } \mu\text{m}^{-2}$ (125 mW per cell) identified using immunohistochemistry is an upper bound, we also investigated whether there was any light induced changes in the electrical properties of neurons using electrophysiology. We did not observe any light-induced changes in action potential amplitude or width at any of the tested powers (Supplementary Figure 16b), however we found that the latency of action potential firing slightly increased at all powers tested (0.1 ms, Supplementary Figure 16b). This effect was observed 15 seconds before a similar increase in latency was seen in control experiments (Supplementary figure 16b). Whilst a 10 percent change is not huge, the immunohistochemistry and electrophysiology results imply a laser-induced perturbation of physiology for powers > 125 mW per cell.

Scanless two-photon voltage imaging of multiple targets with low repetition rate lasers

To test the capability of multiplexed 2P-TF-GPC to image multiple neurons simultaneously we used a custom low-repetition rate source (940 nm, pulse duration 100 fs, repetition rate 250 kHz, 600 mW average output power). Low-repetition rate sources, used for two-photon optogenetics, can provide higher peak energies and lower average power, hence potentially minimize photoinduced thermal effects and scale up the number of neurons that can be imaged simultaneously. Low-repetition rate lasers are particularly well suited for techniques with long times, such as scanless two-photon imaging. We found that using the low repetition rate laser, action potentials could be detected in single trials with power densities as small as $0.01 \text{ mW } \mu\text{m}^{-2}$ (1.5 mW per cell, Supplementary Figure 17). In contrast to the results obtained using the high repetition rate source (80 MHz, previous section), no changes in action potential properties were detected at any of the tested powers (Supplementary Figure 17). Immunohistochemistry targeted against HSP70/72 and activated-Caspase-3 (Supplementary Figure 17) did not reveal thermal or non-linear damage at power densities below $0.09 \text{ mW } \mu\text{m}^{-2}$ (10 mW per

cell) using 2P-TF-CGH, two-fold higher than the maximum powers we found typically necessary to image neural activity. Extrapolating from the results related to photobleaching and photostability obtained in CHO cells, we anticipate higher non-linear damage thresholds for 2P-TF-GPC and 2P-TF-Gaussian.

As a result of the increased energy per pulse of the low-repetition rate source, we were able to increase the number of neurons imaged simultaneously without exceeding the power damage threshold. For example, we recorded spontaneous activity in up to 8 neurons in the dentate gyrus of hippocampal organotypic slices simultaneously (2P-TF-GPC, power densities: $0.04 - 0.08 \text{ mW } \mu\text{m}^{-2}$ ($5 - 9 \text{ mW}$ per cell, total power $< 75 \text{ mW}$), Figure 6, Supplementary Figure 18). The sub-threshold activity of most neurons was found to be highly synchronized, a characteristic feature of the immature hippocampus⁵⁶. Control traces recorded adjacent to targeted neurons confirmed that this was not an artefact due to crosstalk. We were able to combine data from separate acquisitions to perform voltage imaging throughout a large region ($200 \times 150 \mu\text{m}^2$) as demonstrated in Figure 6. Since this data was acquired on a prototype system, the period between sequential acquisitions was on the order of seconds. However, by optimizing the acquisition pipeline, the period between sequential acquisitions could feasibly be reduced to milliseconds to enable scanless two-photon voltage imaging of populations of neurons.

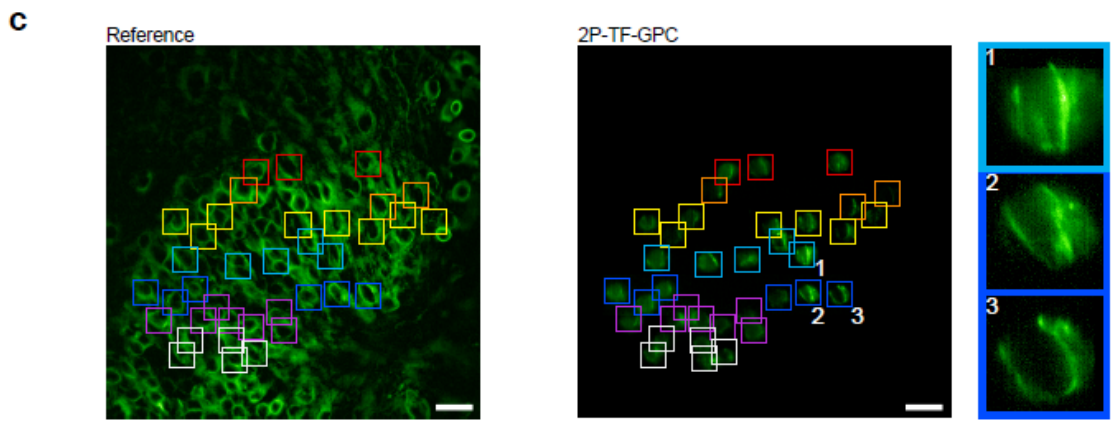
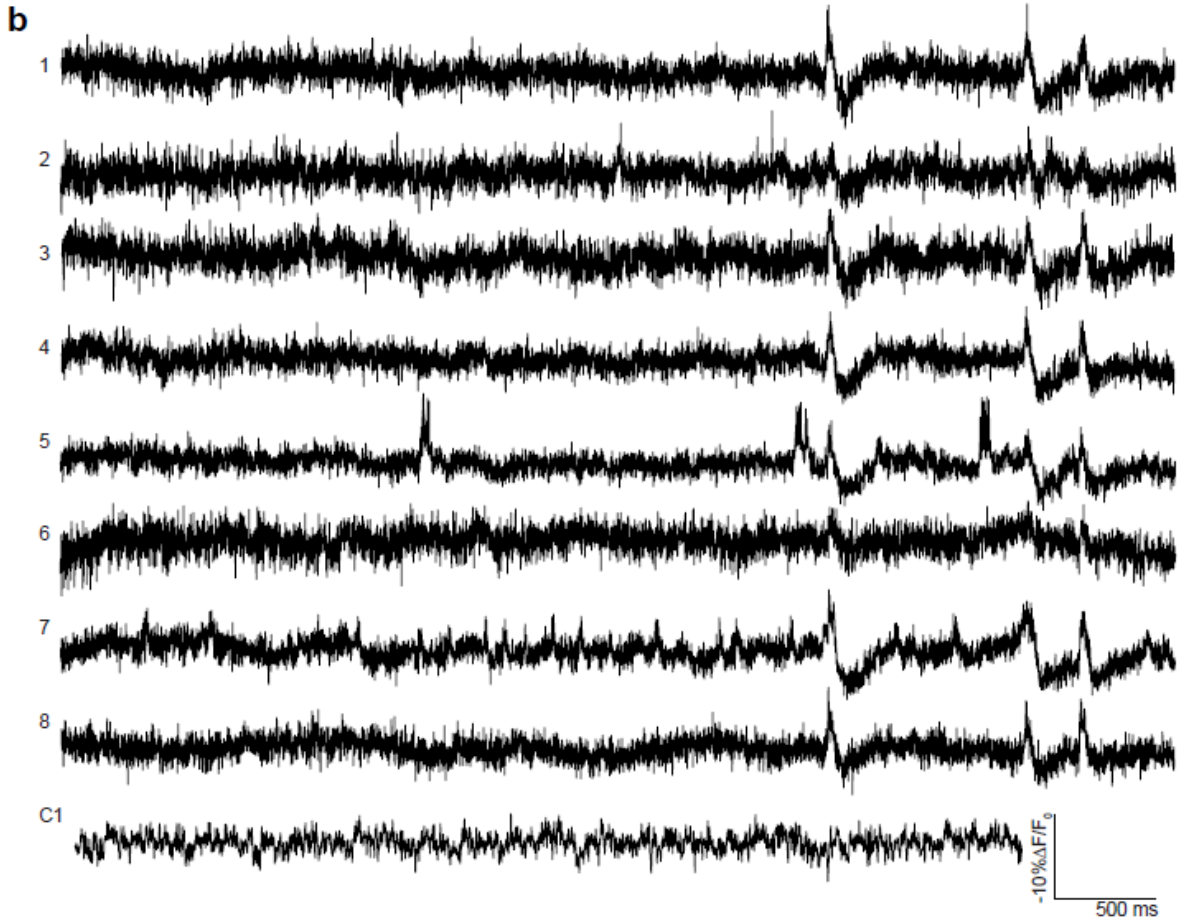
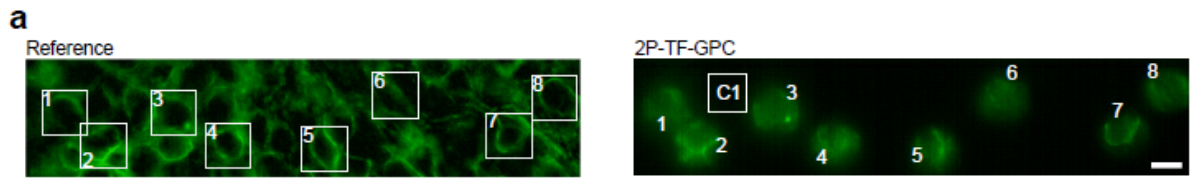


Figure 6. Multi-cell recordings of spontaneous neural activity in JEDI-2P-kv expressing hippocampal organotypic slices using multiplexed 2P-TF-GPC. (a) Reference image of a hippocampal organotypic slice expressing JEDI-2P-kv in the dentate gyrus (left panel) and average projection of the corresponding voltage imaging dataset (right panel). 8 neurons targeted simultaneously with 8, 12- μm 2P-TF-GPC spots can be identified (as numbered and highlighted by the square boxes). The scale bar represents 10 μm . C1 refers to the area used to generate the control trace plotted in (b). This ROI was not targeted with a GPC spot during experiments. (b) Fluorescent traces plotted for each of the neurons indicated in (a), including the control trace. (c) Voltage imaging throughout a large field of view using multiplexed 2P-TF-GPC. Left panel: cross-section of a hippocampal organotypic slice expressing JEDI-2P-kv in the dentate gyrus. Middle panel: combined maximum projections of data from 7 consecutive acquisitions (indicated by the coloured squares), spanning a total area of $200 \times 150 \mu\text{m}^2$. Zoom in for best viewing. Scale bars represent 25 μm . Right panel: zoomed in regions of the central panel (indicated by numbering and coloured boxes) showing maximum projections of data acquired from individual cells targeted with multiplexed 2P-TF-GPC. All data was acquired using laser C (940 nm, power density: $0.02 - 0.09 \text{ mW } \mu\text{m}^{-2}$, $2.5 - 10 \text{ mW}$ per cell) and camera A with an acquisition rate of 1 kHz (See Supplementary Figure 1 and Supplementary Tables 1 and 2).

The number of achievable targets per acquisition and/or the imaging depth could be further increased, as demonstrated for two-photon photostimulation of multiple cells⁵⁷ using high-power, low repetition rate, industrial light sources such as Ytterbium-doped fibre lasers which can provide much higher output powers (tens of Watts), and comparable pulse energies to the 940 nm source used in this work. These lasers are commonly fixed wavelength sources (1030 – 1040 nm), which means that they are not typically compatible with GFP-based fluorescent indicators. However, since the excitation spectrum of JEDI-2P-kv is slightly red-shifted as compared with previous GFP-based voltage indicators⁴⁰, we tested whether it was possible to record neural activity using scanless two-photon voltage imaging with 1030 nm excitation. We repeated protocol 2 (see above) in CHO cells and imaged electrically evoked action potentials and spontaneous activity in sparsely labelled hippocampal organotypic slices (Supplementary Figure 19).

Scanless two-photon voltage imaging and photostimulation of multiple targets with a single beam

Next, we performed simultaneous two-photon voltage imaging and photostimulation of neurons co-expressing JEDI-2P-kv and a soma-targeted channelrhodopsin. ChroME-ST and JEDI-2P-kv were co-expressed in the dentate gyrus of hippocampal organotypic slices by bulk transduction of two Adeno-Associated Virus (AAV) vectors (Figure 7a). We characterised the photophysical properties of ChroME-ST excited using the low-repetition rate laser using whole cell patch clamp electrophysiology (voltage-clamp). ChroME-ST mediated photocurrents in CHO cells saturated at $0.02 \text{ mW } \mu\text{m}^{-2}$ (2.5 mW per cell) (Supplementary Figure 20, $n=4$). In hippocampal organotypic slices, power densities between 0.02 and $0.04 \text{ mW } \mu\text{m}^{-2}$ ($2.5 - 5 \text{ mW}$ per cell) generated sufficiently large photocurrents to reliably evoke APs with short ($< 5 \text{ ms}$) latency and sub-millisecond jitter (Supplementary Figure 20, $n=7$).

We performed simultaneous photostimulation, imaging and whole-cell patch clamp recordings on neurons co-expressing ChroME-ST and JEDI-2P-kv and confirmed that optically evoked action potentials could be detected in voltage imaging recordings (Figure 7b). We next performed an all-optical characterisation of ChroME-ST. By modifying the power, duration and frequency of the illumination, we explored the joint-parameter space of imaging and stimulation conditions to optimize the probability of optically evoking and recording action potentials (Figure 7c). Unlike in neurons exclusively expressing JEDI-2P-kv, at power densities below $0.02 \text{ mW } \mu\text{m}^{-2}$ (2.5 mW per cell), the SNR of action potentials

from single trials did not exceed the SNR threshold and hence could not be detected optically (Figure 7c), although electrophysiological recordings performed simultaneously indicated that the probability of optically evoking an AP was greater than 75% (Supplementary Figure 20b). We attribute the reduction in SNR to a reduction in the expression efficiency of JEDI-2P-kv as a result of co-expressing a voltage indicator and channelrhodopsin, which results in a difference between the optical and electrophysiological results. However, for power densities above $0.02 \text{ mW } \mu\text{m}^{-2}$ (2.5 mW per cell), we were able to detect action potentials in single trials and measured similar latencies to those obtained using whole-cell patch clamp recordings ($4.3 \pm 0.2 \text{ ms}$, mean \pm s.e.m.) and jitter on the order of a millisecond (Supplementary Figure 20c-d).

The action potential probability decreased as a function of stimulation frequency, feasibly a result of channelrhodopsin desensitization at the saturating powers used, although in some cases it was possible to stimulate and image action potentials at 50 Hz (Figure 7c, right panel). Based on this characterisation, we determined that the optimal photostimulation and imaging parameters to robustly optically evoke and detect action potentials were a frequency of 5 Hz and 15 ms photoactivation pulses. The extended illumination time relative to typical photostimulation protocols was necessary for having sufficient baseline to calculate $-\% \Delta F/F_0$ and to robustly detect optically evoked action potentials. Results obtained for these parameters are summarized for 27 cells in the raster plot in Figure 7d with representative fluorescence traces of optically evoked APs shown in Figure 7e. For each cell, the power density was increased until a spike was detected optically in at least one of five repeats. The final set of power densities used was between 0.02 and $0.08 \text{ mW } \mu\text{m}^{-2}$ (2.5 and 9 mW per cell), below the power threshold found to induce physiological perturbations (see above). The average $-\% \Delta F/F_0$ of optically evoked action potentials was found to be $20 \pm 8 \%$ ($n=33$; Figure 7f), consistent with results obtained for electrically evoked action potentials (Figures 3d and f).

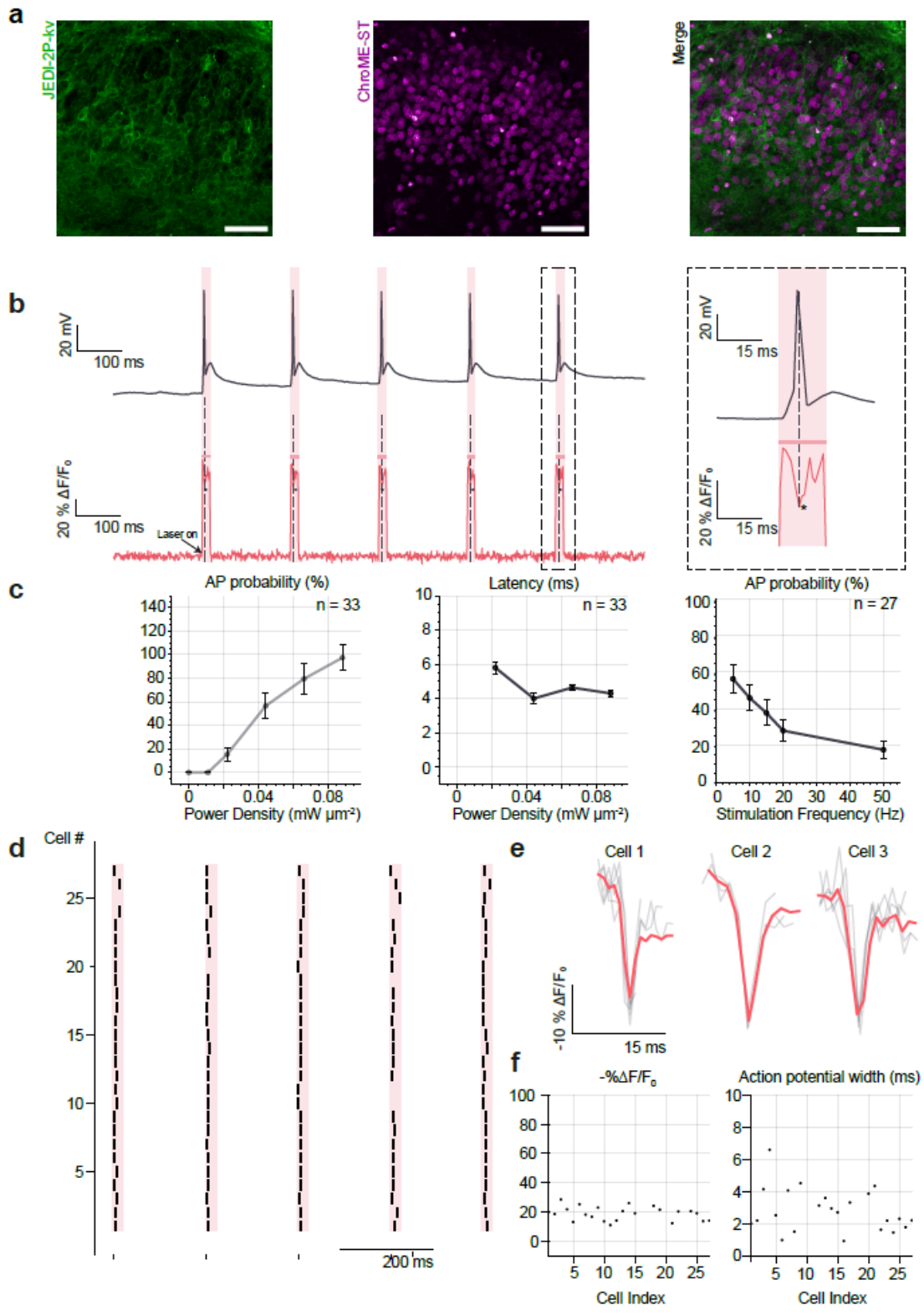


Figure 7. Fluorescence recordings of photo-evoked spikes in hippocampal organotypic slices co-expressing JEDI-2P-kv and ChroME-ST, using 2P-TF-CGH. (a) Cross-sections of hippocampal organotypic slices co-expressing the genetically encoded voltage indicator JEDI-2P-kv and the soma-targeted channelrhodopsin ChroME-ST in the dentate gyrus. Channelrhodopsin-expressing cells were identified according to their nuclear-localized fluorescence (see Methods). Scale bar represents 50 μm . (b) (left) Simultaneous optical and electrophysiological recordings demonstrating that action potentials can be evoked and imaged using a single excitation spot (12 μm diameter, power density 0.02 $\text{mW } \mu\text{m}^{-2}$ (2.5 mW per cell), 15 ms strobed illumination at 5 Hz). (right) Zoom on simultaneous optical and electrophysiological recordings of one action potential. (c) All-optical in-situ characterisation of photo evoked action potentials. Error bars represent the standard error of recordings obtained for 33 cells. The probability of evoking and recording action potentials is plotted as a function of power density. Only cells in which at least one optically evoked action potential was detected are included. The latency of optically evoked action potentials is plotted as a function of power density. The average latency measured all-optically matches that obtained using electrophysiology (Supplementary Figure 20c). The action potential probability is plotted as a function of stimulation frequency. Action potential probability is calculated as the number of action potentials evoked and recorded over five trials (power density: 0.01 – 0.09 $\text{mW } \mu\text{m}^{-2}$, 1.5 – 10 mW per cell). Error bars represent the standard error of recordings obtained for 33 cells. (d) Raster plot of 27 cells showing the number and timing of optically evoked action potentials (black) relative to the imaging/photostimulation epoch (red) (power density: 0.02 – 0.08 $\text{mW } \mu\text{m}^{-2}$, 2.5 – 9 mW per cell). (e) Examples of fluorescence recordings of optically evoked action potentials for three representative cells. Individual trials are plotted in grey. The average trace across all trials is plotted in red (power density: 0.02 – 0.08 $\text{mW } \mu\text{m}^{-2}$, 2.5 – 9 mW per cell). (f) Summary statistics for the amplitude ($-\% \Delta F/F_0$) and width of the optically evoked action potentials from (d). All data were acquired using laser C fixed at 940 nm and camera A (See Supplementary Figure 1 and Supplementary Tables 1 and 2).

Next, we extended the unique capability of our approach of scanless two-photon voltage imaging to perform simultaneous two-photon photostimulation and imaging of multiple cells (Figure 8). In each experimental session, we first sequentially targeted cells that were expressing one or both constructs to quantify the probability of false positives (Figure 8a-c). We detected an increase in fluorescence when targeting cells only expressing ChroME-ST, due to excitation and detection of the nuclear-targeted fluorophore. No action potentials were identified in cells that were not co-expressing the two constructs but were detected optically in approximately fifty percent of co-expressing cells. We then simultaneously stimulated and imaged the same group of cells (Figure 8d) with no deterioration of SNR or $-\% \Delta F/F_0$ of evoked and imaged action potentials (Figure 8d) and were able to determine the number and timing of action potentials evoked, and identify failures, during the stimulation period in multiple cells simultaneously (Figure 8e).

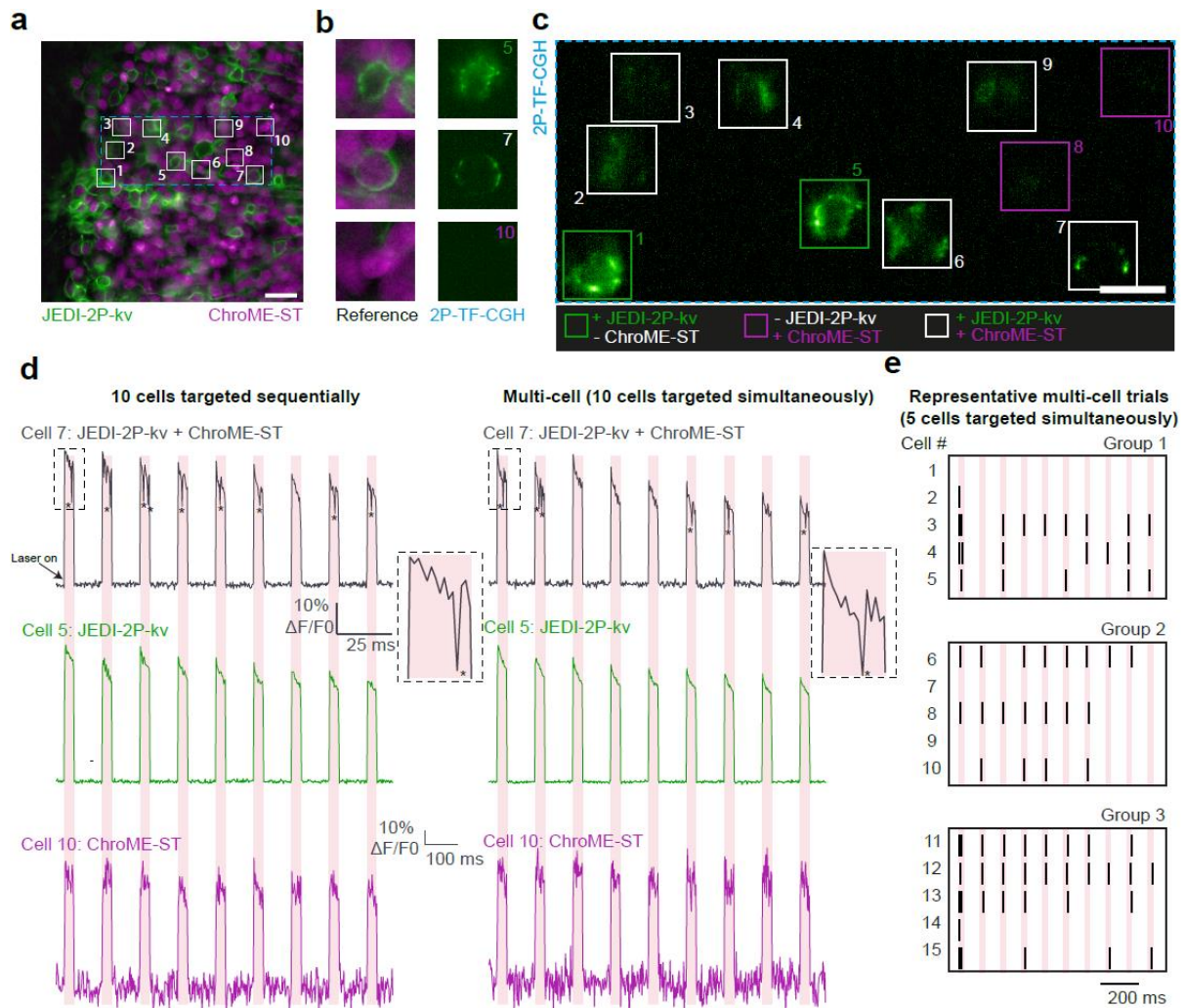


Figure 8. Characterisation of simultaneous multi-target photostimulation and voltage imaging using a single beam scanless two-photon excitation. (a) Cross-sections of hippocampal organotypic slices co-expressing JEDI-2P-kv and ChroME-ST in the dentate gyrus. The boxes indicate cells that were targeted simultaneously during a representative experiment (as numbered). Scale bar represents 25 μ m. **(b)** Reference widefield images of individual targeted cells (left) and corresponding images obtained using 2P-TF-CGH. Upper: a cell exclusively expressing JEDI-2P-kv. Middle: a cell co-expressing JEDI-2P-kv and ChroME-ST. Lower: a cell exclusively expressing ChroME-ST. **(c)** Data acquired when the 10 cells identified in (a) were targeted simultaneously using 2P-TF-CGH and imaged at 500 Hz. Scale bar represents 15 μ m. **(d)** Traces from the three cells highlighted in (b) when targeted sequentially (left) or simultaneously (right). Of the three selected cells, as expected, no action potentials were detected for cell 5 (green) or cell 10 (purple), which did not co-express the two constructs. In both the sequential and multi-cell acquisitions, action potentials were only evoked/recorded in the cells co-expressing JEDI-2P-kv and ChroME-ST (black). **(e)** Raster plots from 3 further experiments in which 5 cells were targeted simultaneously. Black lines indicate the time at which a cell fired; the red lines indicate the imaging/photostimulation laser. All data were acquired using laser C fixed at 940 nm and camera A (See Supplementary Figure 1 and Supplementary Tables 1 and 2).

These results demonstrate that simultaneous, scanless two-photon voltage imaging and photostimulation can be performed in multiple cells simultaneously using high-energy, low-repetition rate lasers, using powers well-below the damage threshold.

Discussion

In this work, we introduced scanless two-photon voltage imaging and performed high-contrast, high-resolution voltage imaging of single and multiple neurons expressing the newly developed GEVI JEDI-2P-kv. Due to the axial confinement conferred by temporal focusing we were able to perform high-contrast two-photon voltage imaging in densely labelled intact brain slices.

We performed a thorough characterisation of three, temporally focused, parallel excitation modalities (2P-TF-Gaussian, 2P-TF-GPC and 2P-TF-CGH) for scanless two-photon voltage imaging. A strong advantage of 2P-TF-Gaussian illumination (similarly to 3D-SHOT) is that it is the easiest and most cost-effective approach to implement. 2P-TF-Gaussian beams have been used for volumetric Calcium imaging^{58,59}. However, it is the least photon-efficient approach. Conversely, the photon-dense speckle grains in 2P-TF-CGH spots result in efficient two-photon excitation and hence the highest SNR. In the case of limited power budget, 2P-TF-CGH is thus the optimal modality for scanless multitarget voltage imaging. However, since we observed higher photorecovery with 2P-TF-GPC and 2P-TF-Gaussian, these modalities are preferred for prolonged (continuous illumination for hundreds of milliseconds or more) recordings such as imaging spontaneous activity. Looking ahead, one of the primary advantages of 2P-TF-GPC is the capability of sculpting well-defined lateral shapes³⁶ in order to target the most responsive regions of the cell membrane. In contrast with existing two-photon voltage imaging approaches, the high lateral resolution (0.1625 μm pixel size) of the experimental system presented in this manuscript would also be capable of sculpted, scanless two-photon voltage imaging of thin subcellular processes.

We used 2P-TF-GPC to demonstrate many of the theorized advantages of imaging neural activity with GEVIs by imaging action potentials (single-trial), subthreshold depolarizations and resolving single action potentials in high-frequency spike trains up to 125 Hz. We performed simultaneous imaging and electrophysiology to comprehensively characterize the performance of, and optimize, scanless two-photon voltage imaging with the genetically encoded indicator JEDI-2P-kv. Consistent with previous reports³⁰, we found that it was generally possible to reduce the imaging speed down to 500 Hz (and consequently the required power) without a critical loss in the ability to determine the number and timing of action potentials. However, these imaging speeds reduce the accuracy of action potential detection for spike trains with frequencies > 100 Hz. The optimal imaging conditions will also depend on the characteristics of the specific GEVI used. In principle, a major advantage of voltage versus calcium imaging in neuroscience is the ability to detect sub-threshold changes in somatic membrane potential. In our current configuration, we found that imaging small sub-threshold signals required averaging data from up to 25 individual trials to reach a SNR above 1 for depolarizations larger than 0.5 mV. Whilst these findings highlight the challenges of detecting subthreshold unitary PSPs (< 2.5 mV) *in vivo* with current state-of-the-art GEVIs under two-photon excitation, they also indicate that such experiments ought to be possible using GEVIs optimized for sub-threshold voltage detection.

Since the current implementation of scanless two-photon voltage imaging requires continuous illumination, we carefully investigated whether the illumination conditions required to observe different aspects of neural activity induced any observable physiological perturbations. We found that single cells

could be imaged using 100 fs, 80 MHz sources, at lower average powers than those commonly used for existing kilohertz scanning microscopes applied to two-photon voltage imaging^{28,60,61} and did not observe any changes in AP properties at these powers. However, we found that the latency of electrically induced APs was increased slightly at all powers tested, and irreversible thermal damage was revealed with 2P-TF-CGH at the highest powers tested using immunohistochemistry. In contrast, Caspase-3 staining did not reveal any non-linear damage at the investigated powers. In fact, we found that one of the biggest impediments to long-term voltage imaging was sample drift, a problem we imagine will be significantly more severe for scanless two-photon imaging during future *in-vivo* experiments. To overcome this problem, we plan to use a tandem construct containing the voltage indicator and a nuclear targeted, spectrally shifted, fluorescent reporter in order to track the sample drift and to dynamically update the co-ordinates of the multiplexed spots. Use of such a construct would also allow segmentation of the field of view and automated estimation of neuron location, which also ought to increase the accuracy of spot position relative to the soma membrane.

We also demonstrated that scanless two-photon voltage imaging could be performed with a much lower effective repetition rate (250 kHz) than used with existing kilohertz scanning microscopes. Even with this low-repetition rate laser, fluorescence was excited with more than 50x the number of pulses per voxel than for the scanning approaches. As a result, scanless two-photon voltage imaging is much more robust to fluctuations in output laser power than the scanning approaches. We demonstrated AP detection in single trials using 15-30 times lower average power than required using the high-repetition rate laser. Under these conditions, we did not find any histological evidence of thermal stress or physiological perturbations with whole-cell patch clamp recordings. As demonstrated in the case of two-photon optogenetics⁵⁷, the major advantage of low-repetition rate lasers is that multiple targets can be illuminated simultaneously, whilst the average power delivered to the sample is kept below the thermal damage threshold, and much lower than the average powers used for existing kilohertz scanning microscopes. Specifically, in this work we were able to perform simultaneous two-photon voltage imaging of spontaneous activity in multiple neurons (up to 8) using a 100 fs, 250 kHz, 940 nm laser source (with between 200 - 600 mW exit power, corresponding to a maximum average power of 60 mW at the sample). In order to increase the number of target cells, it would be necessary to replace the laser source used in our experiments with a higher-power, low-repetition rate industrial light source such as existing Ytterbium-doped fibre lasers (1030 nm, > 10 W output power). In this work, we demonstrated that electrically evoked action potentials and spontaneous activity in hippocampal organotypic slices could be recorded by exciting JEDI-2P-kv at 1030 nm. Based on the results presented in this manuscript, with a 1030 nm Ytterbium-doped fibre source it would be feasible to record the voltage of 40 cells simultaneously (5 mW per cell) using the existing configuration for scanless two-photon voltage imaging, whilst remaining below the damage threshold (200 mW total average power).

The use of an SLM for holographic light multiplexing of the temporally focused, sculpted light resulted in a nominal FOV of 250 x 250 μm^2 . However, the effective FOV used for individual high-speed voltage imaging recordings was reduced in one dimension due to the maximum number of rows of pixels that could be read out at a given acquisition rate. We demonstrated that it was possible to perform voltage

imaging throughout the $250 \times 250 \mu\text{m}^2$ area and to combine data in post-processing, although this was not optimized on our prototype system, and increasing the lateral field of view is one of the most urgent future avenues of development. The field of view of scanless two-photon voltage imaging could be trivially increased by reducing the magnification of the detection axis, although this would not be suitable for all experiments. Furthermore, the sCMOS could be replaced with a detector capable of higher (full frame) readout speeds. A primary motivation behind the development of holographic light multiplexing was to enable multitarget photostimulation at axially distinct planes^{43,62,63}. Although our system is also capable of targeting neurons in three-dimensions, we can currently only perform high-contrast imaging of a single plane. Performing scanless activity recordings from multiple planes simultaneously would require increasing the depth of field of the detection axis. For a very small number of discrete planes, this would be feasible using existing approaches, such as remote focusing^{64,65}. More generally, camera-based volumetric voltage imaging will require the implementation of computational imaging approaches, such as variants of light-field microscopy, which have already been applied to imaging in scattering tissue⁶⁶.

All experiments in this study were performed at relatively superficial depths ($<50 \mu\text{m}$) in scattering tissue where the expression pattern of JEDI-2P-kv was confined due to the approach used for viral delivery (bulk transduction). The next step will be to monitor the membrane potential of multiple neurons simultaneously *in-vivo*. It has already been demonstrated that temporal focusing preserves the profile and axial confinement of sculpted light up to $500 \mu\text{m}$ in scattering tissue for the three excitation modalities used in this work^{38,45}, and camera detection has also been used to perform functional imaging with multi-spot excitation at depths up to $300 \mu\text{m}$ *in-vivo*^{67,68}. Hence it ought to be possible to perform scanless two-photon voltage imaging in the upper cortical layer. Reaching deeper brain structures could be achieved by combining camera detection with excitation through graded index lenses (GRIN) lenses^{69,70} or via emerging computation approaches capable of overcoming scattering-induced ambiguity and of de-mixing the fluorescent transients emanating from different sources⁷¹.

We combined two-photon voltage imaging and optogenetics for the first time in proof-of-principle all-optical neurophysiology experiments. We capitalized on the overlapping excitation spectra of JEDI-2P-kv and the channelrhodopsin Chrome-ST to simultaneously evoke and record APs using a single beam. This approach could be incorporated into all-optical experiments to dynamically tune the incident power necessary for photostimulation and obtain the desired actuation on each of the targeted neurons *in situ*. In contrast to approaches relying on inferring neural activity from GCaMP fluorescence⁷², we demonstrated that voltage imaging provides a direct readout of the precise number and timing of optically-evoked action potentials with single spike precision at high spiking rates. The single beam approach to optically induce and read out neuronal activity will also be a major addition in connectivity mapping to non-invasively confirm the successful optical induction of an action potential in the potential pre-synaptic cell population. We demonstrated that scanless two-photon imaging can be performed with any of the existing modalities used for parallel two-photon photostimulation. As seen in our all-optical recordings (Figure 7d), the excitability of the targeted cells can vary between cells and over time, advising a confirmation of the pre-synaptic spike in each instance. In contrast to current connectivity

mapping approaches, which do not confirm pre-synaptic spiking⁷³ or use GECIs⁷², an approach using a voltage indicator would additionally reveal the precise timing of the pre-synaptic spike, which would facilitate correlation of the post-synaptic response and discrimination from noise. We anticipate that improved stoichiometric co-expression of the GEVI and the channelrhodopsin, possibly using a fusion-construct for tandem expression where they are covalently coupled, would facilitate the adoption of this approach.

The development of spectrally orthogonal voltage indicators and excitatory channelrhodopsins would facilitate the next-generation all-optical neurophysiology experiments. For example, it would be possible to record sensory-evoked activity patterns using voltage imaging, replay this activity using optogenetic stimulation and, also tune the excitation parameters in order to explore the logic and syntax of neural computation. Furthermore, this configuration would enable all-optical connectivity experiments whereby putative presynaptic neurons are stimulated optogenetically and sub-threshold post-synaptic responses are recorded optically. However, performing crosstalk-free all-optical neurophysiology experiments based on two-photon excitation is not trivial since the majority of two-photon compatible voltage indicators are optimally excited between 920 and 980 nm, a region of the electromagnetic spectrum where all commonly used channelrhodopsin variants are persistently activated⁷⁴. While all-optical experiments with calcium indicators have been reported, similar results with GEVIs are more challenging due to the higher average powers required for high-SNR millisecond-timescale voltage imaging. The development of performant red-shifted genetically encoded voltage indicators, which could be combined with spectrally orthogonal blue-shifted channelrhodopsins, will remove these remaining challenges and fill an important gap in the optogenetic toolbox.

We anticipate that the description and thorough characterisation of scanless two-photon voltage imaging presented in this manuscript will motivate its application to deciphering the logic and syntax of neural circuits.

Methods

Experimental setup for performing two-photon voltage imaging with temporally focused, sculpted light

All two-photon voltage imaging presented in this manuscript was performed using the experimental setup presented in Supplementary Figure 1. In the schematic diagram, all reflective spatial light modulators (SLMs) are shown as transmissive for illustrative purposes. Path 1 was used to generate temporally focused, multiplexed, GPC (12 μm FWHM, 2PE) or low NA, apertured, Gaussian beams (12 μm FWHM, 2PE) respectively (upper path, Supplementary Figure 1). Path 2 (lower path, Supplementary Figure 1) was used to generate temporally focused holographic disks (12 μm FWHM, 2PE). Three different laser sources were used to acquire all data presented, referred to as Lasers A, B and C respectively throughout the manuscript. The specific source used to acquire each dataset is specified in each case and all experimental configurations used to acquire the data presented in each figure are summarised in Supplementary Tables 1 and 2. Laser A refers to a tuneable femtosecond source (Coherent Discovery, 80 MHz, 100 fs) tuned to 920, 940 or 1030 nm (as specified). Laser B refers to a femtosecond source with a fixed wavelength output (Spark Alcor, 4 W, 80 MHz, 100 fs,

920 nm). Laser C refers to a custom OPA pumped by an amplified laser, also with fixed wavelength output (Amplitude Satsuma Niji, 0.2 - 0.6 W, 250 kHz, 100 fs, 940 nm). By virtue of the removable mirrors indicated in Supplementary Figure 1, light from each of the lasers could be directed through path 1 or path 2 during a given experiment as indicated by the dashed lines in Supplementary Figure 1. In all cases, the average laser power at the sample plane was controlled using a half-wave plate (Thorlabs, WPHSM05-980) mounted on a motorised rotation mount (Thorlabs, PRM1Z8) in combination with a polarising beam splitter (PBS), (Thorlabs, CCM1-PBS253/M). Prior to each experiment, the efficiency of each path was measured. The power at the sample plane was recorded using a handheld power meter (Thorlabs, S121C) and the power of the s-polarised light exiting the PBS at each laser output was measured with a second power meter (Ophir, 30(150) A-BB-18, Nova II). The power of the s-polarised beam was monitored continuously during experiments and used to update the rotation of the half-wave plate to deliver the desired power at the sample plane during a given acquisition (calculated using the experimentally measured efficiency of each path). All half-wave plates were externally triggered prior to each acquisition. The output of lasers A and B was modulated by a mechanical shutter (Thorlabs, SH05R/M) or using a high-speed modulator (Thorlabs, OM6NH/M) whereas the output of laser C was gated directly. In all cases the external trigger was a TTL signal generated by pCLAMP (Molecular Devices, Sunnyvale, CA) controlling an acquisition system (Molecular Devices, Axon Digidata 1550B).

In path 1, a telescope formed of two lenses (L1, $f = 80$ mm, (Thorlabs, AC508-80-B) and L2, $f = 300$ mm, (Thorlabs, AC508-300-B), for GPC and L1, $f = 80$ mm, (Thorlabs, AC508-80-B) and L2, $f = 200$ mm, (Thorlabs, AC508-200-B) for low-NA Gaussian illumination) was used to expand and project the beam onto a spatial light modulator (SLM1), (Hamamatsu, LCOS 10468-07, 600×800 pixels, $20 \mu\text{m}$ pitch). In the case of GPC, SLM1 was used to apply a π phase shift to the portion of the beam overlapping with the circular spot and a phase shift of zero elsewhere. The modulated beam was Fourier transformed by L3, $f = 400$ mm, (Thorlabs, AC508-400-B), resulting in a spatial displacement between the low and high spatial frequency components of the field in the Fourier plane. The low spatial frequency components were selectively phase shifted by π using a phase contrast filter (PCF) with $60 \mu\text{m}$ radius (Double Helix Optics, custom design) positioned in the Fourier plane of L3. The spatial frequencies were recombined in the image plane by L4, $f = 300$ mm, (Thorlabs, AC508-300-B). For more details, refer to³⁶. For parallel two-photon excitation using a low NA Gaussian beam, the corrective phase mask provided by the manufacturer was displayed on SLM1 and the PCF was displaced from the optical path as indicated in Figure 1. A blazed diffraction grating (Richardson Gratings, 600 lines/mm) located at the focal plane of L4, a conjugate image plane, disperses the different spectral frequency components of the ultrafast beam as required for temporal focusing. The grating was oriented at the blaze angle to maximize light throughput. The dispersed beam was collimated in one direction and Fourier transformed in the orthogonal direction by L5, $f = 500$ mm, (Thorlabs, AC508-500-B), resulting in an asymmetric “line” illumination of SLM2 (Hamamatsu, LCOS 10468-07, 600×800 pixels, $20 \mu\text{m}$ pitch), as described previously⁶³. For this work, SLM2 was used for 2-dimensional multiplexing of the beam, although 3-dimensional multiplexing would be possible. Phase masks were generated using a weighted Gerchberg-Saxton algorithm as described previously^{48,75}. For all data presented in

Figures 1, 2 and 3, SLM2 was used to displace the sculpted light from the optical axis and the zeroth-diffraction order, which was removed using a physical beam block positioned in a conjugate image plane. Lenses 6 ($f = 500$ mm, (Thorlabs, AC508-500-B)) and 7 ($f = 300$ mm, (Thorlabs, AC508-300-B)) were used to de-magnify the beam to the back focal plane of the objective lens (Nikon, CFI APO NIR, x40, 0.8 NA, $f = 5$ mm) which projected the light (and re-combined the different spectral frequency components) onto the focal plane. A half-wave plate was included downstream of SLM2 in path 1 to convert s-polarised light to p-polarised.

In path 2, a Galilean beam expander formed of two lenses (L8, $f = -75$ mm, (Thorlabs, LC1258-B) and L9, $f = 500$ mm, (Thorlabs, AC508-500-B)), expanded the beam onto SLM3, (Hamamatsu, LCOS X13138-07, 1272×1024 pixels, $12.5 \mu\text{m}$ pitch). For the single cell experiments, 5 holograms designed to generate a single $12 \mu\text{m}$ holographic spot (located in the same position) were computed prior to each session. For each recording, one of these phase masks was randomly selected and displayed on the SLM in order to minimize any effects of the variable speckle distribution on the resulting dataset. The holograms displayed on SLM3 were designed to generate multiple $12 \mu\text{m}$ holographic spots targeted to chosen neurons throughout the field of excitation following the calibration procedure outlined in the Supplementary Information. All holograms were calculated using an iterative Gerchberg-Saxton algorithm⁷⁶. The zeroth diffraction order was removed using a physical beam block positioned in a conjugate image plane. The modulated beam was Fourier transformed by L10 ($f = 750$ mm, (Thorlabs, AC508-750-B)), to form the holographic disks in a conjugate image plane where a blazed grating (Thorlabs, GR50-0610, 600 lines/mm) was located. A 2" diffraction grating was used to maximise the field of excitation. The diffraction grating was oriented perpendicular to the optical axis and the illumination angle was chosen such that the first diffraction order of the central wavelength propagated along the optical axis. This orientation did not coincide with the blaze angle, and hence was not the most efficient²³ but was allowed the temporal focusing plane of each of the holographic disks to coincide with the focal plane of the objective lens. A pair of telescopes comprised of L11 ($f = 500$ mm, (Thorlabs, AC508-500-B)), L12 ($f = 300$ mm, (Thorlabs, AC508-300-B)), L7 ($f = 300$ mm, (Thorlabs, AC508-300-B)) and the objective lens (Nikon, CFI APO NIR, x40, 0.8 NA, $f = 5$ mm, water) was used to de-magnify and relay the holographic spots on to the sample plane. In experiments where non-temporally focused spots were used (1030 nm excitation), the diffraction grating was replaced by a mirror.

Excitation paths 1 and 2 were combined prior to the tube lens (L7) using a polarising beam splitter (Thorlabs, PBS253). The linear polarisation of the light exiting the objective was changed using a half-wave plate following the PBS. For each modality, the rotation of the half-wave plate was set to that which was found to maximise the two-photon excited JEDI-2P-kv fluorescence.

SLM1 was also used to optimise the alignment of the GPC path by translating the position of the π phase disk relative to the centre of the incident Gaussian beam and adding tip/tilt/defocus phases to translate the position of the focus with respect to the PCF filter. SLMs 1, 2 and 3 were also used to correct for system aberrations by adjusting the coefficients of Zernike modes (evaluated at the centre of each SLM pixel) in order to maximise the efficiency, uniformity and contrast of two-photon excited fluorescence excited in a thin rhodamine layer.

In all experiments, fluorescence was captured using a simple widefield detection axis comprised of a microscope objective (Nikon, CFI APO NIR, x40, 0.8 NA, f = 5 mm, water), a tube lens (TL), (Thorlabs, TTL200-A) and a scientific complementary metal-oxide semiconductor (sCMOS) camera (Hamamatsu ORCAFlash 4.0 or Photometrics Kinetix, as summarised in Supplementary Table 1). For both sCMOS detectors, the pixel size at the sample plane was 0.1625 μm and 1x1 binning was used for all experiments. The fluorescence was separated from the excitation light using a dichroic mirror (Semrock #FF705-Di01, 70 x 50 mm). Widefield, single photon, epi-fluorescence excitation was accomplished by means of two LED sources (Thorlabs M490L4, 490 nm to excite JEDI-2P-kv fluorescence and Thorlabs M430L5, 430 nm to excite BFP fluorescence), filtered by bandpass excitation filters (Semrock FF02-482/18, FF01-414/46) and focused onto the back focal plane of the objective lens by means of an achromatic lens (Thorlabs f = 50 mm). Long exposure times (1s) and low excitation power densities were used to acquire all images based on single photon fluorescence. For single photon or dual-colour imaging (for instance during all-optical experiments), fluorescence was filtered using either a quad-band filter (Chroma ZET405/488/561/640) or individual bandpass filters (Chroma ET525/50, ET605/7). Infrared light used for two-photon excitation of fluorescence was blocked from the camera using a shortpass filter (Semrock #FF01-750sp).

Data were acquired using a control scheme based on custom scripts written to control *micro-manager 2.0 Gamma*⁷⁷ from Python via *Pycro-manager*⁷⁸. All experiments were controlled using two desktop computers running Windows 10. During voltage imaging experiments, the micro-manager acquisition engine was bypassed. Data from the camera was streamed directly to disk on one of the acquisition computers. The first step of any experiment was to acquire 2 (JEDI-2P-kv and transmitted light) or 3 (JEDI-2P-kv, ChromE-ST (H2B-BFP2) and transmitted light) widefield images of the sample. These images were used to select targeted cells during a given experiment. The centroids of all targeted cells were written to file for all experiments. All widefield images presented in this text are background subtracted for visualization purposes (rolling ball background subtraction, ImageJ, rolling ball radius 50 pixels). All the voltage imaging data presented in this manuscript were acquired in “dynamic range”, 16-bit mode, which meant that a maximum of 266 rows of pixels could be acquired at 1 kHz (43 x 250 μm^2 FOV). In practice we used an exposure time of 1 ms resulting in an effective acquisition rate of 980 Hz following 0.02 ms readout (similarly for the recordings referred to as 500 and 750 Hz in the manuscript). For single cell experiments (corresponding to data presented in Figures 2-5), data were only acquired for a square region with diameter less than 266 pixels centred on a given cell. For the multi-cell experiments, neurons were grouped to find the maximal number which could be imaged within 266 pixels. The relative centroids of all targeted cells within this cropped region, and the upper left-hand coordinate of each cropped region were written to file for all experiments. These coordinates were used to “stitch” data from sequential acquisitions into a single dataset. In “dynamic range” mode, the field of view is inversely proportional to the exposure time, such that we could acquire data from 532 rows (86 x 250 μm^2 FOV) at 500 Hz. The field of view could be increased by a factor of 6 using “speed” mode, where data is read out at 8-bit. The camera was triggered using a 5 V, TTL signal generated by pCLAMP (Molecular Devices, Sunnyvale, CA) controlling an acquisition system (Molecular Devices, Axon

Digidata 1550B). During experiments, widefield images were visualised using the open-source image viewer Napari and voltage imaging traces were visualised using pyqtgraph.

All fluorescence traces were analysed using the same analysis pipeline written in Python, as outlined in the main text and Supplementary Information, derived from⁷⁹. When multiple cells were imaged simultaneously, the (known) centroid of the excitation spot in camera co-ordinates was used to crop a rectangular region of interest (ROI) surrounding each cell (generally 100 x 100 pixels). In rare cases where the ROIs of independent cells overlapped, a region of each independent cell was identified manually. Individual cells were then defined according by regression of each pixel in the ROI against the average fluorescence trace of the manually segmented pixels.

Preparation of CHO cells

CHO cells were acquired from Sigma (Sigma, 85050302) and cultured in T25 flasks (Falcon, 353107) in a medium consisting of DMEM-F12 + Glutamax (Fisher, Gibco™ 10565018), supplemented with 10% SBF (Fisher, Gibco™ 10500-064) and 1% penicillin/streptomycin (5000 U ml⁻¹). Cells were passaged every 2-3 days. Prior to each experiment, cells were seeded on coverslips (Fisher, 10252961) in 24-well plates (50 000 cells/ml). After 24 hours, cells were transiently transfected with a plasmid using the Jet prime kit (Ozyme, POL101000015) (Table 1). The medium was then replaced after 4 hours. Experiments were performed 48 hours post transfection.

Table 1: List of plasmids

Plasmid	Transfection ratio
pAAV_hSyn_JEDI-2P_GSS3_Kv2.1	0.75 µg DNA: 1.5 µl transfectant
pAAV_CamKIIa_ChRoME-ST_P2A_H2B_BFP	0.75 µg DNA: 1.5 µl transfectant

Electrophysiology for scanless two-photon voltage imaging in CHO cells

48 hours post transfection, whole-cell voltage clamp recordings of JEDI-2P-kv-expressing CHO cells were performed at room temperature (21 - 23°C). An upright microscope (Scientifica, SliceScope) was equipped with a far-red LED (Thorlabs, M660L4), oblique condenser, microscope objective (Nikon, CFI APO NIR, 40X, 0.8 NA), tube lens (Thorlabs, TTL200-A), and an sCMOS camera (Photometrics, Kinetix, or Hamamatsu, Flash4.0) to collect light transmitted through the sample. Patch clamp recordings were performed using an amplifier (Molecular Devices, Multiclamp 700B), a digitizer (Molecular Devices, Digidata 1550B) at a sampling rate of 10 kHz and controlled using pCLAMP11 (Molecular Devices). Cells were continuously perfused with artificial cerebrospinal fluid (ACSF) comprised of 125 mM NaCl, 2.5 mM KCl, 1.5 mM CaCl₂, 1 mM MgCl₂, 26 mM NaHCO₃, 0.3 mM ascorbic acid, 25 mM D-glucose, 1.25 mM NaH₂PO₄. Continuous aeration of the recording solution with 95% O₂ and 5% CO₂, resulted in a final pH of 7.4 (measured). Borosilicate pipettes (with filament, OD: 1.5 mm, ID: 0.86 mm, 10 cm length, fire polished, WPI) were pulled using a Sutter Instruments P1000 puller, to a tip resistance of 3.5–6 MΩ. Pipettes were filled with an intracellular solution consisting of 135 mM K-

gluconate, 4 mM KCl, 4 mM Mg-ATP, 0.3 mM Na₂-GTP, 10 mM Na₂-phosphocreatine, and 10 mM HEPES (pH 7.35). All membrane potentials reported in this manuscript are Liquid Junction Potential (LJP) corrected by -15 mV (measured). Recordings were compensated for capacitance (C_m) and series resistance (R_s) to 70 % (C_m = 11.6 ± 4.7 pF; R_s = 16.1 ± 8.2 MΩ; mean ± s.d.). Only recordings with an access resistance below 35 MΩ were included in subsequent analysis.

All experiments were performed with laser A, except data presented in Supplementary Figure 20 where laser C was used.

For protocols 1 and 2 (Figure 2), JEDI-2P-kv-expressing CHO cells were patched and clamped at -55 mV and 3, 100 mV steps were applied under either continuous (3 s, power density: 0.88 mW μm⁻², corresponding to 100 mW per cell) or strobed illumination (200 ms every 2.5 s, power densities ranging from 0.66 to 1.55 mW μm⁻² (75 to 175 mW per cell), as specified in the main text). The fluorescent responses to the depolarization steps were simultaneously recorded at 100 Hz. For protocol 3, JEDI-2P-kv-expressing CHO cells were patched and clamped at -75 mV to mimic the resting potential of neurons in the dentate gyrus of hippocampal organotypic slices. A 20 Hz train of 10, 3 ms, 100 mV steps was electrically induced, and the fluorescent response to different scanless illumination methods was recorded simultaneously (500 ms, power density: 1.33 mW μm⁻², corresponding to 150 mW per cell, 1 kHz acquisition).

The ability to record voltage responses using JEDI-2P-kv under 1030 nm illumination was assessed using protocol 2 with a holographic spot (12 μm diameter, not temporally focused, power density: 0.4 mW μm⁻², corresponding to 45 mW per cell, Supplementary Figure 19).

For data presented in Supplementary Figure 20, ChroME-ST expressing cells were patched in whole cell voltage clamp configuration at -55 mV and photocurrents in response to 17.5 ms pulses of light (power densities ranging from 0.02 to 0.04 mW μm⁻², corresponding to 2.5 to 5 mW per cell) were recorded.

Preparation of hippocampal organotypic slice cultures for validating scanless two-photon voltage imaging of neuronal activity using JEDI-2P-kv

All experimental procedures were conducted in accordance with guidelines from the European Union and institutional guidelines on the care and use of laboratory animals (Council Directive 2010/63/EU of the European Union). Hippocampal organotypic slices were prepared from mice (Janvier Labs, C57Bl6J) at postnatal day 8 (P8). Hippocampi were sliced with a tissue Chopper (McIlwain type 10180, Ted Pella) into 300 μm thick sections in a cold dissecting medium consisting of GBSS (Sigma, G9779) supplemented with 25 mM D-glucose, 10 mM HEPES, 1 mM Na-Pyruvate, 0.5 mM α-tocopherol, 20 nM ascorbic acid, and 0.4% penicillin/streptomycin (5000 U ml⁻¹).

After 30 - 45 min of incubation at 4 °C in the dissecting medium, slices were placed onto a porous membrane (Millipore, Millicell CM PICM03050) and cultured at 37 °C, 5% CO₂ in a medium consisting of 50% Opti-MEM (Fisher 15392402), 25% heat-inactivated horse serum (Fisher 10368902), 24%

HBSS, and 1% penicillin/streptomycin (5000 U ml⁻¹). This medium was supplemented with 25 mM D-glucose, 1 mM Na-Pyruvate, 20 nM ascorbic acid, and 0.5 mM α -tocopherol. After three days in-vitro (DIV), the medium was replaced with one containing 82% neurobasal-A (Fisher 11570426), 15% heat-inactivated horse serum (Fisher 11570426), 2% B27 supplement (Fisher, 11530536), 1% penicillin/streptomycin (5000 U ml⁻¹), which was supplemented with 0.8 mM L-glutamine, 0.8 mM Na-Pyruvate, 10 nM ascorbic acid and 0.5 mM α -tocopherol. This medium was removed and replaced once every 2-3 days.

Slices were transduced with AAV9_hSyn_JEDI-2P_Kv2.1 at DIV 3 by bulk application of 1 μ l of virus per slice (see Table 2). Experiments were performed between DIV 7 and 15.

Electrophysiology for validating scanless two-photon voltage imaging of neuronal activity using JEDI-2P-kv in hippocampal organotypic slices

At DIV 10-15, whole-cell patch clamp recordings of JEDI-2P-kv expressing granule cells in DG were performed at temperatures varying between 31-35°C. During experiments, slices were perfused with ACSF as previously described. This extracellular solution was supplemented with 1 μ M AP5 (Abcam, ab120003) and 1 μ M NBQX (Abcam, ab120046) in all experiments except for the spontaneous activity recordings (Figures 5-6, Supplementary Figures 14 and 18). Patch pipettes were filled with intracellular solution (see above).

Neurons were held at -75 mV in voltage clamp configuration and recordings were compensated for capacitance (C_m) and series resistance (R_s) to 70 % ($C_m = 21 \pm 6.3$ pF; $R_s = 19.2 \pm 8.5$ M Ω ; mean \pm s.d.). In current clamp configuration, neurons were injected with some current (less than 100 pA) if necessary to maintain their resting membrane potential to -75 mV. In the latter configuration, bridge potential was corrected (Bridge potential = 13.9 ± 4.2 M Ω ; mean \pm s.d.).

Neurons were first patched in whole-cell voltage clamp configuration. Protocol 1 was then performed to confirm that the fluorescence of the patched cell was voltage responsive (Supplementary Figure 12).

The ability to record single action potentials in neurons (Figure 3c and d) was assessed by electrically triggering a 1 Hz train of 50 action potentials with short latency and jitter under strobed illumination (10 ms, power densities ranging from 0.66 to 1.55 mW μ m⁻², corresponding to 75 to 175 mW per cell) while recording at three different acquisition rates (500 Hz, 750 Hz and 1 kHz). Action potentials were triggered by injecting 700-900 pA currents for 2 ms.

Then, to assess the ability to record fast spike trains in neurons, trains of 10 action potentials from 25 to 125 Hz were electrically induced under illumination at different power densities (from 0.66 to 1.55 mW μ m⁻², corresponding to 75 to 175 mW per cell) and recorded at acquisition rates varying between 500 Hz, 750 Hz and 1 kHz. The amount of current injected was one that was sufficient to evoke 10 action potentials at each of the different spike trains. Recordings where one action potential was missing in the electrophysiological trace were dismissed. 125 Hz was found to be the limit at which the granule cells could spike in our conditions (Figure 3e-f and Supplementary Figure 13).

For data presented in Figure 4, 6, 20 ms steps separated by 30 ms and ranging from 0 to 2.5 mV (in 0.5 mV steps) were induced in JEDI-2P-kv expressing neurons under strobed illumination (40 ms centered around the steps, power density: $1.33 \text{ mW } \mu\text{m}^{-2}$, corresponding to 150 mW per cell) while recording the fluorescence response at 1 kHz. This was repeated 50 - 75 times.

To record spontaneous activity (Figure 5), JEDI-2P-kv expressing neurons were patched and their membrane potential was monitored under continuous illumination for 30 s at a power density of $1.33 \text{ mW } \mu\text{m}^{-2}$ (150 mW per cell) while recording the fluorescent response at 1 kHz. Cells were not patched for the recordings presented in Supplementary Figure 14. The same protocol was repeated to perform long-term voltage imaging of JEDI-2P-kv expressing neurons for a maximum of 20 min with a dark period of <10 s in between each recording (due to limitations in data transfer rates). To overcome this issue, we performed longer recordings (1 min) at a lower acquisition rate (500 Hz) with the same power density ($1.33 \text{ mW } \mu\text{m}^{-2}$, corresponding to 150 mW per cell). This allowed us to shorten the dark period in between recordings to < 5 s (Supplementary Figure 15).

The axial resolution of JEDI-2P-kv (Supplementary Figure 12) was measured by electrically triggering an action potential and measuring the fluorescence response while displacing the objective in the z axis (from +50 to -50 μm , in 5 μm steps). The lateral resolution was measured (from +20 to -20 μm , in 2 μm steps) by mechanically moving the sample in the x-y axis.

To measure the performances of JEDI-2P-kv under 1030 nm illumination, hippocampal organotypic slices were infected with a mixture of AAV1_EF1a_DIO_JEDI-2P_Kv2.1_WPRE and AAV9_hSyn_Cre_WPRE_hGH (see Table 2) at DIV 3 in order to get a sparser expression. Isolated expressing cells in the dentate gyrus were then patched in whole cell current clamp configuration and illuminated with a holographic spot (12 μm diameter, not temporally focused) at 1030 nm (power density: $1.21 \text{ mW } \mu\text{m}^{-2}$, corresponding to 137 mW per cell). Single action potentials and spontaneous activity recordings were obtained as described previously (Supplementary figure 19).

Preparation of hippocampal organotypic slices for two-photon actuation and imaging of neural activity using ChroME-ST and JEDI-2P-kv

All animal procedures followed national and European animal care guidelines (Directive 2010/63/EU) and institutional guidelines on animals used for research purposes. Hippocampal organotypic slice preparations were prepared as described in reference⁸⁰ with a few modifications. Briefly, hippocampi were extracted from P5-P8 C56Bl/6J mouse pups sacrificed by decapitation. The dissection was carried out in filter sterilized (0.2 μm pore size) ice cold medium containing: 248 mM sucrose, 26 mM NaHCO_3 , 10 mM glucose, 4 mM KCl, 5 mM MgCl_2 , 1 mM CaCl_2 , 2 mM kynurenic acid and 0.001 % phenol red saturated with 95 % O_2 / 5 % CO_2 . Transverse slices of 300 – 400 μm thickness were cut with Mcllwain Tissue Chopper using double edge stainless steel razor blades. Using a plastic transfer pipette, undamaged slices were individually transferred onto the small pieces of PTFE membrane (Millipore FHL04700) placed on membrane inserts (Millicell PICM0RG50) in the 6-well-plate containing 1 mL pre-warmed culture medium. The slices were cultured at 37 °C and 5 % CO_2 in antibiotic free culture

medium consisting of 80 % MEM and 20 % Heat-inactivated horse serum supplemented with 1 mM L-glutamine, 0.01 mg/ml Insulin, 14.5 mM NaCl, 2 mM MgSO₄, 1.44 mM CaCl₂, 0.00125 % Ascorbic acid and 13mM D-glucose. The culture medium was partially replaced with fresh, 37 °C warmed culture medium every 3 days.

Various titrations were tested to achieve sufficient levels of expression of both sensor and actuator. When slices were transduced with both viruses on the same day, we observed a reduction in the expression of JEDI-2P-kv. Furthermore, overexpression-mediated apoptosis was observed in some cases when slices were transduced with both viruses simultaneously. The best results were obtained by transducing slices with JEDI-2P-kv first, followed a week later by ChroME-ST which resulted in strong co-expression of both proteins (Figure 8a). However, in general we found that the expression levels of both proteins were more variable when the two constructs were co-expressed than when either construct was expressed independently.

Slices were transduced firstly with AAV9-hSyn-JEDI-2P-Kv2.1 at DIV 3 and secondly with AAV9_Camk2a_ChroME-ST_P2A_H2B_tagBFP2 (provided by H. Adesnik, University of California, Berkeley, USA) at DIV 10 by bulk application of 1 µl of virus per slice (Table 2). Channelrhodopsin-expressing cells were visualized using stable expression of an H2B–BFP2 fusion, which resulted in nuclear localized BFP2 fluorescence. Experiments were performed between DIV 13 and 17.

To characterize the performances of ChroME-ST (Figure 7), ChroME-ST and JEDI-2P-kv co-expressing granule cells in DG were patched in whole-cell current clamp configuration. 5, 17.5 ms pulses of light at 5 Hz were applied at different power densities ranging from 0 to 0.09 mW µm⁻² (0 to 10 mW per cell) to photo-evoked action potentials. The fluorescent responses were recorded at an acquisition rate of 1 kHz. The latency and jitter of light-evoked action potentials, respectively defined as the mean and standard deviation of the time between the onset of stimulation and the peak of the action potential, were measured using the same protocol. The axial resolution of ChroME-ST was measured using a similar protocol, while displacing the spot axially by mechanically moving the objective from +75 to -50 µm, in 5 µm steps in the vicinity of the cell (from +55 µm to -10 µm) and then in 10 µm steps (Figure 7 and Supplementary Figure 20).

For each cell, the power density was increased until a spike was detected optically in at least one of five repeats. The final set of power densities used was between 0.02 – 0.08 mW µm⁻² (2.5 – 9 mW) per cell.

Table 2: List and final titres of viruses

Virus	Final titer (vg ml ⁻¹)
AAV9_hSyn_JEDI-2P_GSS3_Kv2.1	3.12×10^{13}
AAV9_CamKIIa_ChRoME-ST_P2A_H2B_BFP	4.46×10^{12}
AAV1_EF1a_DIO_JEDI-2P_Kv2.1_WPRE	2.36×10^{13}
AAV9_hSyn_Cre_WPRE_hGH	2.3×10^{11}

Immunostaining

Immunostaining was performed on hippocampal organotypic slices to assess the potential non-linear photodamage induced by two different laser sources (A and C) during our experiments.

In the case of laser A, slices expressing JEDI-2P-kv were illuminated with a holographic spot (12 μ m diameter, temporally focused, power densities between 0.66 – 1.55 mW μ m⁻², corresponding to 75 – 175 mW per cell) in the dentate gyrus. The illumination protocol consisted of 50, 10 ms pulses of light, using the same protocol used to record single action potentials (see previous section), repeated on > 15 cells per region illuminated. A negative control (no illumination) and a positive control where a whole region was continuously illuminated for 30 min (power density: 1.64 mW μ m⁻², corresponding to 185 mW per cell) were also performed.

Slices expressing JEDI-2P-kv and ChroME-ST were illuminated with 5 holographic spots generated with laser source C (12 μ m diameter, power densities ranging between 0.02 – 0.09 mW μ m⁻² (2.5 – 10 mW per cell), 45 μ m separation), and moved laterally across 120 μ m in 20 μ m steps. The illumination protocol used to characterize the ChroME-ST (see previous section) was repeated 5 times at each position, and the hologram was recomputed each time.

After experiments, slices were immediately fixed in PFA 4% for 3-5 min. Permeabilization of the tissue was performed by incubation of the slice in a solution comprising of Triton X-100 in PBS (0.5 %) for 12 hours at 4 °C. Non-specific sites were then blocked by incubation in a blocking solution (BSA 20 % in PBS) for 4 hours at room temperature (21-23 °C).

Slices were incubated with primary antibodies diluted in a solution of BSA 5 % in PBS (Table 3) overnight at 4 °C and placed in a solution of BSA 5 % in PBS on a horizontal shaker for 10 minutes to wash off excess antibodies. This process was repeated three times.

Slices were then incubated with species-appropriate secondary antibodies conjugated to Alexa fluor 555 (to detect anti-activated-Caspase-3 immunostaining) and Alexa fluor 647 (to detect anti-HSP70/72 immunostaining) diluted in the same solution as the primary ones, for 3-4 hours at room temperature (21-23 °C). They were then washed again following the same process, but in PBS only.

Slices were immediately mounted in Fluoromount-g mounting medium (Southern Biotech, 0100-01) to be imaged using confocal microscopy (Olympus FV3000, 20X magnification, 0.8 NA, pixel size 0.6214 μm , λ 488, 561, 640 nm). The same imaging parameters were used for all experimental conditions.

Table 3: List and dilutions of antibodies used for immunostaining

Antibody	Supplier	Reference	Species	Working dilution
HSP70 / HSP72	Enzo Life Science	ADI-SPA-810-D	Mouse	1:400
Cleaved Caspase-3 (Asp175)	Cell Signaling	9661	Rabbit	1:250
Anti-mouse, Alexa fluor 647	Thermofisher Scientific	A21235	Goat	1:500
Anti-rabbit, Alexa fluor 555	Thermofisher Scientific	A21429	Goat	1:500

Statistics

All experiments were repeated for at least two (and generally many more) independent passages of cells, transfections or infections. The Shapiro test (`scipy.stats.shapiro`) was used to test whether data were normally distributed. For normally distributed data, the paired or unpaired two-tailed students t-test was used to compare two independent samples. The non-parametric Mann-Whitney *U*-test (`scipy.stats.mannwhitneyu`) was used to compare two samples in the case when either or both samples were found not to be normally distributed. 'n' refers to the number of independent biological replicates, as stated in each figure caption and summarized in Supplementary Table 2. A statistical comparison was deemed significant if the p-value was less than 0.05. For all figures * denotes $p < 0.05$, ** denotes $p < 0.01$ and *** denotes $p < 0.0001$. All results reported in the manuscript are communicated as the mean value \pm standard deviation of at least three technical replicates unless otherwise stated. As specified, error bars in plots denote either the standard deviation or the standard error. All biological replicates were included in each estimate. Estimation stats were performed using the Python package `dabestr`⁸¹.

References

- 1 Scanziani, M. & Hausser, M. Electrophysiology in the age of light. *Nature* **461**, 930–939 (2009).
- 2 Emiliani, V. *et al.* Optogenetics for light control of biological systems. *Nat. Rev. Methods Primer* **2**, 55 (2022)
- 3 Abdelfattah, A. *et al.* Neurophotonic Tools for Microscopic Measurements and Manipulation: Status Report. *Neurophotonics* **9**, 1–86 (2022).
- 4 Clapham, D. E. Calcium Signaling. *Cell* **131**, 1047–1058 (2007).
- 5 Grienberger, C. & Konnerth, A. Imaging Calcium in Neurons. *Neuron* **73**, 862–885 (2012).
- 6 Tsien, R. Y. New calcium indicators and buffers with high selectivity against magnesium and protons: design, synthesis, and properties of prototype structures. *Biochemistry* **19**, 2396–2404 (1980).
- 7 Tian, L., Andrew Hires, S. & Looger, L. L. Imaging neuronal activity with genetically encoded calcium indicators. *Cold Spring Harb. Protoc.* **7**, 647–656 (2012).
- 8 Chen, Y. *et al.* Soma-Targeted Imaging of Neural Circuits by Ribosome Tethering. *Neuron* **107**, 454–469.e6 (2020).

- 9 Shemesh, O. A. *et al.* Precision Calcium Imaging of Dense Neural Populations via a Cell-Body-Targeted Calcium Indicator. *Neuron* **107**, 470-486.e11 (2020).
- 10 Zhu, M. H., Jang, J., Milosevic, M. M. & Antic, S. D. Population imaging discrepancies between a genetically-encoded calcium indicator (GECI) versus a genetically-encoded voltage indicator (GEVI). *Sci. Rep.* **11**, 1–15 (2021).
- 11 Peterka, D. S., Takahashi, H. & Yuste, R. Imaging Voltage in Neurons. *Neuron* **69**, 9–21 (2011).
- 12 Davila, H. V, Salzberg, B. M., Cohen, L. B. & Waggoner, A. S. A Large Change in Axon Fluorescence that Provides a Promising Method for Measuring Membrane Potential. *Nature. New Biol.* **241**, 160–161 (1973).
- 13 Loew, L. M. *et al.* A naphthyl analog of the aminostyryl pyridinium class of potentiometric membrane dyes shows consistent sensitivity in a variety of tissue, cell, and model membrane preparations. *J. Membr. Biol.* **130**, 1–10 (1992).
- 14 Abdelfattah, A. S. *et al.* Bright and photostable chemigenetic indicators for extended in vivo voltage imaging. *Science* **365**, 699–704 (2019).
- 15 Knöpfel, T. & Song, C. Optical voltage imaging in neurons: moving from technology development to practical tool. *Nat. Rev. Neurosci.* **20**, 719–727 (2019).
- 16 Lu, X. *et al.* Detecting rapid pan-cortical voltage dynamics in vivo with a brighter and faster voltage indicator Authors. *bioRxiv* (2022) doi:10.1101/2022.08.29.505018.
- 17 Quicke, P. *et al.* Single-Neuron Level One-Photon Voltage Imaging With Sparsely Targeted Genetically Encoded Voltage Indicators. *Front. Cell. Neurosci.* **13**, 1–12 (2019).
- 18 Hochbaum, D. R. *et al.* All-optical electrophysiology in mammalian neurons using engineered microbial rhodopsins. *Nat. Methods* **11**, 825–833 (2014).
- 19 Parot, V. J. *et al.* Compressed Hadamard microscopy for high-speed optically sectioned neuronal activity recordings. *J. Phys. Appl. Phys.* **52**, (2019).
- 20 Fan, L. Z. *et al.* All-Optical Electrophysiology Reveals the Role of Lateral Inhibition in Sensory Processing in Cortical Layer 1. *Cell* **180**, 521-535.e18 (2020).
- 21 Xiao, S. *et al.* Large-scale voltage imaging in behaving mice using targeted illumination. *iScience* **24**, (2021).
- 22 Fisher, J. A. N., Salzberg, B. M. & Yodh, A. G. Near infrared two-photon excitation cross-sections of voltage-sensitive dyes. *J Neurosci Methods* **148**, 94–102 (2005).
- 23 Sims, R. R. *et al.* Optical manipulation and recording of neural activity with wavefront engineering. in *Neuromethods* (ed. Papagiakoumou, E.) vol. 191 (Humana Press New York, 2023).
- 24 Acker, C. D., Yan, P. & Loew, L. M. Single-voxel recording of voltage transients in dendritic spines. *Biophys. J.* **101**, L11–L13 (2011).
- 25 Roome, C. J. & Kuhn, B. Simultaneous dendritic voltage and calcium imaging and somatic recording from Purkinje neurons in awake mice. *Nat. Commun.* **9**, 1–14 (2018).
- 26 Brinks, D., Klein, A. J. & Cohen, A. E. Two-Photon Lifetime Imaging of Voltage Indicating Proteins as a Probe of Absolute Membrane Voltage. *Biophys. J.* **109**, 914–921 (2015).
- 27 Fisher, J. a N. *et al.* Two-photon excitation of potentiometric probes enables optical recording of action potentials from mammalian nerve terminals in situ. *J. Neurophysiol.* **99**, 1545–1553 (2008).
- 28 Wu, J. *et al.* Kilohertz two-photon fluorescence microscopy imaging of neural activity in vivo. *Nat. Methods* **17**, 287–290 (2020).
- 29 Villette, V. *et al.* Ultrafast Two-Photon Imaging of a High-Gain Voltage Indicator in Awake Behaving Mice. *Cell* **179**, 1590-1608.e23 (2019).
- 30 Platasa, J. *et al.* High-Speed Low-Light In Vivo Two-Photon Voltage Imaging of Large Neuronal Populations. *bioRxiv* 2021.12.07.471668 (2021) doi:10.1101/2021.12.07.471668.
- 31 Kulkarni, R. U. *et al.* In Vivo Two-Photon Voltage Imaging with Sulfonated Rhodamine Dyes. *ACS Cent. Sci.* **4**, 1371–1378 (2018).
- 32 Kazemipour, A. *et al.* Kilohertz frame-rate two-photon tomography. *Nat. Methods* **16**, 778–786 (2019).
- 33 Bando, Y., Wenzel, M. & Yuste, R. Simultaneous two-photon imaging of action potentials and subthreshold inputs in vivo. *Nat. Commun.* **12**, 1–12 (2021).
- 34 Cornejo, V. H., Ofer, N. & Yuste, R. Voltage compartmentalization in dendritic spines in vivo. *Science* **375**, 82–86 (2022).
- 35 Li, B. *et al.* Two-Photon Voltage Imaging of Spontaneous Activity from Multiple Neurons Reveals Network Activity in Brain Tissue. *iScience* **23**, 101363 (2020).
- 36 Papagiakoumou, E. *et al.* Scanless two-photon excitation of channelrhodopsin-2. *Nat. Methods* **7**, 848–854 (2010).
- 37 Papagiakoumou, E., de Sars, V., Oron, D. & Emiliani, V. Patterned two-photon illumination by spatiotemporal shaping of ultrashort pulses. *Opt. Express* **16**, 22039–22047 (2008).
- 38 Papagiakoumou, E. *et al.* Functional patterned multiphoton excitation deep inside scattering tissue. *Nat. Photonics* **7**, 274–278 (2013).
- 39 Pégard, N. M., Oldenburg, I., Sridharan, S., Waller, L. & Adesnik, H. 3D scanless holographic optogenetics with temporal focusing. *Nat. Commun.* **8**, 1228 (2017).
- 40 Liu, Z. *et al.* Sustained deep-tissue voltage recording using a fast indicator evolved for two-photon microscopy. *Cell* **185**, 3408-3425.e29 (2022).
- 41 Oron, D., Tal, E. & Silberberg, Y. Scanningless depth-resolved microscopy. *Opt. Express* **13**, 1468–1476 (2005).

- 42 Zhu, G., van Howe, J., Durst, M., Zipfel, W. & Xu, C. Simultaneous spatial and temporal focusing of femtosecond pulses. *Opt. Express* **13**, 2153–2159 (2005).
- 43 Papagiakoumou, E., Ronzitti, E. & Emiliani, V. Scanless two-photon excitation with temporal focusing. *Nat. Methods* **17**, 571–581 (2020).
- 44 Mardinly, A. R. *et al.* Precise multimodal optical control of neural ensemble activity. *Nat. Neurosci.* **21**, 881–893 (2018).
- 45 Bègue, A. *et al.* Two-photon excitation in scattering media by spatiotemporally shaped beams and their application in optogenetic stimulation. *Biomed. Opt. Express* **4**, 2869–2879 (2013).
- 46 al Maschio, M., Donovan, J. C., Helmbrecht, T. O. & Baier, H. Linking Neurons to Network Function and Behavior by Two-Photon Holographic Optogenetics and Volumetric Imaging. *Neuron* **94**, 774–789.e5 (2017).
- 47 Golan, L., Reutsky, I., Farah, N. & Shoham, S. Design and characteristics of holographic neural photo-stimulation systems. *J. Neural Eng.* **6**, 66004 (2009).
- 48 Yang, S. *et al.* Three-dimensional holographic photostimulation of the dendritic arbor. *J. Neural Eng.* **8**, 46002 (2011).
- 49 Xie, M. E. *et al.* High-fidelity estimates of spikes and subthreshold waveforms from 1-photon voltage imaging in vivo. *Cell Rep.* **35**, (2021).
- 50 Cai, C. *et al.* VolPy: Automated and scalable analysis pipelines for voltage imaging datasets. *PLoS Comput. Biol.* **17**, 1–27 (2021).
- 51 Kralj, J. M., Douglass, A. D., Hochbaum, D. R., Maclaurin, D. & Cohen, A. E. Optical recording of action potentials in mammalian neurons using a microbial rhodopsin. *Nat Methods* **9**, 90–5 (2012).
- 52 Hopt, A. & Neher, E. Highly nonlinear photodamage in two-photon fluorescence microscopy. *Biophys. J.* **80**, 2029–36 (2001).
- 53 Quicke, P., Howe, C. L. & Foust, A. J. Balancing the fluorescence imaging budget for all-optical neurophysiology experiments. in *Neuromethods* (ed. Papagiakoumou, E.) vol. 191 (Humana Press New York, 2023).
- 54 Wu, J. *et al.* KiloHertz two-photon fluorescence microscopy imaging of neural activity in vivo. *Nat. Methods* **17**, 287–290 (2020).
- 55 Xiao, S. *et al.* Large-scale voltage imaging in behaving mice using targeted illumination. *iScience* **24**, (2021).
- 56 Blankenship, A. G. & Feller, M. B. Mechanisms underlying spontaneous patterned activity in developing neural circuits. *Nat. Rev. Neurosci.* **11**, 18–29 (2010).
- 57 Ronzitti, E. *et al.* Sub-millisecond optogenetic control of neuronal firing with two-photon holographic photoactivation of Chronos. *J. Neurosci.* **37**, 1246–17 (2017).
- 58 Schrödel, T., Prevedel, R., Aumayr, K., Zimmer, M. & Vaziri, A. Brain-wide 3D imaging of neuronal activity in *Caenorhabditis elegans* with sculpted light. *Nat. Methods* **10**, 1013–1020 (2013).
- 59 Prevedel, R. *et al.* Fast volumetric calcium imaging across multiple cortical layers using sculpted light. *Nat. Methods* **13**, 1021–1028 (2016).
- 60 Demas, J. *et al.* High-speed, cortex-wide volumetric recording of neuroactivity at cellular resolution using light beads microscopy. *Nature Methods* vol. 18 (2021).
- 61 Song, A. *et al.* Volumetric Two-photon Imaging of Neurons Using Stereoscopy (vTwINS). *Nat. Methods* **14**, 420–426 (2017).
- 62 Hernandez, O. *et al.* Three-dimensional spatiotemporal focusing of holographic patterns. *Nat. Commun.* **7**, 11928 (2016).
- 63 Accanto, N. *et al.* Multiplexed temporally focused light shaping for high-resolution multi-cell targeting. *Optica* **5**, 1478–1491 (2018).
- 64 Botcherby, E. J. *et al.* Aberration-free three-dimensional multiphoton imaging of neuronal activity at kHz rates. *Proc. Natl. Acad. Sci.* **109**, 2919–2924 (2012).
- 65 Botcherby, E. J., Juskaitis, R., Booth, M. J., Wilson, T. & Juškaitis, R. An optical technique for remote focusing in microscopy. *Opt. Commun.* **281**, 880–887 (2008).
- 66 Nöbauer, T. *et al.* Video rate volumetric Ca²⁺ imaging across cortex using seeded iterative demixing (SID) microscopy. *Nat. Methods* **14**, 811–818 (2017).
- 67 Bovetti, S. *et al.* Simultaneous high-speed imaging and optogenetic inhibition in the intact mouse brain. *Sci. Rep.* **7**, 40041 (2017).
- 68 Zhang, T. *et al.* KiloHertz two-photon brain imaging in awake mice. *Nat. Methods* **16**, 1119–1122 (2019).
- 69 Moretti, C., Antonini, A., Bovetti, S., Liberale, C. & Fellin, T. Scanless functional imaging of hippocampal networks using patterned two-photon illumination through GRIN lenses. *Biomed. Opt. Express* **7**, 3958 (2016).
- 70 Accanto, N. *et al.* A flexible two-photon fiberscope for fast activity imaging and precise optogenetic photostimulation of neurons in freely moving mice. *Neuron* **111**, 1–14 (2023).
- 71 Moretti, C. & Gigan, S. Readout of fluorescence functional signals through highly scattering tissue. *Nat. Photonics* **14**, 361–364 (2020).
- 72 Printz, Y. *et al.* Determinants of functional synaptic connectivity among amygdala-projecting prefrontal cortical neurons. (2021).
- 73 Hage, T. A. *et al.* Synaptic connectivity to L2/3 of primary visual cortex measured by two-photon optogenetic stimulation. *eLife* **11**, (2022).

- 74 Sridharan, S. *et al.* High-performance microbial opsins for spatially and temporally precise perturbations of large neuronal networks. *Neuron* 1–17 (2022) doi:10.1016/j.neuron.2022.01.008.
- 75 Di Leonardo, R., Ianni, F. & Ruocco, G. Computer generation of optimal holograms for optical trap arrays. *Opt. Express* **15**, 1913–22 (2007).
- 76 Gerchberg, R. W. & Saxton, W. O. A practical algorithm for the determination of the phase from image and diffraction pictures. *Optik* **35**, 237–246 (1972).
- 77 Edelstein, A. D. *et al.* Advanced methods of microscope control using μ Manager software. *J. Biol. Methods* **1**, e10 (2014).
- 78 Pinkard, H. *et al.* Pycro-Manager: open-source software for customized and reproducible microscope control. *Nat. Methods* **18**, 226–228 (2021).
- 79 Cai, C. *et al.* VolPy: Automated and scalable analysis pipelines for voltage imaging datasets. *PLoS Comput. Biol.* **17**, 1–27 (2021).
- 80 Gee, C. E., Ohmert, I., Wiegert, J. S. & Oertner, T. G. Preparation of slice cultures from rodent hippocampus. *Cold Spring Harb. Protoc.* **2017**, 126–130 (2017).
- 81 Ho, J., Tumkaya, T., Aryal, S., Choi, H. & Claridge-Chang, A. Moving beyond P values: data analysis with estimation graphics. *Nat. Methods* **16**, 565–566 (2019).
- 82 Johnston, J., Forsythe, I. D. & Kopp-Scheinflug, C. SYMPOSIUM REVIEW: Going native: voltage-gated potassium channels controlling neuronal excitability. *J. Physiol.* **588**, 3187–3200 (2010).
- 83 Bähring, R. & Covarrubias, M. Mechanisms of closed-state inactivation in voltage-gated ion channels. *J. Physiol.* **589**, 461–479 (2011).
- 84 Debanne, D., Campanac, E., Bialowas, A., Carlier, E. & Alcaraz, G. Axon Physiology. *Physiol. Rev.* **91**, 555–602 (2011).
- 85 Erecińska, M. & Silver, I. A. Ions and energy in mammalian brain. *Prog. Neurobiol.* **43**, 37–71 (1994).

Acknowledgements

The project was supported by the ‘Agence Nationale de la Recherche’ through the projects SLALLOM (ANR-17-CE16-0021), HOLOPTOGEN (ANR-19-CE16-0026), LabEx LIFESENSES (ANR-10-LABX-65) and IHU FOReSIGHT (ANR-18-IAHU-01) (V.E., E.P., R.S.), the AXA research foundation (V.E.) and the European Research Council (“HOLOVIS-AdG” ERC2019-ADG-885090 to V.E.), Deutsche Forschungsgemeinschaft (DFG, German Research Foundation, Postdoc fellowship 442616457 to C.G.), the Klingenstein-Simons Fellowship Award in Neuroscience (F.S.-P.); the McNair Medical Foundation (F.S.-P.); the John S. Dunn Foundation (F.S.-P.); Welch Foundation grants Q-2016-20190330 and Q-2016-20220331 (F.S.-P.); NIH grants R01EB027145 (F.S.-P.), U01NS113294 (F.S.-P.), U01NS118288 (F.S.-P.), and R01EB032854 (F.S.-P.); and NSF grants 1707359 (F.S.-P) and 1935265 (F.S.-P.).

We thank Yoann Zaouter and Alexandre Thai from Amplitude Systemes for the generous loan and installation of the Satsuma Niji laser, Christophe Tourain for the fabrication of custom electronic and mechanical components, Vincent de Sars for continued software development and Hillel Adesnik for the gift of the ChRoME-ST virus.

We thank the viral vector facility at the Institut de la Vision for producing AAVs, the Vision Institute animal house facility for the handling of laboratory animals and Stéphane Fouquet from the Vision Institute imaging facility for technical assistance with confocal microscopy.

We thank Dr. B. Arenkiel, J. Ortiz-Guzman, and Z. Chen at the TCH Neuroconnectivity Core for AAV packaging; this Core is supported by NIH grant P50HD103555 and the Charif Souki Fund.

3. Discussion

In this work, we demonstrated *in vitro* that scanless approaches are suitable for 2P, high contrast voltage imaging in densely labelled samples. Using organotypic hippocampal slices expressing the voltage indicator JEDI-2P and GPC-TF illumination, we were able to optically record single and trains of action potentials up to 125 Hz, with acquisition rates varying from 500 Hz to 1 kHz. Recording at high speed allowed to infer the precise number and timing of fast trains of action potentials, with sub-millisecond resolution.

One of the main advantages of voltage imaging over calcium imaging is the possibility to detect sub-threshold changes in the membrane potential of a neuron, in the soma. Here, we showed detection of subthreshold depolarizations, as small as 1 mV with averaging of 25 trials. Although still challenging, this ability would greatly benefit the field of connectivity mapping, where electrophysiological recordings are still the gold standard technique, despite being low-throughput and extremely difficult *in vivo*. It is also important to note that other voltage indicators, specifically designed for subthreshold membrane potential changes, with a steep $\Delta F/F_0$ slope near the resting membrane potential could reduce the number of trials necessary to detect subthreshold activity.

The technique is in principle easier to implement in laboratories already performing scanless 2P optogenetics, as it only necessitates the addition of a suitable camera. We have shown that using camera detection enables recording a true image of the illuminated cells, thus achieving a good lateral and axial resolution, even in densely labelled samples. This will also enable to detect and correct sample motion online, using techniques such as remote focusing for an axial shift of the excitation volume.

We demonstrated 2P scanless approaches for voltage imaging by using single or multiple round spots of 12 μm of diameter. However, light shaping methods such as GPC and CGH can also allow targeting the light only to the regions of interest, such as the membrane of a neuron soma, instead of using a large spot that cover the whole cell body. This would allow to reduce the laser power while maintaining a similar SNR. Secondly, since levels of expression vary between cells, it would also be possible to independently tune the power of each spot placed in a FOV, with the possibility to send less power to the highly expressing cells than to the low expressing ones. Implementing these two approaches would minimize the total power used, therefore the risks of heating and/or nonlinear damage and increasing the maximum number of cells that could be recorded simultaneously.

By using a single laser source, we photo-evoked and imaged action potentials in neurons from organotypic hippocampal slices co-expressing the voltage indicator JEDI-2P and the soma-targeted rhodopsin ChRME-ST. This approach can be useful when performing optogenetics experiments, since

it allows to confirm the photostimulation of a neuron. Similar strategies have been successfully used using calcium imaging (*Printz et al. 2023*). However, the slow kinetics of calcium transients only allowed to infer the successful triggering of a spike, without information on the precise timing of the event. Our technique provided confirmation of photostimulation, as well as the precise timing of the photo-evoked action potential, with sub-millisecond resolution. This may prove to be extremely useful during connectivity mapping experiments, since false negative connections, in which no response is detected in the post-synaptic cell because the pre-synaptic cell did not fire an action potential, could be identified. Moreover, knowing the precise timing of the action potential in the pre-synaptic neuron could simplify the correlation between the firing of the pre-synaptic cell and the response recorded in the post-synaptic neuron, and help discriminate post-synaptic response from noise or spontaneous activity.

Alternative applications could require photoactivation and read-out from distinct cell populations. In this configuration, the rhodopsin and indicator spectra would need to be as separate as possible, in order to decouple the imaging from the photostimulation. To date, all rhodopsins (including the most red-shifted Chrimson) show a non-negligible sensitivity in the range of the spectrum (920 – 1030 nm) where existing voltage indicators can efficiently be excited under 2P excitation. The development of red-shifted indicators will allow to reduce the crosstalk between photoactivation and imaging when combined with blue-shifted rhodopsins.

a. Voltage imaging at 1030 nm

Although *in vitro* experiments can shed light on many questions in neuroscience, understanding the precise mechanisms underlying sensory perceptions requires to perform experiments *in vivo*. Voltage imaging, as a less invasive technique than electrophysiology, would allow to study these mechanisms with less perturbations in the physiology of the network.

In vivo 2P voltage imaging would benefit from using red-shifted wavelengths and low repetition rate, high peak energy sources (fixed output at 1030 – 1040 nm, exit power up to 80 W). With respect to conventional high repetition rate, tunable lasers, the use of these sources would enable larger penetration depth, and the possibility to target a large number of cells in a given FOV. Combined with a red-shifted indicator, this would allow performing crosstalk-free all-optical experiments *in vivo*.

i. VADER vs. JEDI-2P

The laboratory of François St-Pierre, which already developed and published the voltage indicator JEDI-2P (Zhuohe Liu et al. 2022a) that was used in this work, is currently working on the development of red-shifted, positive-going, VSD-based voltage indicators.

To assess their potential usability for *in vivo* voltage imaging under 1030 nm illumination, I tested two variants that his lab has recently produced: the so-called VADER indicators (#3286 and #3361) and compared their performances with those of JEDI-2P when excited at the same wavelength.

As for the experiments reported in Figure 2 of the paper, I transfected CHO cells with the two variants of VADER and JEDI-2P, patched those cells in the voltage clamp, whole-cell configuration and performed protocol 1 under 1030 nm illumination. The results are summarized below [Figure III.3.1].

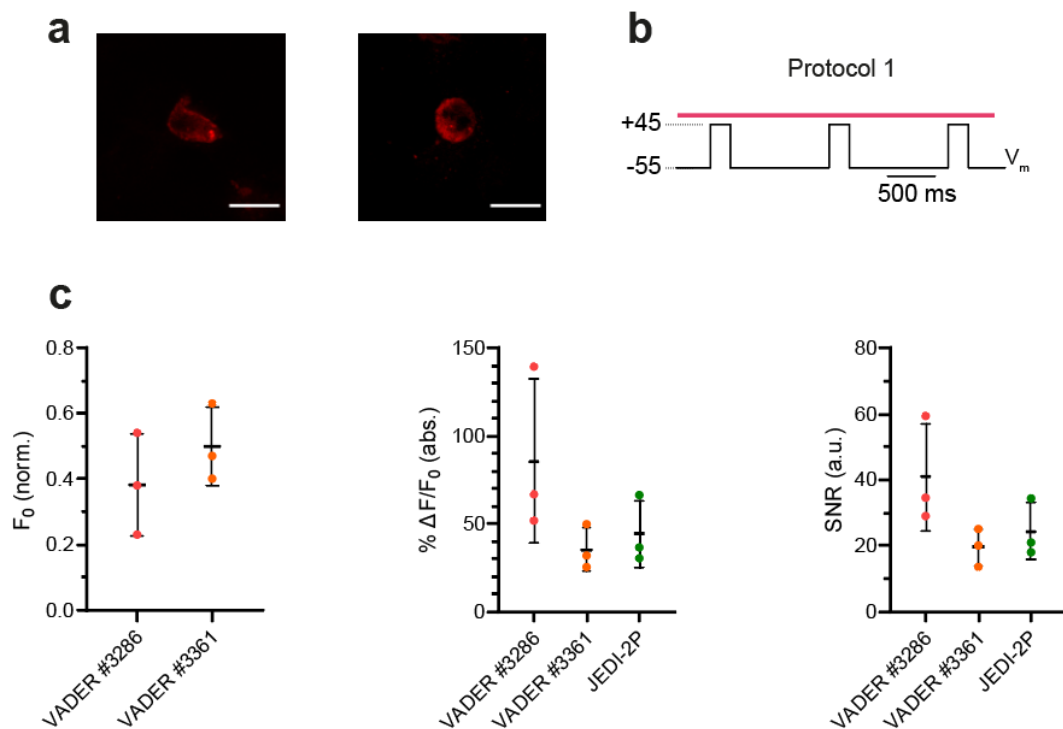


Figure III.3.1. In-vitro electrophysiological characterisation of VADER #3286, #3361 and JEDI-2P under 1030 nm illumination in cultured CHO cells. (a) Confocal image of a (left) VADER #3286 and (right) VADER #3361 expressing CHO cell. Scale bars represent 10 μm . **(b)** Representation of the electrophysiology protocol used to test the performance of each indicator under 1030 nm illumination. The red bar above the electrophysiology trace indicates the illumination epoch. **(c)** Quantification of data for all cells from protocol 1. Baseline fluorescence F_0 of both VADER variants normalized to JEDI-2P F_0 (left), absolute $\% \Delta F/F_0$ (middle) and SNR (right) are reported (power density: $0.80 \text{ mW } \mu\text{m}^{-2}$, 91 mW per cell, $n = 3$). Each point represents a measurement from an individual cell. The mean \pm s.d. is plotted for each condition. All data was acquired with laser A (80 MHz, 100 fs) tuned to 1030 nm and camera A (See Supplementary Figure 1 and Supplementary Table 1).

Both VADER variants were expressing in CHO cells, and displayed a lower level of basal fluorescence than JEDI-2P (0.38 ± 0.16 and 0.50 ± 0.12 for VADER #3286 and VADER #3361 respectively, compared to JEDI-2P), as expected for a positive-going indicator [Figure III.3.1, c]. They also showed high responses to a 200 ms, 100-mV depolarization, with $\% \Delta F/F_0$ of 85.77 ± 46.96 for #3286 and 35.33 ± 12.60 for #3361. In comparison, under the same conditions, JEDI-2P showed a $\% \Delta F/F_0$ of -44.07 ± 19.25 (mean \pm s.d.) [Figure III.3.1, d].

To assess the possibility to detect action potentials, I performed protocol 3 on CHO cells, which consisted in a 20 Hz train of 3 ms, 100 mV depolarizations, under continuous illumination for 500 ms and an acquisition rate of 1 kHz. No fluctuation of the fluorescence was detected in response to protocol 3 with VADER #3286 (2.6 ± 2.25 , mean \pm s.d.), whereas VADER #3361 showed a $\% \Delta F/F_0$ of 6.8 ± 4.13 (mean \pm s.d.) [Figure III.3.2, a and b]. Increasing the duration of the depolarizations to 10 ms allowed to increase the $\% \Delta F/F_0$ for all constructs tested (7.43 ± 5.74 and 12.57 ± 3.91 for VADER #3286 and #3361 respectively) implying that the VADERS kinetics may be too slow for action potential detection [Figure III.3.2, a and c]. JEDI-2P, on the contrary, showed a $\% \Delta F/F_0$ of -19.17 ± 7.41 and -30.34 ± 11.64 for 3 ms and 10 ms respectively, under 1030 nm illumination. Overall, these results indicate that JEDI-2P is suitable for detecting electrical activity in neurons under 1030 nm illumination, while the VADER variants require further optimization.

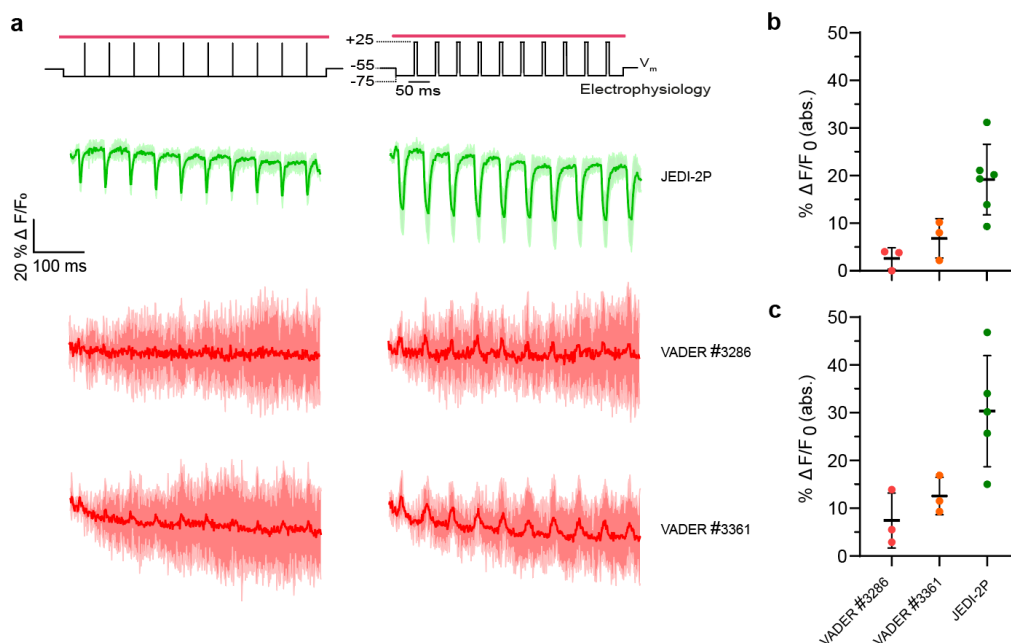


Figure III.3.2. In-vitro electrophysiological characterization of VADER #3286, #3361 and JEDI-2P under 1030 nm illumination in cultured CHO cells. (a) Data from protocol 3 used to test the performance of each voltage indicator for action potential detection. Protocol 3 consisted of a 20 Hz train of 100 mV depolarizations, of 3 ms (left) or 10 ms (right). Responses are reported as the fluorescence change (ΔF) normalized by the baseline fluorescence (F_0), expressed as a percentage of the baseline fluorescence ($\% \Delta F/F_0$). The average trace and 95 percent confidence interval from all cells imaged with each indicator are plotted. The corresponding electrophysiology control signals are plotted in black. The red bar above the electrophysiology trace indicates the 1030 nm illumination epoch. **(b)** Absolute $\% \Delta F/F_0$ of all indicators tested in response to protocol 3 with 3 ms or **(c)** 10 ms depolarizations (power density: $1.41 \text{ mW } \mu\text{m}^{-2}$, 160 mW per cell , $n = 3 - 6$). Each point represents a measurement from an individual cell. The mean \pm s.d. is plotted for each condition. All data was acquired with laser A (80 MHz, 100 fs) tuned to 1030 nm and camera A (See Supplementary Figure 1 and Supplementary Table 1).

ii. JEDI-2P at 1030 nm

We then tested if we could detect neuronal activity using JEDI-2P under 1030 nm illumination. Using a low repetition rate, high peak energy laser source, we illuminated neurons from organotypic hippocampal slices expressing JEDI-2P for 15 seconds and recorded the fluorescence response at 500

Hz acquisition rate. We were able to record single and trains of action potentials, as well as subthreshold depolarizations and hyperpolarizations of membrane potential [Figure III.3.3].



Figure III.3.3. Optical recording of spontaneous activity in JEDI-2P-expressing organotypic hippocampal slices, under CGH-TF 1030 nm illumination, using a low repetition rate, high peak energy laser source (500 kHz, 300 fs). Representative trace of spontaneous activity recorded from a JEDI-2P expressing neuron in the dentate gyrus of an organotypic hippocampal slice. Fluorescence in response to 1030 nm, CGH-TF illumination was recorded for 15 s (power density: $0.042 \text{ mW } \mu\text{m}^{-2}$, 7.5 mW per cell).

b. Outlook

This work has demonstrated the usability of two-photon scanless approaches for voltage imaging. All the results showed here were acquired *in vitro*, in organotypic hippocampal slices on the superficial layers (up to $50 \mu\text{m}$). However, as mentioned previously, studying the mechanisms and networks underlying sensory perceptions requires to perform experiments in living animals.

One question that arises with *in vivo* experiments, especially in non-transparent tissue, such as the mouse brain, is how scattering will affect the signal recording when using camera detection with respect to the use of approaches using scanning excitation and PMT detection. More precisely, in the latter case, photons arriving at the PMT at any given moment can be tracked to a precise position, regardless of the scattering. This is not the case for scanless excitation combined with camera detection, where the scattering of emitted photons from one cell may contaminate the signal emitted by a neighboring cell, making it difficult to discriminate and identify the different patterns of neuronal activity.

Previous experiments have reported two-photon scanless Ca^{2+} imaging with camera detection at depths up to $250 \mu\text{m}$ *in vivo*, with the possibility to discriminate signals coming from two adjacent cells ($\approx 10 \mu\text{m}$ apart) with minimal crosstalk (Bovetti *et al.* 2017). Thus, we expect that we should be able to reach comparable depths using two-photon scanless voltage imaging, which would grant access to superficial layers of the mouse brain cortex. To extend it to deeper layers, advanced computational approaches would be necessary in order to disentangle mixed signals (Moretti and Gigan 2020).

IV. CONCLUSION AND FUTURE OUTLOOK

My thesis project aimed to demonstrate and characterize the use of two-photon scanless approaches for the bidirectional control of neuronal activity and for voltage imaging.

In the first part, I characterized the performances of a new tool, termed BiPOLES and developed in the laboratories of Peter Hegemann and J. Simon Wiegert, under two-photon holographic excitation. This construct, a fusion of a blue-shifted inhibitory channelrhodopsin and a red-shifted excitatory channelrhodopsin, allows the bidirectional control of neuronal activity by tuning the wavelength of excitation. We showed that neurons expressing BiPOLES could be reliably photo-activated using 1100 nm illumination and inhibited using 920 nm. This was the first demonstration of bidirectional control of neurons under two-photon excitation. Although we only demonstrated single cell photostimulation due to our output power available at 1100 nm, advanced optical approaches could be implemented and would increase the number of cells that could be probed simultaneously. The tool was successfully used *in vivo*, in a variety of organisms, under single-photon, widefield excitation. The use of two-photon excitation will allow to extend the use of BiPOLES to the investigation of the neuronal networks underlying sensory stimuli processing, with single cell resolution.

The second part of my project consisted in demonstrating the usability of the three scanless approaches (low-NA gaussian beam, CGH and GPC) for two-photon voltage imaging, using camera detection. Using CHO cells expressing the GEVI JEDI-2P, we showed that all three modalities are suitable for two-photon, scanless voltage imaging. Using GPC in organotypic hippocampal slices expressing JEDI-2P, we demonstrated single trial, optical detection of single and trains of action potentials up to 125 Hz, and characterized the powers and acquisition rates necessary. We were also able to record low amplitude depolarizations, down to 1 mV by averaging up to 25 trials, and recorded spontaneous activity in single and multiple cells simultaneously. Finally, by co-expressing JEDI-2P with the rhodopsin ChromE-ST, we successfully photostimulated and recorded action potentials using a single beam, which could prove to be useful to confirm successful stimulation of neurons in two-photon optogenetics experiments. The next step will be to demonstrate that this approach can be used *in vivo* and to characterize its performance, in the mouse brain. Based on previous studies using scanless approaches coupled with camera detection to record calcium transients, we are confident that we will be able to record neuronal activity within layer 2/3 of the mouse brain.

All in all, these results enabled to advance the field of all-optical circuit investigation, an emerging technology which, by combining recent progresses in engineering of genetic actuators and reporters, laser development and illumination methods, has propelled optogenetics into a new dimension,

where it is now possible to mimic specific patterns of brain activity with light and relate them to animal behavior, a key step towards the methodological foundation of computational neuroscience.

REFERENCES

- Abdelfattah, Ahmed S., Takashi Kawashima, Amrita Singh, Ondrej Novak, Hui Liu, Yichun Shuai, Yi Chieh Huang, et al. 2019a. "Bright and Photostable Chemigenetic Indicators for Extended in Vivo Voltage Imaging." *Science* 365 (6454): 699–704. <https://doi.org/10.1126/science.aav6416>.
- Abdelfattah, Ahmed S., Takashi Kawashima, Amrita Singh, Ondrej Novak, Hui Liu, Yichun Shuai, Yi Chieh Huang, et al. 2019b. "Bright and Photostable Chemigenetic Indicators for Extended in Vivo Voltage Imaging." *Science* 365 (6454): 699–704. <https://doi.org/10.1126/science.aav6416>.
- Abdelfattah, Ahmed S., Rosario Valenti, Jihong Zheng, Allan Wong, Kaspar Podgorski, Minoru Koyama, Douglas S. Kim, and Eric R. Schreier. 2020. "A General Approach to Engineer Positive-Going EFRET Voltage Indicators." *Nature Communications* 11 (1): 3444. <https://doi.org/10.1038/s41467-020-17322-1>.
- Accanto, Nicolò, François G. C. Blot, Antonio Lorca-Cámara, Valeria Zampini, Florence Bui, Christophe Tourain, Noam Badt, Ori Katz, and Valentina Emiliani. 2023. "A Flexible Two-Photon Fiberscope for Fast Activity Imaging and Precise Optogenetic Photostimulation of Neurons in Freely Moving Mice." *Neuron* 111 (2): 176–189.e6. <https://doi.org/10.1016/j.neuron.2022.10.030>.
- Accanto, Nicolò, I-Wen Chen, Emiliano Ronzitti, Clément Molinier, Christophe Tourain, Eirini Papagiakoumou, and Valentina Emiliani. 2019. "Multiplexed Temporally Focused Light Shaping through a Gradient Index Lens for Precise In-Depth Optogenetic Photostimulation." *Scientific Reports* 9 (1): 7603. <https://doi.org/10.1038/s41598-019-43933-w>.
- Accanto, Nicolò, Clément Molinier, Dimitrii Tanese, Emiliano Ronzitti, Zachary L. Newman, Claire Wyart, Ehud Isacoff, Eirini Papagiakoumou, and Valentina Emiliani. 2018. "Multiplexed Temporally Focused Light Shaping for High-Resolution Multi-Cell Targeting." *Optica* 5 (11): 1478–91. <https://doi.org/10.1364/OPTICA.5.001478>.
- Adam, Yoav, Jeong J. Kim, Shan Lou, Yongxin Zhao, Michael E. Xie, Daan Brinks, Hao Wu, et al. 2019a. "Voltage Imaging and Optogenetics Reveal Behaviour-Dependent Changes in Hippocampal Dynamics." *Nature* 569 (7756): 413–17. <https://doi.org/10.1038/s41586-019-1166-7>.
- . 2019b. "Voltage Imaging and Optogenetics Reveal Behaviour-Dependent Changes in Hippocampal Dynamics." *Nature* 569 (7756): 413–17. <https://doi.org/10.1038/s41586-019-1166-7>.
- Aharoni, Tal, and Shy Shoham. 2018. "Phase-Controlled, Speckle-Free Holographic Projection with Applications in Precision Optogenetics." *Neurophotonics* 5 (2): 025004. <https://doi.org/10.1117/1.NPh.5.2.025004>.
- Ahrens, Kurt, Barbara Heider, Hanson Lee, Ehud Isacoff, and Ralph Siegel. 2012. "Two-Photon Scanning Microscopy of in Vivo Sensory Responses of Cortical Neurons Genetically Encoded with a Fluorescent Voltage Sensor in Rat." *Frontiers in Neural Circuits* 6. <https://www.frontiersin.org/articles/10.3389/fncir.2012.00015>.
- Akemann, Walther, Hiroki Mutoh, Amélie Perron, Yun Kyung Park, Yuka Iwamoto, and Thomas Knöpfel. 2012. "Imaging Neural Circuit Dynamics with a Voltage-Sensitive Fluorescent Protein." *Journal of Neurophysiology* 108 (8): 2323–37. <https://doi.org/10.1152/jn.00452.2012>.
- Akemann, Walther, Mari Sasaki, Hiroki Mutoh, Takeshi Imamura, Naoki Honkura, and Thomas Knöpfel. 2013. "Two-Photon Voltage Imaging Using a Genetically Encoded Voltage Indicator." *Scientific Reports* 3 (1): 2231. <https://doi.org/10.1038/srep02231>.
- Akerboom, Jasper, Nicole Carreras Calderón, Lin Tian, Sebastian Wabnig, Matthias Prigge, Johan Tolö, Andrew Gordus, et al. 2013. "Genetically Encoded Calcium Indicators for Multi-Color Neural Activity Imaging and Combination with Optogenetics." *Frontiers in Molecular Neuroscience* 6. <https://www.frontiersin.org/articles/10.3389/fnmol.2013.00002>.

- Alberio, Laura, Andrea Locarno, Andrea Saponaro, Edoardo Romano, Valérie Bercier, Shahad Albadri, Federica Simeoni, et al. 2018. "A Light-Gated Potassium Channel for Sustained Neuronal Inhibition." *Nature Methods* 15 (11): 969–76. <https://doi.org/10.1038/s41592-018-0186-9>.
- Andrasfalvy, B K, B V Zemelman, J Tang, and Alipasha Vaziri. 2010. "Two-Photon Single-Cell Optogenetic Control of Neuronal Activity by Sculpted Light." *Proceedings of the National Academy of Sciences of the United States of America* 107 (26): 11981–86.
- Azimi Hashemi, Negin, Amelie C. F. Bergs, Christina Schüler, Anna Rebecca Scheiwe, Wagner Steuer Costa, Maximilian Bach, Jana F. Liewald, and Alexander Gottschalk. 2019. "Rhodopsin-Based Voltage Imaging Tools for Use in Muscles and Neurons of *Caenorhabditis Elegans*." *Proceedings of the National Academy of Sciences* 116 (34): 17051–60. <https://doi.org/10.1073/pnas.1902443116>.
- Bähring, Robert, and Manuel Covarrubias. 2011. "Mechanisms of Closed-State Inactivation in Voltage-Gated Ion Channels." *The Journal of Physiology* 589 (3): 461–79. <https://doi.org/10.1113/jphysiol.2010.191965>.
- Bando, Yuki, Christiane Grimm, Victor H Cornejo, and Rafael Yuste. 2019. "Genetic Voltage Indicators." *BMC Biology* 17 (1): 71. <https://doi.org/10.1186/s12915-019-0682-0>.
- Bando, Yuki, Masayuki Sakamoto, Samuel Kim, Inbal Ayzenshtat, and Rafael Yuste. 2019. "Comparative Evaluation of Genetically Encoded Voltage Indicators." *Cell Reports* 26 (3): 802-813.e4. <https://doi.org/10.1016/j.celrep.2018.12.088>.
- Bando, Yuki, Michael Wenzel, and Rafael Yuste. 2021. "Simultaneous Two-Photon Imaging of Action Potentials and Subthreshold Inputs in Vivo." *Nature Communications* 12 (1): 7229. <https://doi.org/10.1038/s41467-021-27444-9>.
- Barrett, J. N., K. L. Magleby, and B. S. Pallotta. 1982. "Properties of Single Calcium-Activated Potassium Channels in Cultured Rat Muscle." *The Journal of Physiology* 331 (1): 211–30. <https://doi.org/10.1113/jphysiol.1982.sp014370>.
- Bègue, Aurélien, Eirini Papagiakoumou, Ben Leshem, Rossella Conti, Leona Enke, Dan Oron, and Valentina Emiliani. 2013. "Two-Photon Excitation in Scattering Media by Spatiotemporally Shaped Beams and Their Application in Optogenetic Stimulation." *Biomedical Optics Express* 4 (12): 2869–79.
- Beyene, Abraham G., Kristen Delevich, Jackson Travis Del Bonis-O'Donnell, David J. Piekarski, Wan Chen Lin, A. Wren Thomas, Sarah J. Yang, et al. 2019. "Imaging Striatal Dopamine Release Using a Nongenetically Encoded near Infrared Fluorescent Catecholamine Nanosensor." *Science Advances* 5 (7): eaaw3108. <https://doi.org/10.1126/sciadv.aaw3108>.
- Bovetti, Serena, Claudio Moretti, Stefano Zucca, Marco Dal Maschio, Paolo Bonifazi, and Tommaso Fellin. 2017. "Simultaneous High-Speed Imaging and Optogenetic Inhibition in the Intact Mouse Brain." *Scientific Reports* 7 (1): 40041. <https://doi.org/10.1038/srep40041>.
- Boyden, Edward S, Feng Zhang, Ernst Bamberg, Georg Nagel, and Karl Deisseroth. 2005. "Millisecond-Timescale, Genetically Targeted Optical Control of Neural Activity." *Nature Neuroscience* 8 (9): 1263–68. <https://doi.org/10.1038/nn1525>.
- Buchanan, E. Kelly, Ian Kinsella, Ding Zhou, Rong Zhu, Pengcheng Zhou, Felipe Gerhard, John Ferrante, et al. 2018. "Penalized Matrix Decomposition for Denoising, Compression, and Improved Demixing of Functional Imaging Data," 1–36.
- Cai, Changjia, Johannes Friedrich, Amrita Singh, M. Hossein Eybposh, Eftychios A. Pnevmatikakis, Kaspar Podgorski, and Andrea Giovannucci. 2021. "VolPy: Automated and Scalable Analysis Pipelines for Voltage Imaging Datasets." *PLoS Computational Biology* 17 (4): 1–27. <https://doi.org/10.1371/journal.pcbi.1008806>.
- Canepari, Marco, Maja Djuricic, and Dejan Zecevic. 2007. "Dendritic Signals from Rat Hippocampal CA1 Pyramidal Neurons during Coincident Pre- and Post-Synaptic Activity: A Combined Voltage- and Calcium-Imaging Study." *The Journal of Physiology* 580 (2): 463–84. <https://doi.org/10.1113/jphysiol.2006.125005>.

- Carrillo-Reid, Luis, Shuting Han, Weijian Yang, Alejandro Akrouh, and Rafael Yuste. 2019. "Controlling Visually Guided Behavior by Holographic Recalling of Cortical Ensembles." *Cell* 178 (2): 447-457.e5. <https://doi.org/10.1016/j.cell.2019.05.045>.
- Chaigneau, Emmanuelle, Emiliano Ronzitti, A. Marta Gajowa, J. Gilberto Soler-Llavina, Dimitrii Tanese, Y.B. Anthony Brureau, Eirini Papagiakoumou, Hongkui Zeng, and Valentina Emiliani. 2016. "Two-Photon Holographic Stimulation of ReaChR." *Frontiers in Cellular Neuroscience* 10: 234.
- Chamberland, Simon, Helen H Yang, Michael M Pan, Stephen W Evans, Sihui Guan, Mariya Chavarha, Ying Yang, et al. 2017. "Fast Two-Photon Imaging of Subcellular Voltage Dynamics in Neuronal Tissue with Genetically Encoded Indicators." *ELife* 6: e25690. <https://doi.org/10.7554/eLife.25690>.
- Chen, I-Wen, Eirini Papagiakoumou, and Valentina Emiliani. 2018. "Towards Circuit Optogenetics." *Current Opinion in Neurobiology, Neurotechnologies*, 50 (June): 179–89. <https://doi.org/10.1016/j.conb.2018.03.008>.
- Chen, I-Wen, Emiliano Ronzitti, Brian R. Lee, Tanya L. Daigle, Deniz Dalkara, Hongkui Zeng, Valentina Emiliani, and Eirini Papagiakoumou. 2019. "In Vivo Submillisecond Two-Photon Optogenetics with Temporally Focused Patterned Light." *Journal of Neuroscience* 39 (18): 3484–97. <https://doi.org/10.1523/JNEUROSCI.1785-18.2018>.
- Chow, Brian Y., Xue Han, and Edward S. Boyden. 2012. "Genetically Encoded Molecular Tools for Light-Driven Silencing of Targeted Neurons." In *Progress in Brain Research*, 196:49–61. Elsevier. <https://doi.org/10.1016/B978-0-444-59426-6.00003-3>.
- Cohen, L. B., B. M. Salzberg, H. V. Davila, W. N. Ross, D. Landowne, A. S. Waggoner, and C. H. Wang. 1974. "Changes in Axon Fluorescence during Activity: Molecular Probes of Membrane Potential." *The Journal of Membrane Biology* 19 (1): 1–36. <https://doi.org/10.1007/BF01869968>.
- Cohen, L. B., B. M. Salzberg, and A. Grinvald. 1978. "Optical Methods for Monitoring Neuron Activity." *Annual Review of Neuroscience* 1 (1): 171–82. <https://doi.org/10.1146/annurev.ne.01.030178.001131>.
- Crick, F. H. C. 1979. "Thinking about the Brain." *Scientific American* 241 (3): 219–33.
- Cundy, H. Martyn, and A. P. Rollett. 1989. *Mathematical Models*. Tarquin Publications.
- Dalgleish, Henry WP, Lloyd E Russell, Adam M Packer, Arnd Roth, Oliver M Gauld, Francesca Greenstreet, Emmett J Thompson, and Michael Häusser. 2020. "How Many Neurons Are Sufficient for Perception of Cortical Activity?" Edited by Brice Bathellier, Ronald L Calabrese, Brice Bathellier, and Luis Carrillo-Reid. *ELife* 9 (October): e58889. <https://doi.org/10.7554/eLife.58889>.
- Dana, Hod, Boaz Mohar, Yi Sun, Sujatha Narayan, Andrew Gordus, Jeremy P Hasseman, Getahun Tsegaye, et al. 2016. "Sensitive Red Protein Calcium Indicators for Imaging Neural Activity." *ELife* 5: e12727. <https://doi.org/10.7554/eLife.12727>.
- Dana, Hod, Yi Sun, Boaz Mohar, Brad K. Hulse, Aaron M. Kerlin, Jeremy P. Hasseman, Getahun Tsegaye, et al. 2019. "High-Performance Calcium Sensors for Imaging Activity in Neuronal Populations and Microcompartments." *Nature Methods* 16 (7): 649–57. <https://doi.org/10.1038/s41592-019-0435-6>.
- Davie, Jenny T., Maarten H. P. Kole, Johannes J. Letzkus, Ede A. Rancz, Nelson Spruston, Greg J. Stuart, and Michael Häusser. 2006. "Dendritic Patch-Clamp Recording." *Nature Protocols* 1 (3): 1235–47. <https://doi.org/10.1038/nprot.2006.164>.
- Debanne, Dominique, Emilie Campanac, Andrzej Bialowas, Edmond Carlier, and Gisèle Alcaraz. 2011. "Axon Physiology." *Physiological Reviews* 91 (2): 555–602. <https://doi.org/10.1152/physrev.00048.2009>.
- Demas, Jeffrey, Jason Manley, Frank Tejera, Kevin Barber, Hyewon Kim, Francisca Martínez Traub, Brandon Chen, and Alipasha Vaziri. 2021. "High-Speed, Cortex-Wide Volumetric Recording of Neuroactivity at Cellular Resolution Using Light Beads Microscopy." *Nature Methods* 18 (9): 1103–11. <https://doi.org/10.1038/s41592-021-01239-8>.

- Denk, Winifried, James H. Strickler, and Watt W. Webb. 1990. "Two-Photon Laser Scanning Fluorescence Microscopy." *Science* 248 (4951): 73–76. <https://doi.org/10.1126/science.2321027>.
- Deo, Claire, Ahmed S. Abdelfattah, Hersh K. Bhargava, Adam J. Berro, Natalie Falco, Benjamien Moeyaert, Mariam Chupanova, Luke D. Lavis, and Eric R. Schreier. 2020. "Bright and Tunable Far-Red Chemigenetic Indicators." bioRxiv. <https://doi.org/10.1101/2020.01.08.898783>.
- Drobizhev, Mikhail, Nikolay S. Makarov, Shane E. Tillo, Thomas E. Hughes, and Aleksander Rebane. 2011. "Two-Photon Absorption Properties of Fluorescent Proteins." *Nature Methods* 8 (5): 393–99. <https://doi.org/10.1038/nmeth.1596>.
- Emiliani, V., A. E. Cohen, K. Deisseroth, and M. Hausser. 2015. "All-Optical Interrogation of Neural Circuits." *Journal of Neuroscience* 35 (41): 13917–26. <https://doi.org/10.1523/JNEUROSCI.2916-15.2015>.
- Erecińska, Maria, and Ian A. Silver. 1994. "Ions and Energy in Mammalian Brain." *Progress in Neurobiology* 43 (1): 37–71. [https://doi.org/10.1016/0301-0082\(94\)90015-9](https://doi.org/10.1016/0301-0082(94)90015-9).
- Ernst, Oliver P., David T. Lodowski, Marcus Elstner, Peter Hegemann, Leonid S. Brown, and Hideki Kandori. 2014. "Microbial and Animal Rhodopsins Structures, Function and Molecular Mechanisms.Pdf." *Chemical Reviews* 114 (1): 126–63. <https://doi.org/10.1021/cr4003769>.
- Ernst, Oliver P., Pedro A. Sánchez Murcia, Peter Daldrop, Satoshi P. Tsunoda, Suneel Kateriya, and Peter Hegemann. 2008. "Photoactivation of Channelrhodopsin." *Journal of Biological Chemistry* 283 (3): 1637–43. <https://doi.org/10.1074/jbc.M708039200>.
- Evans, S. Wenceslao, Dong-Qing Shi, Mariya Chavarha, Mark H. Plitt, Jiannis Taxidis, Blake Madruga, Jiang Lan Fan, et al. 2023. "A Positively Tuned Voltage Indicator for Extended Electrical Recordings in the Brain." *Nature Methods* 20 (7): 1104–13. <https://doi.org/10.1038/s41592-023-01913-z>.
- Faini, Giulia, Dimitrii Tanese, Clément Molinier, Cécile Telliez, Massilia Hamdani, Francois Blot, Christophe Tourain, et al. 2023. "Ultrafast Light Targeting for High-Throughput Precise Control of Neuronal Networks." *Nature Communications* 14 (1): 1888. <https://doi.org/10.1038/s41467-023-37416-w>.
- Fan, Linlin Z., Simon Kheifets, Urs L. Böhm, Hao Wu, Kiryl D. Piatkevich, Michael E. Xie, Vicente Parot, et al. 2020a. "All-Optical Electrophysiology Reveals the Role of Lateral Inhibition in Sensory Processing in Cortical Layer 1." *Cell* 180 (3): 521–535.e18. <https://doi.org/10.1016/j.cell.2020.01.001>.
- . 2020b. "All-Optical Electrophysiology Reveals the Role of Lateral Inhibition in Sensory Processing in Cortical Layer 1." *Cell* 180 (3): 521–535.e18. <https://doi.org/10.1016/j.cell.2020.01.001>.
- Felix-Ortiz, A. C., A. Burgos-Robles, N. D. Bhagat, C. A. Leppla, and K. M. Tye. 2016. "Bidirectional Modulation of Anxiety-Related and Social Behaviors by Amygdala Projections to the Medial Prefrontal Cortex." *Neuroscience, Animal Models of Neuropsychiatric Disease*, 321 (May): 197–209. <https://doi.org/10.1016/j.neuroscience.2015.07.041>.
- Ferezou, Isabelle, Sonia Bolea, and Carl C. H. Petersen. 2006. "Visualizing the Cortical Representation of Whisker Touch: Voltage-Sensitive Dye Imaging in Freely Moving Mice." *Neuron* 50 (4): 617–29. <https://doi.org/10.1016/j.neuron.2006.03.043>.
- Filipis, Luiza, Laila Ananda Blömer, Jérôme Montnach, Gildas Loussouarn, Michel De Waard, and Marco Canepari. 2023. "Nav1.2 and BK Channel Interaction Shapes the Action Potential in the Axon Initial Segment." *The Journal of Physiology* 601 (10): 1957–79. <https://doi.org/10.1113/JP283801>.
- Fisher, Jonathan A. N., Jonathan R. Barchi, Cristin G. Welle, Gi-Ho Kim, Paul Kosterin, Ana Lía Obaid, Arjun G. Yodh, Diego Contreras, and Brian M. Salzberg. 2008. "Two-Photon Excitation of Potentiometric Probes Enables Optical Recording of Action Potentials From Mammalian Nerve Terminals In Situ." *Journal of Neurophysiology* 99 (3): 1545–53. <https://doi.org/10.1152/jn.00929.2007>.

- Foust, Amanda J., Valeria Zampini, Dimitrii Tanese, Eirini Papagiakoumou, and Valentina Emiliani. 2015. "Computer-Generated Holography Enhances Voltage Dye Fluorescence Discrimination in Adjacent Neuronal Structures." *Neurophotonics* 2 (2): 021007. <https://doi.org/10.1117/1.NPh.2.2.021007>.
- Fus-Kujawa, Agnieszka, Pawel Prus, Karolina Bajdak-Rusinek, Paulina Teper, Katarzyna Gawron, Agnieszka Kowalczyk, and Aleksander L. Sieron. 2021. "An Overview of Methods and Tools for Transfection of Eukaryotic Cells in Vitro." *Frontiers in Bioengineering and Biotechnology* 9. <https://www.frontiersin.org/articles/10.3389/fbioe.2021.701031>.
- Golan, Lior, and Shy Shoham. 2009. "Speckle Elimination Using Shift-Averaging in High-Rate Holographic Projection." *Optics Express* 17 (3): 1330–39. <https://doi.org/10.1364/OE.17.001330>.
- Gong, Yiyang. 2015. "The Evolving Capabilities of Rhodopsin-Based Genetically Encoded Voltage Indicators." *Current Opinion in Chemical Biology*, Molecular imaging, 27 (August): 84–89. <https://doi.org/10.1016/j.cbpa.2015.05.006>.
- Gong, Yiyang, Cheng Huang, Jin Zhong Li, Benjamin F. Grewe, Yanping Zhang, Stephan Eismann, and Mark J. Schnitzer. 2015. "High-Speed Recording of Neural Spikes in Awake Mice and Flies with a Fluorescent Voltage Sensor." *Science* 350 (6266): 1361–66. <https://doi.org/10.1126/science.aab0810>.
- Govorunova, Elena G., Yueyang Gou, Oleg A. Sineshchekov, Hai Li, Xiaoyu Lu, Yumei Wang, Leonid S. Brown, François St-Pierre, Mingshan Xue, and John L. Spudich. 2022. "Kalium Channelrhodopsins Are Natural Light-Gated Potassium Channels That Mediate Optogenetic Inhibition." *Nature Neuroscience* 25 (7): 967–74. <https://doi.org/10.1038/s41593-022-01094-6>.
- Govorunova, Elena G., Oleg A. Sineshchekov, Roger Janz, Xiaoqin Liu, and John L. Spudich. 2015. "Natural Light-Gated Anion Channels: A Family of Microbial Rhodopsins for Advanced Optogenetics." *Science* 349 (6248): 647–50. <https://doi.org/10.1126/science.aaa7484>.
- Govorunova, Elena G., Oleg A. Sineshchekov, Hai Li, Roger Janz, and John L. Spudich. 2013. "Characterization of a Highly Efficient Blue-Shifted Channelrhodopsin from the Marine Alga *Platymonas Subcordiformis*." *Journal of Biological Chemistry* 288 (41): 29911–22. <https://doi.org/10.1074/jbc.M113.505495>.
- Gradinaru, Viviana, Kimberly R. Thompson, and Karl Deisseroth. 2008. "ENpHR: A *Natronomonas Halorhodopsin* Enhanced for Optogenetic Applications." *Brain Cell Biology* 36 (1): 129–39. <https://doi.org/10.1007/s11068-008-9027-6>.
- Gradinaru, Viviana, Feng Zhang, Charu Ramakrishnan, Joanna Mattis, Rohit Prakash, Ilka Diester, Inbal Goshen, Kimberly R. Thompson, and Karl Deisseroth. 2010. "Molecular and Cellular Approaches for Diversifying and Extending Optogenetics." *Cell* 141 (1): 154–65. <https://doi.org/10.1016/j.cell.2010.02.037>.
- Grienberger, Christine, and Arthur Konnerth. 2012. "Imaging Calcium in Neurons." *Neuron* 73 (5): 862–85. <https://doi.org/10.1016/j.neuron.2012.02.011>.
- Grødem, Sverre, Ingeborg Nymoen, Guro Helén Vatne, Frederik Sebastian Rogge, Valgerður Björnsdóttir, Kristian Kinden Lensjø, and Marianne Fyhn. 2023. "An Updated Suite of Viral Vectors for in Vivo Calcium Imaging Using Intracerebral and Retro-Orbital Injections in Male Mice." *Nature Communications* 14 (1): 608. <https://doi.org/10.1038/s41467-023-36324-3>.
- Grynkiewicz, G, M Poenie, and R Y Tsien. 1985. "A New Generation of Ca²⁺ Indicators with Greatly Improved Fluorescence Properties." *Journal of Biological Chemistry* 260 (6): 3440–50. [https://doi.org/10.1016/S0021-9258\(19\)83641-4](https://doi.org/10.1016/S0021-9258(19)83641-4).
- Gunaydin, Lisa A., Ofer Yizhar, André Berndt, Vikaas S. Sohal, Karl Deisseroth, and Peter Hegemann. 2010. "Ultrafast Optogenetic Control." *Nature Neuroscience* 13 (3): 387–92. <https://doi.org/10.1038/nn.2495>.

- Han, Xue, and Edward S. Boyden. 2007. "Multiple-Color Optical Activation, Silencing, and Desynchronization of Neural Activity, with Single-Spike Temporal Resolution." Edited by Aldo Rustichini. *PLoS ONE* 2 (3): e299. <https://doi.org/10.1371/journal.pone.0000299>.
- Han, Xue, Xiaofeng Qian, Patrick Stern, Amy S. Chuong, and Edward S. Boyden. 2009. "Informational Lesions: Optical Perturbation of Spike Timing and Neural Synchrony Via Microbial Opsin Gene Fusions." *Frontiers in Molecular Neuroscience* 2. <https://doi.org/10.3389/neuro.02.012.2009>.
- Hayward, Rebecca Frank, F. Phil Brooks, Shang Yang, Shiqiang Gao, and Adam E. Cohen. 2023. "Diminishing Neuronal Acidification by Channelrhodopsins with Low Proton Conduction." *bioRxiv*. <https://doi.org/10.1101/2023.02.07.527404>.
- Hernandez, Oscar, Eirini Papagiakoumou, Dimitrii Tanese, Kevin Fidelin, Claire Wyart, and Valentina Emiliani. 2016. "Three-Dimensional Spatiotemporal Focusing of Holographic Patterns." *Nature Communications* 7 (1): 11928. <https://doi.org/10.1038/ncomms11928>.
- Hires, S. Andrew, Lin Tian, and Loren L. Looger. 2008. "Reporting Neural Activity with Genetically Encoded Calcium Indicators." *Brain Cell Biology* 36 (1): 69–86. <https://doi.org/10.1007/s11068-008-9029-4>.
- Hochbaum, Daniel R., Yongxin Zhao, Samouil L. Farhi, Nathan Klapoetke, Christopher A. Werley, Vikrant Kapoor, Peng Zou, et al. 2014. "All-Optical Electrophysiology in Mammalian Neurons Using Engineered Microbial Rhodopsins." *Nature Methods* 11 (8): 825–33. <https://doi.org/10.1038/nmeth.3000>.
- Hodgkin, A. L., and A. F. Huxley. 1939. "Action Potentials Recorded from Inside a Nerve Fibre." *Nature* 144 (3651): 710–11. <https://doi.org/10.1038/144710a0>.
- Icha, Jaroslav, Michael Weber, Jennifer C. Waters, and Caren Norden. 2017. "Phototoxicity in Live Fluorescence Microscopy, and How to Avoid It." *BioEssays* 39 (8): 1700003. <https://doi.org/10.1002/bies.201700003>.
- Iyer, Vijay, Tycho M. Hoogland, and Peter Saggau. 2006. "Fast Functional Imaging of Single Neurons Using Random-Access Multiphoton (RAMP) Microscopy." *Journal of Neurophysiology* 95 (1): 535–45. <https://doi.org/10.1152/jn.00865.2005>.
- Jackman, Skyler L, Christopher H Chen, Heather L Offermann, Iain R Drew, Bailey M Harrison, Anna M Bowman, Katelyn M Flick, Isabella Flaquer, and Wade G Regehr. 2020. "Cerebellar Purkinje Cell Activity Modulates Aggressive Behavior." Edited by Vatsala Thirumalai and Richard B Ivry. *eLife* 9: e53229. <https://doi.org/10.7554/eLife.53229>.
- Jercog, Pablo, Thomas Rogerson, and Mark J. Schnitzer. 2016. "Large-Scale Fluorescence Calcium-Imaging Methods for Studies of Long-Term Memory in Behaving Mammals." *Cold Spring Harbor Perspectives in Biology* 8 (5): a021824. <https://doi.org/10.1101/cshperspect.a021824>.
- Jin, Lei, Zhou Han, Jelena Platasa, Julian R. A. Wooltorton, Lawrence B. Cohen, and Vincent A. Pieribone. 2012. "Single Action Potentials and Subthreshold Electrical Events Imaged in Neurons with a Fluorescent Protein Voltage Probe." *Neuron* 75 (5): 779–85. <https://doi.org/10.1016/j.neuron.2012.06.040>.
- Johnston, Jamie, Ian D. Forsythe, and Conny Kopp-Scheinpflug. 2010. "SYMPOSIUM REVIEW: Going Native: Voltage-Gated Potassium Channels Controlling Neuronal Excitability." *The Journal of Physiology* 588 (17): 3187–3200. <https://doi.org/10.1113/jphysiol.2010.191973>.
- Kandel, Eric R., John Koester, Sarah Mack, and Steven Siegelbaum, eds. 2021. *Principles of Neural Science*. Sixth edition. New York: McGraw Hill.
- Kannan, Madhuvanathi, Ganesh Vasana, Simon Haziza, Cheng Huang, Radosław Chrapkiewicz, Junjie Luo, Jessica A. Cardin, Mark J. Schnitzer, and Vincent A. Pieribone. 2022. "Dual-Polarity Voltage Imaging of the Concurrent Dynamics of Multiple Neuron Types." *Science* 378 (6619): eabm8797. <https://doi.org/10.1126/science.abm8797>.
- Kannan, Madhuvanathi, Ganesh Vasana, Cheng Huang, Simon Haziza, Jin Zhong Li, Hakan Inan, Mark J. Schnitzer, and Vincent A. Pieribone. 2018. "Fast, in Vivo Voltage Imaging Using a Red Fluorescent Indicator." *Nature Methods* 15 (12): 1108–16. <https://doi.org/10.1038/s41592-018-0188-7>.

- Khorana, H. Gobind, Barry E Knox, Enrico Nasi, Richard Swanson, and Debra A Thompson. 1988. "Expression of a Bovine Rhodopsin Gene in *Xenopus* Oocytes: Demonstration of Light-Dependent Ionic Currents." *PNAS*. <https://doi.org/10.1073/pnas.85.21.7917>.
- Kim, Seulah, Michael L. Wallace, Mahmoud El-Rifai, Alexa R. Knudsen, and Bernardo L. Sabatini. 2022. "Co-Packaging of Opposing Neurotransmitters in Individual Synaptic Vesicles in the Central Nervous System." *Neuron* 110 (8): 1371-1384.e7. <https://doi.org/10.1016/j.neuron.2022.01.007>.
- Klapoetke, Nathan C., Yasunobu Murata, Sung Soo Kim, Stefan R. Pulver, Amanda Birdsey-Benson, Yong Ku Cho, Tania K. Morimoto, et al. 2014. "Independent Optical Excitation of Distinct Neural Populations." *Nature Methods* 11 (3): 338–46. <https://doi.org/10.1038/nmeth.2836>.
- Kleinlogel, Sonja, Ulrich Terpitz, Barbara Legrum, Deniz Gökbüget, Edward S. Boyden, Christian Bamann, Phillip G. Wood, and Ernst Bamberg. 2011. "A Gene-Fusion Strategy for Stoichiometric and Co-Localized Expression of Light-Gated Membrane Proteins." *Nature Methods* 8 (12): 1083–88. <https://doi.org/10.1038/nmeth.1766>.
- Kralj, Joel M., Daniel R. Hochbaum, Adam D. Douglass, and Adam E. Cohen. 2011. "Electrical Spiking in *Escherichia Coli* Probed with a Fluorescent Voltage-Indicating Protein." *Science* 333 (6040): 345–48. <https://doi.org/10.1126/science.1204763>.
- Kuhn, Bernd, and Christopher J. Roome. 2019. "Primer to Voltage Imaging with ANNINE Dyes and Two-Photon Microscopy." *Frontiers in Cellular Neuroscience* 13 (July): 1–15. <https://doi.org/10.3389/fncel.2019.00321>.
- Lacagnina, Anthony F., Emma T. Brockway, Chelsea R. Crovetti, Francis Shue, Meredith J. McCarty, Kevin P. Sattler, Sean C. Lim, Sofia Leal Santos, Christine A. Denny, and Michael R. Drew. 2019. "Distinct Hippocampal Engrams Control Extinction and Relapse of Fear Memory." *Nature Neuroscience* 22 (5): 753–61. <https://doi.org/10.1038/s41593-019-0361-z>.
- Li, Binglun, Mariya Chavarha, Yuho Kobayashi, Satoshi Yoshinaga, Kazunori Nakajima, Michael Z. Lin, and Takafumi Inoue. 2020. "Two-Photon Voltage Imaging of Spontaneous Activity from Multiple Neurons Reveals Network Activity in Brain Tissue." *iScience* 23 (8): 101363. <https://doi.org/10.1016/j.isci.2020.101363>.
- Li, Xiang, Davina V. Gutierrez, M. Gartz Hanson, Jing Han, Melanie D. Mark, Hillel Chiel, Peter Hegemann, Lynn T. Landmesser, and Stefan Herlitze. 2005. "Fast Noninvasive Activation and Inhibition of Neural and Network Activity by Vertebrate Rhodopsin and Green Algae Channelrhodopsin." *Proceedings of the National Academy of Sciences* 102 (49): 17816–21. <https://doi.org/10.1073/pnas.0509030102>.
- Lim, Diana H., Jeffrey M. LeDue, and Timothy H. Murphy. 2015. "Network Analysis of Mesoscale Optical Recordings to Assess Regional, Functional Connectivity." *Neurophotonics* 2 (4): 041405. <https://doi.org/10.1117/1.NPh.2.4.041405>.
- Lin, Michael Z., and Mark J. Schnitzer. 2016. "Genetically Encoded Indicators of Neuronal Activity." *Nature Neuroscience* 19 (9): 1142–53. <https://doi.org/10.1038/nn.4359>.
- Liu, Zhuohe, Xiaoyu Lu, Vincent Villette, Yueyang Gou, Kevin L. Colbert, Shujuan Lai, Sihui Guan, et al. 2022a. "Sustained Deep-Tissue Voltage Recording Using a Fast Indicator Evolved for Two-Photon Microscopy." *Cell* 185 (18): 3408-3425.e29. <https://doi.org/10.1016/j.cell.2022.07.013>.
- . 2022b. "Sustained Deep-Tissue Voltage Recording Using a Fast Indicator Evolved for Two-Photon Microscopy." *Cell* 185 (18): 3408-3425.e29. <https://doi.org/10.1016/j.cell.2022.07.013>.
- Liu, Ziqing, Olivia Chen, J. Blake Joseph Wall, Michael Zheng, Yang Zhou, Li Wang, Haley Ruth Vaseghi, Li Qian, and Jiandong Liu. 2017. "Systematic Comparison of 2A Peptides for Cloning Multi-Genes in a Polycistronic Vector." *Scientific Reports* 7 (1): 2193. <https://doi.org/10.1038/s41598-017-02460-2>.

- Loew, L.M., L.B. Cohen, B.M. Salzberg, A.L. Obaid, and F. Bezanilla. 1985. "Charge-Shift Probes of Membrane Potential. Characterization of Aminostyrylpyridinium Dyes on the Squid Giant Axon." *Biophysical Journal* 47 (1): 71–77. [https://doi.org/10.1016/S0006-3495\(85\)83878-9](https://doi.org/10.1016/S0006-3495(85)83878-9).
- Mager, Thomas, David Lopez de la Morena, Verena Senn, Johannes Schlotte, Anna D'Errico, Katrin Feldbauer, Christian Wrobel, et al. 2018. "High Frequency Neural Spiking and Auditory Signaling by Ultrafast Red-Shifted Optogenetics." *Nature Communications* 9 (1): 1750. <https://doi.org/10.1038/s41467-018-04146-3>.
- Mahn, Mathias, Inbar Saraf-Sinik, Pritish Patil, Mauro Pulin, Eyal Bitton, Nikolaos Karalis, Felicitas Bruentgens, et al. 2021. "Efficient Optogenetic Silencing of Neurotransmitter Release with a Mosquito Rhodopsin." *Neuron* 109 (10): 1621–1635.e8. <https://doi.org/10.1016/j.neuron.2021.03.013>.
- Mardinly, Alan R., Ian Antón Oldenburg, Nicolas C. Pégard, Savitha Sridharan, Evan H. Lyall, Kirill Chesnov, Stephen G. Brohawn, Laura Waller, and Hillel Adesnik. 2018a. "Precise Multimodal Optical Control of Neural Ensemble Activity." *Nature Neuroscience* 21 (6): 881–93. <https://doi.org/10.1038/s41593-018-0139-8>.
- . 2018b. "Precise Multimodal Optical Control of Neural Ensemble Activity." *Nature Neuroscience* 21 (6): 881–93. <https://doi.org/10.1038/s41593-018-0139-8>.
- Marshel, James H., Yoon Seok Kim, Timothy A. Machado, Sean Quirin, Brandon Benson, Jonathan Kadmon, Cephra Raja, et al. 2019. "Cortical Layer-Specific Critical Dynamics Triggering Perception." *Science* 365 (6453): eaaw5202. <https://doi.org/10.1126/science.aaw5202>.
- Marvin, Jonathan S., Bart G. Borghuis, Lin Tian, Joseph Cichon, Mark T. Harnett, Jasper Akerboom, Andrew Gordus, et al. 2013. "An Optimized Fluorescent Probe for Visualizing Glutamate Neurotransmission." *Nature Methods* 10 (2): 162–70. <https://doi.org/10.1038/nmeth.2333>.
- Maschio, Marco dal, Joseph C. Donovan, Thomas O. Helmbrecht, and Herwig Baier. 2017. "Linking Neurons to Network Function and Behavior by Two-Photon Holographic Optogenetics and Volumetric Imaging." *Neuron* 94 (4): 774–789.e5. <https://doi.org/10.1016/j.neuron.2017.04.034>.
- Miyawaki, Atsushi, Juan Llopis, Roger Heim, J. Michael McCaffery, Joseph A. Adams, Mitsuhiro Ikura, and Roger Y. Tsien. 1997. "Fluorescent Indicators for Ca²⁺-based on Green Fluorescent Proteins and Calmodulin." *Nature* 388 (6645): 882–87. <https://doi.org/10.1038/42264>.
- Moretti, Claudio, and Sylvain Gigan. 2020. "Readout of Fluorescence Functional Signals through Highly Scattering Tissue." *Nature Photonics* 14 (6): 361–64. <https://doi.org/10.1038/s41566-020-0612-2>.
- Murata, Yoshimichi, Hirohide Iwasaki, Mari Sasaki, Kazuo Inaba, and Yasushi Okamura. 2005. "Phosphoinositide Phosphatase Activity Coupled to an Intrinsic Voltage Sensor." *Nature* 435 (7046): 1239–43. <https://doi.org/10.1038/nature03650>.
- Nagel, Georg, Doris Ollig, Markus Fuhrmann, Suneel Kateriya, Anna Maria Musti, Ernst Bamberg, and Peter Hegemann. 2002. "Channelrhodopsin-1: A Light-Gated Proton Channel in Green Algae." *Science* 296 (5577): 2395–98. <https://doi.org/10.1126/science.1072068>.
- Nagel, Georg, Tanjef Szellas, Wolfram Huhn, Suneel Kateriya, Nona Adeishvili, Peter Berthold, Doris Ollig, Peter Hegemann, and Ernst Bamberg. 2003. "Channelrhodopsin-2, a Directly Light-Gated Cation-Selective Membrane Channel." *Proceedings of the National Academy of Sciences* 100 (24): 13940–45. <https://doi.org/10.1073/pnas.1936192100>.
- Nakai, Junichi, Masamichi Ohkura, and Keiji Imoto. 2001. "A High Signal-to-Noise Ca²⁺ Probe Composed of a Single Green Fluorescent Protein." *Nature Biotechnology* 19 (2): 137–41. <https://doi.org/10.1038/84397>.
- Neher, Erwin, and Bert Sakmann. 1976. "Single-Channel Currents Recorded from Membrane of Denervated Frog Muscle Fibres." *Nature* 260 (5554): 799–802. <https://doi.org/10.1038/260799a0>.
- Oron, Dan, and Yaron Silberberg. 2015. "Temporal Focusing Microscopy." *Cold Spring Harbor Protocols* 2015 (2): pdb.top085928. <https://doi.org/10.1101/pdb.top085928>.

- Oron, Dan, Eran Tal, and Yaron Silberberg. 2005. "Scanningless Depth-Resolved Microscopy." *Optics Express* 13 (5): 1468–76. <https://doi.org/10.1364/OPEX.13.001468>.
- Packer, Adam M., Lloyd E. Russell, Henry W. P. Dagleish, and Michael Häusser. 2015. "Simultaneous All-Optical Manipulation and Recording of Neural Circuit Activity with Cellular Resolution in Vivo." *Nature Methods* 12 (2): 140–46. <https://doi.org/10.1038/nmeth.3217>.
- Papagiakoumou, Eirini, Francesca Anselmi, Aurélien Bègue, Vincent de Sars, Jesper Glückstad, Ehud Y Isacoff, and Valentina Emiliani. 2010. "Scanless Two-Photon Excitation of Channelrhodopsin-2." *Nature Methods* 7 (10): 848–54. <https://doi.org/10.1038/nmeth.1505>.
- Papagiakoumou, Eirini, Aurélien Bègue, Ben Leshem, Osip Schwartz, Brandon M. Stell, Jonathan Bradley, Dan Oron, and Valentina Emiliani. 2013. "Functional Patterned Multiphoton Excitation Deep inside Scattering Tissue." *Nature Photonics* 7: 274–78.
- Papagiakoumou, Eirini, Emiliano Ronzitti, and Valentina Emiliani. 2020. "Scanless Two-Photon Excitation with Temporal Focusing." *Nature Methods* 17 (6): 571–81. <https://doi.org/10.1038/s41592-020-0795-y>.
- Papagiakoumou, Eirini, Vincent de Sars, Dan Oron, and Valentina Emiliani. 2008. "Patterned Two-Photon Illumination by Spatiotemporal Shaping of Ultrashort Pulses." *Optics Express* 16 (26): 22039–47. <https://doi.org/10.1364/OE.16.022039>.
- Paredes, R. Madelaine, Julie C. Etzler, Lora Talley Watts, Wei Zheng, and James D. Lechleiter. 2008. "Chemical Calcium Indicators." *Methods, Optical Methods in Calcium Signaling*, 46 (3): 143–51. <https://doi.org/10.1016/j.ymeth.2008.09.025>.
- Peng, Yangfan, Franz Xaver Mittermaier, Henrike Planert, Ulf Christoph Schneider, Henrik Alle, and Jörg Rolf Paul Geiger. 2019. "High-Throughput Microcircuit Analysis of Individual Human Brains through next-Generation Multineuron Patch-Clamp." Edited by John Huguenard, Eve Marder, and Tim Jarsky. *ELife* 8 (November): e48178. <https://doi.org/10.7554/eLife.48178>.
- Perkins, Katherine L. 2006. "Cell-Attached Voltage-Clamp and Current-Clamp Recording and Stimulation Techniques in Brain Slices." *Journal of Neuroscience Methods* 154 (1–2): 1–18. <https://doi.org/10.1016/j.jneumeth.2006.02.010>.
- Peterka, Darcy S., Hiroto Takahashi, and Rafael Yuste. 2011. "Imaging Voltage in Neurons." *Neuron* 69 (1): 9–21. <https://doi.org/10.1016/j.neuron.2010.12.010>.
- Piatkevich, Kiryl D., Erica E. Jung, Christoph Straub, Changyang Linghu, Demian Park, Ho-Jun Suk, Daniel R. Hochbaum, et al. 2018. "A Robotic Multidimensional Directed Evolution Approach Applied to Fluorescent Voltage Reporters." *Nature Chemical Biology* 14 (4): 352–60. <https://doi.org/10.1038/s41589-018-0004-9>.
- Platisa, Jelena, Xin Ye, Allison M. Ahrens, Chang Liu, Ichun Anderson Chen, Ian G. Davison, Lei Tian, Vincent A. Pieribone, and Jerry L. Chen. 2023. "High-Speed Low-Light in Vivo Two-Photon Voltage Imaging of Large Neuronal Populations." *Nature Methods*, March, 1–9. <https://doi.org/10.1038/s41592-023-01820-3>.
- Podgorski, Kaspar, and Gayathri Ranganathan. 2016. "Brain Heating Induced by Near-Infrared Lasers during Multiphoton Microscopy." *Journal of Neurophysiology* 116 (3): 1012–23. <https://doi.org/10.1152/jn.00275.2016>.
- Prevedel, Robert, Aart J Verhoef, Alejandro J Pernía-Andrade, Siegfried Weisenburger, Ben S Huang, Tobias Nöbauer, Alma Fernández, et al. 2016a. "Fast Volumetric Calcium Imaging across Multiple Cortical Layers Using Sculpted Light." *Nature Methods* 13 (12): 1021–28. <https://doi.org/10.1038/nmeth.4040>.
- Prevedel, Robert, Aart J. Verhoef, Alejandro J. Pernía-Andrade, Siegfried Weisenburger, Ben S. Huang, Tobias Nöbauer, Alma Fernández, et al. 2016b. "Fast Volumetric Calcium Imaging across Multiple Cortical Layers Using Sculpted Light." *Nature Methods* 13 (12): 1021–28. <https://doi.org/10.1038/nmeth.4040>.
- Printz, Yoav, Pritish Patil, Mathias Mahn, Asaf Benjamin, Anna Litvin, Rivka Levy, Max Bringmann, and Ofer Yizhar. 2023. "Determinants of Functional Synaptic Connectivity among Amygdala-

- Projecting Prefrontal Cortical Neurons in Male Mice." *Nature Communications* 14 (1): 1667. <https://doi.org/10.1038/s41467-023-37318-x>.
- Purves, Dale, and Stephen Mark Williams, eds. 2004. *Neuroscience*. 3. ed. Sunderland, Mass: Sinauer Associates.
- Quicke, Peter, Chenchen Song, Eric J. McKimm, Milena M. Milosevic, Carmel L. Howe, Mark Neil, Simon R. Schultz, Srdjan D. Antic, Amanda J. Foust, and Thomas Knöpfel. 2019. "Single-Neuron Level One-Photon Voltage Imaging With Sparsely Targeted Genetically Encoded Voltage Indicators." *Frontiers in Cellular Neuroscience* 13. <https://www.frontiersin.org/articles/10.3389/fncel.2019.00039>.
- Raimondo, Joseph V., Louise Kay, Tommas J. Ellender, and Colin J. Akerman. 2012. "Optogenetic Silencing Strategies Differ in Their Effects on Inhibitory Synaptic Transmission." *Nature Neuroscience* 15 (8): 1102–4. <https://doi.org/10.1038/nn.3143>.
- Rial Verde, Emiliano, Leonardo Zayat, Roberto Etchenique, and Rafael Yuste. 2008. "Photorelease of GABA with Visible Light Using an Inorganic Caging Group." *Frontiers in Neural Circuits* 2. <https://www.frontiersin.org/articles/10.3389/neuro.04.002.2008>.
- Rickgauer, John Peter, Karl Deisseroth, and David W Tank. 2014. "Simultaneous Cellular-Resolution Optical Perturbation and Imaging of Place Cell Firing Fields." *Nature Neuroscience* 17 (12): 1816–24. <https://doi.org/10.1038/nn.3866>.
- Rickgauer, John Peter, and David W. Tank. 2009. "Two-Photon Excitation of Channelrhodopsin-2 at Saturation." *Proceedings of the National Academy of Sciences* 106 (35): 15025–30. <https://doi.org/10.1073/pnas.0907084106>.
- Robinson, Nick T. M., Lucie A. L. Descamps, Lloyd E. Russell, Moritz O. Buchholz, Brendan A. Bicknell, Georgy K. Antonov, Joanna Y. N. Lau, Rebecca Nutbrown, Christoph Schmidt-Hieber, and Michael Häusser. 2020. "Targeted Activation of Hippocampal Place Cells Drives Memory-Guided Spatial Behavior." *Cell* 183 (6): 1586-1599.e10. <https://doi.org/10.1016/j.cell.2020.09.061>.
- Rodriguez-Rozada, Silvia, Jonas Wietek, Federico Tenedini, Kathrin Sauter, Neena Dhiman, Peter Hegemann, Peter Soba, and J. Simon Wiegert. 2022. "Aion Is a Bistable Anion-Conducting Channelrhodopsin That Provides Temporally Extended and Reversible Neuronal Silencing." *Communications Biology* 5 (1): 1–15. <https://doi.org/10.1038/s42003-022-03636-x>.
- Ronzitti, E, R Conti, V Zampini, D Tanese, A J Foust, N Klapoetke, E S Boyden, E Papagiakoumou, and V Emiliani. 2017. "Sub-Millisecond Optogenetic Control of Neuronal Firing with Two-Photon Holographic Photoactivation of Chronos." *The Journal of Neuroscience* 37 (44): 10679–89. <https://doi.org/10.1523/JNEUROSCI.1246-17.2017>.
- Siegel, Micah S, and Ehud Y Isacoff. 1997. "A Genetically Encoded Optical Probe of Membrane Voltage." *Neuron* 19 (4): 735–41. [https://doi.org/10.1016/S0896-6273\(00\)80955-1](https://doi.org/10.1016/S0896-6273(00)80955-1).
- Sims, Ruth R., Imane Bendifallah, Kris Blanchard, Dimitrii Tanese, Valentina Emiliani, and Eirini Papagiakoumou. 2023. "Optical Manipulation and Recording of Neural Activity with Wavefront Engineering." In *All-Optical Methods to Study Neuronal Function*, edited by Eirini Papagiakoumou, 1–48. *Neuromethods*. New York, NY: Springer US. https://doi.org/10.1007/978-1-0716-2764-8_1.
- Sjulson, Lucas, and Gero Miesenböck. 2008. "Rational Optimization and Imaging in Vivo of a Genetically Encoded Optical Voltage Reporter." *Journal of Neuroscience* 28 (21): 5582–93. <https://doi.org/10.1523/JNEUROSCI.0055-08.2008>.
- Song, Alexander, Adam S. Charles, Sue Ann Koay, Jeff L. Gauthier, Stephan Y. Thiberge, Jonathan W. Pillow, and David W. Tank. 2017. "Volumetric Two-Photon Imaging of Neurons Using Stereoscopy (VTwINS)." *Nature Methods* 14 (4): 420–26. <https://doi.org/10.1101/073742>.
- Song, Chenchen, Quyen B. Do, Srdjan D. Antic, and Thomas Knöpfel. 2017. "Transgenic Strategies for Sparse but Strong Expression of Genetically Encoded Voltage and Calcium Indicators." *International Journal of Molecular Sciences* 18 (7): 1461. <https://doi.org/10.3390/ijms18071461>.

- Ståhl, Stefan, Per-Åke Nygren, and Mathias Uhlén. 1997. "Strategies for Gene Fusions." In *Recombinant Gene Expression Protocols*, by Rocky S. Tuan, 62:37–54. New Jersey: Humana Press. <https://doi.org/10.1385/0-89603-480-1:37>.
- Storace, Douglas A., Oliver R. Braubach, Lei Jin, Lawrence B. Cohen, and Uhna Sung. 2015. "Monitoring Brain Activity with Protein Voltage and Calcium Sensors." *Scientific Reports* 5 (1): 10212. <https://doi.org/10.1038/srep10212>.
- St-Pierre, François, Jesse D. Marshall, Ying Yang, Yiyang Gong, Mark J. Schnitzer, and Michael Z. Lin. 2014. "High-Fidelity Optical Reporting of Neuronal Electrical Activity with an Ultrafast Fluorescent Voltage Sensor." *Nature Neuroscience* 17 (6): 884–89. <https://doi.org/10.1038/nn.3709>.
- Südhof, Thomas C. 2012. "Calcium Control of Neurotransmitter Release." *Cold Spring Harbor Perspectives in Biology* 4 (1): a011353. <https://doi.org/10.1101/cshperspect.a011353>.
- Svoboda, Karel, and Ryohei Yasuda. 2006. "Principles of Two-Photon Excitation Microscopy and Its Applications to Neuroscience." *Neuron* 50 (6): 823–39. <https://doi.org/10.1016/j.neuron.2006.05.019>.
- Tanese, Dimitrii, Ju-Yun Weng, Valeria Zampini, Vincent De Sars, Marco Canepari, Balazs Rozsa, Valentina Emiliani, and Dejan Zecevic. 2017. "Imaging Membrane Potential Changes from Dendritic Spines Using Computer-Generated Holography." *Neurophotonics* 4 (3): 031211. <https://doi.org/10.1117/1.NPh.4.3.031211>.
- Tang, Wannan, Ingrid Ehrlich, Steffen B. E. Wolff, Ann-Marie Michalski, Stefan Wöfl, Mazahir T. Hasan, Andreas Lüthi, and Rolf Sprengel. 2009. "Faithful Expression of Multiple Proteins via 2A-Peptide Self-Processing: A Versatile and Reliable Method for Manipulating Brain Circuits." *Journal of Neuroscience* 29 (27): 8621–29. <https://doi.org/10.1523/JNEUROSCI.0359-09.2009>.
- Tasaki, Ichiji, A Watanabe, R Sandlin, and L Carnay. 1968. "Changes in Fluorescence, Turbidity, and Birefringence Associated with Nerve Excitation." 1968. <https://doi.org/10.1073/pnas.61.3.883>.
- Theer, P, and W Denk. 2006. "On the Fundamental Imaging-Depth Limit in Two-Photon Microscopy." *J Opt Soc Am A Opt Image Sci Vis* 23 (12): 3139–49.
- Theer, P, M T Hasan, and W Denk. 2003. "Two-Photon Imaging to a Depth of 1000 μm in Living Brains by Use of a Ti : Al₂O₃ Regenerative Amplifier." *Optics Letters* 28 (12): 1022–24.
- Thompson, Kimberly R., and Chris Towne. 2018. "A Hitchhiker's Guide to the Selection of Viral Vectors for Optogenetic Studies." In *Optogenetics: A Roadmap*, edited by Albrecht Stroh, 1–23. Neuromethods. New York, NY: Springer. https://doi.org/10.1007/978-1-4939-7417-7_1.
- Tritsch, Nicolas X., Adam J. Granger, and Bernardo L. Sabatini. 2016. "Mechanisms and Functions of GABA Co-Release." *Nature Reviews Neuroscience* 17 (3): 139–45. <https://doi.org/10.1038/nrn.2015.21>.
- Tsien, R. Y. 1980. "New Calcium Indicators and Buffers with High Selectivity against Magnesium and Protons: Design, Synthesis, and Properties of Prototype Structures." *Biochemistry* 19 (11): 2396–2404. <https://doi.org/10.1021/bi00552a018>.
- Ventalon, C, and J Mertz. 2005. "Quasi-Confocal Fluorescence Sectioning with Dynamic Speckle Illumination." *Optics Letters* 30: 3350–52.
- Vierock, Johannes, Enrico Peter, Christiane Grimm, Andrey Rozenberg, I-Wen Chen, Linda Tillert, Alejandro G. Castro Scalise, et al. 2022. "WiChR, a Highly Potassium-Selective Channelrhodopsin for Low-Light One- and Two-Photon Inhibition of Excitable Cells." *Science Advances* 8 (49): eadd7729. <https://doi.org/10.1126/sciadv.add7729>.
- Villette, Vincent, Mariya Chavarha, Ivan K. Dimov, Jonathan Bradley, Lagnajeet Pradhan, Benjamin Mathieu, Stephen W. Evans, et al. 2019. "Ultrafast Two-Photon Imaging of a High-Gain Voltage Indicator in Awake Behaving Mice." *Cell* 179 (7): 1590-1608.e23. <https://doi.org/10.1016/j.cell.2019.11.004>.

- Walt, Stéfan Van Der, Johannes L. Schönberger, Juan Nunez-Iglesias, François Boulogne, Joshua D. Warner, Neil Yager, Emmanuelle Goullart, and Tony Yu. 2014. "Scikit-Image: Image Processing in Python." *PeerJ* 2014 (1): 1–18. <https://doi.org/10.7717/peerj.453>.
- Watanabe, Miho, and Atsuo Fukuda. 2015. "Development and Regulation of Chloride Homeostasis in the Central Nervous System." *Frontiers in Cellular Neuroscience* 9. <https://www.frontiersin.org/articles/10.3389/fncel.2015.00371>.
- Wiegert, J. Simon, Mathias Mahn, Matthias Prigge, Yoav Printz, and Ofer Yizhar. 2017. "Silencing Neurons: Tools, Applications, and Experimental Constraints." *Neuron* 95 (3): 504–29. <https://doi.org/10.1016/j.neuron.2017.06.050>.
- Wietek, Jonas, and Matthias Prigge. 2016. "Enhancing Channelrhodopsins: An Overview." In *Optogenetics*, edited by Arash Kianianmomeni, 1408:141–65. Methods in Molecular Biology. New York, NY: Springer New York. https://doi.org/10.1007/978-1-4939-3512-3_10.
- Wu, Jianglai, Yajie Liang, Shuo Chen, Ching Lung Hsu, Mariya Chavarha, Stephen W. Evans, Dongqing Shi, Michael Z. Lin, Kevin K. Tsia, and Na Ji. 2020a. "Kilohertz Two-Photon Fluorescence Microscopy Imaging of Neural Activity in Vivo." *Nature Methods* 17 (3): 287–90. <https://doi.org/10.1038/s41592-020-0762-7>.
- Wu, Jianglai, Yajie Liang, Shuo Chen, Ching-Lung Hsu, Mariya Chavarha, Stephen W. Evans, Dongqing Shi, Michael Z. Lin, Kevin K. Tsia, and Na Ji. 2020b. "Kilohertz Two-Photon Fluorescence Microscopy Imaging of Neural Activity in Vivo." *Nature Methods* 17 (3): 287–90. <https://doi.org/10.1038/s41592-020-0762-7>.
- Xiao, Sheng, Eric Lowet, Howard J. Gritton, Pierre Fabris, Yangyang Wang, Jack Sherman, Rebecca A. Mount, et al. 2021a. "Large-Scale Voltage Imaging in Behaving Mice Using Targeted Illumination." *iScience* 24 (11). <https://doi.org/10.1016/j.isci.2021.103263>.
- . 2021b. "Large-Scale Voltage Imaging in Behaving Mice Using Targeted Illumination." *iScience* 24 (11): 103263. <https://doi.org/10.1016/j.isci.2021.103263>.
- Xie, Caroline, John Power, and Asheeta A. Prasad. 2022. "Bidirectional Optogenetic Modulation of the Subthalamic Nucleus in a Rodent Model of Parkinson's Disease." *Frontiers in Neuroscience* 16. <https://www.frontiersin.org/articles/10.3389/fnins.2022.848821>.
- Xue, Yi, Laura Waller, Hillel Adesnik, and Nicolas Pégard. 2022. "Three-Dimensional Multi-Site Random Access Photostimulation (3D-MAP)." *eLife* 11: e73266. <https://doi.org/10.7554/eLife.73266>.
- Zhang, Feng, Li-Ping Wang, Martin Brauner, Jana F. Liewald, Kenneth Kay, Natalie Watzke, Phillip G. Wood, et al. 2007. "Multimodal Fast Optical Interrogation of Neural Circuitry." *Nature* 446 (7136): 633–39. <https://doi.org/10.1038/nature05744>.
- Zhang, Tong, Oscar Hernandez, Radosław Chrapkiewicz, Adam Shai, Mark J. Wagner, Yanping Zhang, Cheng Hsun Wu, et al. 2019. "Kilohertz Two-Photon Brain Imaging in Awake Mice." *Nature Methods* 16 (11): 1119–22. <https://doi.org/10.1038/s41592-019-0597-2>.
- Zhao, Yongxin, Satoko Araki, Jiahui Wu, Takayuki Teramoto, Yu-Fen Chang, Masahiro Nakano, Ahmed S. Abdelfattah, et al. 2011. "An Expanded Palette of Genetically Encoded Ca²⁺ Indicators." *Science* 333 (6051): 1888–91. <https://doi.org/10.1126/science.1208592>.
- Zhou, Xinqi, Kayla J. Belavek, and Evan W. Miller. 2021. "Origins of Ca²⁺ Imaging with Fluorescent Indicators." *Biochemistry* 60 (46): 3547–54. <https://doi.org/10.1021/acs.biochem.1c00350>.
- Zhu, Guanghao, James van Howe, Michael Durst, Warren Zipfel, and Chris Xu. 2005. "Simultaneous Spatial and Temporal Focusing of Femtosecond Pulses." *Optics Express* 13 (6): 2153–59. <https://doi.org/83023> [pii].
- Zincarelli, Carmela, Stephen Soltys, Giuseppe Rengo, and Joseph E Rabinowitz. 2008. "Analysis of AAV Serotypes 1–9 Mediated Gene Expression and Tropism in Mice After Systemic Injection." *Molecular Therapy* 16 (6): 1073–80. <https://doi.org/10.1038/mt.2008.76>.

ANNEX: Scanless two-photon voltage imaging: Supplementary Information

Ruth R. Sims*¹, Imane Bendifallah*¹, Christiane Grimm¹, Aysha Mohamed-Lafirdeen¹, Xiaoyu Lu², François St-Pierre^{2,3,4}, Eirini Papagiakoumou^{1§}, and Valentina Emiliani^{1§}

¹Institut de la Vision, Sorbonne Université, INSERM, CNRS, F-75012 Paris, France

²Systems, Synthetic, and Physical Biology Program, Rice University, Houston, TX, USA

³Department of Neuroscience and Department of Biochemistry and Molecular Biology, Houston, TX, USA

⁴Department of Electrical and Computer Engineering, Rice University, Houston, TX, USA

*Equal contribution

§valentina.emiliani@inserm.fr

§eirini.papagiakoumou@inserm.fr

This file includes:

- Supplementary Notes 1 - 3
- Supplementary Tables 1 - 3
- Supplementary Methods
- Supplementary Figures 1 - 20
- Supplementary References

Table of contents

Supplementary Note 1 – Experimental setup used for widefield 2P-voltage imaging

- Supplementary Table 1: List of components
- Supplementary Table 2: Experimental configurations

Supplementary Note 2 – Optimal excitation and detection for widefield voltage imaging

Supplementary Note 3 – Extracting fluorescence time series from widefield voltage imaging data

Supplementary Methods

- Simulations
- Supplementary Table 3: Simulation parameters
- Calibration procedure for multi-cell experiments

Supplementary Figures

1. Optical setup for scanless two-photon voltage imaging
2. Investigation of the optimal excitation profile for parallel illumination in combination with a widefield detection axis for an isolated spherical cell
3. Investigation of the optimal excitation profile for parallel illumination in combination with a widefield detection axis for a spherical cell in a densely packed configuration of labelled cells
4. Investigation of the optimal excitation profile for 2P voltage imaging with temporally focused low-NA Gaussian beams
5. Investigation of the impact of the speckle in holographic spots for 2P voltage imaging with temporally focused Computer-Generated Holography
6. Summary of data analysis pipeline
7. Evaluation of analysis pipeline used to generate fluorescent timeseries from raw voltage imaging data acquired using scanless two-photon voltage imaging in combination with a widefield detection axis
8. Comparison of different parallel illumination approaches for scanless two-photon voltage imaging (protocol 1)
9. Comparison of different parallel illumination approaches for scanless two-photon voltage imaging (protocol 2)
10. Comparison of different parallel illumination approaches for scanless two-photon voltage imaging (protocol 3)
11. Fluorescence-Voltage (F-V/Sensitivity) curves for the genetically encoded voltage indicator JEDI-2P-kv
12. Comparison of scanless two-photon voltage imaging between isolated CHO cells and densely labelled hippocampal organotypic slices
13. Characterisation of scanless two-photon voltage imaging for imaging trains of action potentials
14. Imaging spontaneous activity in hippocampal organotypic slices with scanless two-photon voltage imaging
15. Long term imaging of spontaneous activity in hippocampal organotypic slices with scanless two-photon voltage imaging
16. Investigation of potential physiological perturbations induced by scanless two-photon voltage imaging with a high-repetition rate laser
17. Investigation of potential physiological perturbations induced by scanless two-photon voltage imaging with a low-repetition rate laser
18. Simultaneous imaging of spontaneous activity in multiple neurons in hippocampal organotypic slices with scanless two-photon voltage imaging
19. Characterization of two-photon voltage imaging with JEDI-2P-kv using an excitation wavelength of 1030 nm
20. Electrophysiological characterization of photostimulation of neurons expressing ChroME-ST in the dentate gyrus of hippocampal organotypic slices

Supplementary References

Supplementary Note 1 – Experimental setup used for widefield 2P-voltage imaging

Component	Description	Manufacturer, Part Reference
Laser A	Tuneable femtosecond source, tuned to 920, 940 or 1030 nm (1.4 W, 80 MHz, 100 fs)	Coherent, Chameleon Discovery
Laser B	Femtosecond source, fixed output 920 nm (4W, 80 MHz, 100 fs)	Alcor, Spark Lasers
Laser C	Custom OPA pumped by amplified laser, fixed output 940 nm (0.5-0.5 W, 250 kHz, 100 fs)	Amplitude, Satsuma Niji
$\lambda/2$	Half-wave plate	Thorlabs, WPHSM05-980
PBS	Polarizing beam splitter	Thorlabs, CCM1-PBS253/M
MS	Mechanical Shutter or high-speed modulator	Thorlabs, SH05R/M or OM6NH/M
L1	Lens, focal length = 80 mm	Thorlabs, AC508-80-B
L2	Lens, focal length = 300 mm (GPC) or 200 mm (Low-NA Gaussian beam)	Thorlabs, AC508-300-B or AC508-200-B
SLM1	Spatial Light Modulator, 600 x 800 pixels, 20 μm pitch	Hamamatsu, LCOS 10468-07
L3	Lens, focal length = 400 mm	Thorlabs, AC508-400-B
PCF	Phase Contrast Filter, 60 μm radius	Double Helix Optics, custom design
L4	Lens, focal length = 300 mm	Thorlabs, AC508-300-B
G1	Blazed diffraction grating, 600 lines/mm	Richardson Gratings
L5	Lens, focal length = 500 mm	Thorlabs, AC508-500-B
SLM2	Spatial Light Modulator, 600 x 800 pixels, 20 μm pitch	Hamamatsu, LCOS 10468-07
L6	Lens, focal length = 500 mm	Thorlabs, AC508-500-B
L7	Lens, focal length = 300 mm	Thorlabs, AC508-300-B
L8	Lens, focal length = -75 mm	Thorlabs, LC1258-B
L9	Lens, focal length = 500 mm	Thorlabs, AC508-500-B
SLM3	Spatial Light Modulator, 1272 x 1024 pixels, 12.5 μm pitch	Hamamatsu, LCOS X13138-07
L10	Lens, focal length = 750 mm	Thorlabs, AC508-750-B
G2	Blazed diffraction grating, 600 lines/mm	Thorlabs, GR50-0610
L11	Lens, focal length = 500 mm	Thorlabs, AC508-500-B
L12	Lens, focal length = 300 mm	Thorlabs, AC508-300-B
Obj	Objective lens, 40X, 0.8 NA, f = 5 mm, water	Nikon, CFI APO NIR
DC	Dichroic mirror, 70 x 50 mm	Semrock, #FF705-Di01
QB	Quad-band filter, 405, 488, 561, 640 nm	Chroma, ZET405/488/561/640
BP	Band-pass filters, 525/50 and 605/7	Chroma ET525/50, ET605/7
SP	Short-pass filter, 2P excitation fluorescence blocker	Semrock #FF01-750sp
LEDs	LED sources, 490 and 430 nm	Thorlabs, M490L4 or M430L5
TL	Tube lens	Thorlabs, TTL200-A
Camera A	sCMOS camera, 6.5 μm pixel, 95 % QE	Photometrics Kinetix
Camera B	sCMOS camera, 6.5 μm pixel, 85 % QE	Hamamatsu ORCA Flash 4.0

Supplementary Table 1: List of components

Figure	Panel	Samples	Expressing proteins	Bath temp (° C)	Laser source	λ (nm)	Camera	Method	Average power per cell (mW)	Power density (mW μm ⁻²)	Acquisition rate (Hz)	Max FOV (μm x μm)	Illumination time (ms)	Number of cells (n)
2	b (left)	CHO cells	JEDI-2P-kv	21 - 23	A	940	A	GPC, Gauss, CGH	100	0.88	100	250 x 250	3000	17 (GPC), 9 (Gauss), 15 (CGH)
	b (middle) - c	CHO cells	JEDI-2P-kv	21 - 23	A	940	A	GPC, Gauss, CGH	75 - 175	0.66 - 1.55	100	250 x 250	200 * 3	12 (GPC), 8 (Gauss), 13 (CGH)
	b (right)	CHO cells	JEDI-2P-kv	21 - 23	A	940	A	GPC, Gauss, CGH	150 - 175	1.33 - 1.55	1000	43 x 250	500	11 (GPC), 8 (Gauss), 11 (CGH)
3	c - d	Organotypic	JEDI-2P-kv	31-35	A	940	A	GPC	75 - 175	0.66 - 1.55	variable	43-86 x 250	10 * 50	4 - 6
	e - f	Organotypic	JEDI-2P-kv	31-35	B	920	B	GPC	75 - 175	0.66 - 1.55	variable	43-86 x 250	variable	2 - 5
4	a - d	Organotypic	JEDI-2P-kv	31-35	B	920	B	GPC	125	1.1	1000	43 x 250	40 * 6	6
5	a - b - c	Organotypic	JEDI-2P-kv	31-35	A	940	A	GPC	150	1.33	1000	43 x 250	30000	>10; 5 slices from multiple transductions
6	a - c	Organotypic	JEDI-2P-kv	31-35	C	940	A	GPC	2.5 - 10	0.02 - 0.09	1000	43 x 250	30000	Up to 8 cells simultaneously
7	b	Organotypic	ChroME-ST/JEDI-2P-kv	31-35	C	940	A	CGH	2.5 - 5	0.02 - 0.04	1000	43 x 250	15	>10 cells per slice from multiple transductions
	c	Organotypic	ChroME-ST/JEDI-2P-kv	31-35	C	940	A	CGH	1.5 - 10	0.01 - 0.09	1000	43 x 250	15 * 5	27 - 33
	d - f	Organotypic	ChroME-ST/JEDI-2P-kv	31-35	C	940	A	CGH	2.5 - 9	0.02 - 0.08	1000	43 x 250	15 * 5	27 - 33
8	d - e	Organotypic	ChroME-ST/JEDI-2P-kv	31-35	C	940	A	CGH	2.5 - 5	0.02 - 0.04	500	86 x 250	15	Up to 10 cells
S7	a - e	CHO cells	JEDI-2P-kv	21 - 23	A	940	A	GPC, Gauss, CGH	100	0.88	100	250 x 250	3000	41
S8	a - l	CHO cells	JEDI-2P-kv	21 - 23	A	940	A	GPC, Gauss, CGH	100	0.88	100	250 x 250	3000	17 (GPC), 9 (Gauss), 15 (CGH)

Figure	Panel	Samples	Expressing proteins	Temp (°C)	Laser source	λ (nm)	Camera	Method	Average power per cell (mW)	Power density (mW μm ⁻²)	Acquisition rate (Hz)	Max FOV (μm x μm)	Illumination time (ms)	Number of cells (n)
S9	a - b - c - d	CHO cells	JEDI-2P-kv	21 - 23	A	940	A	GPC, Gauss, CGH	75 - 175	0.66 – 1.55	100	250 x 250	200 * 3	12 (GPC), 8 (Gauss), 13 (CGH)
S10	a - d	CHO cells	JEDI-2P-kv	21 - 23	A	940	A	GPC, Gauss, CGH	150 - 175	1.33 - 1.55	1000	43 x 250	500	11 (GPC), 8 (Gauss), 11 (CGH)
S11	a - c	CHO cells	JEDI-2P-kv	21 - 23	A	940	A	GPC	100	0.88	100	250 x 250	300	8
S12	a - g	CHO cells/ Organotypic	JEDI-2P-kv	21-23/31-35	A	940	A	GPC	100	0.88	100	250 x 250	3000	>15
	h	Organotypic	JEDI-2P-kv	31 - 35	A	940	A	GPC	150	1.3	1000	43 x 250	10	5
S13	a - b	Organotypic	JEDI-2P-kv	31-35	B	920	B	GPC	75	0.66	variable	43-86 x 250	variable	2-5
S14	a - k	Organotypic	JEDI-2P-kv	31-35	A	940	A	GPC	150	1.3	1000	43 x 250	30000	>10; 5 slices
S15	a	Organotypic	JEDI-2P-kv	31-35	A	940	A	GPC	150	1.3	1000	43 x 250	30000 * 36	3
	b	Organotypic	JEDI-2P-kv	31-35	A	940	A	GPC	150	1.3	500	86 x 250	60000 * 20	3
S16	b	Organotypic	JEDI-2P-kv	31-35	A	940	A	CGH	75 - 175	0.66 - 1.55	1000	43 x 250	10 * 50	4 - 8
S17	a	Organotypic	JEDI-2P-kv	31 -35	C	940	A	CGH	1.5 - 5	0.01 - 0.04	1000	43 x 250	10 * 50	2 - 5
	c	Organotypic	JEDI-2P-kv	31 -35	C	940	A	CGH	1.5 - 5	0.01 - 0.04	1000	43 x 250	10 * 50	2 - 5
S18	all	Organotypic	JEDI-2P-kv	31 - 35	C	940	A	GPC	2.5 - 5	0.02 - 0.04	1000	43 x 250	30000	Up to 8 cells simultaneously
S19	c - d	CHO cells	JEDI-2P-kv	21 - 23	A	1030	A	CGH no TF	45	0.4	100	250 x 250	200 * 3	6
S19	e	Organotypic	JEDI-2P-kv	31-35	A	1030	A	CGH no TF	137	1.21	1000	43 x 250	10 * 50	6
	f	Organotypic	JEDI-2P-kv	31-35	A	1030	A	CGH no TF	137	1.21	1000	43 x 250	30000	3
S20	a	CHO cells	JEDI-2P-kv	21 - 23	C	940	A	CGH	0 - 2.5	0 - 0.022	-	-	17.5	4
	b - d	Organotypic	ChroME-ST/ JEDI-2P-kv	31-35	C	940	A	CGH	0 - 4	0 - 0.35	1000	43 x 250	17.5 * 5	7
	g	Organotypic	ChroME-ST/ JEDI-2P-kv	31-35	C	940	A	CGH	2.5 - 5	0.02 – 0.04	-	-	17.5 * 5	8

Supplementary Table 2: Experimental configurations

Supplementary Note 2 – Optimal excitation and detection for widefield voltage imaging

This section accompanies Figures 1 and 2 of the main text, and Supplementary Figures 2 - 5.

Simulations were used to characterize the optimal excitation and detection parameters for voltage imaging with targeted, sculpted light. Note that this analysis is limited to considering signal generation and detection from the soma using a widefield detection axis.

Firstly, the case of a single, isolated, perfectly spherical cell was examined (Supplementary Figure 2). Since all functional voltage indicators, regardless of mechanism, must be proximal to the cell membrane (Kuhn and Roome 2019), fluorophores were simulated as points distributed on a spherical surface (Supplementary Figure 2a). Specific details regarding the simulation are presented in the methods section of the Supplementary Information (SI). According to Archimedes' hat-box principle (Cundy and Rollett 1989), the surface area of any section of the sphere is equal to that of a cylinder with the same height as the section and radius of the sphere. This simple observation has some important consequences for voltage imaging. For instance, assuming all other parameters are kept constant, if the axial Full Width Half Maximum (FWHM) of the excitation profile is smaller than the cell diameter, then the integrated number of excited fluorophores and the average $\Delta F/F_0$ response is independent of the axial position of the excitation profile (Supplementary Figure 2b, c). However, in the case of a widefield detection axis, the 3D distribution of excited fluorescence is projected onto a 2D detector, and the total signal is distributed over the fewest pixels for fluorescence generated close to the equator of the cell (Supplementary Figure 2d). As a result, in widefield voltage imaging, the equator of the cells appears brightest and the signal to noise ratio (SNR) is maximized when the fluorophores contributing to this signal are illuminated (Supplementary Figure 2e). This suggests that SNR could be optimized by targeted excitation of equatorial fluorescence (for instance by sculpting light to form a ring in the focal plane); especially in the case of non-linear fluorescence excitation. However, since the aim of this manuscript is to optimize existing methods used for photostimulation to voltage imaging, we limit our analysis in this section to considering spot-like excitation profiles which are ubiquitously used for parallel optogenetic stimulation. As such, these results imply that the illumination volume should be enlarged to match the cellular volume and the axial location of the excitation spot should be centred on the equator to maximise signal to noise ratio. Enlarged excitation volumes are also more robust to sample motion.

One of the major advantages of voltage imaging is that the dynamics of membrane potential fluctuations can be recorded from many cells in an unbiased manner during a single recording. This can only be achieved by performing functional imaging in densely labelled preparations. To identify the optimal volume of excitation in a densely labelled tissue, we extended the simulation to 3 layers of cells arranged on a closely packed hexagonal grid (Supplementary Figure 3a). The number of layers was limited for computational efficiency. Even in this densely packed configuration, the optimal excitation FWHM would be equal to the diameter of the cell since even the fluorescence that is spread over a larger number of detector pixels (due to the widefield point spread function, Supplementary Figure 3a) contributes useful signal. However, increasing the excitation volume beyond the cell volume results in the generation of extraneous "background" fluorescence from neighbouring cells which reduces the measured transient change in fluorescence recorded for a given change in membrane potential (Supplementary Figure 3d).

Hence, consistent with previous reports (Xiao et al. 2021a), widefield voltage imaging benefits from targeted illumination. Existing targeted illumination approaches have combined single-photon excitation amplitude modulation using digital micromirror devices (DMDs) (Adam et al. 2019b). This approach does not confer any axial sectioning and hence is best suited to sparsely labelled samples. Targeted illumination based on single photon holography using an SLM has also been utilized for single-photon voltage imaging (Fan et al. 2020b), which is advantageous since it is possible to utilize the full numerical aperture of the objective. In this case, the axial decorrelation length of the speckle is proportional to the NA^2 which provides moderate axial resolution (Ventalon and Mertz 2005), sufficient for targeting single

cells in densely labelled samples. However, when multiple cells are targeted simultaneously, the light targeting different regions overlaps above and below the focal plane, generating extraneous fluorescence and off-target photostimulation during all-optical experiments. Furthermore, single-photon holographic excitation is not suitable for selective photostimulation in densely expressing preparations. The most robust approach to overcome these problems is to combine non-linear excitation with temporal focusing, since in this case the axial resolution is independent of the overall lateral extent of the excitation profile (Oron, Tal, and Silberberg 2005; Zhu et al. 2005).

In the context of photostimulation, temporal focusing has been combined with low-NA Gaussian beams (Andrasfalvy et al. 2010; Rickgauer, Deisseroth, and Tank 2014; Mardinly et al. 2018b), holographic spots (Bègue et al. 2013; Chaigneau et al. 2016; Ronzitti et al. 2017; Chen et al. 2019) and Generalized Phase Contrast (GPC) method (Papagiakoumou et al. 2010; 2013). The optimal excitation parameters described simulations outlined above correspond closely to circular spots generated using GPC. As such, GPC will not be analysed any further here. As outlined above, signal to noise ratio in voltage imaging with targeted illumination is maximized when the equatorial fluorescence is efficiently excited. For Gaussian illumination, there is a trade-off between the uniformity of the intensity profile and the efficiency of excitation (Supplementary Figure 4a). Since the heating induced by the incident beam increases linearly with intensity, we opted to generate low-NA Gaussian beams experimentally with 12- μm FWHM 2P-excitation profile and to place an iris in a conjugate image plane prior to the objective to remove extraneous light which would contribute to heating but not useful signal. Whilst this strategy was appropriate for our proof-of-concept experiments, where single cells were imaged, the iris blocked more than 70 percent of the incident light. On the other hand, holographic spots with extent matching the cellular diameter can be generated with high efficiency using a liquid-crystal Spatial Light Modulator (SLM). Since, in typical configurations, the SLM can only modulate the phase of the incident beam, it is not possible to generate arbitrary distributions of light (which would require at least modulating the amplitude, and possibly also the polarization of the beam), depending on the application. Instead, the highest efficiencies are obtained in CGH by allowing the phase of the beam in the output plane to vary freely, resulting in the familiar speckle pattern of holographic patterns, which arises due to the redistribution of intensity by constructive and destructive interference of light with different phase. The confinement of photons in the speckle grains results in very efficient two-photon excitation, which results in an increase in SNR (approximately 2x higher for holographic spots as for low-NA Gaussian beams at a given average power, normalized within the 12 μm spot). Similar increases in SNR were also observed experimentally (Figure 2, main text). The spatial distribution of speckle grains changes each time the algorithm is run. This can be overcome in the case of a single spot but maintaining the speckle pattern when generating different patterns or different arrangements of multiple spots is not trivial. As a result, there is greater variation in the total fluorescence generated (and hence the SNR) with circular holographic spots as compared with GPC or low-NA Gaussian beams (Supplementary Figure 5). Experimentally, we also observed a much higher variability in the steady state $\Delta F/F_0$ values which we attribute to the fact that a spatial variance of voltage dependent fluorescence was observed in CHO cells.

So far, this discussion has neglected the fact that the optimal excitation volume outlined above is 150-fold larger than a diffraction limited PSF; necessitating the use of higher average power to achieve the same rates of 2P excitation:

$$N_{2p} \propto \frac{\langle P \rangle^2}{f\tau}$$

$\langle P \rangle$ is the average power, f the repetition rate and τ its pulse duration.

There is an upper limit of the amount of power that can be delivered into biological tissue before inducing thermal damage (see Results and Supplementary Figures 16 and 17 of the SI for more details). Fortunately, the relatively long pixel dwell time of widefield imaging means that it is well suited to the

use of low-repetition rate lasers which provide more energy per pulse (and hence more efficient non-linear excitation) for a given average power(Theer and Denk 2006; Theer, Hasan, and Denk 2003), provided that the repetition rate is equal to or higher than the image acquisition rate. The 250 kHz repetition rate used in the experiments presented in this manuscript is 320-fold lower than that of the 80 MHz sources used in conventional two-photon microscopy and hence the resulting powers used are of the same order of magnitude as for conventional point scanning, and other two-photon imaging applications(A. Song et al. 2017; Wu et al. 2020a; T. Zhang et al. 2019; Prevedel et al. 2016b). However, the use of higher pulse energy increases the probability of non-linear photodamage. We used a combination of electrophysiology and immunohistochemistry to identify safe imaging regimes with each of the modalities using this low repetition rate source. These results are presented in Supplementary Figure 17.

Supplementary Note 3 – Extracting fluorescence time series from widefield voltage imaging data

Accompanying discussion and data for Figure 2 of the main text and Supplementary Figures 7 and 8.

An appropriate data analysis pipeline was developed based on existing routines(Cai et al. 2021; Abdelfattah et al. 2019a; Buchanan et al. 2018). The pipeline was tested on simulated data (refer to Supplementary Note 2 of the SI) and refined on data collected from CHO cells with an electrophysiological ground truth. The data analysis pipeline was written in Python with dependencies on SciPy, NumPy and Scikit-Image.

1. For multi-cell datasets, crop each cell using the camera co-ordinates of the targeted spot (175 pixels x 175 pixels), for single cell datasets, continue to step 2
2. Whiten data (subtract mean and divide by standard deviation)
3. Convolve each frame of whitened data with a filter (generally 4 or 8 connected pixels)
4. Multiply the result with all frames in the stack. Calculate the temporal mean to generate a 2D image for segmentation.
5. Create an initial binary image using Otsu thresholding on the 2D image computed in step 2
6. Segment the binary image using a random walker algorithm. Remove holes and unconnected pixels in the segmented image.
7. Calculate an initial fluorescence trace as the average value of each acquired frame multiplied by the segmentation mask computed in step 7.
8. Calculate the background fluorescence trace as the average value of each acquired frame multiplied by the pixels outside of the segmentation mask computed in step 4.
9. If necessary:
 - Detrend initial fluorescence trace and original stack with a high-pass (butter) filter, cut on a function of imaging rate (e.g., for 100 Hz imaging, 0.3 Hz cut on used).
10. Generate a spatial filter by ridge regression of the (detrended) trace against the (detrended) stack as per reference(Cai et al. 2021).

A summary of this procedure is presented in Supplementary Figure 6 for the representative case of a CHO cell illuminated by a holographic spot whilst a 20 Hz train of 3 ms, 100-mV “spikes” were electrically evoked.

As demonstrated in Supplementary Figure 8, compared with results generated by calculating the unweighted mean of pixels within segmented cells, the regression-based pixel weighting algorithm improved $\Delta F/F$ with a minor increase in photobleaching, without having a significant impact on SNR. We hypothesise the increase in photobleaching is the result of voltage responsive fluorophores are more likely to be tethered to the membrane and hence less mobile. Based on the results presented in Supplementary Figure 8, this pipeline was used to extract fluorescence timeseries from widefield voltage imaging data for subsequent analysis.

Furthermore, as described in reference(Cai et al. 2021), template matching was used to identify putative action potentials in relevant traces.

Supplementary Methods

Simulations

The location of fluorophores on the surface of a sphere was calculated by drawing pairs of points randomly from two separate uniform distributions and excluding pairs which exceeded a Euclidean distance of 1 from the origin. The final number of pairs was limited to 889,762 corresponding to a density of 2000 fluorophores per μm^2 of membrane (Sjulson and Miesenböck 2008). These points were then transformed to the surface of a unit sphere. This sphere was scaled to have a 12 μm diameter (Supplementary Figure 2a), found to be the approximate average diameter of CHO cells from which data presented in Figure 2 of the main text was acquired. For computational efficiency, these points were discretized onto a three-dimensional grid with isotropic pixel size 0.1625 μm .

To identify the optimal axial location of the excitation profile, the number of molecules in each 1 μm axial section (the approximate axial extent of diffraction limited spots used in conventional 2P-LSM) of the cell were counted as a proxy for the total amount of fluorescence generated (Supplementary Figure 2b). The average fluorescence collected per camera pixel was calculated by dividing this value by the number of non-zero pixels (Supplementary Figure 2d).

Widefield voltage imaging data was simulated by determining whether each molecule was fluorescent or not according to the values drawn from a Bernoulli distribution with probabilities chosen empirically to match the final counts on the camera with typical values obtained during experiments ($p = 0.1$ - high photon flux, $p = 0.01$ - low photon flux). These binary fluorescence values from fluorophores belonging to the same voxel were summed. Shot noise was simulated by replacement of each value with one drawn from the corresponding Poisson distribution. The simulated fluorescence was multiplied with an excitation profile. The resulting data were convolved with the widefield PSF. The PSF was simulated according to the Born and Wolf model of scalar diffraction from a circular aperture and was based on a numerical aperture of 0.8, 40x magnification, 1.33 sample refractive index, central wavelength 525 nm and a pixel size of 0.1625 μm (sample space). The fluorescence was then scaled by the collection efficiency of the microscope objective, assuming isotropic fluorescent emission. The signal recorded by the camera was simulated by integrating the resulting signal along the optical axis, assuming linearity due to the incoherent nature of fluorescence emission. The digitization of this signal was simulated using parameters taken from the specifications of the Camera A which was used to acquire most of the experimental data presented in the manuscript (refer to Table S1 for exact values). Photons were converted to electrons by multiplication with the quantum efficiency of the camera and dark noise was modelled by drawing values from a normal distribution. The number of electrons was converted to counts by multiplying by the sensitivity and, finally, a global camera offset (100 counts) was added to all pixels to avoid negative counts.

Time series were simulated by drawing a value for the fractional change in fluorescence for each fluorophore on the sphere from a skew-normal distribution centred on 50% and standard deviation of 100%, based on experimental observations (Zhuohe Liu et al. 2022b) and for a 100 mV voltage step. The fractional change in fluorescence for a given voxel randomly chosen as that of one of the fluorophores within the voxel. A single voltage step was simulated.

All simulations were performed using Python (with NumPy and SciPy dependencies) running on a personal laptop.

Supplementary Table 3: Simulation parameters

Cell diameter (μm)	12
Number of indicator molecules (μm^{-2})	2000 (ref.(Sjulson and Miesenböck 2008))
Emission wavelength (nm)	525
Immersion refractive index	1.33
Detection NA	0.8
Objective magnification	40
Simulated lateral FOV (μm)	30
Simulated axial FOV (μm)	30
Top hat excitation radius (μm)	6
GPC excitation radius (μm)	variable, as stated
Gaussian excitation radius (μm)	variable, as stated
CGH excitation radius (μm)	variable, as stated
Quantum efficiency (%)	95
Read noise (electrons)	1.6
Dark current (e-/p/se)	1.27
1/sensitivity (e-/count)	0.23
Camera offset (counts)	100

Calibration procedure for multi-cell experiments

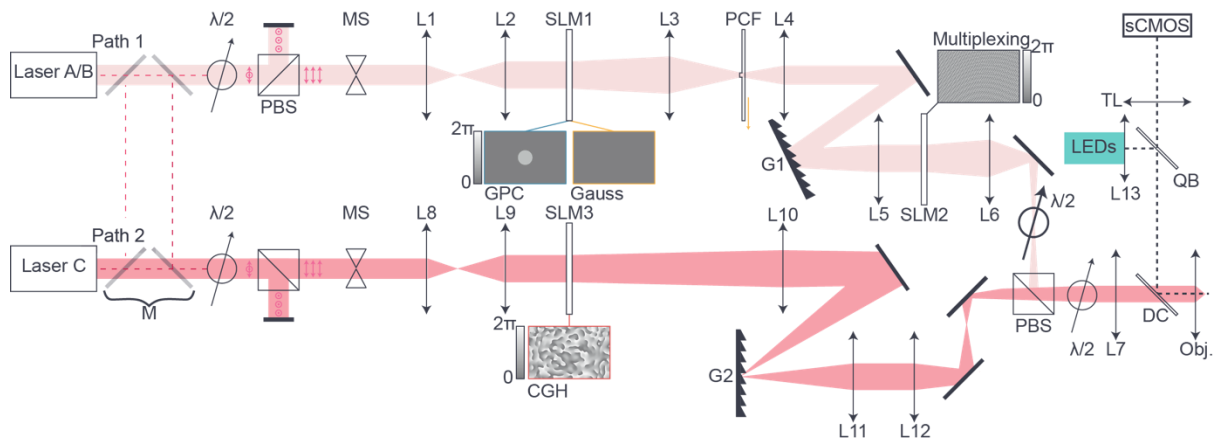
In order to target the excitation spots to specific locations in the field of view, it is necessary to estimate the mapping between “camera” and “SLM” co-ordinates. For all modalities (CGH/ GPC/ low-NA Gaussian), this was achieved prior to all experiments as follows:

1. A thin spin-coated rhodamine layer was placed in the focal plane of the microscope.
2. A spot was generated at the optical axis (the origin of the SLM coordinate system). 10 images were recorded and averaged.
3. A spot was generated at the edge of the desired FOV. 10 images were recorded and averaged.
4. A grid of spots spanning the desired FOV was generated. 10 images were recorded and averaged.
5. The locations of the spots in the images acquired in steps 2-4 (in camera coordinates) were estimated using built-in circle detection functions of scikit-image(Van Der Walt et al. 2014).
6. The affine transformation between “camera” and “SLM” co-ordinates was calculated based on the estimated positions in step 5. This transformation was used to generate SLM co-ordinates to target spots to cells.

Prior to experiments, the calibration procedure was repeated until the error in spot position was less than 1 camera pixel.

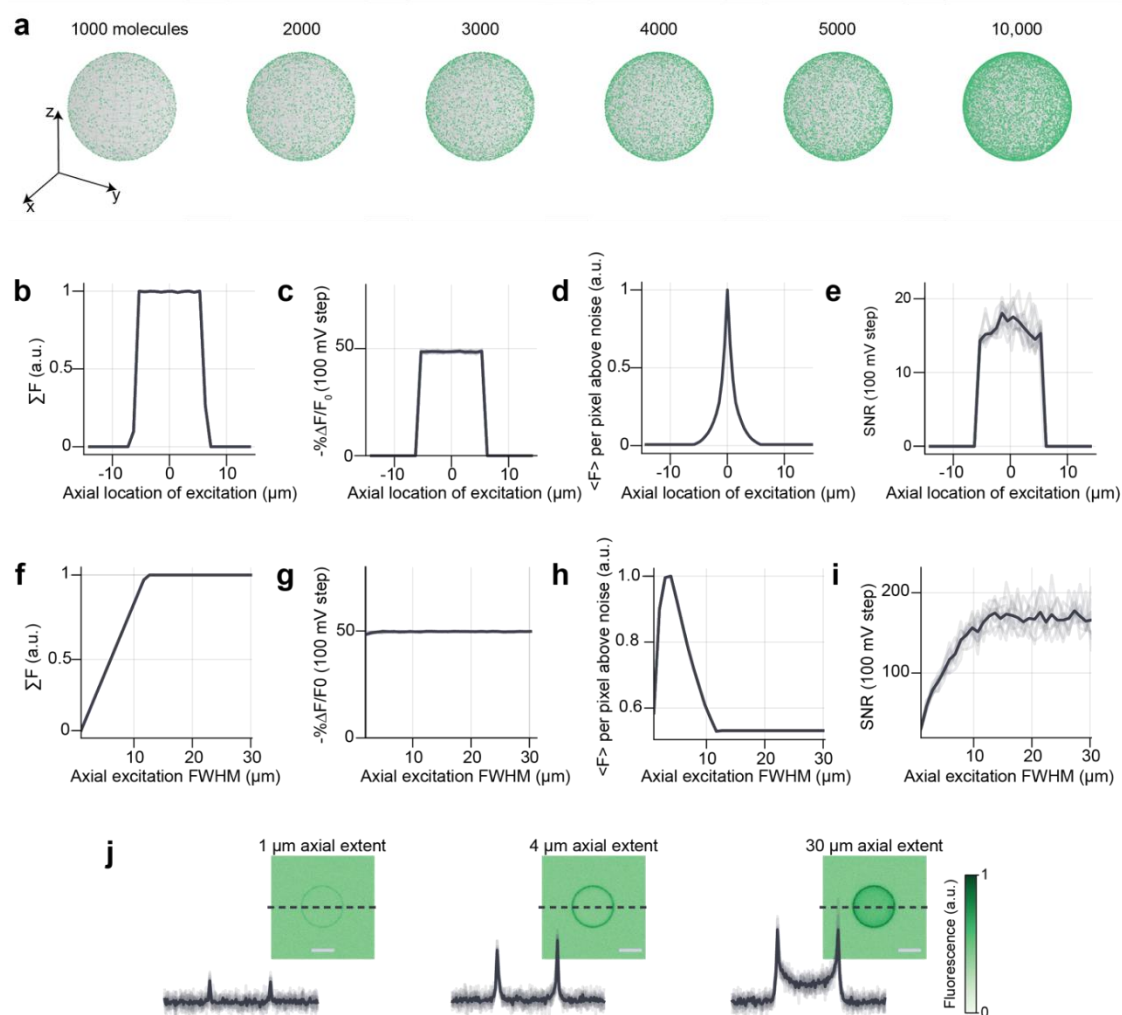
The data acquired in step 4 was also used to generate a map of diffraction efficiency which was used to tune the power delivered to cells in different portions of the field of view.

This calibration procedure was repeated daily to ensure accurate targeting in all experiments and to measure the stability of the system alignment.



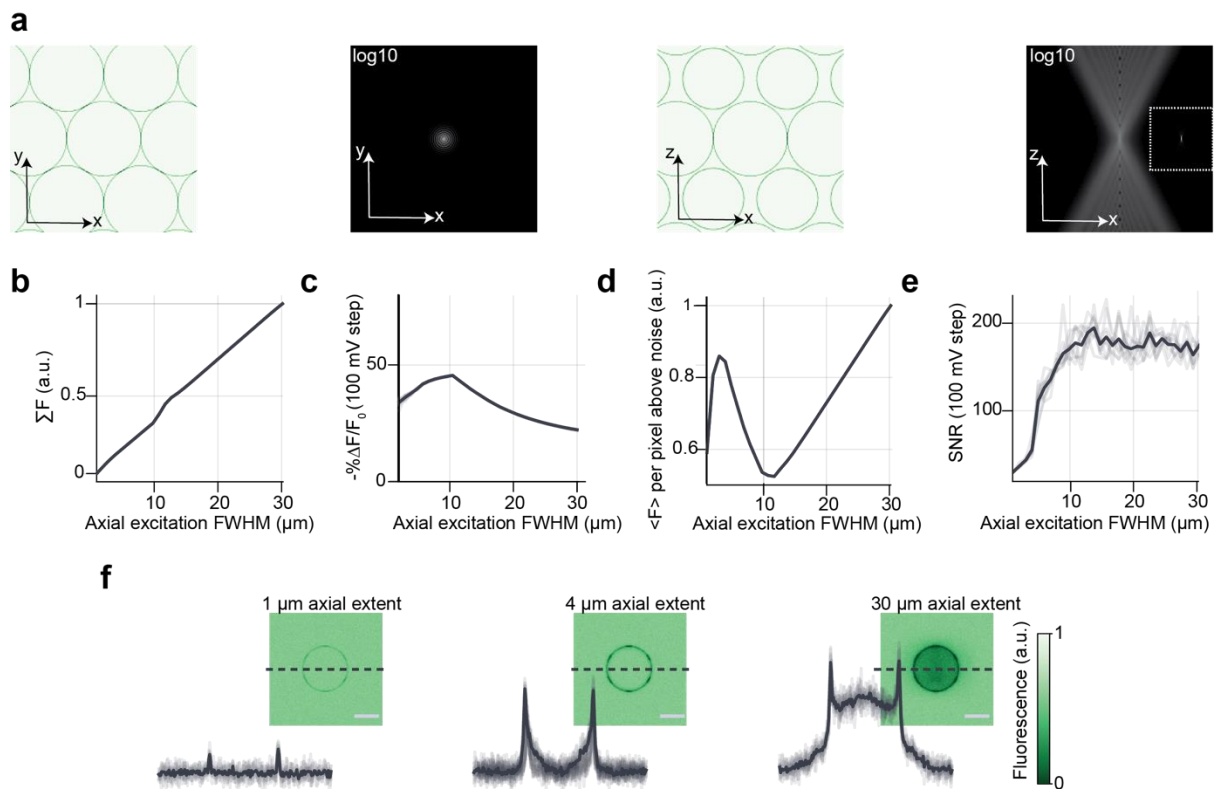
Supplementary Figure 1. Optical setup for scanless two-photon voltage imaging. *This figure accompanies Figure 1 of the main text, Supplementary Note 1 and Supplementary Methods.*

Schematic diagram of the optical setup designed to generate 12 μm (FWHM), temporally focused, Gaussian (Gauss), Generalised Phase Contrast (GPC) and Computer-Generated Holography (CGH) spots. The setup was equipped with three lasers. Laser A refers to a tuneable femtosecond source (Coherent Discovery, 1 W, 80 MHz, 100 fs) tuned to 920, 940 or 1030 nm. Laser B refers to a femtosecond source with a fixed wavelength output (Spark Alcor, 4 W, 80 MHz, 100 fs, 920 nm). Laser C refers to a custom OPA pumped by an amplified laser, also with fixed wavelength output (Amplitude Satsuma Niji, 0.2 – 0.6 W, 250 kHz, 100 fs, 940 nm). Gaussian and GPC spots were generated using Path 1 (upper, see label) and holographically multiplexed through the spatial light modulator SLM2. CGH spots were generated using path 2 (lower, see label), where an expanded beam was sent to a spatial modulator addressed with a computer-generated phase profile. Paths 1 and 2 were combined prior to the objective (Obj.) with a polarising beam splitter (PBS). Acronyms: $\lambda/2$ (half-wave plate), MS (Mechanical Shutter), L (Lens), SLM (Spatial Light Modulator), PCF (Phase Contrast Filter), G (Grating), DC (Dichroic), QB (Quad-band filter), TL (Tube Lens).



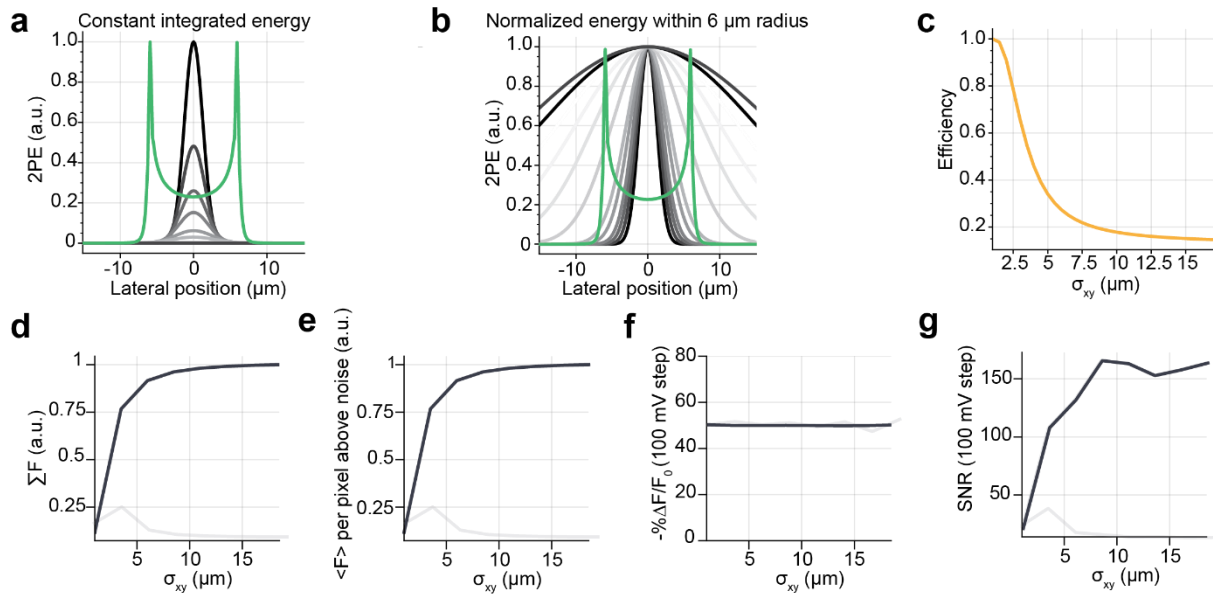
Supplementary Figure 2. Investigation of the optimal excitation profile for parallel illumination in combination with a widefield detection axis for an isolated spherical cell. This figure accompanies Figure 1 of the main text, and Supplementary Note 2.

(a) Visualisation of an increasing number of points (as specified) uniformly distributed on the surface of a sphere. As a result of the projection from 3D to 2D, the uniform distribution of points appears denser at the edges. (b) Top hat excited fluorescence produced by a beam profile with 12 μm lateral diameter and 1 μm axial extent (corresponding to the approximate axial extent of a diffraction-limited spot used in conventional 2P-LSM) simulating imaging of a 100-mV step depolarization of the cell membrane. This excitation profile was scanned in 1 μm steps over a total 30 μm axial range. The widefield point spread function (PSF) was translated axially such that the illuminated portion of the cell was always in focus. (c) Fluorescence change $-\% \Delta F/F_0$ over the axial range of 30 μm . (d) The average fluorescence per pixel, excluding pixels which do not collect any fluorescence above noise. Since the same number of fluorophores are distributed over a smaller projected surface area when the axial location of the excitation coincides with the cellular equator, this curve is sharply peaked at the axial position $z=0$. (e) Data from each of 10 repeats of the simulation is plotted (light grey), the average from all repeats is plotted in black. (f – i) The same quantities as in (b – e) are presented here for a spot with 12 μm lateral diameter and increasing axial extent (1 – 30 μm), centred on the axial position $z=0$. The focal plane of the widefield detection axis was centred in the middle of the spherical cell. The peak in (h) occurs at approximately 4 μm whilst the SNR increases until the axial excitation FWHM matches the axial cell diameter. (j) Lateral cross-sections through simulated camera images of membrane localised fluorescence as a function of the axial extent of the excitation profile. Inset: simulated camera images for idealised top-hat excitation profiles with different axial extents (labelled). Scale bars represent 5 μm . In the case of an isolated single cell, when the axial extent of the excitation profile exceeds the diameter of the cell, the equatorial fluorescence remains prominent, but “out-of-focus” signal nonetheless improves the SNR of the resulting fluorescence trace.

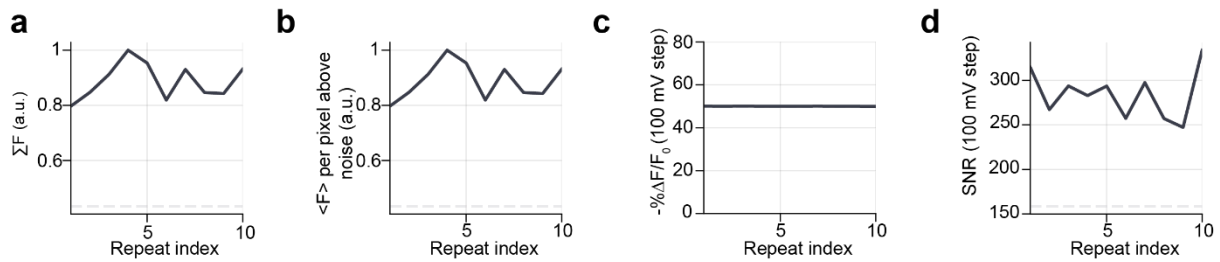


Supplementary Figure 3. Investigation of the optimal excitation profile for parallel illumination in combination with a widefield detection axis for a spherical cell in a densely packed configuration of labelled cells. *This figure accompanies Figure 1 of the main text, and Supplementary Note 2.*

Simulations used to optimize the excitation profile for parallel illumination in combination with a widefield detection axis in the case of densely labelled samples. **(a)** A closely packed hexagonal lattice of spheres with fluorophores randomly distributed about the surface was simulated to approximate densely labelled voltage imaging preparations. The intensity PSF of the widefield detection axis is plotted with the same pixel size for comparison with the extent of the simulated cells. The base-10 log of the PSF is plotted for ease of visualization. Inset: xz projection of the widefield point spread function plotted on a linear intensity scale. **(b – e)** As for (f – i) of Supplementary Figure 2 in the case of a densely labelled sample. Simulations performed using a spot with 12 μm lateral diameter and increasing axial extent (1 – 30 μm). Data from each of 10 repeats of the simulation is plotted (light grey), the average from all repeats is plotted in black. The peak in (d) also occurs at approximately 4 μm , but even in the case of a densely labelled sample, it is still beneficial to increase the axial extent of the excitation spot since fluorescence from other cells is divided between a large number of pixels due to the PSF of the widefield detection axis. Hence the SNR does not rapidly decrease as a function of axial excitation extent when cells above and below the target cell are illuminated (as shown in (e)). **(f)** Lateral cross-sections through simulated camera images of membrane localised fluorescence as a function of the axial extent of the excitation profile. Inset: simulated camera images for idealised top-hat excitation profiles with different axial extents (labelled). Scale bars represent 5 μm . In the case of a densely labelled tightly packed network of cells, when the axial extent of the excitation profile exceeds the diameter of the cell, the sum of fluorescence excited in other cells contributes to significant background signal which reduces the estimated $\% \Delta F / F_0$ for a given change in membrane potential (as plotted in (c)).

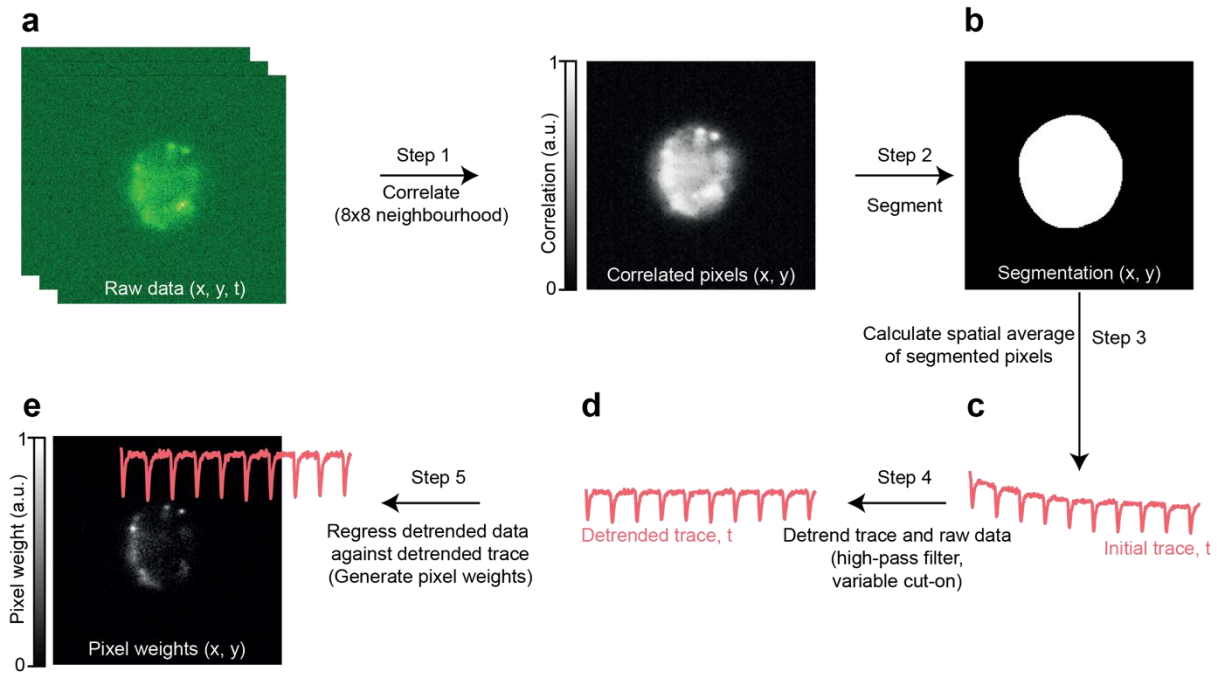


Supplementary Figure 4. Investigation of the optimal excitation profile for 2P voltage imaging with temporally focused low-NA Gaussian beams. *This figure accompanies Figure 1 of the main text, and Supplementary Note 2.* **(a)** Greyscale: Lateral profile of Gaussian beam as a function of beam waist (total integrated energy normalized to a constant value throughout the simulated 2D plane). Green: 2D projection of simulated fluorescence from a 12 μm cell excited by a beam extending 12 μm axially. Increasing the width of the Gaussian beam drastically reduces the peak energy. **(b)** As for (a) with all Gaussian beams normalized to have the same integrated energy within a 12 μm circular region. **(c)** Fraction of energy of the Gaussian beam within a 12 μm circular profile as a function of the beam waist (σ) of the incident Gaussian beam. **(d – g)** Total excited fluorescence, fluorescence per pixel above noise, $\Delta F/F_0$ and SNR as a function of Gaussian beam waist. The black lines represent the case where the energy is normalized within a 12 μm circular spot and the grey lines represent the case of equal integrated energy for the different beam waists. In the case where the total beam energy is kept constant, it is preferable to use a $\sigma = 3.5$ μm Gaussian beam. Neglecting input power considerations, it is optimal to use a $\sigma = 15$ μm Gaussian beam to efficiently excite membrane localized fluorophores.



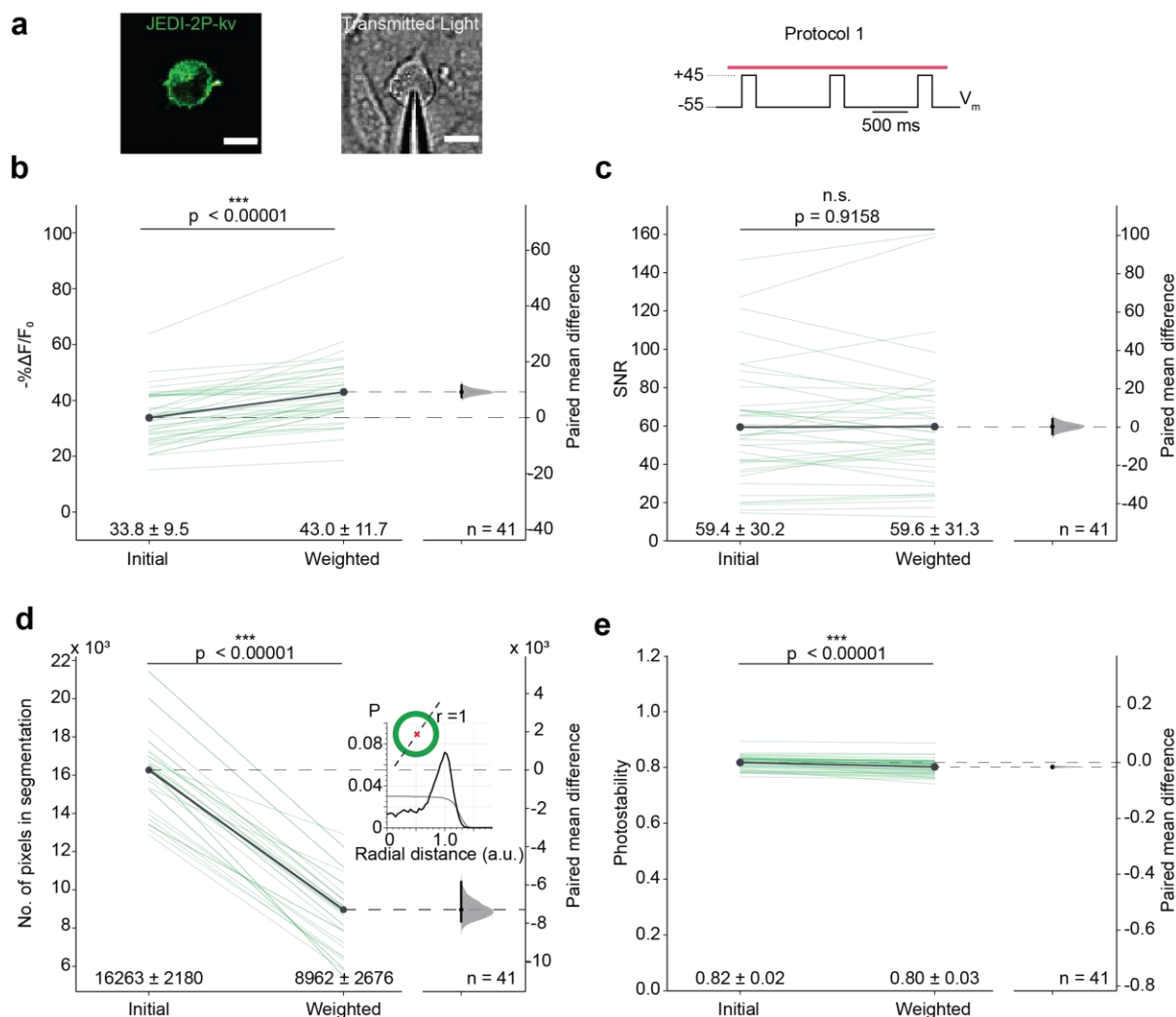
Supplementary Figure 5. Investigation of the impact of the speckle in holographic spots for 2P voltage imaging with temporally focused Computer-Generated Holography. *This figure accompanies Figure 1 of the main text, and Supplementary Note 2.*

Results of simulations used to test the effect of the speckle grains in holographic spots on various metrics relevant for voltage imaging. Each simulation was repeated 10 times. In each repeat the Gerchberg-Saxton algorithm was rerun, resulting in a different speckle pattern within a circular (12 μm diameter) holographic spot. **(a)** Total excited two-photon fluorescence for CGH vs a 12 μm top hat profile with equal total incident intensity. **(b)** The average fluorescence per pixel, excluding pixels which do not collect any fluorescence above noise for CGH vs a 12 μm top hat profile with equal total incident intensity. **(c)** Fractional change in fluorescence due to a 100-mV voltage step for CGH vs a 12 μm top hat profile with equal total incident intensity. **(d)** SNR of the fluorescence transient due to a 100-mV voltage step for CGH vs a 12 μm top hat profile with equal total incident intensity. Results for the holographic spots are plotted in black, and the corresponding results for a 12 μm top-hat profile (corresponding to GPC or an expanded Gaussian beam) are also plotted (grey dashed line).



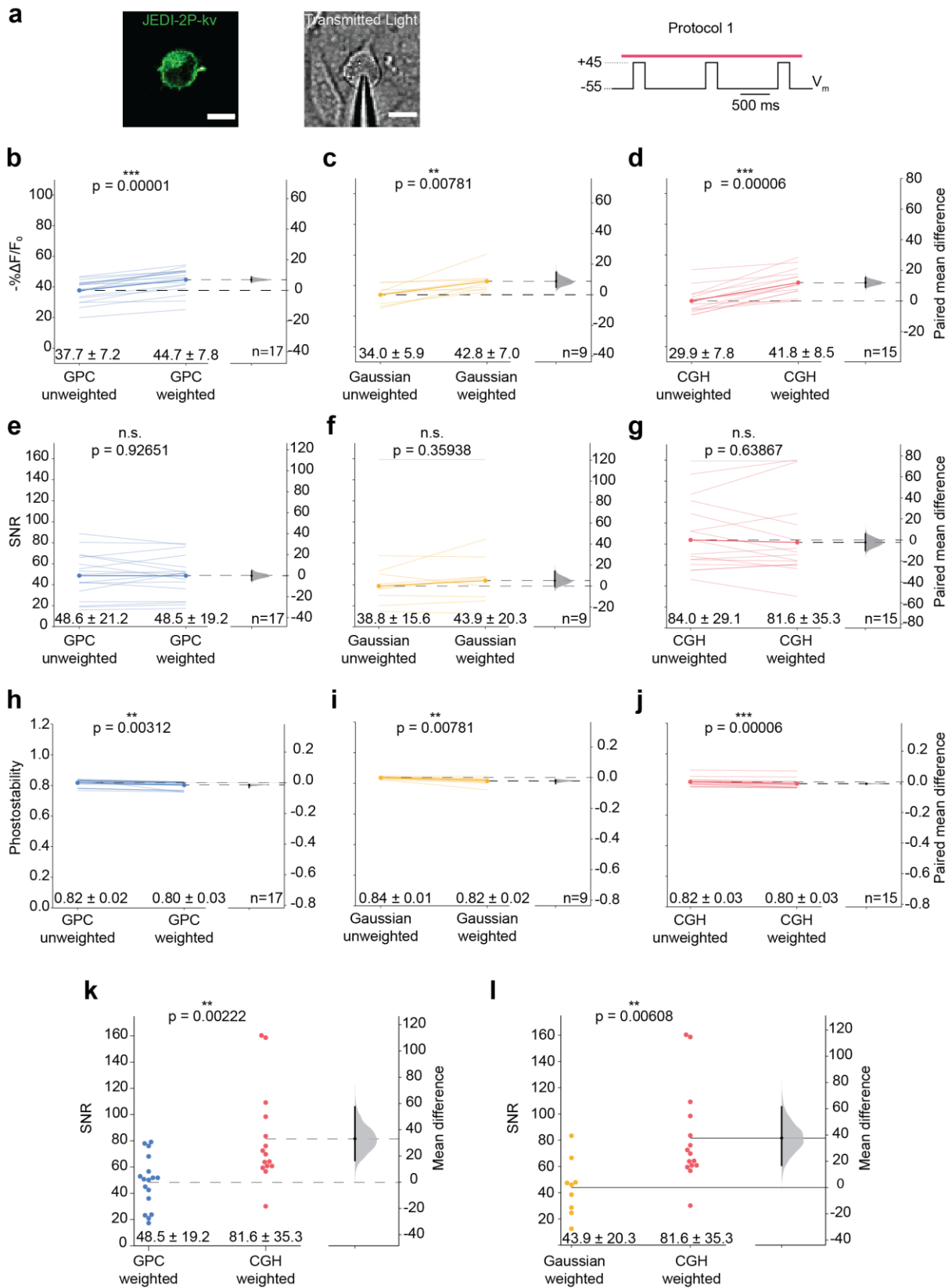
Supplementary Figure 6. Summary of data analysis pipeline. This figure accompanies Figure 2 of the main text, and Supplementary Note 3.

(a) The temporal cross-correlation of each pixel with its adjacent neighbours was calculated (using an 8x8 pixel kernel unless otherwise stated). (b) Initial segmentation estimate generated as follows: i) Spatially filter each raw data frame using Gaussian kernel (sigma set to match average cell radius in pixels, usually 30, using inbuilt *gaussian_filter* function from Python library SciPy). ii) Otsu thresholding (using inbuilt *threshold_otsu* function from Python library scikit-image). iii) Random walker segmentation (using inbuilt *random_walker* function from Python library scikit-image, beta parameter set to 130 and 'cg' mode). iv) Clean segmentation (using inbuilt *binary_fill_holes* function from Python library SciPy, and inbuilt functions erosion, dilation and disk from Python library scikit-image, with disk radius 1.2 times the kernel size used for Gaussian filtering in step (i)). v) Retain the segment containing the largest number of connected pixels (using inbuilt function *label* from the Python library scikit-image). (c) The mask calculated in (b) was used to generate an initial estimate of the fluorescence trace, calculated as the average timeseries of the pixels within the binary mask calculated in (b), a representative trace has been plotted. (d) Both the initial estimate of the trace and the dataset itself were detrended by high-pass filtering (using inbuilt functions *butter* and *filtfilt* from Python library SciPy) or using the procedure outlined in reference²⁶, a representative detrended trace has been plotted. (e) A spatial filter was generated using Ridge-regression, as detailed in Cai et al.²⁴. The final timeseries (plotted, inset) was calculated as the weighted average of the spatial filter and the detrended dataset.



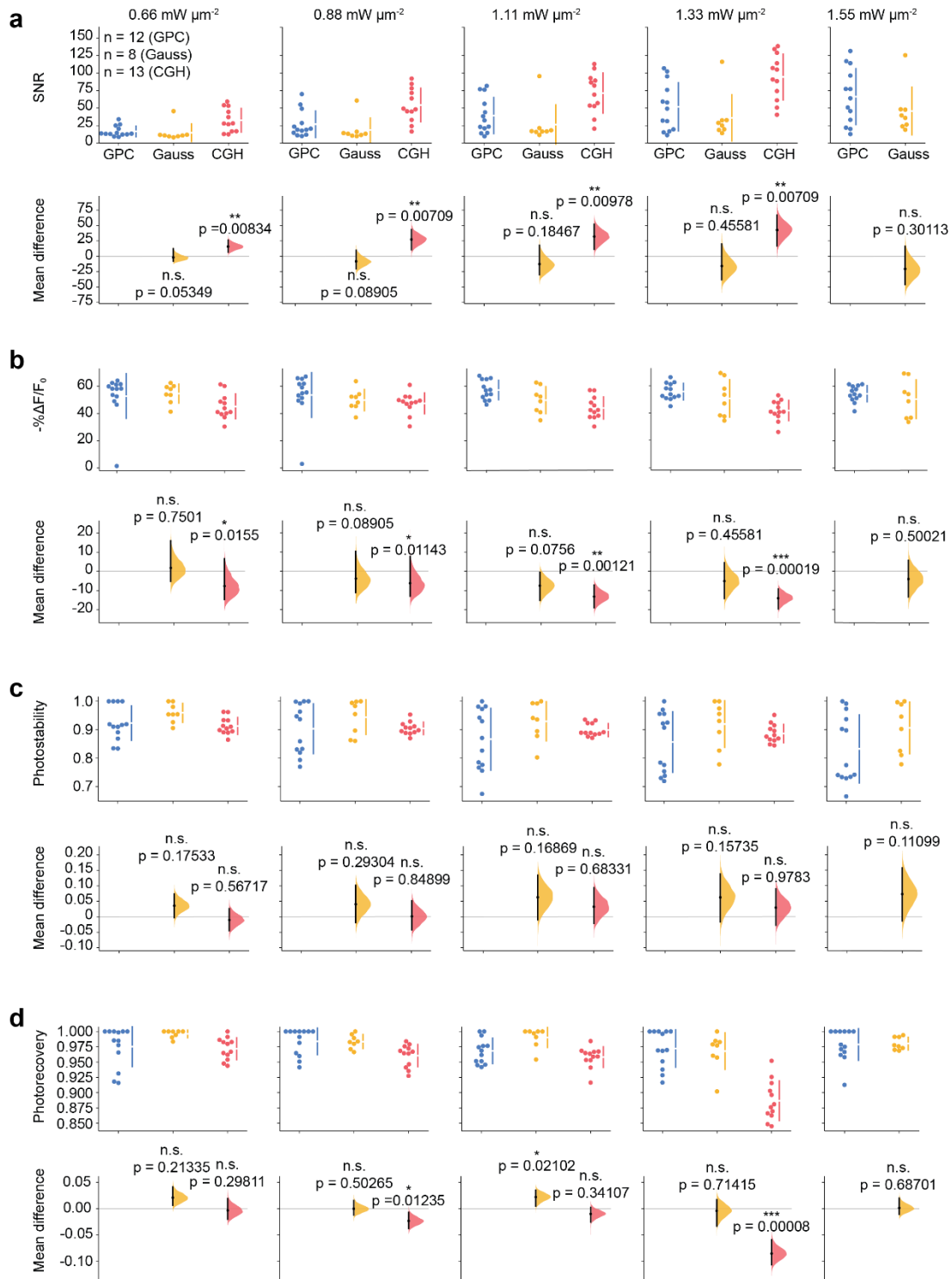
Supplementary Figure 7. Evaluation of analysis pipeline used to generate fluorescent timeseries from raw voltage imaging data acquired using scanless two-photon voltage imaging in combination with a widefield detection axis. This figure accompanies Figure 2 of the main text, and Supplementary Note 3.

Quantitative comparison demonstrating the utility of applying a regression-based approach to extract time series from widefield voltage imaging data (Method 2, as outlined in Supplementary Figure 6) in contrast to simple segmentation (Method 1). **(a)** Cross-section through a confocal stack of a JEDI-2P-kv expressing CHO cell (left) and transmitted light image of a patched cell (middle). Scale bars represent 10 μ m. The electrophysiology protocol used during data acquisition is plotted in black (right). The red bar above the electrophysiology trace indicates the illumination duration (3 s). **(b)** Paired comparison of $-\% \Delta F / F_0$, **(c)** SNR, **(d)** number of pixels per mask between traces generated using the initial or weighted segmentations (as summarized in Supplementary Figure 6) and Gardner-Altman plots associated (see Methods and reference³⁰). **(inset, d)** The average radial probability distribution functions of pixels used in the weighted mask for all cells calculated using Methods 1 and 2. In the case of Method 2, the distribution function is strongly peaked at the cell membrane indicating that the analysis pipeline successfully identified pixels which recorded membrane localized (and hence responsive) fluorescence. **(e)** Paired comparison and Gardner-Altman plot of the photostability between traces generated using the initial or weighted segmentations (as summarized in Supplementary Figure 6). Each line in each plot represents a cell, the mean of all cells is plotted in black. * denotes $p < 0.05$, ** denotes $p < 0.01$ and *** denotes $p < 0.0001$.



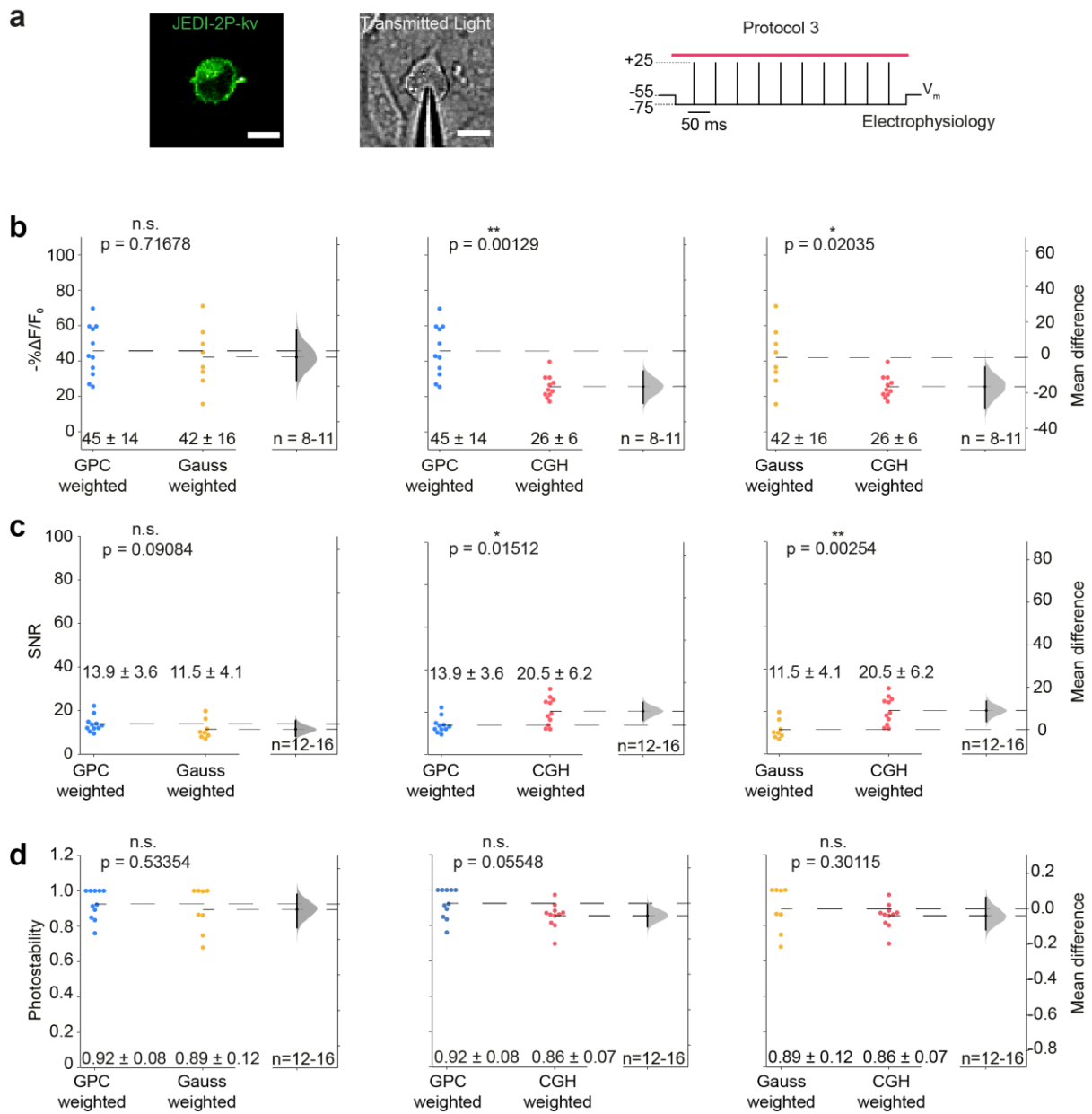
Supplementary Figure 8. Comparison of different parallel illumination approaches for scanless two-photon voltage imaging (protocol 1). *This figure accompanies Figure 2 of the main text.*

Comparison of different parallel illumination approaches for widefield voltage imaging obtained using Protocol 1, as described in the main text. **(a)** Cross-section through a confocal stack of a JEDI-2P-kv expressing CHO cell (left) and transmitted light image of a patched cell (middle). Scale bars represent 10 μm . The electrophysiology protocol used to compare both methods is plotted in black (right). The red bar above the electrophysiology trace indicates the illumination duration (3 s). **(b-d)** Paired comparison (and Gardner-Altman plots associated) of $-\% \Delta F / F_0$ between Methods 1 (unweighted) and 2 (weighted) for each of the different modalities; GPC (b, blue), Gaussian (c, yellow) and CGH (d, red). Each line represents a measurement from an individual cell. The average values are plotted in a darker shade, $n = 10-20$ for all modalities. **(e-g)** Paired comparison and Gardner-Altman plot of SNR between Methods 1 (unweighted) and 2 (weighted) for each of the different modalities; GPC (e, blue), Gaussian (f, yellow) and CGH (g, red). Each line represents a measurement from an individual cell. The average values are plotted in a darker shade, $n = 10-20$ for all modalities. **(h-j)** Paired comparison and Gardner-Altman plot of SNR between Methods 1 (unweighted) and 2 (weighted) for each of the different modalities; GPC (h, blue), Gaussian (i, yellow) and CGH (j, red). Each line represents a measurement from an individual cell. The average measurement for all cells is plotted in a darker shade for each modality. $n=10-20$ for all modalities. **(k-l)** Comparison and Gardner-Altman plot of SNR between the three different modalities; (k) GPC vs CGH and (l) Gaussian vs CGH. The results are consistent with those found for Protocol 2, discussed in detail in the main text. * denotes $p < 0.05$, ** denotes $p < 0.01$ and *** denotes $p < 0.0001$.



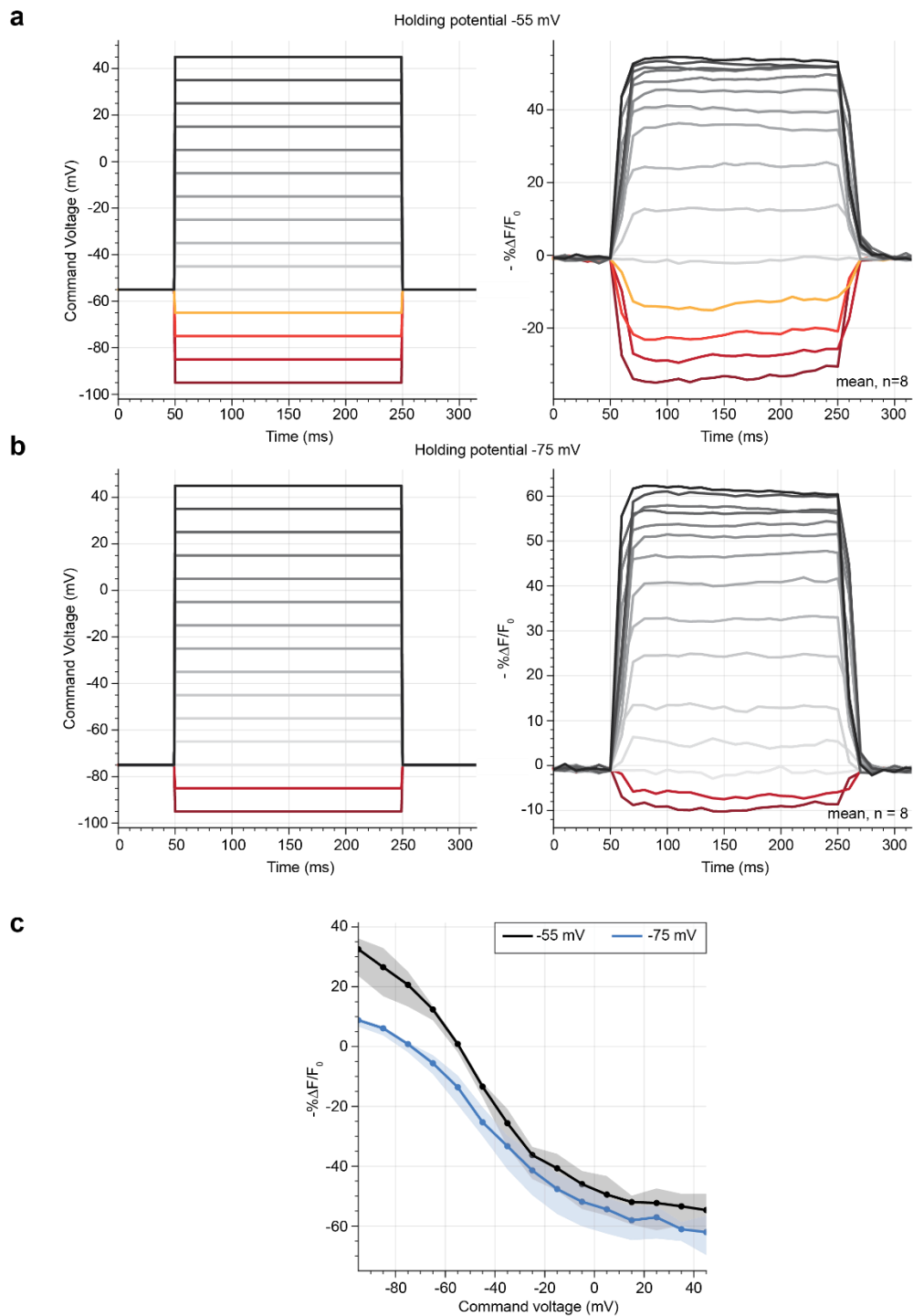
Supplementary Figure 9. Comparison of different parallel illumination approaches for scanless two-photon voltage imaging (protocol 2). This figure accompanies Figure 2 of the main text.

Comparison of parallel illumination approaches for widefield voltage imaging obtained using protocol 2, as described in the main text and corresponding Gardner-Altman plots. **(a)** $-\% \Delta F/F_0$, **(b)** SNR, **(c)** photostability and **(d)** photorecovery for each of the different modalities (as defined in the main text); GPC (blue), Gaussian (yellow) and CGH (red), and at power densities ranging from 0.66 and 1.55 $\text{mW } \mu\text{m}^{-2}$, as labelled (75 – 175 mW per cell). Individual points represent measurements from individual cells. (n = 8 – 13), * denotes $p < 0.05$, ** denotes $p < 0.01$ and *** denotes $p < 0.0001$.



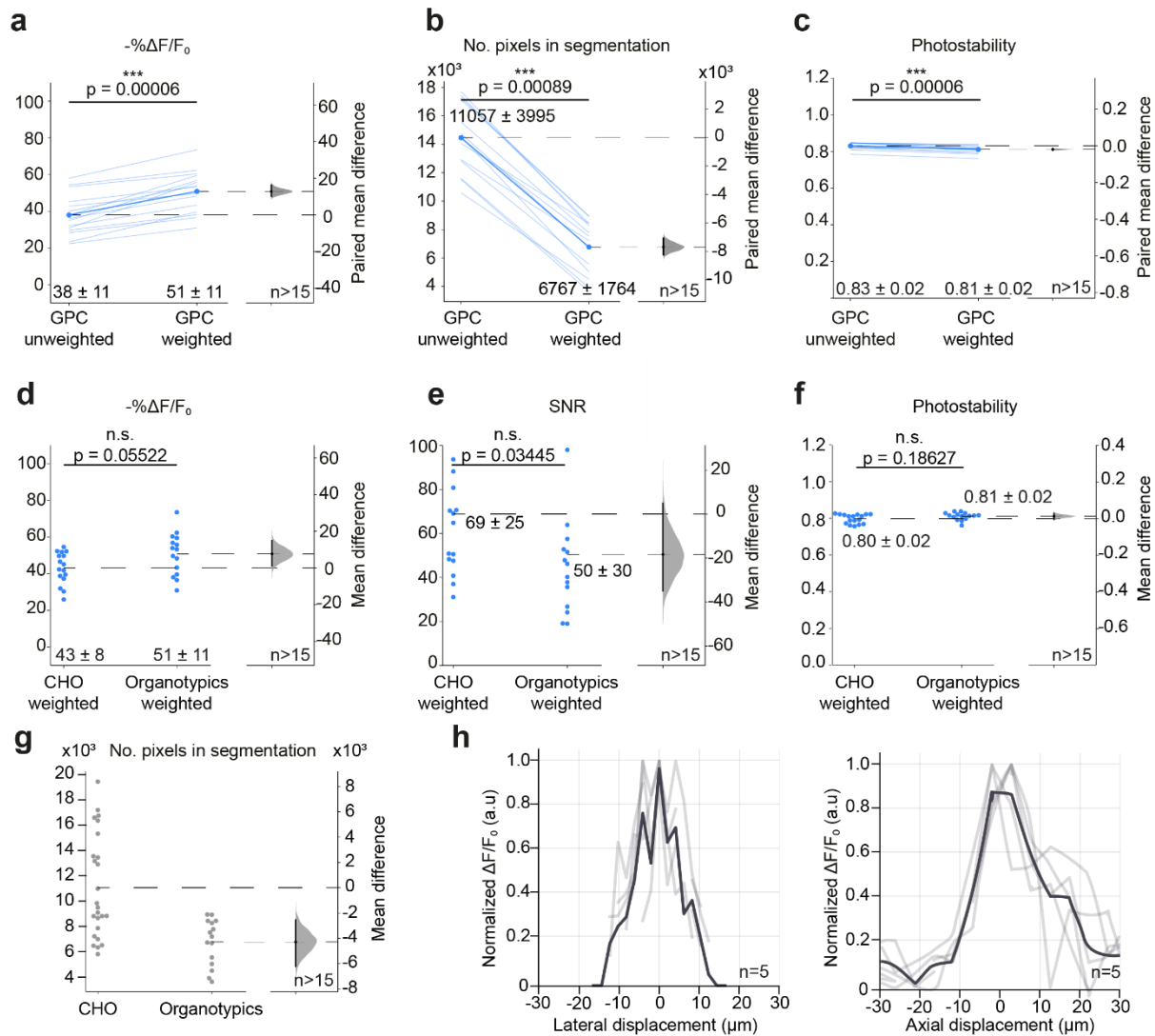
Supplementary Figure 10. Comparison of different parallel illumination approaches for scanless two-photon voltage imaging (protocol 3). This figure accompanies Figure 2 of the main text.

Comparison of parallel illumination approaches for widefield voltage imaging obtained using Protocol 3, as described in the main text. **(a)** Cross-section through a confocal stack of a JEDI-2P-kv expressing CHO cell (left) and transmitted light image of a patched cell (middle). Scale bars represent 10 μm . The electrophysiology protocol used to compare both methods is plotted in black (right). The red bar above the electrophysiology trace indicates the illumination duration (500 ms). Comparison and Gardner-Altman plots of **(b)** $-\% \Delta F/F_0$, **(c)** SNR and **(d)** photostability between each of the different modalities; GPC (blue, $n=11$), Gaussian (yellow, $n=8$) and CGH (red, $n=11$) (power density: $1.33 \text{ mW } \mu\text{m}^{-2}$, 150 mW per cell, 1 kHz acquisition rate). The results are consistent with those found for Protocol 2, as discussed in the main text. However, these results were obtained in a low photon flux regime, as the data was acquired at 1 kHz. Since, for all modalities, the SNR is > 1 for an AP-like event we conclude that all modalities can be used for widefield, two-photon voltage imaging.



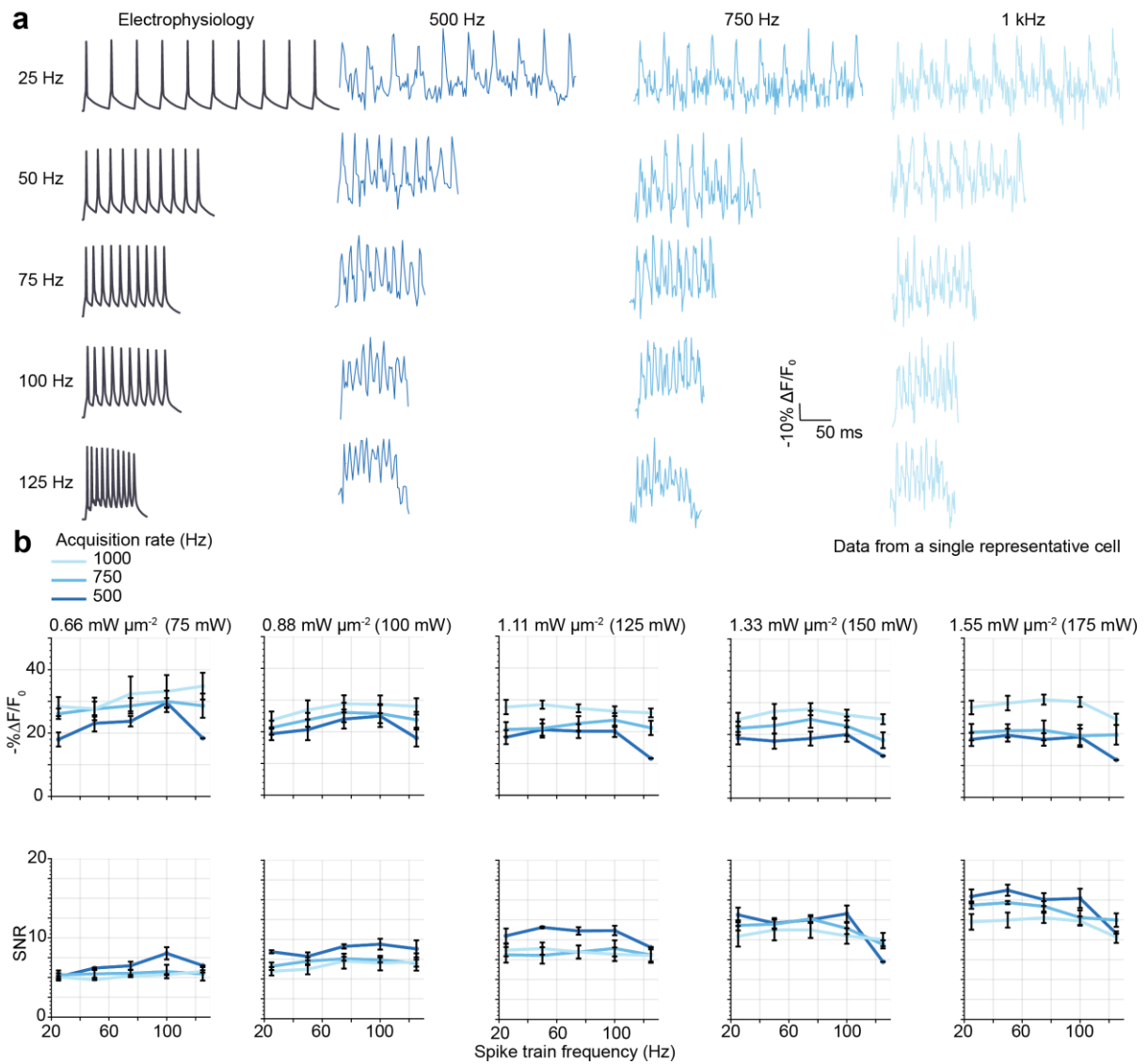
Supplementary Figure 11. Fluorescence-Voltage (F-V/Sensitivity) curves for the genetically encoded voltage indicator JEDI-2P-kv. This figure accompanies Figures 2 and 3 of the main text.

Sensitivity curves for the genetically encoded voltage indicator JEDI-2P-kv measured in CHO cells using 2P-TF-GPC. Command voltage steps from -95 mV to +45 mV (left) and average fluorescence responses recorded (right) at a resting potential of **(a)** -55 mV **(b)** -75 mV. The mean of 8 cells is plotted. **(c)** $-\% \Delta F / F_0$ as a function of command voltage at a resting potential of -55 mV (black) or -75 mV (blue). The average trace and 95 percent confidence interval from all cells are plotted (n=8). All data were acquired with laser A tuned at 940 nm, with power density: $0.88 \text{ mW } \mu\text{m}^{-2}$ (100 mW per cell), 100 Hz acquisition rate and camera A (Refer to Supplementary Figure 1 and Supplementary Tables 1 and 2).



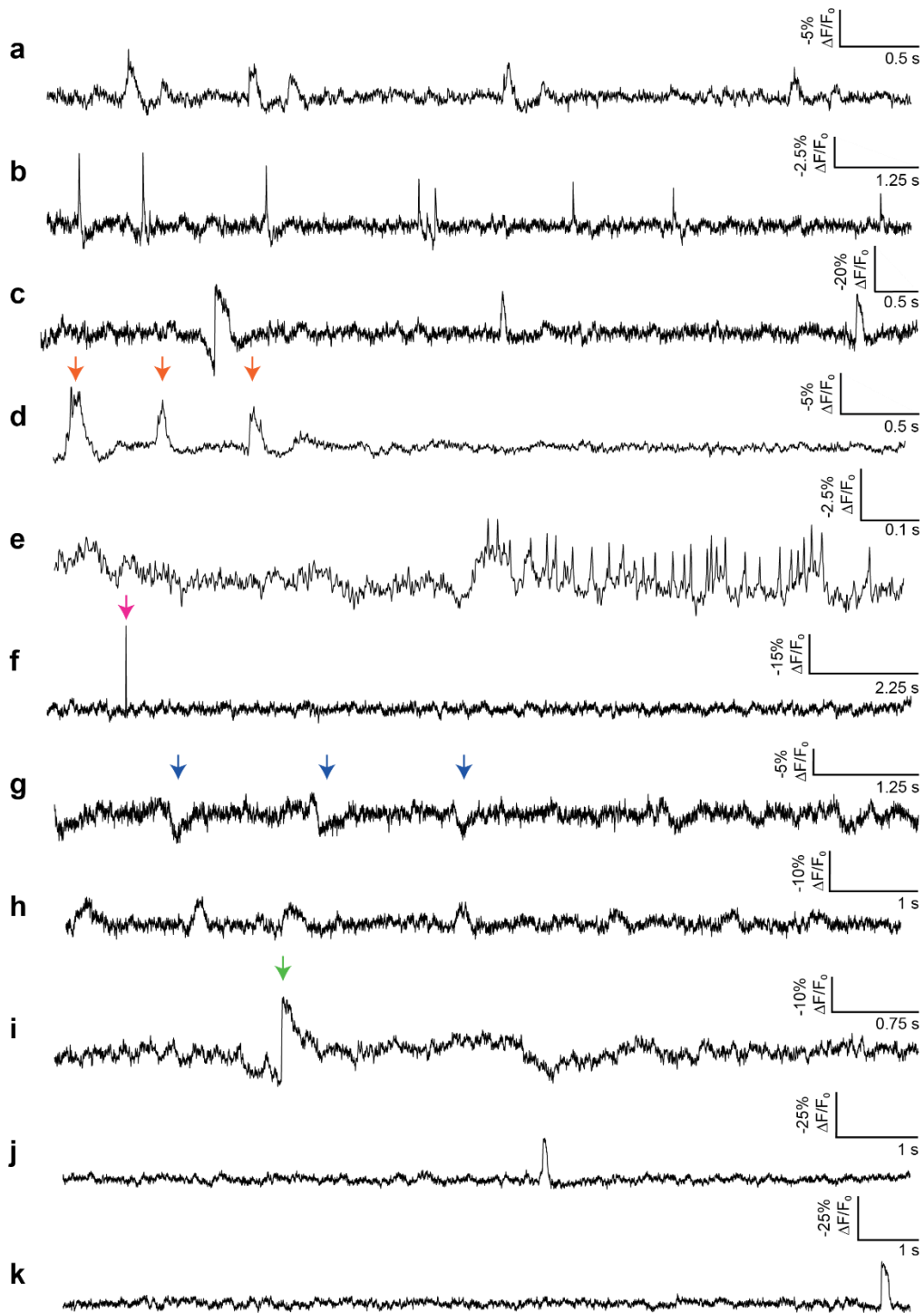
Supplementary Figure 12. Comparison of scanless two-photon voltage imaging between isolated CHO cells and densely labelled hippocampal organotypic slices. This figure accompanies Figures 2 and 3 of the main text.

(a-c) Paired comparison and Gardner-Altman plots of (a) $-\% \Delta F/F_0$, (b) number of pixels in segmentation and (c) photostability of all cells in response to protocol 1, in hippocampal organotypic slices, using two-photon, TF-GPC (power density: $0.88 \text{ mW } \mu\text{m}^{-2}$, 100 mW per cell, 100 Hz acquisition rate), calculated with Methods 1 (unweighted) and 2 (weighted). Each line represents data from individual cells ($n=10-20$). (d-g) Comparison of data obtained using protocol 1 between densely labelled hippocampal organotypic slices and CHO cells (and corresponding Gardner-Altman plots) - (d) $-\% \Delta F/F_0$, (e) SNR, (f) photostability and (g) number of pixels in segmentation. The results demonstrate that the performance of the method does not deteriorate in densely labelled slices due to the axial sectioning conferred by temporal focusing. Each point represents data from individual cells. ($n=10-20$). (h) Physiological lateral and axial resolution profiles quantified as the relative $\Delta F/F_0$ of an electrically evoked spike as a function of the distance between the excitation spot and the soma ($14 \mu\text{m}$ lateral and $13 \mu\text{m}$ axial FWHM respectively) ($n=5$).



Supplementary Figure 13. Characterisation of scanless two-photon voltage imaging for imaging trains of action potentials. *This figure accompanies Figure 3 of the main text.*

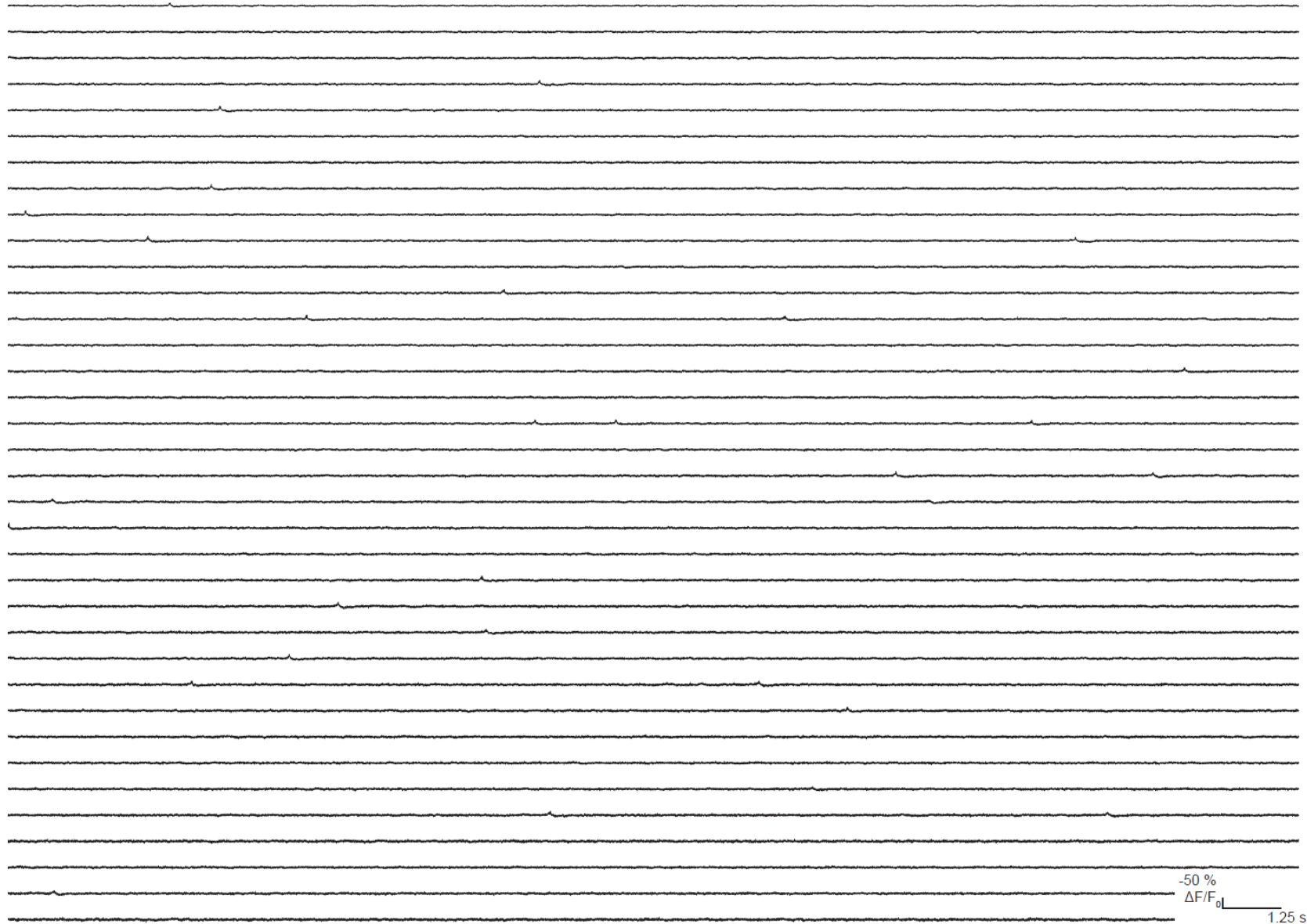
(a) Representative fluorescence traces recorded from an individual (representative) cell to different rates of electrically evoked spike trains recorded at different acquisition rates plotted in different shades of blue (see legend) (power density: $0.66 \text{ mW } \mu\text{m}^{-2}$ in all cases, 75 mW per cell). **(b)** $-\% \Delta F/F_0$ and SNR plotted as a function of action potential train rate for different acquisition rates (500 Hz, 750 Hz, 1 kHz, see legend) and power densities (as labelled). All data were acquired using laser B fixed at 920 nm, and camera B (Refer to Supplementary Figure 1 and Supplementary Tables 1 and 2).



Supplementary Figure 14. Imaging spontaneous activity in hippocampal organotypic slices with scanless two-photon voltage imaging. *This figure accompanies Figure 5 of the main text.*

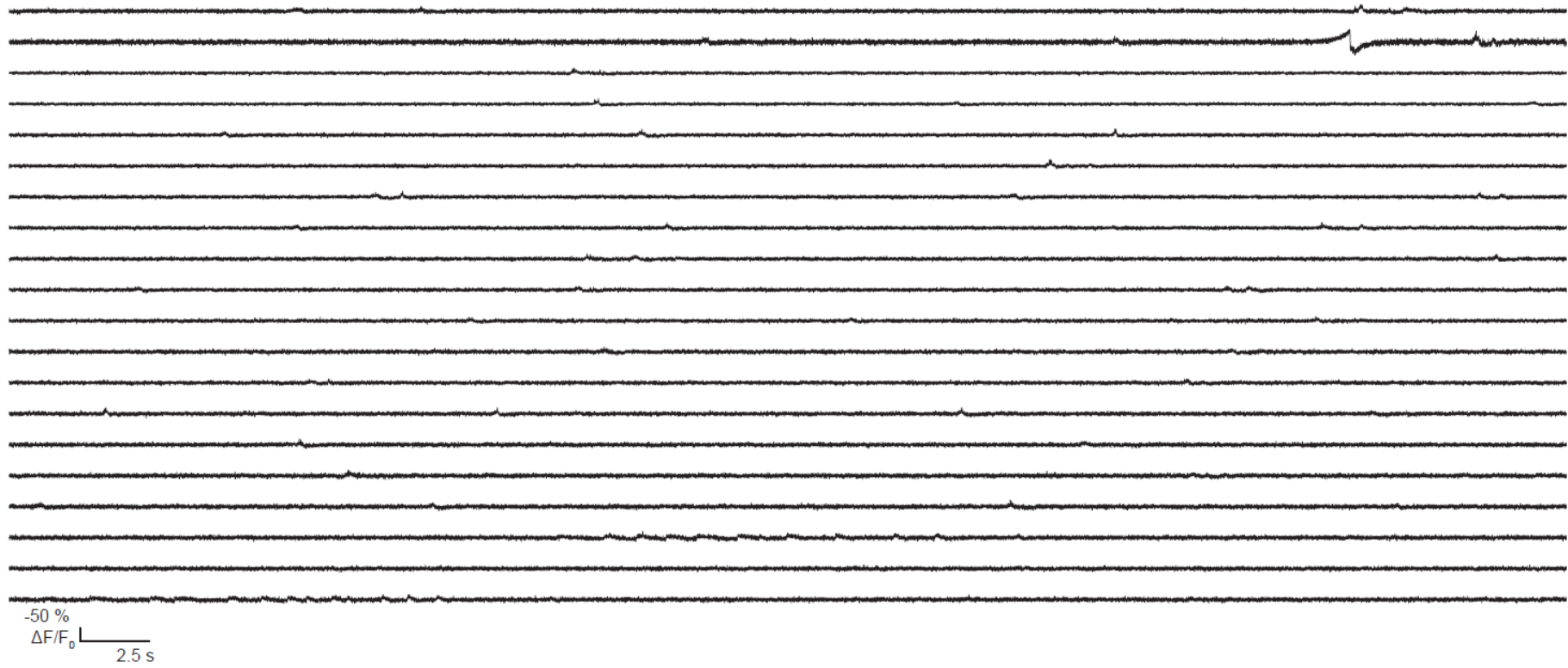
(a-k) Examples of different types of spontaneous activity recorded in single neurons expressing JEDI-2P-kv in the dentate gyrus of hippocampal organotypic slices using two-photon TF-GPC (power density: 1.33 mW μm^{-2} , 150 mW per cell, 30s continuous illumination, 1 kHz acquisition rate). Orange arrows in (d) point to rhythmic depolarizations. Pink arrow in (f) shows a single AP. Blue arrows in (g) indicate hyperpolarization events. Green arrow in (i) shows a long depolarization. As specified in the Methods, cells were not patched for the recordings presented here. All data was acquired using laser A tuned at 940 nm and camera A (See Supplementary Figure 1 and Supplementary Tables 1 and 2).

a



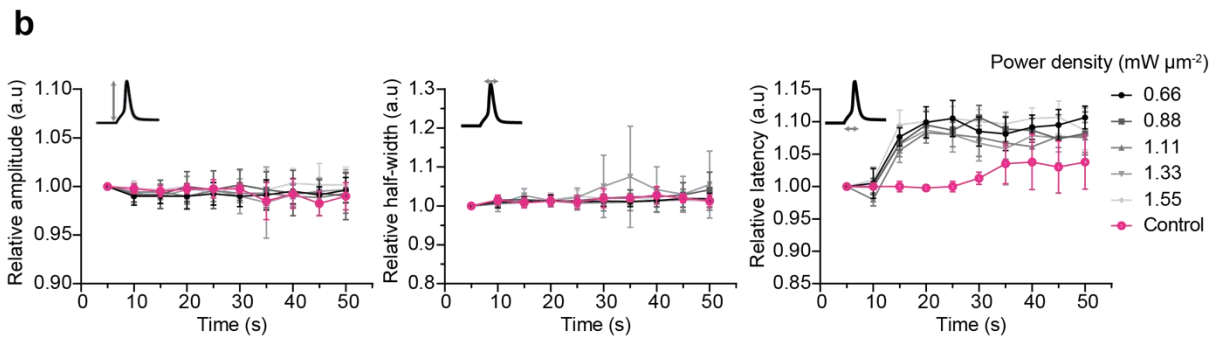
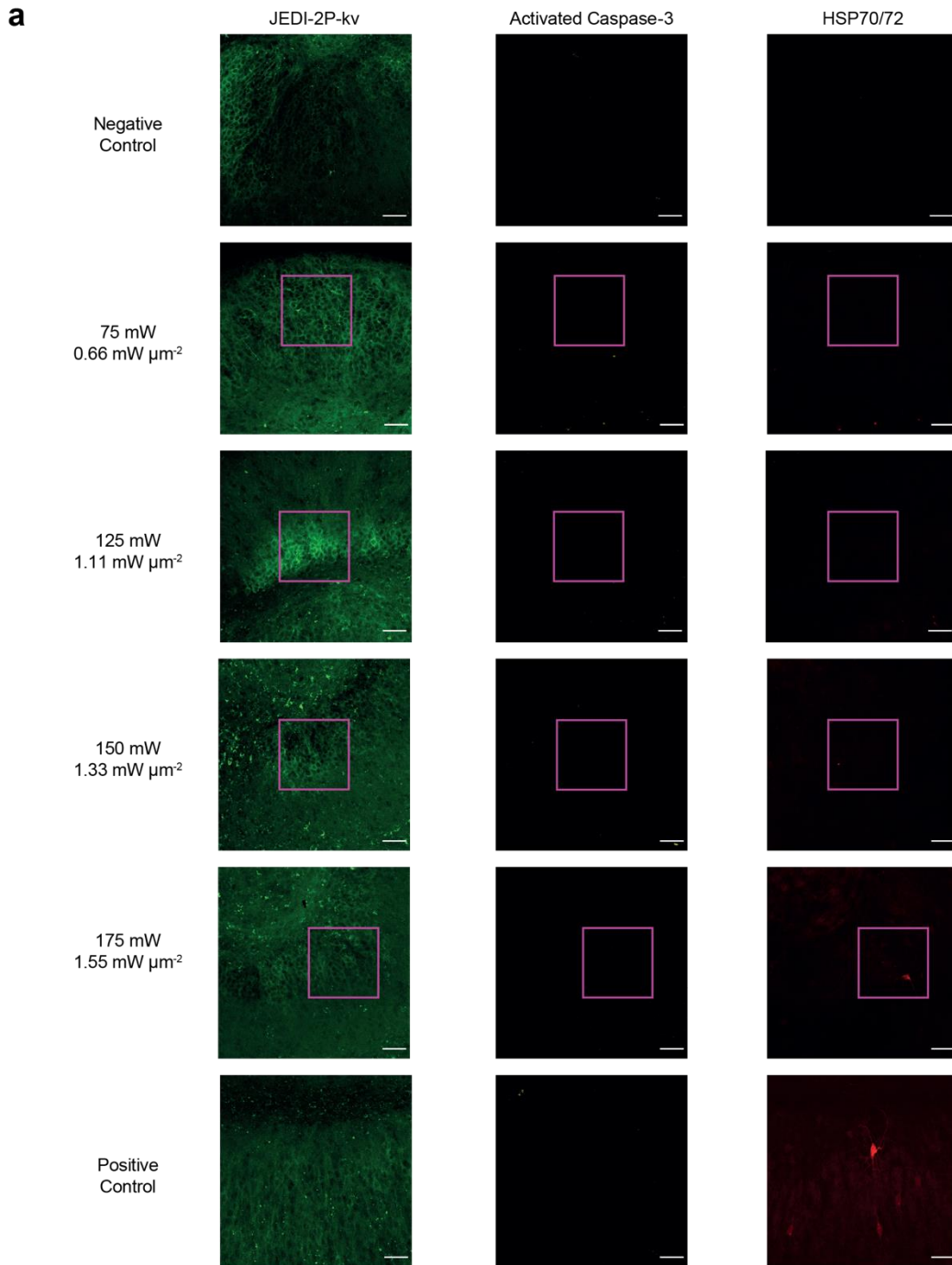
-50 %
 $\Delta F/F_0$
1.25 s

b

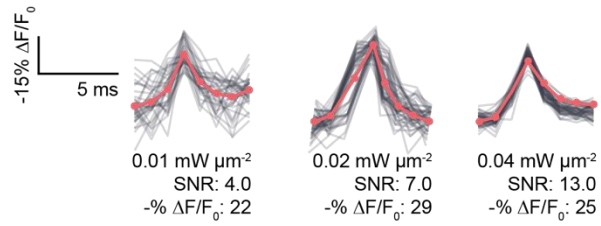
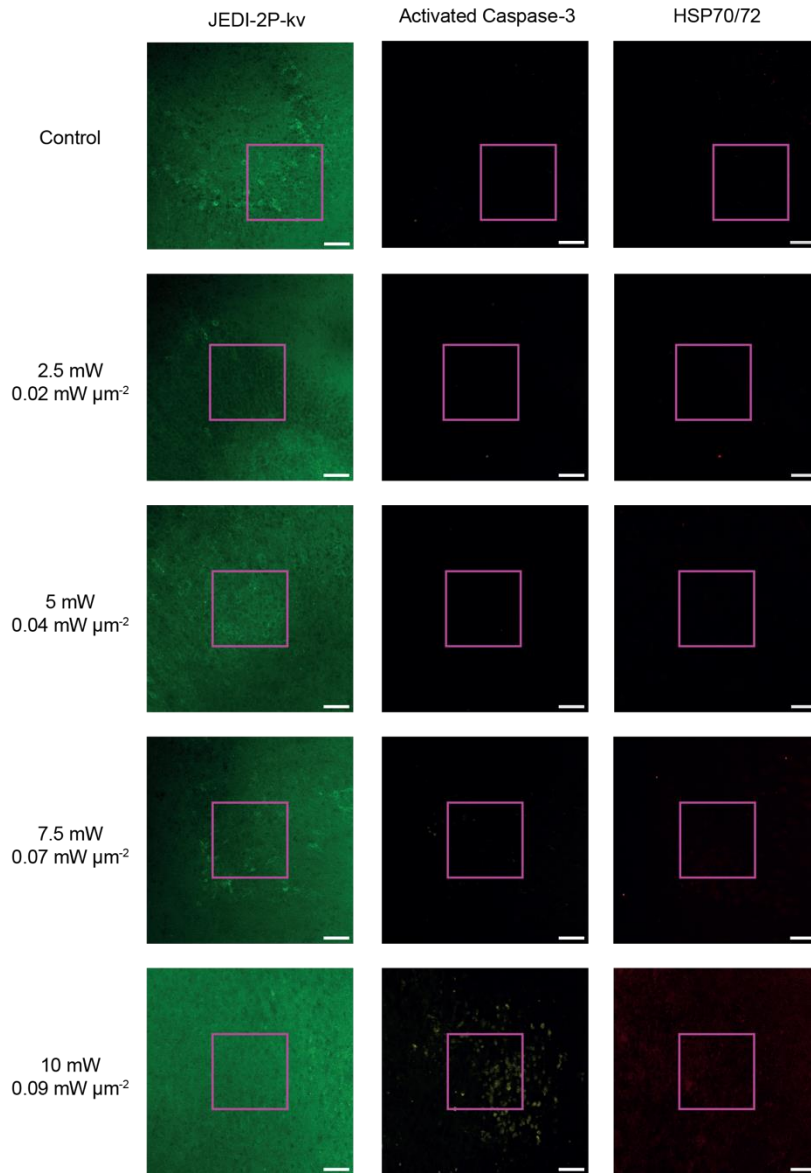
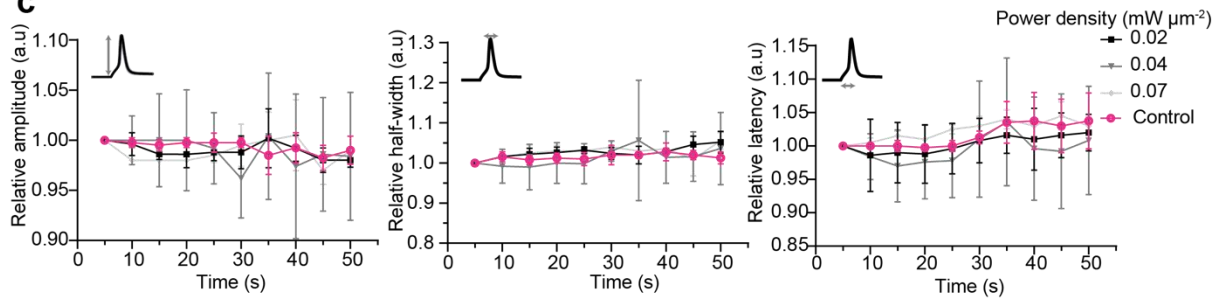


Supplementary Figure 15. Long term imaging of spontaneous activity in hippocampal organotypic slices with scanless two-photon voltage imaging.

(a) Representative traces of long-term spontaneous activity recordings in a neuron expressing JEDI-2P-kv using two-photon TF-GPC (power density: $1.33 \text{ mW } \mu\text{m}^{-2}$, 150 mW per cell, 1 kHz acquisition rate). Each line represents a single recording of 30 s with continuous illumination (refer to Methods). Zoom in for best viewing. A dark period of <10 s followed each recording. **(b)** Representative traces of long-term spontaneous activity recordings in a neuron expressing JEDI-2P-kv using two-photon TF-GPC (power density: $1.33 \text{ mW } \mu\text{m}^{-2}$, 150 mW per cell, 500 Hz acquisition rate). Each line represents a single recording of 1 min with continuous illumination (refer to Methods). All data were acquired using laser A tuned to 940 nm and camera A (Refer to Supplementary Figure 1 and Supplementary Tables 1 and 2).

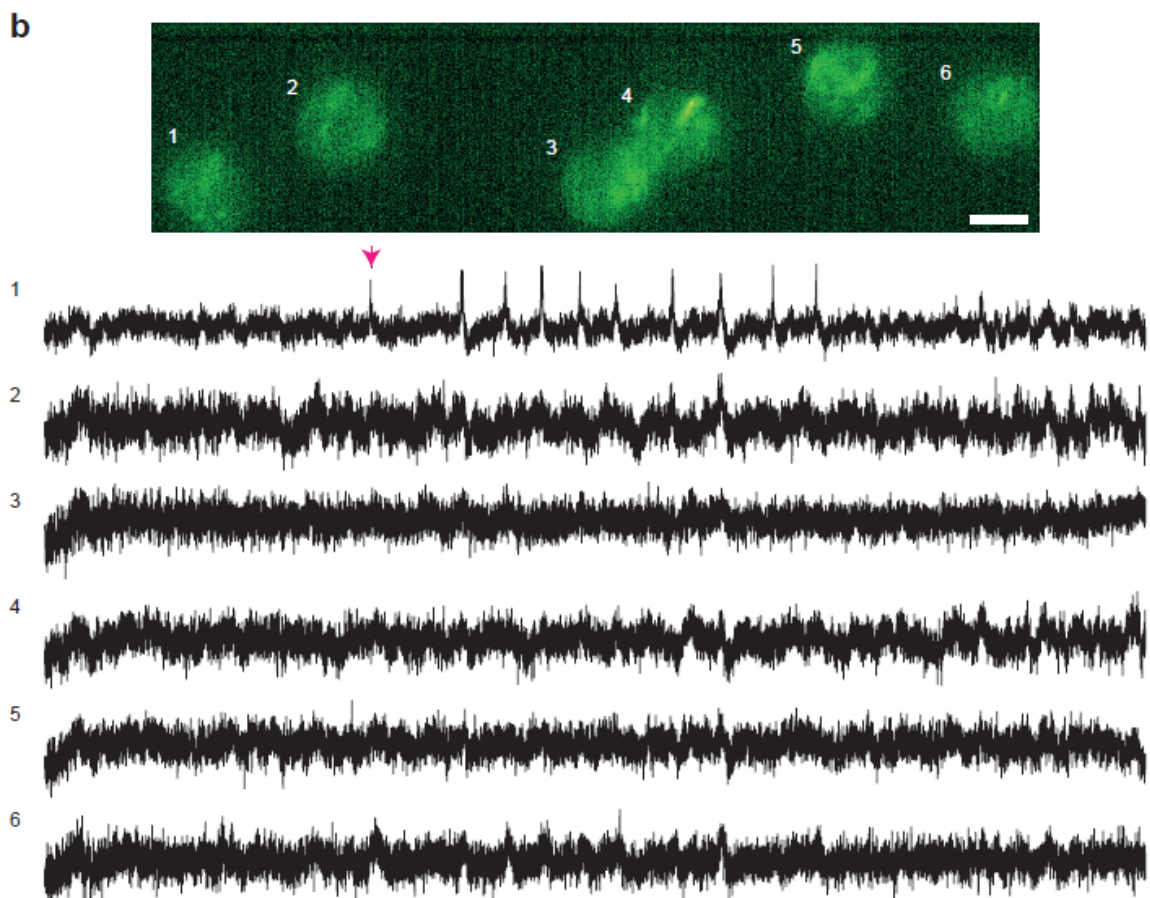
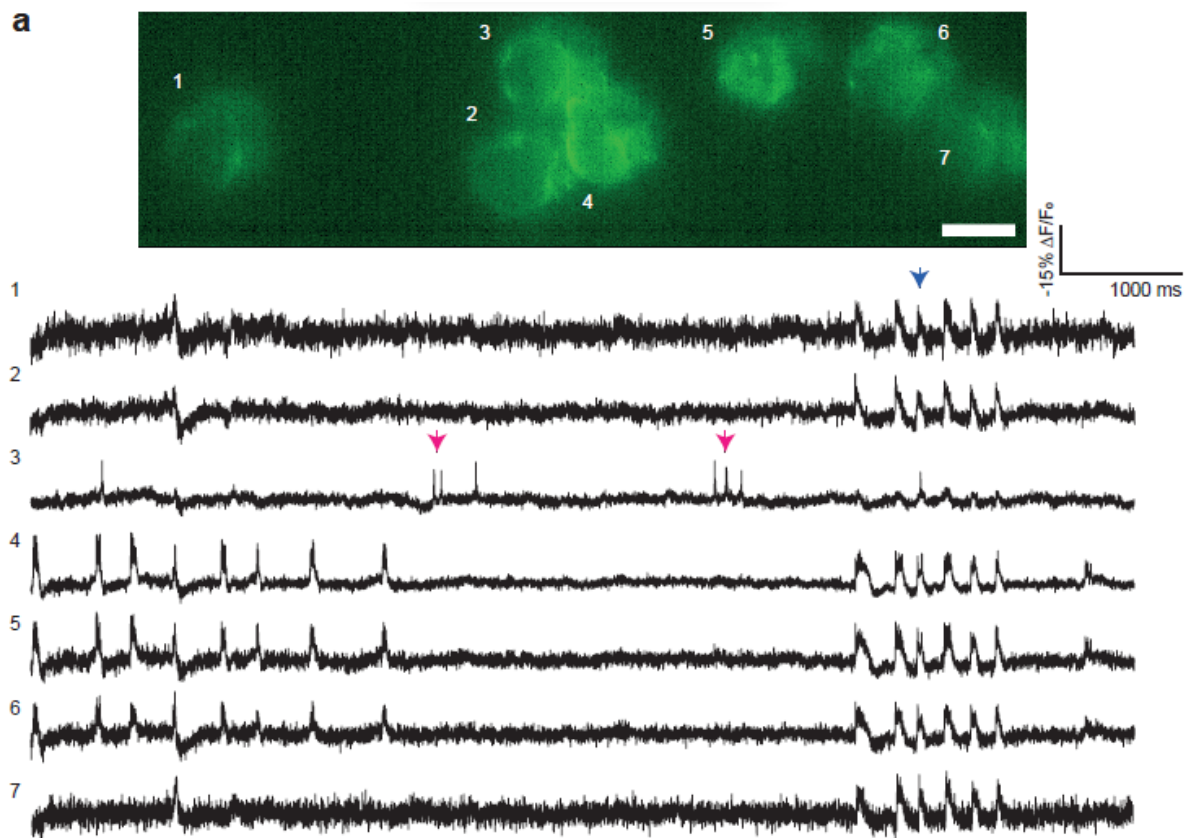


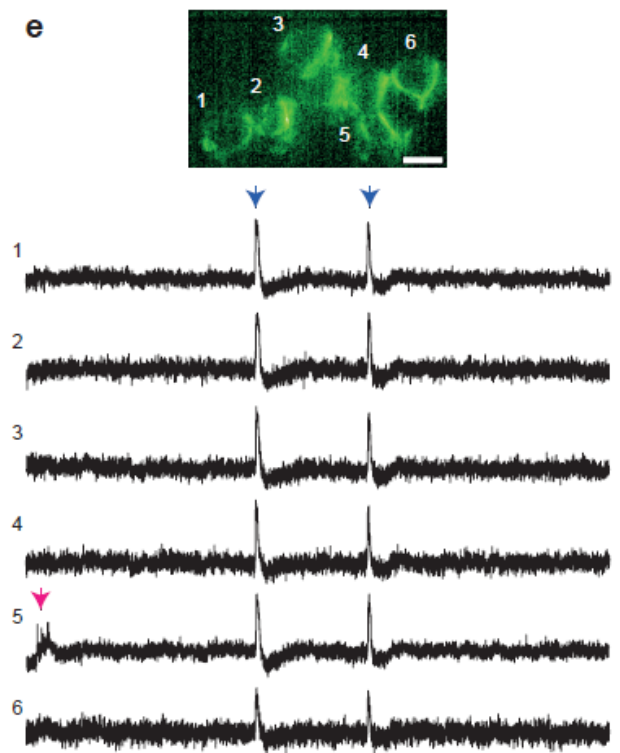
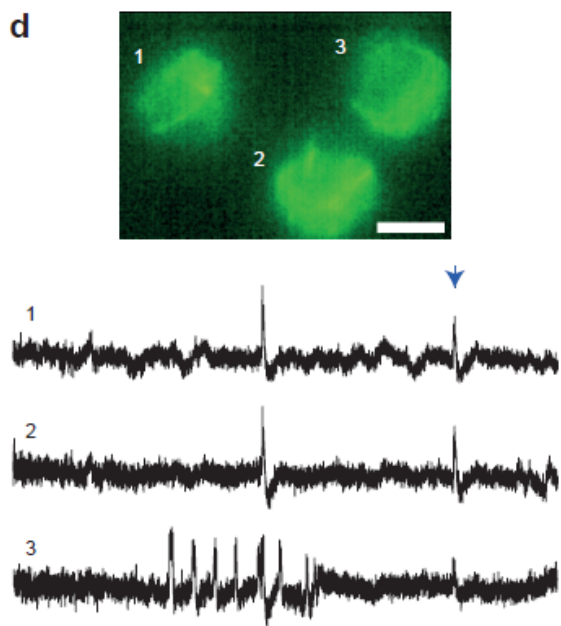
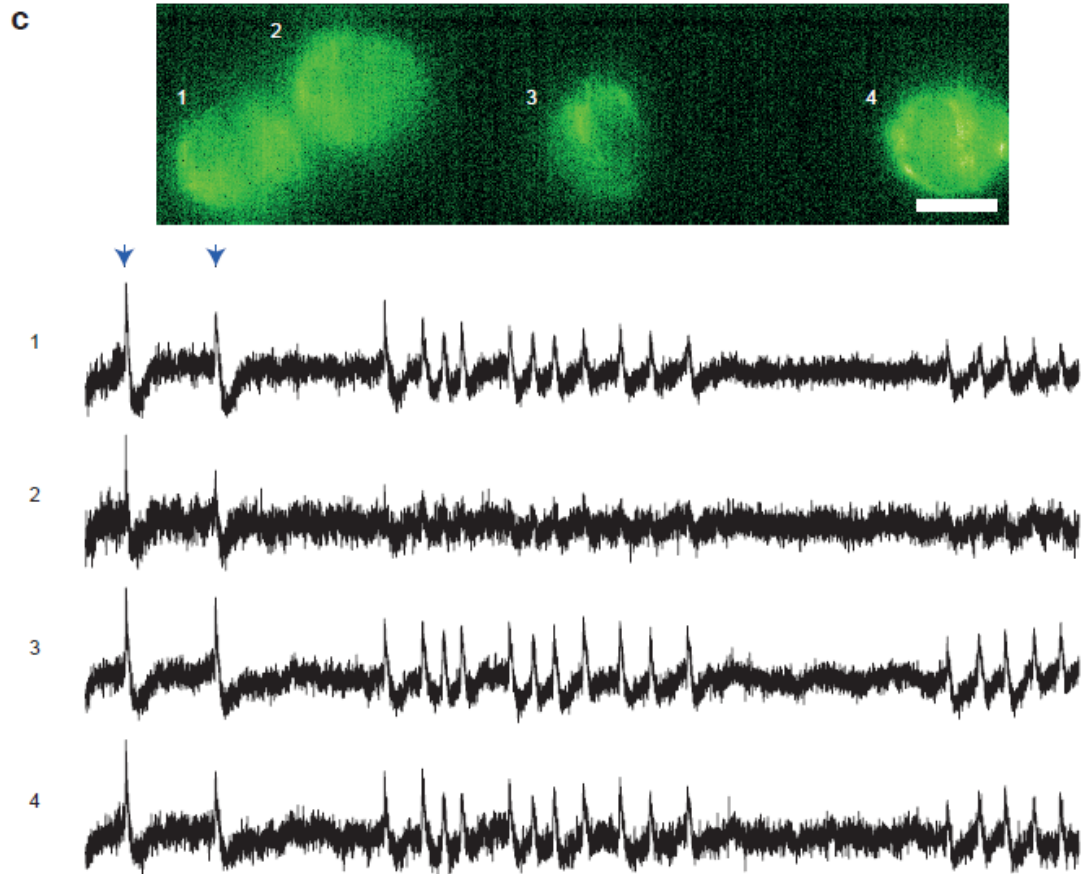
Supplementary Figure 16. Investigation of potential physiological perturbations induced by scanless two-photon voltage imaging with a high-repetition rate laser. *This figure accompanies Figure 3 – 5 of the main text.* To investigate the potential light-induced damage in illuminated cells, cells in the dentate gyrus of hippocampal organotypic slices expressing the genetically encoded voltage indicator JEDI-2P-kv were illuminated repeatedly (80 MHz, 100 fs laser source, 10-ms strobed illumination, 50 cycles, 1 Hz, total illumination time 500 ms, > 15 cells per region, targeted sequentially) at powers found necessary to detect neural activity. **(a)** Confocal images of immunolabeled hippocampal organotypic slices expressing JEDI-2P-kv (left), targeted against activated-Caspase 3 (middle) and HSP70/72 (right). A negative control (not illuminated) and a positive control (continuous and prolonged illumination (30 min) at the maximum power achievable (power density: $1.64 \text{ mW } \mu\text{m}^{-2}$, 185 mW per cell)) were performed to assess the specificity of the immunostaining. Scale bars represent $50 \mu\text{m}$. Pink boxes represent regions of illumination ($150 \mu\text{m} \times 150 \mu\text{m}^2$). **(b)** Investigation of potential light-induced changes in action potential waveforms. Amplitude (left), half-width (middle) and latency (right) of action potentials were recorded using whole-cell patch clamp electrophysiology, whilst simultaneously performing two-photon voltage imaging with TF-GPC at different power densities. The 5-point moving average was plotted (different shades of grey corresponding to different power densities, see legend). The control trace, corresponding to the case where cells were not illuminated is plotted in magenta.

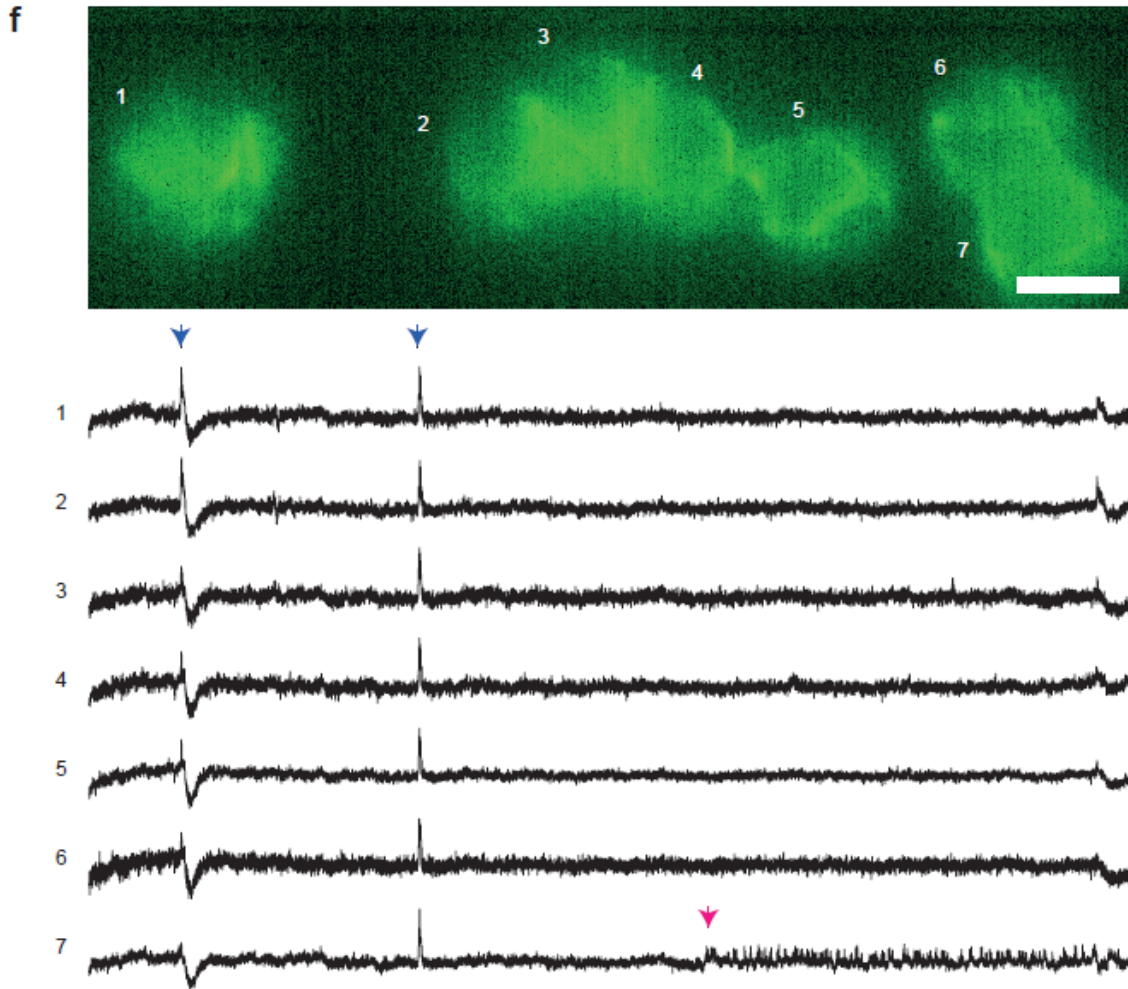
a**b****c**

Supplementary Figure 17. Investigation of potential physiological perturbations induced by scanless two-photon voltage imaging with a low-repetition rate laser. *This figure accompanies Figure 6 – 8 of the main text.*

(a) Single-trial fluorescence traces of action potentials recorded using 2P-TF-CGH and a low-repetition rate laser (250 kHz, 100 fs, 940 nm) at the following power densities: 0.01, 0.02 and 0.04 mW μm^{-2} , as labelled (1.5, 2.5 and 5 mW per cell). Traces from individual trials are plotted in grey. The average trace over 50 trials is plotted in red. An acquisition rate of 1 kHz was used in all cases. **(b)** To investigate the potential light-induced damage in illuminated cells, cells in the dentate gyrus of hippocampal organotypic slices expressing the genetically encoded voltage indicator JEDI-2P-kv were illuminated repeatedly (250 kHz, 100 fs laser source, 10-ms strobed illumination, 50 cycles, 1 Hz, total illumination time 500 ms, > 15 cells per region, targeted sequentially) at powers found necessary to detect neural activity. Confocal images of immunolabeled hippocampal organotypic slices expressing JEDI-2P-kv (left), targeted against activated-Caspase 3 (middle) and HSP70/72 (right). Scale bars represent 50 μm . Pink boxes represent regions of illumination (150 x 150 μm^2). **(c)** Investigation of potential light-induced changes in action potential waveforms. Amplitude (left), half-width (middle) and latency (right) of action potentials were recorded using whole-cell patch clamp electrophysiology, whilst simultaneously performing two-photon voltage imaging with TF-CGH at different power densities. The 5-point moving average was plotted (different shades of grey corresponding to different power densities, see legend). The control trace, corresponding to the case where cells were not illuminated is plotted in magenta.

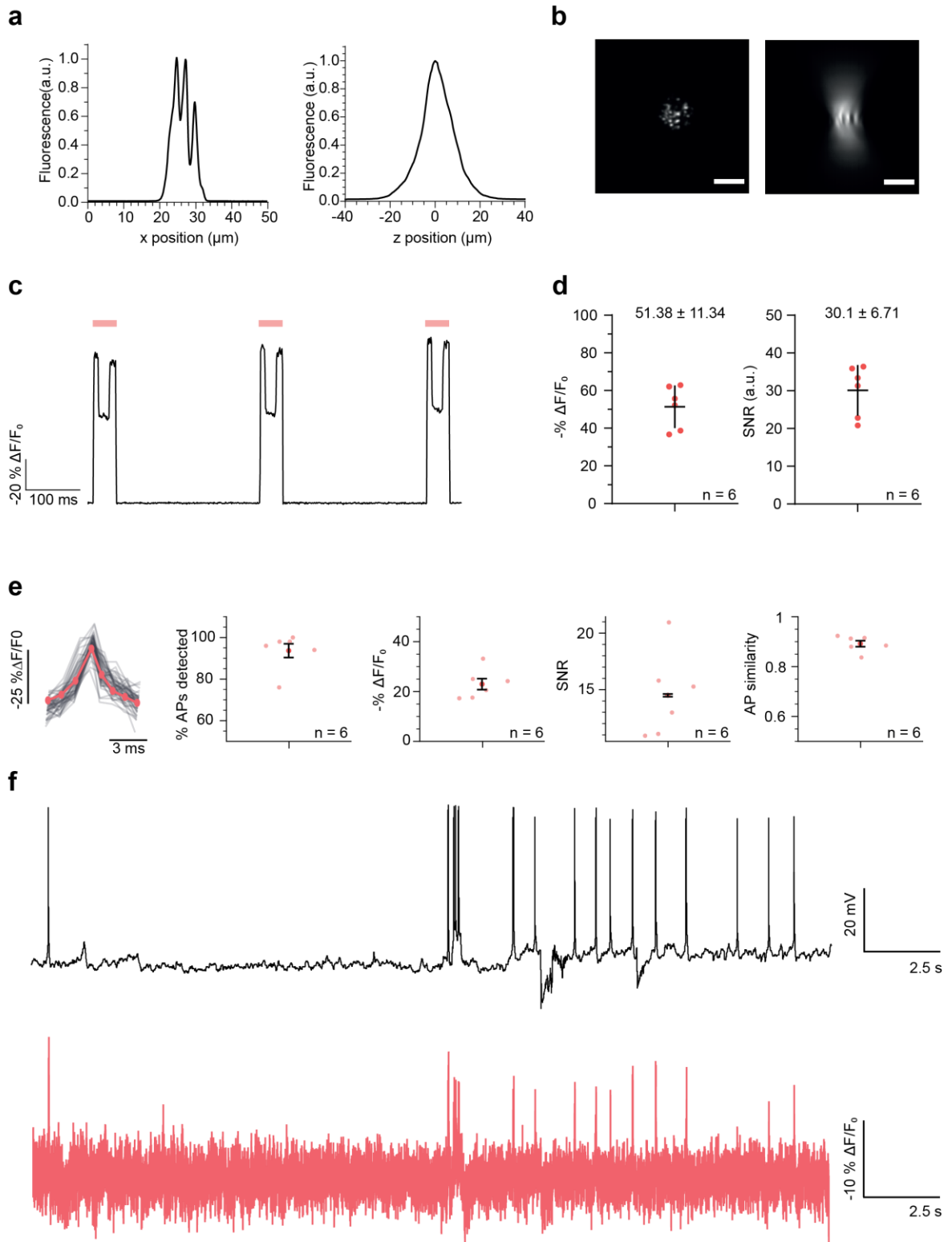






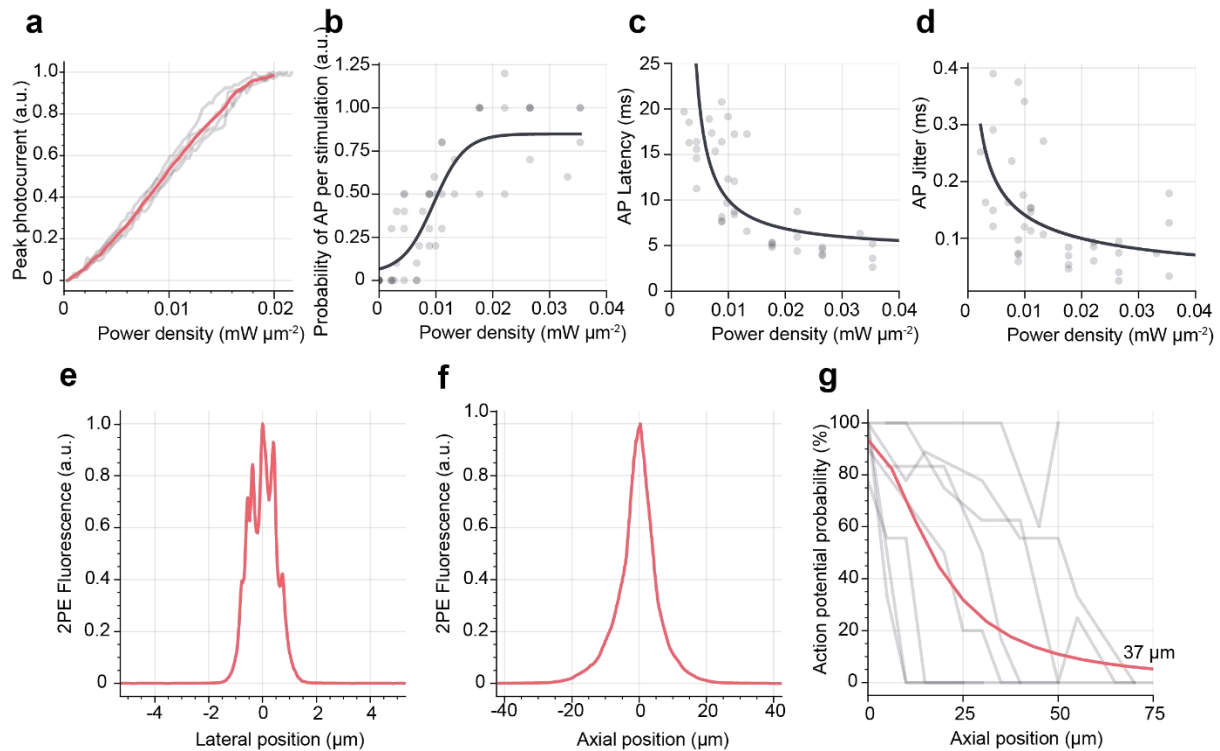
Supplementary Figure 18. Simultaneous imaging of spontaneous activity in multiple neurons in hippocampal organotypic slices with scanless two-photon voltage imaging.

Examples of different types of spontaneous activity recorded simultaneously in multiple neurons expressing JEDI-2P-kv in the dentate gyrus of hippocampal organotypic slices using 2P-TF-GPC (power densities ranging between 0.02 and 0.04 mW μm^{-2} , 2.5 – 5 mW per cell, 1 kHz acquisition rate). Note that although most cells in the same FOV are displaying the same pattern of neural activity, a known characteristic of immature hippocampal organotypic slices (blue arrows), it is still possible to detect some specific activity from adjacent individual cells (pink arrows). All data were acquired using laser C fixed at 940 nm and camera A (See Supplementary Figure 1 and Supplementary Tables 1 and 2).



Supplementary Figure 19. Characterization of two-photon voltage imaging with JEDI-2P-kv using an excitation wavelength of 1030 nm.

Characterization and recording of neural activity in JEDI-2P-kv expressing CHO cells and hippocampal organotypic slices at 1030 nm, with two-photon CGH. **(a)** Lateral (left) and axial (right) profiles of two-photon excited fluorescence generated with two-photon CGH. **(b)** Lateral (left) and axial (right) cross-sections of two-photon excited fluorescence generated with 2P-CGH. Scale bars represent 10 μm . **(c)** Representative trace showing the fluorescence response (expressed as $\% \Delta F/F_0$) to the protocol 2 in CHO cells, under illumination at 1030 nm (power density: $0.4 \text{ mW } \mu\text{m}^{-2}$, 45 mW per cell). **(d)** $\% \Delta F/F_0$ (left) and SNR (right) of data from protocol 2 for all cells. Each point represents a measurement from an individual cell. The mean and standard deviation for all cells are plotted ($n=6$). **(e)** Optically recorded action potentials resolved in single trials under 1030 nm illumination (power density = $1.21 \text{ mW } \mu\text{m}^{-2}$, 137 mW per cell). Single trials are plotted in grey. The average trace across all trials is plotted in red (left). Percentage of action potentials detected, $\% \Delta F/F_0$, SNR and action potential similarity are plotted (right). Each point represents the average from an individual cell. The mean and the standard deviation for all cells are plotted ($n = 6$). **(f)** Simultaneous current clamp (upper) and fluorescence recording (lower) of spontaneous activity in neurons from hippocampal organotypic slices over a continuous 30 s recording period, under 1030 nm illumination (power density: $1.21 \text{ mW } \mu\text{m}^{-2}$, 137 mW per cell). All data were acquired using laser A tuned at 1030 nm and camera A (See Supplementary Figure 1 and Supplementary Tables 1 and 2).



Supplementary Figure 20. Electrophysiological characterization of photostimulation of neurons expressing ChroME-ST in the dentate gyrus of hippocampal organotypic slices. *This figure accompanies Figures 7 and 8 of the main text.*

Characterisation of ChroME-ST in CHO cells and in the dentate gyrus of hippocampal organotypic slices co-expressing ChroME-ST and JEDI-2P-kv. **(a)** Peak photocurrent in response to a 17.5 ms pulse of light plotted as a function of power density (940 nm, 250 kHz repetition rate, 100 fs pulse duration source and 12 μm circular holographic spots) measured in CHO cells ($n = 4$). **(b)** Light-evoked AP probability, **(c)** light-evoked AP latency and **(d)** light-evoked AP jitter (see Methods) measured in neurons plotted as a function of power density. Individual points correspond to data obtained from different cells. Traces correspond to the average result calculated across all cells ($n = 7$). **(e-f)** Lateral and axial excitation profiles of two-photon excited fluorescence from a thin rhodamine layer by two-photon TF-CGH. **(g)** The physiological axial resolution of photoactivation measured as the action potential probability as a function of axial displacement between the cell soma and the excitation spots. Action potentials were recorded using patch clamp electrophysiology and the action potential probability is reported as the fraction of times a cell fired during photostimulation across 5 repeats. The grey lines correspond to trials across all cells ($n = 8$) and the red line corresponds to the interpolated fit of the average of all trials across all cells. The FWHM of this interpolated curve is 37 μm . All data were acquired using laser C fixed at 940 nm and camera A (See Supplementary Figure 1 and Supplementary Tables 1 and 2).

Supplementary References

1. Kuhn, B. & Roome, C. J. Primer to voltage imaging with ANNINE dyes and two-photon microscopy. *Front. Cell. Neurosci.* 13, 1–15 (2019).
2. Cundy, H. M. & Rollett, A. P. *Mathematical models.* (Tarquin Publications, 1989).
3. Xiao, S. et al. Large-scale voltage imaging in behaving mice using targeted illumination. *iScience* 24, (2021).
4. Adam, Y. et al. Voltage imaging and optogenetics reveal behaviour-dependent changes in hippocampal dynamics. *Nature* 569, 413–417 (2019).
5. Fan, L. Z. et al. All-Optical Electrophysiology Reveals the Role of Lateral Inhibition in Sensory Processing in Cortical Layer 1. *Cell* 180, 521–535.e18 (2020).
6. Ventalon, C. & Mertz, J. Quasi-confocal fluorescence sectioning with dynamic speckle illumination. *Opt. Lett.* 30, 3350–3352 (2005).
7. Oron, D., Tal, E. & Silberberg, Y. Scanningless depth-resolved microscopy. *Opt. Express* 13, 1468–1476 (2005).
8. Zhu, G., van Howe, J., Durst, M., Zipfel, W. & Xu, C. Simultaneous spatial and temporal focusing of femtosecond pulses. *Opt. Express* 13, 2153–2159 (2005).
9. Andrasfalvy, B. K., Zemelman, B. V., Tang, J. & Vaziri, A. Two-photon single-cell optogenetic control of neuronal activity by sculpted light. *Proc. Natl. Acad. Sci. U. S. A.* 107, 11981–11986 (2010).
10. Rickgauer, J. P., Deisseroth, K. & Tank, D. W. Simultaneous cellular-resolution optical perturbation and imaging of place cell firing fields. *Nat. Neurosci.* 17, 1816–1824 (2014).
11. Mardinly, A. R. et al. Precise multimodal optical control of neural ensemble activity. *Nat. Neurosci.* 21, 881–893 (2018).
12. Bègue, A. et al. Two-photon excitation in scattering media by spatiotemporally shaped beams and their application in optogenetic stimulation. *Biomed. Opt. Express* 4, 2869–2879 (2013).
13. Chaigneau, E. et al. Two-photon holographic stimulation of ReaChR. *Front. Cell. Neurosci.* 10, 234 (2016).
14. Ronzitti, E. et al. Sub-millisecond optogenetic control of neuronal firing with two-photon holographic photoactivation of Chronos. *J. Neurosci.* 37, 10679–10689 (2017).
15. Chen, I.-W. et al. In Vivo Submillisecond Two-Photon Optogenetics with Temporally Focused Patterned Light. *J. Neurosci.* 39, 3484–3497 (2019).
16. Papagiakoumou, E. et al. Scanless two-photon excitation of channelrhodopsin-2. *Nat. Methods* 7, 848–854 (2010).
17. Papagiakoumou, E. et al. Functional patterned multiphoton excitation deep inside scattering tissue. *Nat. Photonics* 7, 274–278 (2013).
18. Theer, P. & Denk, W. On the fundamental imaging-depth limit in two-photon microscopy. *J Opt Soc Am A Opt Image Sci Vis* 23, 3139–3149 (2006).

19. Theer, P., Hasan, M. T. & Denk, W. Two-photon imaging to a depth of 1000 μm in living brains by use of a Ti : Al₂O₃ regenerative amplifier. *Opt. Lett.* 28, 1022–1024 (2003).
20. Song, A. et al. Volumetric Two-photon Imaging of Neurons Using Stereoscopy (vTwINS). *Nat. Methods* 14, 420–426 (2017).
21. Wu, J. et al. Kilohertz two-photon fluorescence microscopy imaging of neural activity in vivo. *Nat. Methods* 17, 287–290 (2020).
22. Zhang, T. et al. Kilohertz two-photon brain imaging in awake mice. *Nat. Methods* 16, 1119–1122 (2019).
23. Prevedel, R. et al. Fast volumetric calcium imaging across multiple cortical layers using sculpted light. *Nat. Methods* 13, 1021–1028 (2016).
24. Cai, C. et al. VolPy: Automated and scalable analysis pipelines for voltage imaging datasets. *PLoS Comput. Biol.* 17, 1–27 (2021).
25. Abdelfattah, A. S. et al. Bright and photostable chemigenetic indicators for extended in vivo voltage imaging. *Science* (80-.). 365, 699–704 (2019).
26. Buchanan, E. K. et al. Penalized matrix decomposition for denoising, compression, and improved demixing of functional imaging data. 1–36 (2018).
27. Sjulson, L. & Miesenböck, G. Rational optimization and imaging in vivo of a genetically encoded optical voltage reporter. *J. Neurosci.* 28, 5582–5593 (2008).
28. Liu, Z. et al. Sustained deep-tissue voltage recording using a fast indicator evolved for two-photon microscopy. *Cell* 185, 3408–3425.e29 (2022).
29. Van Der Walt, S. et al. Scikit-image: Image processing in python. *PeerJ* 2014, 1–18 (2014).
30. Ho, J., Tumkaya, T., Aryal, S., Choi, H. & Claridge-Chang, A. Moving beyond P values: data analysis with estimation graphics. *Nat. Methods* 16, 565–566 (2019).